ROMA TRE
UNIVERSITÀ DEGLI STUDI

Dipartimento di Matematica e Fisica
PhD in Physics, XXXV Cycle

# The role of future high-precision long-baseline neutrino experiments in constraining BSM models

**Candidate**
Alessio Giarnetti

**Supervisor**
Prof. Davide Meloni

**Coordinator**
Prof. Giuseppe Degrassi

# Contents

# Introduction

The attempt to describe the behaviour of Nature accompanied the human development. At the end of the XIX century, the incredible technological boost allowed scientists to successfully explain macroscopic phenomena using microscopic principles. If, in the beginning, the experimental observations came before the theoretical explanations, in the first decades of the XX century, particle physics studies started to predict the presence of phenomena which would have been observed only years later. This happened in the 1930, when Wolfgang Pauli noticed that, being the $\beta$-decay electron spectrum continuous, a third invisible particle had to be involved. This particle, with null electric charge and extremely light (or massless), was baptized *neutrino* by Enrico Fermi, that in 1934 developed a theory to explain the nuclear $\beta$-decays [1]. The physics community was eager to observe this particle, which seemed to be necessary to explain the experimental results. However, a light neutral particle could not be seen directly in a detector; for this reason, it was clear that neutrinos could only be observed detecting the charged products of their interactions with other particles. In order to do so, physicists required a neutrino source; fortunately, in those years the research about nuclear fission was very vivid and several nuclear plants were available. Since in fission chains $\beta$-decays occur, it was clear that if neutrinos were real, nuclear plant should have been able to provide a large number of neutrinos. However, the Fermi theory predicted a very crucial feature: the neutrino cross sections are extremely small and for this reason their interactions are very rare. It took 20 years to develop a technology adequate to neutrino observation: Clyde Cowans and Fred Reines, placing a detector near to the Savannah River nuclear plant, observed for the first time in 1956 neutrinos [2] through the inverse $\beta$-decay (IBD) reaction

$$\bar{\nu}_e + p \longrightarrow e^+ + n \,. \tag{1}$$

This discovery not only confirmed the existence of a particle postulated 26 years in advance, but also boosted the particle physics research in the neutrino sectors in the theoretical, phenomenological and experimental fields. Indeed, neutrino studies have always been challenging and required a huge scientific effort.

The 1936 discovery of a heavier counterpart of the electron, namely the muon [3], suggested that for each particle, there may exist a few copies with different masses. Thus, after the discovery of the first neutrinos, which coupled to electrons coming from $\beta$-decays, the experimental community started to search for a second neutrino. In 1962, at Brookhaven National Laboratories, Lederman, Schwartz and Steinberg, were able to create and detect a muon neutrino beam from pion decays [4]. One more time, theoretical predictions were confirmed. When in 1975 a third charged lepton, the $\tau$, was observed [5, 6], it became evident that a third neutrino should have existed. But, in this case, its discovery was not so straight-forward. First of all, muon neutrinos can easily be obtained using light meson decays, while tau neutrinos, being always coupled to the heavy $\tau$ lepton, can only come from heavy (charmed, for instance) hadrons, which are clearly more complicated to produce. Moreover, the charged current interactions of neutrinos (like the IBD), which allow to both observe the particle and determine its flavor, in the $\nu_\tau$ case, require high neutrino energies, higher than 3 GeV. 25 years after the $\tau$ lepton discovery, in 2000, the DONUT experiment was able to observe 4 tau neutrinos [7], finding the latest of the leptons. In this experiment, high energy protons interactions were used to produce charmed meson, whose

decays generated neutrinos of all three flavors; using a very performing detector, some events in which a $\tau$ lepton appeared after a neutrino interaction were observed.
Besides the first detection of the three neutrinos, a certain number of neutrino experiments were built in the second half of the XX century. One of their main goal was to observe neutrinos from different sources: the Sun, the atmosphere, supernovae, particle accelerators or nuclear reactors. In particular, solar neutrinos, which come from nuclear fusion reactions, were very interesting, since their abundance is a direct probe of the inner solar composition. The astrophysicist John Bahcall, together with the particle physicists Raymond Davis Jr., in 1960 developed the idea of a detector able to observe solar neutrinos [8] through the radiochemical reaction

$$\nu_e + {}^{37}\mathrm{Cl} \longrightarrow {}^{37}\mathrm{Ar}^+ + e^- \,. \tag{2}$$

In order to lower the background this detector was placed underground in the Homestake mine and lasted from 1970 to 1994. The conclusions [9] were very interesting: solar neutrinos were observed, but their flux was not compatible to any of the solar models. In particular, only 1/3 of the neutrinos predicted by Bahcall seemed to reach the detector. The *solar neutrino problem* started a debate in the scientific community about its origin. The final answer to the problem came in the 1998. The Super-Kamiokande experiments, looking at neutrinos from the atmosphere, observed that, depending on the distance they travelled, the flavor composition of atmospheric neutrinos was different [10]. This suggested that neutrinos undergo the phenomenon of *flavor oscillation*. Flavor oscillations are caused by the fact that the mass states do not correspond to the flavor ones and for this reason, while propagating, particles can change their flavor. The neutrino oscillation hypothesis, which was first studied by Pontecorvo in 1950s [11] and then by Nakagawa, Maki and Sakata [12] in the 1960s, was also able to explain the solar neutrino deficit, but introduced a problem in the particle physics framework: if neutrinos oscillate, they must have a mass. However, this mass is so small that we have not been able to observe it so far; a natural explanation of such small masses is one of the most appealing theoretical aspects of the neutrino sector.
Going back to neutrino oscillations, it can be easily shown that, at least in the standard particle physics approach, they are governed by only 6 parameters: three mixing angles, one CP-violating phase, and the two independent neutrino mass differences (or mass splittings). Differently from the quark sector, in which the oscillation phenomenon is well known since 1960s, neutrino oscillations are characterized by large mixing angles [13]. Moreover, the two mass splittings turned out to be very different; this allowed to search for oscillation in different regimes and using neutrinos from several natural and artificial sources.
In roughly 25 years, oscillation experiments were able to measure almost all the oscillation parameters (only the CP-violating phase is mostly unknown) with a few percents uncertainty. However, other than the phase determination, there are also other open questions in the neutrino oscillation framework; for instance, it is still unknown which of the three mass eigenstates is the heaviest. Indeed, while the sign of the smallest of the two mass splittings has been measured ($m_2^2 - m_1^2 > 0$), the sign of the largest one ($m_3^2 - m_1^2$) is still undetermined. For this reason a few next-generation oscillation experiments are being currently built. Among them, future long baseline accelerator experiments, which use artificial neutrino beams coming from a particle accelerator facility, are very promising. In particular, DUNE [14] in the USA and T2HK [15] in Japan are expected to determine the oscillation parameters with a great precision. For this reason, oscillation measurements in the next decades may be able to catch also tiny new physics effects. Indeed, there exists several Beyond the Standard Model (BSM) models which modify the oscillation probabilities at the percent level. These models may introduce new particles which mix with neutrinos (like light or heavy sterile neutrinos) or new interactions in the leptonic sector. Studies about the capabilities of future experiments in constraining these BSM models suggest that DUNE and T2HK should be be very promising in this context. In this dissertation, we will present some results about the performances of future Long Baseline (LBL) experiments

obtained in [16] (short discussion in Sec. 4.1.4), [17] (Sec. 5.2), [18] (Sec. 5.3), [19] (Sec. 6.1), [20] (Sec. 6.2), [21] (Sec. 6.3) and [22] (Sec. 6.4). The scope of this thesis is to clearly show how the rich phenomenology of the long-baseline experiments is crucial to extend our knowledge about neutrino physics. In particular, we want to underline that the extremely large number of events that the future long-baseline experiments will observe can be analyzed to provide precise measurements of the standard oscillation parameters and give a great opportunity where to search for several different new physics effects. To this aim, in the following chapters we suggest some strategies which can be adopted in order to maximize the sensitivity of the experiments to standard and new physics parameters, taking full advantage of the unprecedent richness of the DUNE and T2HK datasets.
The thesis will be organized as follows. In Chapter 1, the Standard Model of particles will be briefly described, with a focus on the role of neutrinos. In Chapter 2, the phenomenon of neutrino oscillation will be discussed in details and the current experimental results on the measurements of oscillation parameters will be presented. In Chapter 3 we will go beyond the Standard Model, describing how new physics models may affect neutrino oscillations. In particular, we will have a closer look to a few of them, namely the sterile neutrino, the Non Standard Interactions, the neutrino decay and the Non Unitarity models. In Chapter 4, the main features of the two future LBL experiments DUNE and T2HK will be presented. Finally, the main results of this dissertation will be extensively discussed in Chapters 5 and 6. In the former, after a description of the software used for the experiments simulations, we will show two examples on how the complementarity between DUNE and T2HK experiments can be used to improve measurements in the standard oscillation framework and in a BSM model (the Non-Unitarity model). In the latter, we will propose four new approaches to bound different BSM models at DUNE.

# Chapter 1

# Neutrinos and the Standard Model

Since the beginning of our history, we have been aware of the fact that there are some fundamental forces behind natural phenomena. In our current knowledge, we can distinguish four of them: electromagnetic, weak, strong and gravity forces. Quantum field theory [23–25] allowed us to describe in only one theory the first three. This theory, based on the local symmetry $SU(3) \times SU(2) \times U(1)$ is called Standard Model (SM) of particles. The SM is one of the most successful models in physics, being able to predict with an astonishing precision different processes.

The Standard Model describes three of the fundamental forces as mediated by the exchange of particles, in particular spin 1 bosons. The matter particles, on the other hand, are divided in three generation of spin 1/2 fermions, each of them including two quarks and two leptons. The symmetry principles that are behind the construction of the standard model predict that all the particles must be massless. However, we observe that most of the particles we know do have masses [13]. The mechanism that generates such masses is a spontaneous symmetry breaking (SSM) process called Higgs mechanism [26–29]. The particle responsible of this mechanism is a spin 0 boson, the Higgs boson, which completes the particle content of the SM. This particle, introduced in the theory in the 1964 has been observed in 2012 at the Large Hadron Collider [30, 31] confirming the incredible predictive power of the SM.

Despite its great success [32–36], the Standard Model still fails to explain some very important phenomena [37–43]. One of them, will be central topic of this dissertation: neutrino oscillation. We will discuss it in details in the next chapter.

## 1.1 Gauge interactions and particle content

In the SM, fundamental interactions are described by a Yang-Mills theory [44] based on the non-Abelian local (gauge) symmetry group $SU(3)_C \times SU(2)_L \times U(1)_Y$ where C denotes color, L left-handed chirality and Y the weak hypercharge. The generators of this large group are the mediators of the fundamental forces. In particular, the color-charged eight generators of $SU(3)_C$ are the strong force mediators and are called *gluons*. The four generators of the $SU(2)_L \times U(1)_Y$ are on the other hand the mediators of the electromagnetic and weak forces. The gauge bosons lagrangian can be written as

$$\mathcal{L}_{gb} = -\frac{1}{4}[F_{\mu\nu}F^{\mu\nu} + K^i_{\mu\nu}K^{i\mu\nu} + V^j_{\mu\nu}V^{j\mu\nu}]\,, \tag{1.1}$$

where $F_{\mu\nu}$, $K^i_{\mu\nu}$ (i=1,2,3) and $V^j_{\mu\nu}$ (j=1...8) are the field strength tensors for $U(1)_Y$, $SU(2)_L$ and $SU(3)_C$ respectively, which can be written as

$$
\begin{aligned}
F_{\mu\nu} &= \partial_\mu B_\nu - \partial_\nu B_\mu && (1.2)\\
K^i_{\mu\nu} &= \partial_\mu W^i_\nu - \partial_\nu W^i_\mu + g\varepsilon^{ijk} W^j_\mu W^k_\nu && (1.3)\\
V^i_{\mu\nu} &= \partial_\mu G^i_\nu - \partial_\nu G^i_\mu + g'' f^{ijk} G^j_\mu G^k_\nu && (1.4)
\end{aligned}
$$

In these equations, $B_\mu$, $W^i_\mu$ and $G^j_\nu$ are the twelve vector bosons fields which mediate the three fundamental forces described by the SM. Moreover, g and g" are the gauge couplings of $SU(2)_L$ and $SU(3)_C$ and $\varepsilon^{ijk}$ and $f^{ijk}$ are the structure constants of the two groups.

The fermions in the SM are described by the Dirac free massless fermion lagrangian

$$
\mathcal{L}_f = i\bar{\psi}\partial\!\!\!/\psi\,, \tag{1.5}
$$

which, in order to be invariant under the SM symmmetry group, must be modified using the substitution

$$
\partial_{mu} \to D_\mu = \partial_\mu - ig' B_\mu \frac{Y}{2} - igW^i_\mu \tau^i - ig_S G^j_\mu a^j \tag{1.6}
$$

where $g$, $g'$ and $g_S$ are the gauge couplings, Y/2 is the hypercharge operator, $\tau^i$ and $a^j$ are the non-abelian groups generators acting on the $\psi$ field. Mass terms, which can be written as $m\bar{\psi}\psi$ are not invariant under the group $SU(2)_L$, which act differently for the left-handed and right-handed components of the spinors[1]. For this reason, at this point, the SM predict all the fermions to be massless just like the gauge bosons.
We can divide the SM fermions in quarks and leptons. The quarks are organized in a $SU(2)_L$ doublet

$$
Q_L = \begin{pmatrix} u_L \\ d_L \end{pmatrix} \tag{1.7}
$$

and two $SU(2)_L$ singlets $u_R$ and $d_R$ which denote the right handed components. The leptons, on the other hand, are organized in a $SU(2)_L$ doublet

$$
L_L = \begin{pmatrix} \nu_L \\ l_L \end{pmatrix} \tag{1.8}
$$

and one singlet $l_R$. Right-handed neutrinos, which may act as singlet under the full SM group, are not present in the SM. In the following chapter, we will explore the consequences of the addition of the right-handed neutrinos in the model.

## 1.2 The Higgs mechanism

At this stage, none of the matter particles have a mass. This is obviously not in agreement with experimental observation. Indeed, we know that not only all the charged fermions (quarks and leptons), but also the two weak interactions mediator bosons are massive. One single mechanism, introduced in the 1964 [26–29] is able to reconcile all the masses measurements. This process is based on the spontaneous symmetry breaking (SSB) of the $SU(2)_L \times U(1)_Y$ symmetry (electroweak symmetry) down to the electromagnetic gauge symmetry $U(1)_{EM}$. The particle which is responsible of this breaking is a $SU(2)_L$ doublet of scalar fields

$$
\Phi = \begin{pmatrix} \phi^+ \\ \phi^0 \end{pmatrix} \tag{1.9}
$$

[1]In the chiral representation, every spinor can be written as $\psi = (\psi_L, \psi_R)$. Early experiments on weak interactions demonstrated that they involve only the left-handed component of Dirac spinors.

of hypercharg $Y = 1$. This doublet, the Higgs doublet, allows for two new terms in the SM lagrangian

$$\mathcal{L}_H = (D_\mu \Phi)^\dagger (D^\mu \Phi) - V(|\Phi|) \tag{1.10}$$

where the former is the kinetic term and the latter the scalar potential. The presence of such a potential allows these fields to break the electroweak symmetry. Indeed, if the minimum of $V$ is not located at $|\Phi| = 0$, when the scalar field falls into its vacuum state, the lagrangian spontaneously breaks the SM group. The general Higgs potential can be written as

$$V(|\Phi|) = -\mu^2 |\Phi|^2 + \lambda |\Phi|^4. \tag{1.11}$$

This potential, if $\mu^2$ and $\lambda$ are positive, is minimized for $|\Phi| = \mu/\sqrt{2\lambda} = v/\sqrt{2}$ where $v$ is called *vacuum expectation value (vev)* of the Higgs field. Thus, in its vacuum state the scalar fields can assume any value for which $|\Phi| = v/\sqrt{2}$; the most convenient choice is

$$\Phi_0 = \begin{pmatrix} 0 \\ v/\sqrt{2} \end{pmatrix}. \tag{1.12}$$

We can at this point expand around the minimum of the potential, writing the Higgs field as $\Phi = H + \Phi_0$, where $H$ is the physical Higgs particle field which appears as perturbation of the vacuum state. The constant term $\Phi_0$ modifies the gauge boson lagrangian, which now contains the term

$$\mathcal{L}_{gbmass} = \frac{v^2}{8}[(g' B_\mu - g W^3_\mu)^2 + 2g^2 W^+_\mu W^{-\mu}], \tag{1.13}$$

where $W^\pm = (W^1 \mp W^2)/\sqrt{2}$. These two terms correspond to mass terms for a neutral gauge boson, namely the combination $g' B_\mu - g W^3_\mu$ and a charged one (with its antiparticle) $W^+_\mu$. Introducing the so called *Weinberg angle*

$$\tan\theta_W = \frac{g'}{g}, \tag{1.14}$$

we can rotate the two fields $W^3_\mu$ and $B_\mu$ defining two neutral $Z_\mu$ and $A_\mu$ fields

$$Z_\mu = W^3_\mu \cos\theta_W - B_\mu \sin\theta_W \tag{1.15}$$
$$A_\mu = W^3_\mu \sin\theta_W + B_\mu \cos\theta_W. \tag{1.16}$$

After this transformation, the lagrangian mass terms for the gauge boson can be written as

$$\mathcal{L}_{gbmass} = \frac{g^2 v^2}{8}\left(\frac{1}{\cos^2\theta_W} Z_\mu Z^\mu + 2W^+_\mu W^{-\mu}\right) \tag{1.17}$$

that show that Higgs mechanism generates the masses for the $Z$ neutral boson ($m_Z = gv/2\cos\theta_W$) and for the $W$ charged bosons ($m_W = gv/2$). The other field $A_\mu$, which is a combination of two generators of the electroweak gauge group, remains massless. Such a field is nothing but the photon field, the meadiator of the electromagnetic force, which can be considered as the generator of the $U(1)_Q$ symmetry that survives the electroweak SSB. Looking at the fermions-gauge bosons interactions terms in the elctroweak sector, we obtain

$$\begin{aligned}\mathcal{L}_{int} &= g' B_\mu \bar{\psi}\frac{Y}{2}\gamma^\mu \psi + g W^i_\mu \bar{\psi}\tau^i \gamma^\mu \psi = \qquad (1.18)\\ &= e A_\mu \bar{\psi}\gamma^\mu \left(\tau^3 + \frac{Y}{2}\right)\psi + \frac{g}{\cos\theta_W} Z_\mu \bar{\psi}\gamma^\mu \left(\cos^2\theta_w \tau^3 - \sin^2\theta_W \frac{Y}{2}\right)\psi + \\ &\quad + \frac{g}{\sqrt{2}}(W^+_\mu \bar{\psi}\gamma^\mu \tau^+ \psi + W^-_\mu \bar{\psi}\gamma^\mu \tau^- \psi)\end{aligned}$$

| | | Q | $\tau$ | $\tau^3$ | Y |
|---|---|---|---|---|---|
| Lepton Left-Handed Doublet | $\nu_L$ | 0 | 1/2 | +1/2 | -1 |
| | $e_L$ | -1 | 1/2 | -1/2 | -1 |
| Lepton Right-Handed Singlet | $e_R$ | -1 | 0 | 0 | -2 |
| Quark Left-Handed Doublet | $u_L$ | 2/3 | 1/2 | +1/2 | 1/3 |
| | $d_L$ | -1/3 | 1/2 | -1/2 | 1/3 |
| u-quark Right Handed Singlet | $u_R$ | 2/3 | 0 | 0 | 4/3 |
| d-quark Right Handed Singlet | $d_R$ | -1/3 | 0 | 0 | -2/3 |

Table 1.1: Electroweak quantum numbers of the SM particles.

where we have defined the electric coupling $e = g \sin\theta_W$ and $\tau^\pm = \tau^1 \pm i\tau^2$. It is clear that the strength of the interactions is determined by the quantum numbers of the fermions. In particular, these numbers are fixed by the so-called Gell-Mann-Nishijima relation [45, 46] $Q = \tau^3 + Y/2$ which can be defined starting from the electromagnetic interaction term and fixes the electric charge of the fermions. Since neutrino fields are the upper components of the left handed lepton multiplets, we have that $\tau^3_\nu = 1/2$ (see eq. (1.8)). For this reason, we need the hypercharge of the lepton doublet to be $Y_{l_L} = -1$ in order to obtain neutral neutrinos[2]. This choice also allow us to have $Q = -1$ for the charged leptons, which is what we expect experimentally [47]. Given that, we obtain that neutrinos in the SM interact only via weak interactions, which can be neutral current (NC) interactions, mediated by the Z boson

$$\mathcal{L}_{NC} = \frac{g}{2\cos\theta_W} Z^\mu \bar{\nu}_L \gamma^\mu \nu_L \tag{1.19}$$

and charged current (CC) interactions, mediated by the W bosons

$$\mathcal{L}_{CC} = \frac{g}{\sqrt{2}} (W^+ \bar{\nu}_L \gamma^\mu l_L + W^- \bar{l}_L \gamma^\mu \nu_L). \tag{1.20}$$

## 1.3 Neutrino interactions in the SM

Experimentally, we know that the vector bosons $W^\pm$ and $Z$ have a mass of $\sim 80$ and $\sim 90$ GeV, respectively [48–52]. Thus, they are two of the most massive elementary particles, and if their kinetic energy is low in respect to the mass (which is a good approximation when we consider terrestrial neutrino interactions), their mass is the only contribution to the propagator. Thus, when we consider neutrino interactions, it can be convenient to use the four fermions *Fermi effective theory*, in which the effect of the bosonic mediator is only a suppression of the coupling. The effective NC and CC lagrangian can written as a current-current interaction

$$\begin{aligned} \mathcal{L}^{NC}_{eff} &= -\frac{G_F}{\sqrt{2}} j^\dagger_{Z\mu} j^\mu_Z \quad (1.21) \\ \mathcal{L}^{CC}_{eff} &= -\frac{G_F}{\sqrt{2}} j^\dagger_{W\mu} j^\mu_W \end{aligned} \tag{1.22}$$

where we have defined the Fermi constant

$$G_F = \frac{\pi}{\sqrt{2}\sin^2\theta_W m_W^2}. \tag{1.23}$$

[2]See Tab. 1.1 for a summary of the electroweak quantum numbers for quarks and leptons.

Focusing on the leptonic sector (the quark sector is completely analogous) the currents are

$$j^\mu_W = \bar{\nu}\gamma^\mu(1-\gamma^5)l = 2\bar{\nu}\gamma^\mu e_L \tag{1.24}$$

$$j^\mu_Z = \bar{\nu}\gamma^\mu\nu + \left(-1 + \frac{1}{2}\sin^2\theta_W\right)\bar{e}_L\gamma^\mu e_L + 2\sin^2\theta_W\bar{e}_R\gamma^\mu e_R. \tag{1.25}$$

where the factors $-1/2 + \sin^2\theta_W$ and $\sin^2\theta_W$ are usually called $g_L$ and $g_R$, respectively. Using these currents, it is possible to study all the neutrino interactions in the SM. Let us take the simplest case, namely the $\nu_e$ scattering on an electron (we will talk about how the neutrino flavors enter in the game in the next section). In this case, we have two different channels, the $s$ channel, with a W boson exchange, and the $t$ channel with a Z boson exchange. In the Fermi approach, the total effective lagrangian density is

$$\mathcal{L} = \frac{G_F}{\sqrt{2}}\{[\bar{\nu}\gamma^\mu(1-\gamma^5)e][\bar{e}\gamma_\mu(1-\gamma_5)\nu] + [\bar{\nu}\gamma^\mu(1-\gamma^5)\nu][\bar{e}\gamma_\mu(g_V - gA\gamma_5)e]\} \tag{1.26}$$

where $g_V$ and $g_A$ are the neutral current vector and axial electron couplings, namely $g_V = -1/2 + 2\sin^2\theta_W$ and $g_A = -1/2$ (notice that these can be obtained rearranging eq. (1.25) through the relations $2g_L = g_V + g_A$ and $2g_R = g_V - g_A$). Performing a Fierz transformation, this lagrangian becomes

$$\mathcal{L} = \frac{G_F}{\sqrt{2}}[\bar{\nu}\gamma^\mu(1-\gamma^5)\nu][\bar{e}\gamma_\mu(1 + g_v - (1+g_A)\gamma_5)e]\,. \tag{1.27}$$

We can now introduce the inelasticity defined as

$$y = \frac{E_\nu - E_e}{E_\nu}\,; \tag{1.28}$$

this quantity, being a Lorenz invariant, can be expressed in terms of the scattering angle $\theta^*$ in the center of mass frame

$$y = \frac{1}{2}(1 - \cos\theta^*). \tag{1.29}$$

For this reason, it is easy to write the scattering cross section in terms of $y$ considering the angular distribution due to the spin configurations of the process. Indeed, when neutrinos interact with left handed particles, the total spin is forced to be 0, so the angular distribution in the center of mass frame is flat. On the other hand, when neutrino interacts with right handed particles, the total spin is 1, and in terms of the inelasticity, the angular distribution is $(1-y)$. Thus, given the lagrangian in eq. (1.27), we have

$$\frac{d\sigma(\nu - e)}{dy} = \frac{G_F^2 s}{\pi}\left[\left(\frac{1}{2} + \sin^2\theta_W\right)^2 + \sin^4\theta_W(1-y)^2\right] \tag{1.30}$$

where $s$ is the usual total quadrimomentum. Integrating over the entire range of variability of y, namely from 0 to 1, we easily obtain

$$\sigma(\nu - e) = \frac{G_F^2 s}{\pi}\left[\left(\frac{1}{2} + \sin^2\theta_W\right)^2 + \frac{1}{3}\sin^4\theta_W\right] \sim 10^{-41}\left(\frac{E_\nu}{GeV}\right)\ cm^2 \tag{1.31}$$

which is a very small cross section compared to other processes in which charged particles are involved. It is straight-forward to obtain the antineutrino scattering cross section just considering that in this case the spin configurations are the opposite due to the fact that antineutrinos are right handed particles. We obtain

$$\sigma(\bar{\nu}-e) = \frac{G_F^2 s}{\pi}\left[\frac{1}{3}\left(\frac{1}{2}+\sin^2\theta_W\right)^2+\sin^4\theta_W\right] \sim 0.5\times 10^{-41}\left(\frac{E_\nu}{GeV}\right)\ cm^2. \tag{1.32}$$

With the same procedures one can compute the cross sections related to the interactions with quarks and, considering the parton distributions, also with hadrons.

## 1.4 The fermion masses

The Higgs mechanism is able to generate not only the weak interactions bosons masses, but also the fermion masses. Indeed, it is possible to consider new invariant and allowed terms in the lagrangian which correspond to the Higgs-fermions interactions, that can be written as

$$\mathcal{L}_{Yuk} = -y^d\bar{Q}_L\Phi d_R - y^u\bar{Q}_L\Phi^c u_R - y^l\bar{L}_L\Phi l_R + h.c. \tag{1.33}$$

where $y^{u,d}$ are the so called Yukawa couplings, that can be taken as real given a rephasing of the fermion fields, and $\Phi^c = i\tau^2\Phi^*$ is the charge conjugate of $\Phi$. Notice that, given the neutrality of the physical Higgs boson field H, $Y_\Phi = +1$ and $Y_{\Phi^c} = -1$. After the SSB, the vev contribution to $\Phi$ generates fermion mass terms (otherwise not allowed in the lagrangian since left and right handed fields transforms differently under the SM gauge group)

$$\mathcal{L}_{fm} = \frac{v}{\sqrt{2}}[-y^d\bar{d}d - y^u\bar{u}u - y^l\bar{l}l] + h.c. \tag{1.34}$$

that predicts the fermion masses to be proportional to the Higgs vev. It is worth to mention that the Higgs mechanism does not provide neutrino masses, since the right handed neutrino fields are missing in the SM.
The particle physics experiments have so far demonstrated that exist three copies of each SM elementary particle. These copies are called generations and to each generation corresponds a *flavor*. The presence of three generations of particles brings some interesting questions in the game. For instance we do not know why there are exactly three generations and many theoretical efforts have been done in order to understand if there could be a flavor symmetry[3] beyond the SM group that can explain the differences between the particle generations [53, 54]. The three particle generations lead to new phenomenological implications in the SM framework. Let us consider the quarks, which in the Standard Model are represented by a left handed doublet and two right handed singlet for each generation. Their Yukawa lagrangian can be written as

$$\mathcal{L}_{Yuk} = -y^d_{ij}\bar{Q}^i_L\Phi d^j_R - y^u_{ij}\bar{Q}^i_L\Phi u^j_R + h.c. \tag{1.35}$$

where now we have introduced the indices i and j that denotes the three generations. After the SSB, this lagrangian generates the quark masses and the following terms appear

$$\mathcal{L} = -m^d_{ij}\bar{d}^i_L d^j_R - m^u_{ij}\bar{u}^i_L u^j_R + h.c. \tag{1.36}$$

Now we have two complex mass matrices, that can be diagonalized through a bi-unitary trasformation, namely

$$m^d = U_L^\dagger\bar{m}^d U_R \quad and \quad m^u = V_L^\dagger\bar{m}^u V_R \tag{1.37}$$

where the $U$ and $V$ matrices are unitary matrices and the $\bar{m}$ matrices are real and diagonal. If we apply the unitary rotations to the quark fields (obtaining now new fields $u'_{L,R}$ and $d'_{L,R}$),

[3]Notice that in the standard model the three generations are just copies of the same structure, thus the standard model quantum numbers do not depend on the flavor.

the lagrangian is written in the mass basis and there are no terms which mixes the generations. However, this change of basis affects the interactions terms. Let us consider the charged current weak interaction term. In the mass basis it becomes

$$\mathcal{L}_W = \frac{g}{\sqrt{2}} W^+_\mu \bar{u}^i_L \gamma_\mu d^i_L + h.c. = \tag{1.38}$$

$$= \frac{g}{\sqrt{2}} W^+_\mu (V_L U_L^\dagger)_{ij} \bar{u}'^i_L \gamma^\mu d'^j_L + h.c. \tag{1.39}$$

where now it is clear that when we consider the interactions between actual massive particles (which are the mass eigenstates $u'_{L,R}$ and $d'_{L,R}$) we need to take into account the entries of the complex unitary matrix $V_L U_L^\dagger$, that is called the Cabbibo-Kobayashi-Maskawa ($U^{CKM}$) matrix [55, 56]. A general $n \times n$ unitary complex matrix has $n^2$ real parameters, which can be chosen as $n(n-1)/2$ mixing angles and $n(n+1)/2$ phases. In our case, we can remove $2n-1$ phases by rephasing the left handed particle fields; indeed performing the same rephasing on the right handed fields the lagrangian is unaltered, indicating that such phases are not physical. Thus, the mixing matrix is left with only $(n-1)(n-2)/2$ physical phases. In the SM, where the number of generation is $n = 3$, we can write the mixing matrix in terms of 3 mixing angles and one phase in the following way

$$U_{CKM} = = \begin{pmatrix} c_{12}c_{13} & s_{12}c_{13} & s_{13}e^{-i\delta} \\ -s_{12}c_{23} - c_{12}s_{23}s_{13}e^{i\delta} & c_{12}c_{23} - s_{12}s_{23}s_{13}e^{i\delta} & s_{23}c_{13} \\ s_{12}s_{23} - c_{12}c_{23}s_{13}e^{i\delta} & -c_{12}s_{23} - s_{12}c_{23}s_{13}e^{i\delta} & c_{23}c_{13} \end{pmatrix}, \tag{1.40}$$

where $s_{ij} = \sin\theta_{ij}$ and $c_{ij} = \cos\theta_{ij}$. These four parameters in quark sector have been measured with a good precision so far [13, 57] showing that one of the three angles has a considerable effect ($\theta^q_{12} \sim 13°$) while the other two are very small. The phase, which is responsible of the CP violation in quarks processes, has also been determined to be different from zero.
In the leptonic sector, the situation is different. The three charged particles are the electron ($e$), the muon ($\mu$) and the tau ($\tau$), which have masses of respectively 511 KeV, 106 MeV and 1.77 GeV [13]. To each of these three particles correspond a neutrino. In absence of neutrino masses, it is clear that the SM [58] is also invariant under rotations of the electronic, muonic and tau fields, namely under the group $U(1)_e \times U(1)_\mu \times U(1)_\tau$. For this reason, we expect that in all the processes we observe in particle physics, the lepton flavor number must be conserved along with the total lepton number. Thus, for instance, the process $\nu_\mu + e \to \nu_e + e$ can only occur in neutral current, otherwise we would need a muon neutrino to turn into an electron through the W boson exchange violating the lepton flavor number. The fact that neutrinos are massless in the SM, has also another important consequence: differently from the quark sector, the leptonic flavor oscillations should not occur. Indeed, in the SM leptonic sector we only have one mass matrix which is diagonalized by two matrices $U_L$ and $U_R$. Since the rotation matrix is the same for both entries of the $SU(2)$ doublet, the weak interaction lagrangian term is left unaltered.
However, neutrino oscillations have been experimentally observed in 1998, bringing to one of the most important particle physics discoveries of the last decades. The presence of this phenomenon established that neutrinos must be massive and paved the way for a huge number of theoretical, phenomenological and experimental studies, as we will widely discuss in the next chapter.

# Chapter 2

# Neutrino oscillations

Neutrino oscillations have been one of the most studied processes in the last decades. Several neutrino experiments succeeded in observing the phenomenon and in measuring the parameters involved. In this chapter we will discuss the formalism of the oscillations in vacuum and in matter as well as the strategies one can adopt to measure each oscillation parameter. At the end of the chapter we will briefly discuss how the neutrino masses, which are non-vanishing since we observe oscillations, may be introduced in the SM.

## 2.1 Formalism of the oscillations

If neutrinos are massive, whatever their mass is, they can undergo the phenomenon of neutrino oscillations. As we will show in few lines, we only require that all the three neutrinos do not have the same mass. The theory of neutrino oscillations was born at the time of the first neutrino observations [11, 59]. Then, in the following decades, such phenomenon has been used to explain some discrepancies between data and theory [8, 60–64], until it has been observed and discovered in 1998 by the Super-Kamiokande experiment [10]. We will discuss in the following sections how neutrino experiments are able to study this phenomenon.
Neutrino oscillations occur when neutrinos change their flavor during their propagation. This process is governed by the oscillation probabilities, which can be obtained from a mixing matrix and the knowledge of the differences between neutrino masses. The mixing matrix, which theoretically can be obtained in the exact same way of the CKM matrix, is called PMNS (Pontecorvo-Maki-Nakagawa-Sakata) matrix [11, 59] and can be parameterized using three mixing angles and a complex phase.
Let us now discuss how to obtain the neutrino flavor transition probabilities. First of all, we can consider a neutrino flavor eigenstate of momentum p [65]. This state must be created from the vacuum by the neutrino conjugate field, thus can be written as superposition of mass eigenstates in the following way

$$|\nu_\alpha(p)\rangle = \sum_i U^*_{\alpha i} |\nu_\alpha(p)\rangle \tag{2.1}$$

where the greek subscripts denotes the flavors, the latin ones the mass eigenstates. The matrix $U$ is the leptonic PMNS mixing matrix. If we consider the neutrino state after a time t, it evolves, following the Schroedinger equation

$$|\nu_\alpha(p)\rangle = e^{-iE_i t} \sum_i U^*_{\alpha i} |\nu_\alpha(p)\rangle \tag{2.2}$$

where $E$ is the neutrino energy. Experiments were able to set very stringent bounds to the neutrino mass [66–71] so far ($m_\nu < 1\ eV$). Moreover, cosmological observation could set even more stringent bounds on the sum of all neutrino masses $\sum_i m_{\nu_i} < 0.1\ eV$ [72–74]. Thus, when we deal with neutrinos we are always in the ultra-relativistic limit, in which we can write

$$E_i = \sqrt{p^2 + m_i^2} \sim p + \frac{m_i^2}{2p} \tag{2.3}$$

where we assumed that all eigenstates have the same momentum. If we want to determine the probability that a neutrino of flavor $\alpha$ turns into a neutrino of flavor $\beta$ at a given time t, we need the following amplitude

$$\begin{aligned} A_{\alpha\beta} &= \langle \nu_\beta(p)|\nu_\alpha(p,t)\rangle = \sum_{i,j} U_{\beta j} U^*_{\alpha i} e^{-iE_i t} \langle \nu_j(p)|\nu_i(p)\rangle = \\ &= \sum_i U_{\beta i} U^*_{\alpha i} e^{-iE_i t} \end{aligned} \tag{2.4}$$

which has to be squared

$$\begin{aligned} P_{\alpha\beta} &= \left| \sum_i U_{\beta i} U^*_{\alpha i} e^{-iE_i t} \right| = \\ &= \sum_{i,j} U_{\beta i} U^*_{\alpha i} U^*_{\beta j} U_{\alpha j} e^{-i(E_i - E_j)t}. \end{aligned} \tag{2.5}$$

In the ultra-relativistic limit, we can write $t \sim L$ and $p \sim E$, obtaining that $E_i - E_j = (m_i^2 - m_j^2)L/2E = \Delta m_{ij}^2 L/2E$. Thus, as already mentioned, the oscillation probabilities only depend on the so-called *mass spittings* $\Delta m_{ij}^2$; this is the reason why we need not only non-vanishing, but also non-degenerate mass eigenstates to observe neutrino oscillations. Rewriting eq. (2.6) in a convenient way, we obtain the general neutrino oscillation formula

$$\begin{aligned} P_{\alpha\beta} &= \delta_{\alpha\beta} - 4 \sum_{i<j} \Re[U_{\beta i} U^*_{\alpha i} U^*_{\beta j} U_{\alpha j}] \sin^2\left(\frac{\Delta m_{ij}^2}{4E} L\right) + \\ &\quad +2 \sum_{i<j} \Im[U_{\beta i} U^*_{\alpha i} U^*_{\beta j} U_{\alpha j}] \sin\left(\frac{\Delta m_{ij}^2}{2E} L\right). \end{aligned} \tag{2.6}$$

Some remarks about the probabilities. If we consider antineutrinos, we need the substitution $U \to U^*$. Thus, the first two terms of the probabilities are unaltered, while the last term which involves the imaginary part of the combination of matrix elements changes sign. For this reason, if the mixing matrix is real, there are no differences in the probabilities (no CP violation). In the three neutrino framework, however, we have one complex phase surviving in the matrix and for this reason we expect in general to observe CP violation. Moreover, any rephasing of the mixing matrix, do not affect probabilities. Thus, Majorana phases (which will be discussed later) cannot be determined studying oscillations.
Another interesting approach to obtain oscillation probability, makes use of the neutrino Hamiltonian. In this case we describe neutrinos as $n$ level quantum mechanical system. Given that, it is possible to write the flavor eigenstates vector in terms of the mass eigenstates vector through the mixing matrix $\nu_f = U\nu_m$. The Hamiltonian of the system in the mass basis is the free particle one, namely

$$(H_m)_{ij} = \delta_{ij}\left(p + \frac{m_i^2}{2E}\right). \tag{2.7}$$

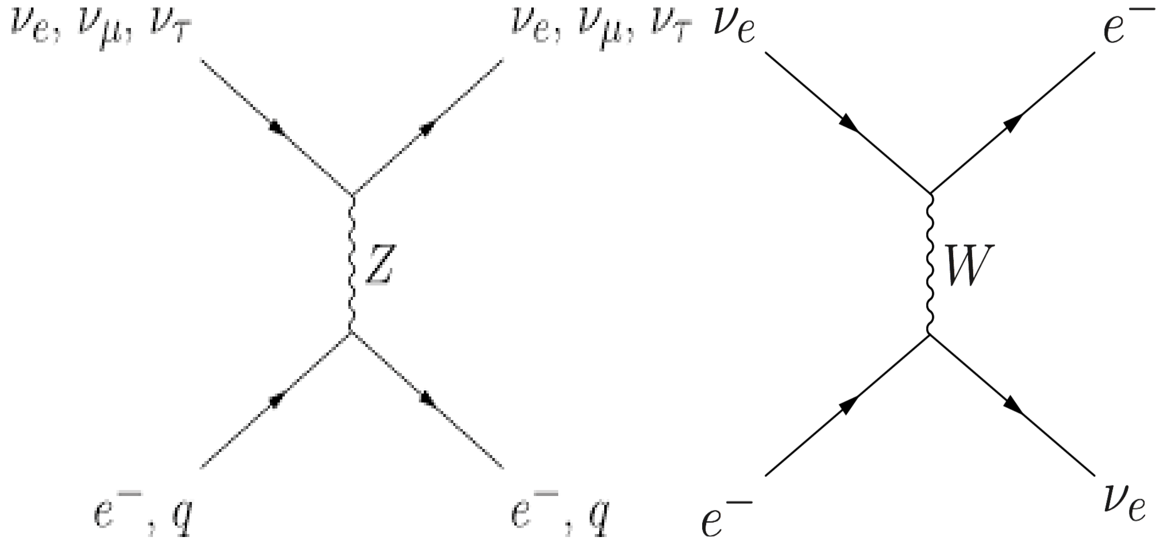


Figure 2.1: Feynman diagrams of the neutral current (left) and charged current (right) neutrino interactions with matter.

The subtraction of a contribution proportional to the identity matrix does not affect the oscillation probabilities. The Hamiltonian matrix can be thus written equivalently as

$$H_m = \frac{1}{2E}\,\mathrm{diag}(0, \Delta m^2_{21}, \Delta m^2_{31}). \tag{2.8}$$

In the flavor basis, the Hamiltonian becomes $H_f = U H_m U^\dagger$. Using the Schroedinger equation for the Hamiltonian operator, we obtain the transition amplitude

$$\begin{aligned} A_{\alpha\beta} &= \nu^\dagger_\beta U e^{-iH_m L} U^\dagger \nu_\alpha = \\ &= U_{\beta j} \nu^\dagger_j e^{-iH_m L} \nu_i U^*_{\alpha i} = \\ &= \sum_i U_{\beta i} U^*_{\alpha i} e^{-i\frac{\Delta m^2_{ij} L}{2E}} \end{aligned} \tag{2.9}$$

which is equivalent to the previous expression.

## 2.2 Oscillations in matter

If neutrino travel through the Earth, or in any matter media, they can undergo weak interactions; this can alter the oscillation probabilities. Wolfestein, Mikheyev and Smirnov [75–77] studied for the first time the effect of the matter (called MSW effect) in neutrino propagation. Indeed, the neutrino Hamiltonian can get contributions at the first order in the small coupling $G_F$ if we consider the coherent forward scattering on the matter particles. Even though the contribution is small, it has to be compared to neutrino mass splittings (which appear in the free Hamiltonian) and for this reason it can become non-negligible.
Let us now consider the processes which occur during neutrino propagation in matter. They can be Neutral Current (NC) interactions, in which a neutrino of whatever flavor scatters on a proton, a neutron or an electron exchanging a Z boson, or Charged Current (CC) interactions, in which only the electron neutrino scatters on matter electrons exchanging a W boson. The Feynmann diagrams corresponding to the two interactions are shown in Fig. 2.1. We will focus on the latter contribution first. The lagrangian term is the usual charged current lagrangian which can be written as

$$\mathcal{L}_{CC} = \frac{G_F}{\sqrt{2}}[\bar{\nu}_e \gamma^\mu (1-\gamma^5) e][\bar{e}\gamma_\mu (1-\gamma_5)\nu_e] \tag{2.10}$$

and becomes

$$\mathcal{L}_{CC} = \frac{G_F}{\sqrt{2}}[\bar{\nu}_e \gamma^\mu (1-\gamma^5)\nu_e][\bar{e}\gamma_\mu(1-\gamma_5)e] \tag{2.11}$$

after a Fierz transformation [78]. Since in the medium in which neutrinos are propagating we have not single particles but an electron number density $N_e$, we can define the electron density matrix

$$\rho_e = \frac{1}{2}\sum_s \int d^3p \frac{|e(\vec{p},s)\rangle \langle e(\vec{p},s)|}{2p_0} N_e f(p,T) \tag{2.12}$$

where $f$ is the normalized statistical momentum distribution of electrons at a given temperature T. Thus, we can integrate out the electrons in the lagrangian using this density matrix in the following way

$$\begin{aligned}
\mathcal{L}_{CC}^{eff} &= Tr(\mathcal{L}_{CC}\rho_e) = \qquad\qquad (2.13)\\
&= -\frac{G_F}{\sqrt{2}}[\bar{\nu}_e\gamma^\mu(1-\gamma^5)\nu_e]\frac{N_e}{2}\sum_s\int\frac{d^3p}{2p_0}\langle e(\vec{p},s)|\,\bar{e}\gamma_\mu(1-\gamma^5)e\,|e(\vec{p},s)\rangle f(p,T) = \\
&= -\frac{G_F N_e}{2\sqrt{2}}[\bar{\nu}_e\gamma^\mu(1-\gamma^5)\nu_e]\int d^3p Tr\left[\frac{\not{p}+m}{2p_0}\gamma_\mu(1-\gamma^5)\right]f(p,T) = \\
&= -\frac{G_F N_e}{\sqrt{2}}[\bar{\nu}_e\gamma^\mu(1-\gamma^5)\nu_e]\int d^3p\frac{p_\mu}{p_0}f(p,T).
\end{aligned}$$

In the rest frame of the matter medium the momentum distribution can be considered an even function. Thus, the integral vanishes unless $\mu = 0$. Using the normalization of the distribution, we finally obtain

$$\mathcal{L}_{CC}^{eff} = -\frac{G_F N_e}{\sqrt{2}}[\bar{\nu}_e\gamma^0(1-\gamma^5)\nu_e]\,. \tag{2.14}$$

This term, linear in the weak coupling $G_F$, becomes a new contribution to the neutrino self energy that can be written as $\xi_{CC} = \sqrt{2}G_F N_e\gamma^0 P_L$ where $P_L = \frac{1-\gamma^5}{2}$ is the operator which picks only the left handed neutrino component. The dispersion relation thus becomes

$$(E-\sqrt{2}G_F N_e)^2 = m^2 + p^2 \tag{2.15}$$

that, in the ultra-relativistic limit, can be written as

$$E \sim p + \frac{m^2}{2p} + \sqrt{2}G_F N_e. \tag{2.16}$$

If we consider the existence of three different neutrino flavors, the Hamiltonian is therefore modified with the addition of the term

$$H_{CC} = \sqrt{2}G_F N_e\,\mathrm{diag}(1,0,0) \tag{2.17}$$

since only the first neutrino flavor, namely the electron one, can undergo CC interactions during the propagation. If we consider antineutrinos, $p_0$ is negative; for this reason, the matter potential term in the Hamiltonian changes sign in this case. Thus, the matter potential, together with the PMNS matrix phase, are the only parameters responsible of the differences between neutrino and antineutrino oscillation probabilities.

Let us now consider the NC contribution. Such interactions can involve any neutrino flavor and any matter particle. If we are in a neutral medium, electrons and protons are in equal number and for this reason their contributions (which have opposite signs) cancel out. The only remaining term is due to the neutrons density. Considering the NC lagrangian and repeating the same procedure discussed for the CC interactions, we obtain a new contribution to the neutrino Hamiltonian

$$H_{NC} = -\frac{G_F N_n}{\sqrt{2}} \,\mathrm{diag}(1,1,1) \tag{2.18}$$

where $N_n$ is the neutron number density. In this case, since the neutral current interactions are flavor independent, this contribution does not affect the oscillations, since it is proportional to the identity and can be subtracted from the Hamiltonian. However, if there are sterile neutrinos or if we consider other exotic physics this term can be important and can affect oscillations (see Ch. 3).

If the electron density is constant through the medium, we only have an additional term in the Hamiltonian which changes its eigenstates and eigenvalues. Thus, the matrix is no longer diagonalized in the flavor basis by the PMNS matrix, but by a new matrix $\tilde{U}$ that depends on the mixing angles and phases and on the matter potential. On the other hand, if the electron density is not constant, the matter neutrino eigenstates in matter will become time-dependent. In the flavor basis the time evolution equation is in this case

$$i\frac{d\nu_f}{dt} = H_f \nu_f \quad \longrightarrow \quad i\frac{d(\tilde{U}\tilde{\nu})}{dt} = \tilde{U} H_d \tilde{U}^\dagger \tilde{U}\tilde{\nu} \tag{2.19}$$

where $\tilde{\nu}$ are the new matter eigenstates and $H_d = \tilde{U}^\dagger H_f \tilde{U}$ is the diagonalized effective Hamiltonian. Since now both the matrix $\tilde{U}$ and the eigenstates are time dependent, the equation becomes

$$i\tilde{U}\frac{d\tilde{\nu}}{dt} + i\frac{d\tilde{U}}{dt}\tilde{\nu} = \tilde{U} H_d \tilde{\nu} \quad \longrightarrow \quad i\frac{d\tilde{\nu}}{dt} = \left(\tilde{U} - i\tilde{U}^\dagger \frac{d\tilde{U}}{dt}\right)\tilde{\nu}. \tag{2.20}$$

From this time evolution equation it is possible to extract the oscillation probabilities in the most general way.

## 2.3 Two flavors oscillations

In nature we know that neutrinos can assume three different flavors (or at least three different active flavors, since we have hints of the presence of sterile neutrinos, but we have not discovered them yet, see Ch. 3). However, it can be useful to study neutrino oscillations in the two flavors approximation. In this case the transition probabilities are easier to handle (in the full framework the expressions can be very cumbersome, as we will discuss later) and can explain different features of the phenomenon. Moreover, given the two measured values of the mass splittings (which are very different one to each other, see Sec. 2.5), in certain circumstances, it is possible to decouple fast oscillations from slow oscillations and study the experimental results using the two flavors formulae [79, 80].

The two-flavors neutrino mixing matrix can be parameterized using only one angle and can be written as

$$U = \begin{pmatrix} \cos\theta & \sin\theta \\ -\sin\theta & \cos\theta \end{pmatrix}. \tag{2.21}$$

Thus, there are no complex phases and for this reason we cannot expect CP violation. The only mass splitting is $\Delta m^2 = m_2^2 - m_1^2$, and the neutrino Hamiltonian (in vacuum) is

$$H_f = \frac{\Delta m^2}{2E}\begin{pmatrix} \cos\theta & \sin\theta \\ -\sin\theta & \cos\theta \end{pmatrix}\begin{pmatrix} 0 & 0 \\ 0 & 1 \end{pmatrix}\begin{pmatrix} \cos\theta & -\sin\theta \\ \sin\theta & \cos\theta \end{pmatrix}. \tag{2.22}$$

which becomes

$$H_f = \frac{\Delta m^2}{2E} \begin{pmatrix} \sin^2\theta & \sin\theta\cos\theta \\ \sin\theta\cos\theta & \cos^2\theta \end{pmatrix}. \tag{2.23}$$

Since we can subtract a contribution proportional to the identity without changing the oscillation probabilities, we can write the Hamiltonian also as

$$H_f = \frac{\Delta m^2}{4E} \begin{pmatrix} -\cos(2\theta) & \sin(2\theta) \\ \sin(2\theta) & \cos(2\theta) \end{pmatrix} \tag{2.24}$$

that allows us to obtain the oscillation probabilities very easily. The two eigenvalues of the Hamiltonian in this basis are indeed just $E_{1/2} = \pm\Delta m^2/4E$, while the two eigenvectors are $\nu_1 = (\cos\theta, \sin\theta)$ and $\nu_2 = (\sin\theta, -\cos\theta)$. Thus, at a given time t (or distance L), the neutrino flavor states are

$$\begin{aligned} |\nu_\alpha\rangle &= \cos\theta e^{-i\frac{\Delta m^2 L}{4E}} |\nu_1\rangle + \sin\theta e^{i\frac{\Delta m^2 L}{4E}} |\nu_2\rangle \\ |\nu_\beta\rangle &= \sin\theta e^{-i\frac{\Delta m^2 L}{4E}} |\nu_1\rangle - \cos\theta e^{i\frac{\Delta m^2 L}{4E}} |\nu_2\rangle \end{aligned} \tag{2.25}$$

and the transition amplitude is simply

$$A_{\alpha\beta} = \langle\nu_\beta(L)|\nu_\alpha(0)\rangle = \sin\theta\cos\theta \left(e^{i\frac{\Delta m^2 L}{4E}} - e^{-i\frac{\Delta m^2 L}{4E}}\right) = i\sin(2\theta)\sin\left(\frac{\Delta m^2 L}{4E}\right). \tag{2.26}$$

Squaring it we obtain the probability that a neutrino of energy E changes its flavor after a distance L, which is

$$P_{\alpha\beta} = \sin^2(2\theta)\sin^2\left(\frac{\Delta m^2 L}{4E}\right). \tag{2.27}$$

We usually refer to this probability as the $\nu_\beta$ *appearance*. We can obtain the same result using the general formula written in terms of entries of the mixing matrix (Eq. (2.7)). It is possible to notice that the mixing angle $\theta$ define the amplitude of the oscillations. Thus, if the angle is very small, the appearance probability is very close to zero, while if it is maximal ($\pi/4$), then the probability can easily reach 1 when the oscillating term is maximized. In particular, we can define an oscillation length

$$L_0 = \frac{2\pi E}{\Delta m^2} \tag{2.28}$$

that refers to the distance that a neutrino of energy E should travel to have the maximum probability of a flavor change, namely $P_{\alpha\beta}^{max} = \sin^2(2\theta)$. Every odd multiples of the length $L_0$ gives maximum probability, while every even multiples the probability is zero. Moreover, since the mixing matrix is real, it is easy to demonstrate that $P_{\alpha\beta} = P_{\beta\alpha}$.
Given a neutrino of flavor $\alpha$, the relation

$$\sum_f P_{\alpha f} = 1 \tag{2.29}$$

must hold, where $f = \alpha, \beta$ is the final flavor. This is a direct consequence of the unitarity of the time evolution operator, but it is also easy to understand from a practical point of view. From this relation we can obtain the so called *disappearance probabilities*

$$P_{\alpha\alpha} = P_{\beta\beta} = 1 - \sin^2(2\theta)\sin^2\left(\frac{\Delta m^2 L}{4E}\right) \tag{2.30}$$

that refers to the probability that a neutrino does not change its flavor after travelling a distance L (or, the probability that a neutrino of a given flavor does not disappear). When the appearance probability is maximum, the disappearance is minimum. Thus, for odd multiples of the length $L_0$, the disappearance probability is zero. Notice that in the literature, the argument of the oscillating sine function can be written in terms of the $\Delta$ parameter defined as

$$\Delta = \frac{\Delta m^2 L}{4E} \tag{2.31}$$

that, if we want to express $\Delta m^2$ in $eV^2$, $L$ in $km$ and $E$ in $GeV$, corresponds to

$$\Delta = 1.27\frac{\Delta m^2[eV]\, L[km]}{E\,[GeV]}. \tag{2.32}$$

Let us now discuss the effect of the matter potential on the two flavor oscillations in the case of constant electron density. Introducing the parameter $V = \sqrt{2}G_F N_e$[1] , in the flavor basis, the Hamiltonian is

$$H_f = \frac{\Delta m^2}{4E}\begin{pmatrix} -\cos(2\theta) & \sin(2\theta) \\ \sin(2\theta) & \cos(2\theta) \end{pmatrix} + V\begin{pmatrix} 1 & 0 \\ 0 & 0 \end{pmatrix}. \tag{2.33}$$

If we subtract an identity matrix proportional to $V/2$, we obtain a traceless Hamiltonian that can be rewritten as

$$H_f = \frac{\Delta m^2}{4E}\begin{pmatrix} -\cos(2\theta) + Q & \sin(2\theta) \\ \sin(2\theta) & \cos(2\theta) - Q \end{pmatrix} \tag{2.34}$$

where $Q = 2VE/\Delta m^2$. With some manipulations of the Hamiltonian matrix, our expression becomes

$$\begin{aligned} H_f &= \frac{\Delta m^2\sqrt{(\cos^2(2\theta) - Q)^2 + \sin^2(2\theta)}}{4E} \times \\ &\times \begin{pmatrix} \frac{-\cos(2\theta)+Q}{\sqrt{(\cos^2(2\theta)-Q)^2+\sin^2(2\theta)}} & \frac{\sin(2\theta)}{\sqrt{(\cos^2(2\theta)-Q)^2+\sin^2(2\theta)}} \\ \frac{\sin(2\theta)}{\sqrt{(\cos^2(2\theta)-Q)^2+\sin^2(2\theta)}} & \frac{\cos(2\theta)-Q}{\sqrt{(\cos^2(2\theta)-Q)^2+\sin^2(2\theta)}} \end{pmatrix} \end{aligned} \tag{2.35}$$

that is identical to the vacuum Hamiltonian except for the redefinition of the mixing angle and the mass splitting, which have to be replaced with

$$\begin{aligned} \Delta\tilde{m}^2 &= \Delta m^2\sqrt{(\cos^2(2\theta) - Q)^2 + \sin^2(2\theta)} \\ \sin^2(2\tilde{\theta}) &= \frac{\sin^2(2\theta)}{[\cos(2\theta) - Q]^2 + \sin^2(2\theta)}. \end{aligned} \tag{2.36}$$

Thus, it is clear that the matter effect both modifies the amplitude and the frequency of the two flavor oscillations. Regardless of the value of the mixing angle, the matter potential introduces a resonance condition in the appearance probability, since if $Q = \cos(2\theta)$ the amplitude of the oscillations is equal to one. This is the MSW (Mikheyev, Smirnov and Wolfenstein) resonance condition [75–77] which has an amplitude proportional to $\sin(2\theta)$. Moreover, at the resonance, the effective mass splitting is $\Delta\tilde{m}_r^2 = \Delta m^2\sin(2\theta)$ which tells us that the oscillation length rapidly increases if the mixing angle is small. However, the resonance condition can be fulfilled by either neutrino or antineutrino oscillations, but not by both. Indeed, since $V > 0$ for neutrinos and $V < 0$ for antineutrino, for a given sign of the mass splitting, the MSW resonance appears

[1] In convenient units, $V \sim 7.5\times10^{-14}\rho(g/cm^3)Y_e\ eV$ where $Y_e$ is the number of electrons per nucleon.

only for particles or antiparticles.
If the electron density is not constant in time, the Schroedinger equation showed in eq. (2.20) does not have a general solution. However, in the so-called adiabatic condition

$$\left|\frac{\Delta\tilde{m}^2}{4E\dot{\tilde{\theta}}}\right| \gg 1, \tag{2.37}$$

namely when the matter potential is slowly changing, the appearance probability is given by [78]

$$P_{\alpha\beta} = \frac{1}{2}[1 - \cos(2\theta_f)\cos(2\theta_i) - \sin(2\theta_f)\sin(2\theta_i)\cos(\Phi_L)] \tag{2.38}$$

where $\theta_i$ and $\theta_f$ are the values of the effective mixing angle at the initial and final time respectively, while $\Phi_L$ is defined as

$$\Phi_L = \int_0^L \frac{\Delta\tilde{m}^2}{2E} dl. \tag{2.39}$$

If, changing the distance L, $\Phi$ rapidly oscillates, $\cos\Phi_L$ can be averaged out to zero, giving a very simple solution for the appearance probability

$$P_{\alpha\beta} = \frac{1}{2}[1 - \cos(2\theta_f)\cos(2\theta_i)] \tag{2.40}$$

that, in the case of neutrinos produced in a medium with a very high electron density which evolves to vacuum adiabatically, simply becomes $P_{\alpha\beta} = \cos^2(\theta)$ that is a constant value. This approximation can, under some conditions, be used to compute the oscillation probability of neutrinos produced in the Sun and detected on the Earth. Other solutions of the time evolution equation have been studied in [81–88].

## 2.4 Three flavors oscillations

The addition of one single flavor to the previous case makes the computation of the oscillation probabilities more complicated. Let us first give a look at the mixing matrix in the 3 flavors case. As already mentioned, a $3\times3$ mixing matrix can be written in terms of three rotation angles and one complex phase. We need to choose where to assign the complex phase and the multiplication order of the rotation matrices; even though the parameterizations are all equivalent, it is widely accepted to use the following

$$\begin{aligned} U_{PMNS} &= \begin{pmatrix} 1 & 0 & 0 \\ 0 & c_{23} & s_{23} \\ 0 & -s_{23} & c_{23} \end{pmatrix} \begin{pmatrix} c_{13} & 0 & s_{13}e^{i\delta} \\ 0 & 1 & 0 \\ -s_{13}e^{-i\delta} & 0 & c_{13} \end{pmatrix} \begin{pmatrix} c_{12} & s_{12} & 0 \\ -s_{12} & c_{12} & 0 \\ 0 & 0 & 1 \end{pmatrix} \\ &= \begin{pmatrix} c_{12}c_{13} & s_{12}c_{13} & s_{13}e^{-i\delta} \\ -s_{12}c_{23} - c_{12}s_{23}s_{13}e^{i\delta} & c_{12}c_{23} - s_{12}s_{23}s_{13}e^{i\delta} & s_{23}c_{13} \\ s_{12}s_{23} - c_{12}c_{23}s_{13}e^{i\delta} & -c_{12}s_{23} - s_{12}c_{23}s_{13}e^{i\delta} & c_{23}c_{13} \end{pmatrix} \end{aligned} \tag{2.41}$$

where $s_{ij} = \sin\theta_{ij}$ and $c_{ij} = \cos\theta_{ij}$. It is clear that the full oscillation probabilities become very cumbersome since each term contains the product of four different mixing matrix entries. However, if one of the mass splittings is zero (or can be neglected) the general oscillation probability reduces to the two flavors one, where now $\theta$ is an effective mixing angle which can be written in terms of the three $\theta_{ij}$. Moreover, also if one of the elements of the mixing matrix is zero, some of the probabilities can be simplified and written in terms of two-flavors oscillations. For instance, as we will discuss in the following section, $s_{13} \ll 1$; thus, $U_{e3}$ is very small. Neglecting it, we obtain that all the mixing matrices combinations which appear in eq. (2.7) where $\alpha = e$

and/or $\beta = e$ are zero. For this reason, all the probabilities which involve the electron flavor can be written in the form

$$P_{\alpha\beta} = \delta_{\alpha\beta} + [1 - 2\delta_{\alpha\beta} \sin^2(2\theta_{eff})] \sin^2\left(\Delta \frac{m^2_{21} L}{4E}\right). \tag{2.42}$$

Such equations can be used in some approximations and can be very useful, even though they are not exact and are not catching all the features of the 3-flavors oscillations. Another approximation that is used in some oscillations regimes, is the fast oscillation one. We will discuss later that one of the mass splittings ($\Delta m^2_{31}$) is bigger than the other ($\Delta m^2_{21}$). Thus, if we are observing oscillations driven by the latter, the ones driven by the former can be averaged out since they are very fast. Defining $K^{ij}_{\alpha\beta} = U_{\beta i} U^*_{\alpha i} U^*_{\beta j} U_{\alpha j}$, the oscillation probabilities become

$$P_{\alpha\beta} = \delta_{\alpha\beta} - 2\Re(K^{13}_{\alpha\beta} + K^{23}_{\alpha\beta}) - 4\Re(K^{12}_{\alpha\beta}) \sin^2\left(\frac{\Delta m^2_{21} L}{4E}\right) - 2\Im(K^{12}_{\alpha\beta}) \sin\left(\frac{\Delta m^2_{21} L}{2E}\right) \tag{2.43}$$

which is much easier to handle than full probabilities. When we are at shorter distances, on the other hand, we can neglect the slow oscillations driven by $\Delta m^2_{21}$ and we can choose a basis in which we observe two flavors oscillations between two neutrino states $\nu'_1 = \nu_e$ and $\nu'_3 = s_{23}\nu_\mu + c_{23}\nu_\tau$. The oscillation probabilities can be obtained from the two flavors one substituting the mixing angle with $\theta_{13}$ and the mass splitting with $\Delta m^2_{31}$.
It is worth to mention that, differently from the two flavors case, in the three neutrinos framework, due to the presence of the PMNS matrix phase, the CP symmetry cannot be conserved unless $\delta_{CP} = 0, \pi$. If we assume CPT conservation, however, we have that $\bar{P}_{\alpha\beta} = P_{\beta\alpha}$. We can therefore in principle define three different CP (or equivalently T) asymmetries as $P_{\alpha\beta} - P_{\beta\alpha} = P_{\alpha\beta} - \bar{P}_{\alpha\beta}$. However, the unitarity of the probabilities imposes that there exists only one independent asymmetry [89, 90] that can be written as

$$P_{\mu e} - P_{e\mu} = -4J \left[\sin\left(\frac{\Delta m^2_{32} L}{2E}\right) + \sin\left(\frac{\Delta m^2_{13} L}{2E}\right) + \sin\left(\frac{\Delta m^2_{21} L}{2E}\right)\right] \tag{2.44}$$

where J is the so called Jarlskog invariant defined as

$$J = c^2_{13} s_{13} s_{12} c_{12} s_{23} c_{23} \sin\delta \tag{2.45}$$

which encodes all the vacuum effects of the CP violation in the oscillations[2].
The inclusion of the matter effects further complicates the treatment of oscillations. In this case there is not an exact expression that can be used to discuss how effective oscillation parameters are modified by the matter potential. However, there are some interesting features that can be discussed. In particular, in this case, we have two MSW resonances, since there are two independent mass splittings. These resonances, depending on the signs of $\Delta m^2_{ij}$, can appear in neutrino probabilities, antineutrino probabilities or both. Being $\Delta m^2_{21} \ll \Delta m^2_{31}$, around the first MSW resonance averaging out the fast oscillation, we obtain an effective Hamiltonian for the remaining two-flavors oscillations is the same as eq. (2.33) after the substitutions $V \to c^2_{13} V$, $\theta \to \theta_{12}$ and $\Delta m^2 \to \Delta m^2_{21}$.
Other regimes in which one of the states decouples for large matter effects or around resonances have been studied in literature. Moreover, in different studies authors have developed strategies to compute approximate expressions for the 3-flavor oscillation probabilities in matter [91–96].

[2] From the experimental point of view, it is convenient, on the other hand, to normalize the asymmetries by the sum of the considered probabilities. This is because in this way we can consider the fact that, even if the effect of the asymmetry is big, it can easily be considered as a fluctuation if also the sum of the probabilities is big. In this case, a different asymmetry for each oscillation channel must be defined, as discussed in the following chapters.

## 2.5 Measurements of oscillation parameters

Many neutrino oscillation experiments have been realized in the last 30 years. They used (and use) neutrinos from different sources to measure the six oscillation parameters (namely $\theta_{12}$, $\theta_{13}$, $\theta_{23}$, $\delta_{CP}$, $\Delta m^2_{21}$ and $\Delta m^2_{31}$). Let us briefly discuss the categories of experiments which have been used so far to measure the oscillation parameters.

### 2.5.1 Solar Neutrino Experiments

The energy source of the Sun are the nuclear fusion reactions inside its core. When such interactions consist in the electron capture of a nucleus, electron neutrinos are produced. Thus, a huge flux of solar neutrinos is expected to reach the Earth. Since the 1960s we were able to observe solar neutrinos with radiochemical methods [8, 9, 60]. The solar neutrino flux provides a direct probe of the internal composition of the Sun [97–99]; however, the first measurements were not in agreement with the solar model. The explanation of this problem, known as *solar neutrino problem* [60, 100, 101], provided a boost in the study of neutrino oscillations, which were confirmed in a different type of experiment years later.
The solar neutrinos energy is small: most of neutrinos are below 500 keV and only a few of them reaches 10 MeV. Since the neutrino interactions cross section grows with energy, we can expect such neutrinos to be very weakly interacting; however, since their flux is very large (up to $10^{11}\ \nu/cm^2/s$) their observation is possible. Considering that the distance from the Sun and the Earth is $10^8\ km$, the $L/E$ ratio that governs the oscillations is of the order of $10^{11}\ km/GeV$, which would need a mass splitting of $10^{-11}\ eV^2$ in order to observe an oscillation pattern; in the hypothesis that both the mass splittings are much larger than such value, we can average out all the oscillations. For low energy electron neutrinos, the matter effect is not important ($Q \ll 1$), thus we can consider the disappearance probability, in the 2-flavor approximation, to be simply

$$P_{ee} = 1 - \frac{1}{2}\sin^2(2\theta_{12}), \tag{2.46}$$

where the angle $\theta_{12}$ has been chosen as the one that drives the solar oscillations. For more energetic solar neutrinos ($E \sim 10\ MeV$), however, experiments observed a drop in the probability. This is because solar neutrinos are produced in the Sun core which has a very high density and this evolves to vacuum almost adiabatically. Thus, for neutrinos that suffer from matter effects, the survival probability can be written, following eq. (2.40), as

$$P_{ee} = 1 - \cos^2\theta_{12}\,. \tag{2.47}$$

It is therefore clear that the solar experiments are particularly sensitive only to one of the three mixing angles (which is called for this reason *solar mixing angle*). The global fit performed on the data from Homestake, GALLEX/GNO, SAGE, SNO, Borexino and Super-Kamiokande [60, 64, 99, 102–110] suggests a value for this mixing angle of [111]

$$\theta_{12} = 33.44^{+0.77}_{-0.74}\ {}^\circ. \tag{2.48}$$

Other global fits agree at a good confidence level on such value [112, 113]. It has to be noticed that this mixing angle is quite large (much larger, for instance, than the quark mixing angles) and it is measured with a good precision (2%). One of the advantages of the presence of matter effects in the solar neutrino oscillations, is that the disappearance probability for the high-energy end of the solar spectrum is no longer sensitive to $\sin^2(2\theta_{12})$ but to $\cos^2\theta_{12}$. This allow us to determine the octant in which $\theta_{12}$ lies (if $\theta_{12} > 45^\circ$ or $< 45^\circ$).
The solar neutrino oscillations can also be used to measure the mass splitting driving slow oscillations ($\Delta m^2_{21}$, or the *solar mass splitting*). Indeed, from the observation that the matter

effect becomes important at around 10 MeV, fixing the solar model that predicts the electron density, one can obtain $\Delta m^2_{21} \sim 10^{-5}\ eV^2$. Notice that the transition from standard oscillation to the MSW resonance for neutrinos, not only suggests us the magnitude of the mass splitting, but also fixes the sign of $\Delta m^2_{21}$ to be positive (if it was negative, the resonance would have occurred only for antineutrinos, which are not produced in the su).
In the three neutrino framework, oscillation probabilities in the solar regime are modified in the following way

$$P^{3\nu}_{ee} = c^4_{13} P^{2\nu}_{ee} + s^4_{13}. \tag{2.49}$$

Since the data are well fitted by the 2-neutrinos approximation, solar experiments tell us that $\theta_{13}$ must be small.

### 2.5.2 Reactor Experiments

Nuclear reactors produce energy through nuclear fission reactions. After the heavy nuclei splittings, $\beta$ decays chains occurs. Such decays produce an intense flux of electron antineutrinos with energies of the order of the MeV. For this reason, nuclear reactors have been widely used as neutrino source [114, 115]. However, being the neutrino emission isotropic, the reactor flux suffers from a $1/r^2$ reduction due to the distance from the source and reactor experiments cannot have a very long baseline. Most of them have a baseline of few meters [116, 117], which is not enough to develop oscillation (at least in the 3-neutrino framework, we will discuss about short baseline reactor experiments anomalies later). However, near very powerful nuclear plants, it has been possible to increase the baseline. At a distance of around 1 km from the antineutrino source, the survival probability (which is the same for neutrinos and antineutrinos since matter effects at short baselines are not important) is

$$P_{ee} \sim 1 - \sin^2(2\theta_{13}) \sin^2\left(\frac{\Delta m^2_{ee} L}{4E}\right) \tag{2.50}$$

where

$$\Delta_{ee} = \frac{\Delta m^2_{ee} L}{4E} = s^2_{12} \sin^2\left(\frac{\Delta m^2_{32} L}{4E}\right) + c^2_{12} \sin^2\left(\frac{\Delta m^2_{31} L}{4E}\right). \tag{2.51}$$

If we consider that $|\Delta m^2_{31}| \sim 10^{-3}\ eV^2 \gg \Delta m^2_{21}$ (from atmospheric experiments, see later), the oscillation probability can be simply written as

$$P_{ee} = 1 - \sin^2(2\theta_{13}) \sin^2\left(\frac{\Delta m^2_{31} L}{4E}\right). \tag{2.52}$$

From the phenomenological point of view, this probability tells us that, when the oscillation term is maximum, we expect to see a depletion on the number of events whose magnitude is determined by the $\theta_{13}$ angle, known as *reactor angle*. RENO and Daya Bay, together with Double CHOOZ [118–120] have been recently able to determine the reactor angle with a very good precision [111]

$$\theta_{13} = 8.57^{+0.13}_{-0.12}{}^{\circ}. \tag{2.53}$$

Notice that, even though the probability depends on $\sin^2(2\theta_{13})$, we already know that the angle lies in the lower octant otherwise we would have seen its effect on solar oscillation. Moreover, since the measurement of this parameter is influenced also by other experiments that suffers from the fact that we still don't know the sign of $\Delta m^2_{31}$ (see next section), the best fit is slightly different if we consider the neutrino mass ordering to be normal ($\Delta m^2_{31} > 0$) or inverted

($\Delta m^2_{31} < 0$).
A very important and unique reactor experiment was KamLAND [121–123]. This experiment had a baseline of 180 km, where we can no longer neglect oscillation driven by the solar mass splitting. In this regime, the oscillation probability becomes

$$P_{ee} = 1 - \sin^2(2\theta_{13})\sin^2\left(\frac{\Delta m^2_{ee}L}{4E}\right) - \sin^2(2\theta_{12})\cos^4(2\theta_{13})\sin^2\left(\frac{\Delta m^2_{21}L}{4E}\right). \tag{2.54}$$

The effect of the second term is a second and more pronounced (due to the fact that $\theta_{12} \gg \theta_{13}$) dip in the oscillation probability for L/E values determined by the solar mass splitting. The KamLAND experiment has been able to observe such a dip and to measure the solar mass splitting, which from global fit results to be [111]

$$\Delta m^2_{21} = 7.42^{+0.21}_{-0.20} \times 10^{-5} \;\; eV^2 \,. \tag{2.55}$$

### 2.5.3 Atmospheric experiments

The first evidence of neutrino oscillations has been observed by the Super-Kamiokande experiment in 1998 [10]. This experiment was looking at neutrinos coming from the Earth's atmosphere. Indeed, when cosmic rays hit the particles in our atmosphere, their interactions will produce neutrinos. Atmospheric neutrino flux is complicated to predict [124–127], but the energy range is very wide, going from few MeV, to $10^9$ GeV. Currently, we are able to observe neutrinos up to 100 TeV [128], but very energetic atmospheric neutrinos are not very useful for oscillations since they have no time to change their flavor[3].
The main process from which atmospheric neutrinos are produced, is the pion decay. These mesons, created by cosmic rays interactions, decay creating muons and muon neutrinos. If the energy is below 5 GeV, the muons have time to decay into an electron, an electron neutrino and a muon neutrino. Thus, for these energies we expect to observe a number of events ratio $N_{\nu_\mu}/N_{\nu_e} \sim 2$. For higher energies, the muons do not have enough time to decay so we expect mainly muon neutrinos on the Earth surface. Varying the zenith angle (ad thus the travelled distance) from which neutrinos were observed, the Super-Kamiokande detector noticed that the number of muon neutrinos was reduced, while the number of electron neutrinos was constant. This was an evidence that for $L/E \sim 10^3\ km/GeV$, $\nu_e \to \nu_\mu$ oscillations (driven by the solar mass splitting) were not developed yet, while muon neutrinos were oscillating in a third neutrino state ($\nu_\tau$) which was not observable by the experiment. The $\nu_\mu \to \nu_\tau$ oscillation probability can be written at the leading order as

$$P_{\mu\tau} = 1 - c^4_{13}\sin^2(2\theta_{23})\sin^2\left(\frac{\Delta m^2_{31}L}{4E}\right). \tag{2.56}$$

This mainly depends on $\theta_{23}$, which is known as *atmospheric angle* and $\Delta m^2_{13}$, or the *atmospheric mass splitting*. Atmospheric neutrino experiments measured these two parameters, which however are also (and better) bounded by accelerator experiments, as we will discuss in the next subsection. The main result of atmospheric experiments is that $|\Delta m^2_{31}| \sim 2.5 \times 10^{-3}\ eV^2$ and $\sin^2(2\theta_{23}) \sim 1$ [109, 129–131]. However, with atmospheric neutrino experiments, it is very difficult to understand in which octant $\theta_{23}$ lies (lower octant, LO, if $\theta_{23} < \pi/4$ and upper octant, UO, if $\theta_{23} > \pi/4$) and which is the sign of the atmospheric mass splitting (normal mass ordering, NO, if $\Delta m^2_{31} > 0$ or inverted mass ordering, IO, if $\Delta m^2_{31} < 0$).

[3]On the other hand, energetic astrophysical neutrinos may be used for oscillation purposes.

### 2.5.4 Accelerator experiments

Neutrino beams are produced since 1960s [4, 132, 133]. They come from protons which are accelerated up to a certain energy and then sent to a fixed target. The interactions of the protons with the target produce a large number of particles, which are mainly pions. After a decay tunnel, we obtain a (mainly) forward beam of neutrinos and leptons coming from the hadron decays. After absorbing or deviating all the charged particles only a pure neutrino beam survives; of this beam we can predict with a good precision the energy spectrum. Most of the neutrinos coming from accelerator beams are muon neutrinos, since the pions decays into muons and muon neutrinos in the majority of the cases. However there is still a remaining contamination (so called *beam contamination*) of electron neutrinos which mainly come from the kaons decays. Placing magnets just before the decay tunnel, one can choose the charge of the pions which generate neutrinos. In this way, we can produce neutrino or antineutrino beams. One of the main problem of neutrino beams is that there is no way to narrow them and for this reason if the neutrino detector is very far from the beam source, it sees only a fraction of the produced neutrinos.

Accelerator experiments usually employ neutrinos with energies from hundreds of MeV to few GeV. The baselines, on the other hand, can be very different. However, usually one can distinguish the accelerator experiments in Short Baseline Experiments (SBL) [134–138] and Long Baseline Experiments (LBL) [139–145]. SBL experiments have a very short baseline, of the order of few meters. For this reason, they should not see any oscillation (we will describe the SBL anomalies later), but they observe a huge flux that can be used to measure, for instance, cross sections [146–148]. Detectors placed few meters from the neutrino beam source can be also used to control and determine the flux that reaches other detectors placed at longer baselines.

The LBL experiments, on the other hand, are built in order to reproduce the physics of low energy atmospheric neutrinos but with a controlled and focused beam. For this reason, the baseline of LBL experiments is chosen in order to sit, at the maximum of the neutrino flux, at the first oscillation maximum, namely

$$L_{LBL} = \frac{2\pi E}{\Delta m^2_{31}}. \tag{2.57}$$

Different LBL experiments have been built so far. The first generation included MINOS, OPERA and ICARUS [141, 142, 142]. The first one mainly measured the atmospheric parameter using the muon disappearance channel. The other two were looking at more energetic neutrinos (their spectrum was peaked at 17 GeV) and successfully [149] tried to observe directly $\nu_\tau$. Observing $\nu_\mu \to \nu_\tau$ oscillations, which are responsible of the atmospheric oscillations, is very difficult. Indeed, the $\nu_\tau$ Charged Current interactions have an energy threshold of 3.1 GeV (due to the fact that a $\tau$ lepton, which is rather massive, must be produced) and such energies are not very typical of LBL experiments, since in order to be at the first oscillation maximum with a neutrino energy of 3 or more GeV, we need a very long baseline ($\sim$ 1500 km).

The second generation of long baseline experiments includes T2K and NO$\nu$A [140, 145]. These two experiments were able to collect a large number of data and are still releasing their results [150, 151]. Their detectors are able to observe not only the muon neutrinos from the disappearance channel, but also electron neutrinos from the appearance channel. The appearance probability in the atmospheric regime can be written as[4]

$$P_{\mu e} \sim \sin^2(2\theta_{13}) \sin^2\theta_{23} \sin^2\left(\frac{\Delta m^2_{31} L}{4E}\right) \tag{2.58}$$

that is very small due to the presence of the reactor angle squared, but it is sensitive to the atmospheric angle octant. However, since LBL are very precise, we cannot rely on this simple

[4] In the following chapters we will write this probability using different expansions and discussing different terms.

vacuum formula, and we can perform a fit considering also small subleading terms, which are all useful for the parameters determination. Defining $\Delta = \Delta m^2_{31} L/4E$, $\hat{V} = V/\Delta m^2_{31}$ where V is the matter potential and $\alpha = \Delta m^2_{21}/\Delta m^2_{31}$, we obtain

$$\begin{aligned} P_{\mu e} \;\sim\; & \sin^2(2\theta_{13})\sin^2\theta_{23}\frac{\sin^2[(1-\hat{V})\Delta]}{(1-\hat{V})^2} + \\ & -\alpha\sin\delta\sin^2(2\theta_{12})\sin(2\theta_{13})\sin(2\theta_{23})\sin\Delta\frac{\sin(\hat{V}\Delta)}{\hat{V}}\frac{\sin[(1-\hat{V})\Delta)}{1-\hat{V}} + \\ & +\alpha\cos\delta\sin(2\theta_{12})\sin(2\theta_{13})\sin(2\theta_{23})\cos\Delta\frac{\sin(\hat{V}\Delta)}{\hat{V}}\frac{\sin[(1-\hat{V})\Delta)}{1-\hat{V}} \end{aligned} \tag{2.59}$$

neglecting all the small $\mathcal{O}(\alpha^2)$ terms ($\alpha \sim 10^{-2}$). It is clear that, if we can observe the appearance channel in both neutrino and antineutrino channels (for which $\hat{V}$ and $\delta$ change sign), our experiment can be sensitive to the CP violating phase $\delta$. Moreover, the two subleading terms are also sensitive to the sign of $\Delta$ and the matter effect can have a non negligible impact.
Thus, long baseline experiments, being able to have access different transition channels (at least $\nu_\mu \to \nu_\mu$ and $\nu_\mu \to \nu_e$ but also $\nu_\mu \to \nu_\tau$ in some cases) and having a good sensitivity to subleading terms in the probabilities, are very performing in the parameter precision measurements. Current LBL have determined that [111]

$$|\Delta m^2_{31}| = 2.515^{+0.028}_{-0.028} \times 10^{-3}\ eV^2. \tag{2.60}$$

with a $2.5\sigma$ preference for the NO solution [112, 113, 152]. Regarding the atmospheric mixing angle, non-maximal values are now preferred, but depending on the mass ordering (sign of $\Delta m^2_{31}$), the value of the CP violating phase and data included in the fit, it can be in the lower ($\sim 42°$) or in the upper octant ($\sim 49°$). For this reason, all the values between 40° and 50° are allowed at $3\sigma$, making the atmospheric angle the most poorly known neutrino mixing angle. Current LBL experiments are not very sensitive to the CP violating phase; their main result is that CP conservation is disfavored by the combination of their datasets. However, recent NO$\nu$A and T2K data analysis have shown a mild tension (which we will discuss later) [153–155].
Future long baseline experiments aim to measure with an unprecedent precision all the neutrino oscillation parameters. In particular the American Deep Underground Neutrino Experiment (DUNE) and the Japanese Tokai-to-HyperKamiokande (T2HK) [156, 157], which will be discussed in details later, may be able to determine the neutrino mass hierarchy, the $\theta_{23}$ octant and the value of the CP-violating phase $\delta$, which are the main open questions in the neutrino oscillation sector[5]; for this reason, they are also expected to be able to probe different Beyond Standard Model (BSM) models.
Finally, next-to-next generation experiments aim also to look at the physics of the second oscillation maximum. At the second atmospheric maximum, we need a ratio L/E which must be three times the one at the first maximum ($\Delta = 3\pi/2$). In this condition, the matter effect is less important and for this reason the main source of CP violation, seen as the difference between neutrino and antineutrino oscillation probabilities, would be the phase $\delta$. Thus, experiments placed at the second atmospheric peak should be able to provide a very clean environment for the measurement of the PMNS matrix phase. One of the proposed experiments of this kind is an upgrade of the T2HK experiment, namely T2HKK [159], which consists in the addition of a new detector in South Korea placed at a baseline which correspond to the second oscillation maximum for the T2HK neutrinos. We will discuss about this experiment later. It is worth to mention also a second maximum LBL experiment proposed in Europe, namely ESS$\nu$B [160].

[5]The JUNO long baseline reactor experiment, which is going to take data very soon, may be able to determine at least the mass ordering at a great confidence level before the future LBL experiment. This will be possible since the electron neutrino disappearance, at long distances, can amplify the interference between solar and atmospheric oscillations, which is sensitive to the mass hierarchy [158].

## 2.6 Parameter degeneracies

In the previous section, we have briefly described how the synergies between different neutrino experiments allowed us to determine all the oscillation parameters with few percents precision (apart from the PMNS phase which is still mostly unknown). In Fig. 2.2, taken from [161], we show the best fits values with their uncertainties from the three global neutrino fits [112, 113, 152]. For the solar parameters $\theta_{12}$ and $\Delta m^2_{21}$, all the fits are in agreement and the best fits are not affected by the atmospheric mass ordering. The reactor angle values and allowed ranges in the three fits are also very similar. However, the situation is different for the atmospheric parameters. Indeed, for $\theta_{23}$ and $|\Delta m^2_{31}|$, while the $3\sigma$ allowed ranges are compatible in the three analysis, the best fits can differ from each other. This is particularly evident for the atmospheric mixing angle. In this case, in IO all the global fits agrees on the fact that the upper octant solution is favoured; in NO, on the other hand, [152] and [113] obtained a best fit in the lower octant, while [112] again in the upper octant. It is therefore clear that the $\theta_{23}$ measurement is still very delicate and need more data to be performed with a good precision. It has to be noticed that in [152], in NO, the preferred octant becomes the upper one if the Super-Kamiokande (SK) atmospheric data [129, 162] are not considered[6]. Finally, for $\delta_{CP}$ all the global fits suggest that its value may be in the range $[180-360]^\circ$. The best fits are around the maximal value $270^\circ$ in IO and closer to $180^\circ$ in NO. The CP-conserving values $0, 180^\circ$ are excluded at only $2\sigma$.
The difficulties in the measurements of oscillation parameters appear since while solar parameters can be obtained in a rather independent way looking at solar neutrinos, the other four parameters $\theta_{13}$, $\theta_{23}$, $\delta$[7] and $\Delta m^2_{31}$ suffer from the so-called *eight-fold degeneracy* [96, 163–168].

### 2.6.1 The eight-fold degeneracy

It is well known that the appearance probability[8] for neutrinos at a fixed baseline and energy with input parameters $\theta_{13}$ and $\delta$ has not an unique solution; indeed, there exist a continuous number of parameter couples $(\bar{\theta}_{13}, \bar{\delta})$ for which the equation

$$P_{\alpha\beta}(\theta_{13}, \delta) = P_{\alpha\beta}(\bar{\theta}_{13}, \bar{\delta})\,. \tag{2.61}$$

holds. The most interesting $(\bar{\theta}_{13}, \bar{\delta})$ pair is the one for which the same equation holds also for antineutrino probabilities, namely

$$\bar{P}_{\alpha\beta}(\theta_{13}, \delta) = \bar{P}_{\alpha\beta}(\bar{\theta}_{13}, \bar{\delta})\,. \tag{2.62}$$

Thus, we have that, at least at fixed energy and baseline, there exist two couples of $\theta_{13}$ and $\delta$ which produce identical appearance probabilities for neutrinos and antineutrinos. This is the so-called intrinsic *$\theta_{13}$-$\delta$ degeneracy*. However, as already discussed, there are currently two other ambiguities in the oscillation parameters measurements: the sign of the atmospheric mass splitting and the octant of the atmospheric angle. As a consequence, other degenerate solutions to the equiprobability equations may arise. Defining the two discrete variables [168]

$$\begin{aligned} s_{MH} &= \mathrm{sign}(\Delta m^2_{31}) && (2.63)\\ s_{oct} &= \mathrm{sign}(\tan 2\theta_{23}) && (2.64) \end{aligned}$$

we have that in the normal ordering case, namely $m_1 < m_2 < m_3$, $s_{MH} = +1$, while for the inverted ordering case, namely $m_3 < m_1 < m_2$, $s_{MH} = -1$ (see Fig. 2.3); conversely, in the

[6] Notice that in Ch. 6 we will use in the simulations the best fits from [152] obtained without the inclusion of SK data, in which the preferred octant is the upper one. These best fits coincide with the ones of the previous analysis from the same group, in [111].

[7] From now on, we will refer to the PMNS phase as $\delta$ or $\delta_{CP}$.

[8] In current oscillation experiments, the most interesting appearance probability is the $\nu_\mu \to \nu_e$ one.

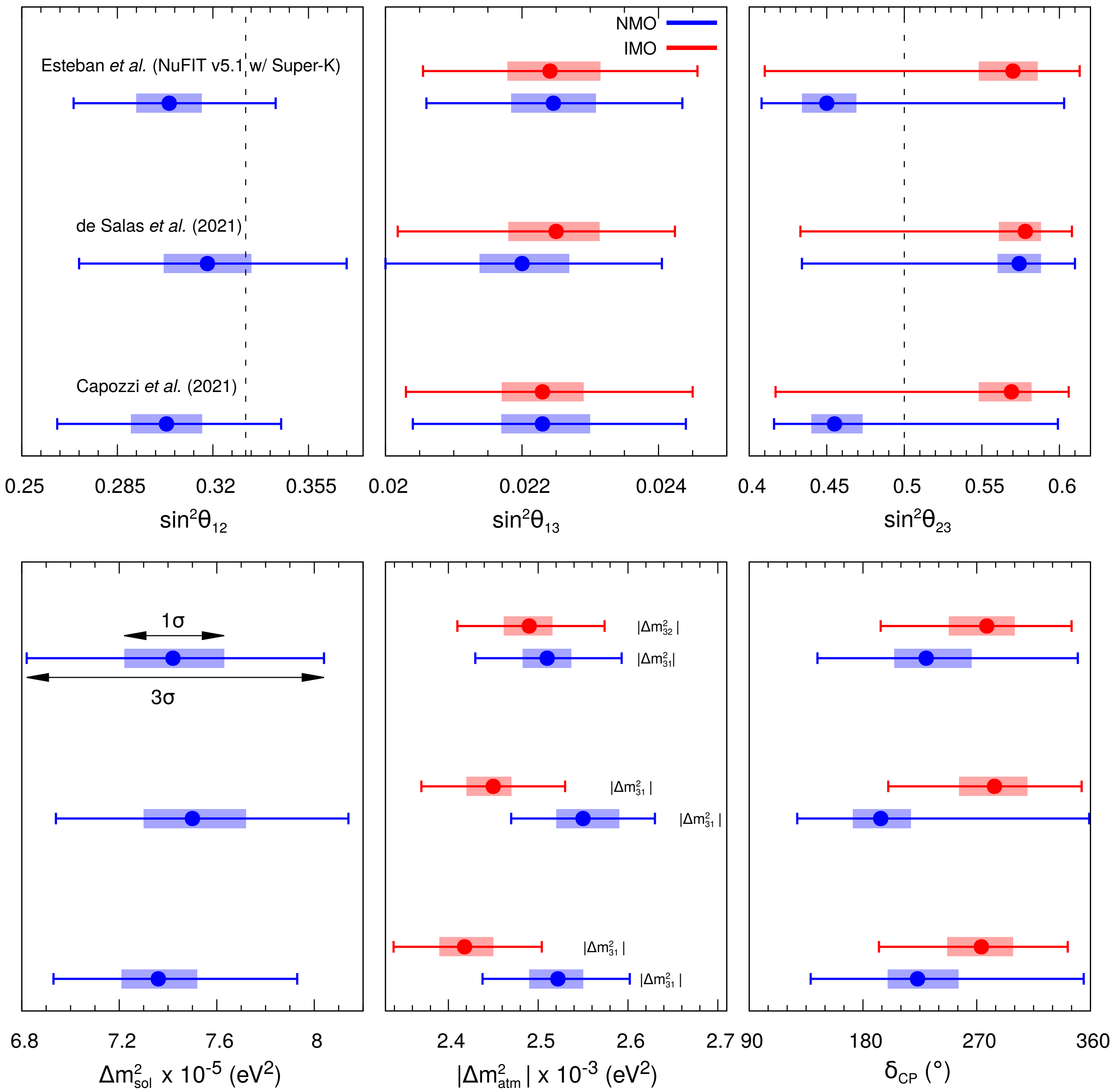


Figure 2.2: Current $1\sigma$ (rectangular boxes) and $3\sigma$ (horizontal lines) allowed ranges for oscillation parameters obtained by the three global fits in [112, 113, 152]. The blue (red) dots are the best fits in NMO (IMO). Figure from [161].

upper octant (UO) case ($\theta_{23} < \pi/4$), $s_{oct} = +1$, while in the lower octant (LO) case ($\theta_{23} < \pi/4$), $s_{oct} = -1$. Thus, given the fact that we have not determined yet neither $s_{MH}$ nor $s_{oct}$, the following equiprobability equations should be considered in addition to the previous ones

$$\begin{aligned} \overset{(-)}{P}_{\alpha\beta}(\theta_{13}, \delta, s_{MH}, s_{oct}) &= \overset{(-)}{P}_{\alpha\beta}(\bar{\theta}_{13}, \bar{\delta}, \bar{s}_{MH} = -s_{MH}, \bar{s}_{oct} = s_{oct}) \\ \overset{(-)}{P}_{\alpha\beta}(\theta_{13}, \delta, s_{MH}, s_{oct}) &= \overset{(-)}{P}_{\alpha\beta}(\bar{\theta}_{13}, \bar{\delta}, \bar{s}_{MH} = s_{MH}, \bar{s}_{oct} = -s_{oct}) \\ \overset{(-)}{P}_{\alpha\beta}(\theta_{13}, \delta, s_{MH}, s_{oct}) &= \overset{(-)}{P}_{\alpha\beta}(\bar{\theta}_{13}, \bar{\delta}, \bar{s}_{MH} = -s_{MH}, \bar{s}_{oct} = -s_{oct}) \,. \end{aligned} \tag{2.65}$$

Clearly, the sets of parameters that solve each of the equations is not the same; however, we still expect that there exist eight different degenerate solutions

- The true solution and the intrinsic degenerate one obtained solving eqs. (2.61) and (2.62);
- The two *wrong hierarchy* solutions obtained starting from the true and the instrinsic degenerate pairs of $\theta_{13}$ and $\delta$ considering $\theta_{23}$ in the true octant and $\Delta m^2_{31}$ with opposite sign;
- The two *wrong octant* solutions obtained starting from the true and the instrinsic degenerate pairs of $\theta_{13}$ and $\delta$ considering $\theta_{23}$ in the opposite octant and $\Delta m^2_{31}$ with true sign;
- The *mixed solutions* obtained starting from the true and the instrinsic degenerate pairs of $\theta_{13}$ and $\delta$ considering $\theta_{23}$ in the opposite octant and $\Delta m^2_{31}$ with the opposite sign.

In order to have a complete understanding of the oscillation phenomenon one must completely break the eight-fold degeneracy, for instance measuring the parameters in different oscillation regimes which allow to independently measure only one parameter at-a-time. Currently, the measurement of the reactor angle using electron disappearance at medium baseline reactor experiments, already allowed us to disentangle $\theta_{13}$ to the other parameters like $\delta$. The breaking of the other degeneracies is the aim of future oscillation experiments. For instance, through precision measurements of the muon disappearance channel $\nu_\mu \to \nu_\mu$, in absence of matter effect, one may determine the $\theta_{23}$ value independently from the other parameters. On the other hand, precise measurements of the $\nu_\mu \to \nu_e$ appearance at LBL experiments or the $\nu_e \to \nu_e$ disappearance at long baseline reactor experiments, should be able to finally break also the mass hierarchy degeneracy[9].

## 2.7 Neutrino mass models

We have now discussed how to determine all the oscillation parameters and which are the criticism in the oscillation measurements. However there still is an issue that we have not discussed yet. If in the SM neutrinos are massless, is it possible to build a model that include the SM but predict massive neutrinos, that is what we observe experimentally? The answer is yes, and in the last decades many different mechanisms have been studied. However, all of them need to introduce in the model new particles which have not been seen so far and for this reason they all remain plausible. The easiest way to include neutrino masses is to couple them to the Higgs field, but in this case there exist a problem: why neutrino masses are so small compared to

[9] In order to break the degeneracies also neutrino factories, namely facilities that produce electron neutrino beams from muon decays [169–172] have been proposed. In this case, the study of another independent appearance channel, namely $\nu_e \to \nu_\tau$ channel may help in the degenercy breaking. However, none of these facilities has been approved so far.

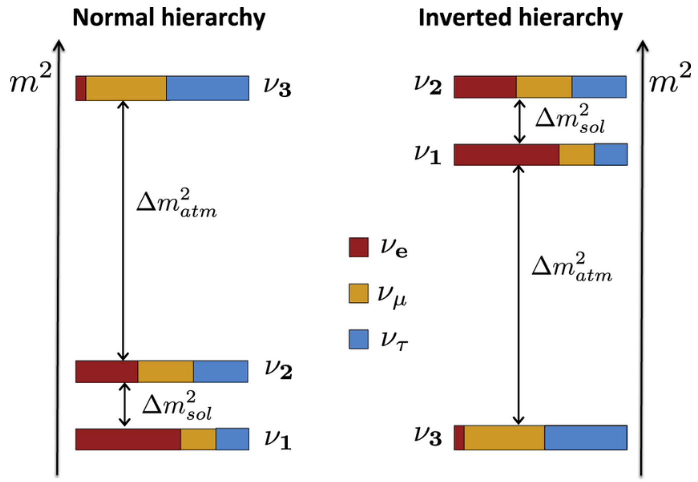


Figure 2.3: Schematic view of the two possible mass orderings (or mass hierarchies). The colors indicate the different flavor components of the neutrino mass eigenstates.Figure from [173].

the other fermions? Indeed, different experiments which aim to measure the absolute neutrino mass are telling us that neutrinos cannot be heavier than 1 eV [66–74]; on the other hand, the lightest of the massive fermions is the electron, which has a mass of 511 KeV. Moreover, we must consider that neutrinos do not carry any color nor electric charge. This implies that they can actually be their own antiparticles. These kind of fermions are known as Majorana fermions (unlike the Dirac fermions for which particles and antiparticles are different). At the time being, there are no observations which have been able to determine whether neutrinos are Dirac or Majorana particles and this is one of the most important goals of non-oscillation neutrino experiments. However, also the inclusion of neutrinos as Majorana particles fails in describing such particles in a natural way.
Among all the models that predict neutrino masses, some of the most appealing and simple ones are the so called *seesaw* models[10]. In this case we have both Majorana and Dirac mass terms in the lagrangian. We will discuss them in the following subsections.

### 2.7.1 Dirac masses

We can include a neutrino mass term in the lagrangian adding SM right-handed neutrinos $\nu_R$ which are singlets under all the symmetries of the standard model. For this reason, they do not couple directly to any of the gauge bosons. Apart for their kinetic term, they can only appear in the Yukawa interaction term

$$\mathcal{L}_Y = -y^\nu \bar{L}_L \Phi^c \nu_R + h.c. \tag{2.66}$$

that after the SSB becomes

$$\mathcal{L}_Y^v = -\frac{y^\nu v}{\sqrt{2}} \bar{\nu}_L \nu_R + h.c. \tag{2.67}$$

This term is a mass term completely analogous to the other fermions ones. However, if Yukawa couplings $y^\nu$ are of the order of magnitude of the other fermions ones (and there are no reasons to believe that this is not the case), neutrinos should not be so light. The introduction of a Dirac mass term has as one of the main consequences, the possibility to have a mixing matrix and thus explain neutrino oscillations. Indeed, one can construct the PMNS matrix in the exact same way of the CKM matrix.

[10]For other neutrino mass models see [174–181].

### 2.7.2 Majorana masses

In principle, there is no need to introduce other new particles like right-handed neutrinos in the game in order to have neutrino masses. Due to the fact that neutrinos are neutral and not charged under $SU(3)_C$, it is possible to write a Majorana mass term, that do not distinguish particles for antiparticles

$$\mathcal{L}_{Maj} = i\frac{m}{2}\nu_L^T\sigma^2\nu_L + h.c. \tag{2.68}$$

which if we denote the different generations with the indices $i, j$ becomes

$$\mathcal{L}_{Maj} = i\frac{M_{M,ij}}{2}\nu_L^{iT}\sigma^2\nu_L^j + h.c. \tag{2.69}$$

where $M_M$ is the Majorana mass matrix. Considering the anti-commutativity of the Weyl spinors, the particle content in this mass term is symmetrical. For this reason, $M_M$ can be taken as a complex symmetric matrix. Thus, we can diagonalize it with a unitary matrix $U_M$ and its eigenvalues are real. Redefining the neutrino states in the diagonal basis $\nu_L'^i = U_{M,ij}\nu_L^j$, the interaction term with W boson becomes

$$\mathcal{L}_W = \frac{g}{\sqrt{2}}W_\mu^+(U_M U_L^\dagger)_{i\alpha}\bar{\nu}_L'^i\gamma^\mu l_L'^\alpha + h.c. \tag{2.70}$$

where $U_L$ is the left-handed unitary matrix involved in the diagonalization of the charged leptons mass terms; in this way a mixing matrix $U = U_L U_M^\dagger$ arises. However, differently from the Dirac case, a rephasing of the Majorana neutrino fields is not possible, since the Majorana mass matrix eigenvalues would not be real. For this reason, in the Majorana mass matrix $n-1$ new phases appear. Usually, the mixing matrix in the Majorana case is written as $U_D K$ where $U_D$ is the usual PMNS matrix and $K = \mathrm{diag}(1, e^{i\alpha_1}, e^{i\alpha_2})$ in the 3-flavor framework. The new phases are called Majorana phases; such parameters do not enter in the oscillation probabilities since when we compute the square of the transition amplitude, the Majorana phases are canceled.
Majorana particles, being particles which coincide with their antiparticles, have a different phenomenology with respect to the pure Dirac particles. Indeed, if there are no differences between $\nu$ and $\bar{\nu}$, some processes that are forbidden in the SM, can be observed. The most important one is the *neutrinoless double beta decay* ($0\nu2\beta$) [182–188]. This process involves some peculiar isotopes that can undergo two $\beta$ decays at the same time, being the final nucleus more stable than the intermediate one that could be reached with a single decay. In the SM, this process, which is very rare ($T_{1/2} \sim 10^{20}\ yrs$) occurs with the emission of two neutrinos

$$(A, Z) \longrightarrow (A, Z+2) + 2e^- + 2\nu_e. \tag{2.71}$$

If neutrinos are Majorana's, they two $\nu_e$ can annihilate each other, allowing a process in which we only have two electrons in the final state

$$(A, Z) \longrightarrow (A, Z+2) + 2e^-. \tag{2.72}$$

The decay time for this process is proportional to the quantity

$$\langle m_{ee}\rangle = \left|\sum_i U_{ei}^2 m_i\right| \tag{2.73}$$

which is called *effective Majorana neutrino mass*, that depends on the absolute neutrino masses and on the mixing matrix entries. Since the matrix entries do not appear in their moduli squared, this quantity depends also on the Majorana phases. Several experiments are searching for this

very rare process, however none of them successfully observed it. For this reason we could only put stringent limits on the effective Majorana mass, namely $m_{ee} \sim \mathcal{O}(0.1)\ eV$ which corresponds to $T_{1/2} \sim 10^{26}\ yrs$ [189–194].
The addition of a pure Majorana term in the SM lagrangian still have some problems, one of the most important is that it explicitely violates $SU(2)_L$. Moreover, the Majorana masses in this case are free parameters and there are no reasons why they should be very small.

### 2.7.3 The seesaw mechanism

The simplest and most natural way to introduce very small neutrino masses in the SM is the *seesaw mechanism* [195–207]. Through this mechanism, neutrinos are very light since there are other very heavy particles (with masses at the scale of grand unified theory, namely $\sim 10^{10}$ GeV) that we have not seen yet. There are different seesaw models that have been studied so far; we will briefly introduce here the most famous ones.

**Type-I seesaw**

When we include right handed neutrinos in the SM in order to write Dirac mass terms, we have to take into account that such new particles can also be Majorana particles. Their mass term can be written as

$$\mathcal{L}_{\nu_R,\,Maj} = -i\frac{M_R}{2}\nu_R^\dagger \sigma^2 \nu_R^* + h.c\,. \tag{2.74}$$

The mass $M_R$ of the Majorana particles is expected to be at a scale above the electroweak one. Using the charged conjugate of the right-handed neutrinos $n_L^i = -i\sigma^2\nu_R^{i*}$, the Majorana mass term becomes

$$\mathcal{L}_{\nu_R,\,Maj} = i\frac{M_{R,ij}}{2} n_L^{iT} \sigma^2 n_L^j + h.c \tag{2.75}$$

Now, both Dirac and Majorana mass terms can be merged together in an unique lagrangian term

$$\mathcal{L}_{mass} = i\frac{\mathcal{M}_{ij}}{2} N_L^{iT} \sigma^2 N_L^j + h.c. \tag{2.76}$$

where $N_L = \nu_L^i$ for the first $n$ entries (where $n$ is the number of flavors) and $N_L = n_L^{i-n}$ for the last $n$ entries. The full mass matrix is in this case

$$\mathcal{M} = \begin{pmatrix} 0 & m_D \\ m_D^T & M_R \end{pmatrix} \tag{2.77}$$

where $m_D$ is the Dirac mass matrix and $M_R$ is the Majorana one. This block matrix can be easily diagonalized. Since $M_R \gg m_D$, neglecting terms $\mathcal{O}(1/M_R^2)$ we obtain

$$\tilde{\mathcal{M}} = \begin{pmatrix} -m_D M_R^{-1} M_D^T & 0 \\ 0 & M_R \end{pmatrix} \tag{2.78}$$

where the diagonalizing matrix can be written as

$$U = \begin{pmatrix} 1 & m_D^* M_R^{*-1} \\ -M_R^{-1} m_D^T & 1 \end{pmatrix} = \begin{pmatrix} 1 & \alpha \\ -\alpha^\dagger & 1 \end{pmatrix}. \tag{2.79}$$

In the diagonal basis we have basically built a Majorana mass term for the combination $N_L'^i = \nu_L^i + \alpha_{ij} n_L^j$, that, since $\alpha \sim \mathcal{O}(m_D/M_R) \ll 1$, correspond to a Majorana mass term for the physical left-handed neutrinos. In this way, we have produced naturally small neutrino masses. However, we introduced new particles in the SM, but their extremely big mass make them impossible to be produced. On the other hand, we need to consider that now the lepton mixing matrix is a $6 \times 6$ matrix (in the 3 neutrino framework), since we do not only have the three left handed neutrinos, but also the three right handed ones. Thus, the mixing matrix that we observe and measure, is only a submatrix of the total mixing matrix; this submatrix in principle has no reason to be unitary. For this reason, a way to probe the presence of right handed states which can mix with left handed ones, is to measure deviations from unitarity of the PMNS matrix. However, one mast consider that the terms outside the PMNS submatrix are suppressed by $m_D/M_R$ and for this reason are expected to be very small.

#### Type-II seesaw

In the type-II seesaw, we do not introduce right handed neutrinos, but a heavy $SU(2)_L$ triplet of scalars with hypercharge +2, that can be represented by the matrix

$$\Delta = \begin{pmatrix} \Delta^+/\sqrt{2} & \Delta^{++} \\ \Delta^0 & -\Delta^+\sqrt{2} \end{pmatrix}. \tag{2.80}$$

The lagrangian for this triplet can be written as

$$\mathcal{L}_\Delta = -m_\Delta^2 Tr(\Delta\Delta^\dagger) + [\mu\Phi^{c\dagger}\Delta \dagger \Phi + ikL_L^T\sigma^2(i\tau^2)\Delta L_L] + h.c \tag{2.81}$$

where $m_\Delta$ is the mass of the triplet, $k$ and $\mu$ are couplings. After the SSB, the triplet acquire an effective potential that can be written as

$$V = m_\Delta^2(|\Delta^{++}|^2 + |\Delta^+|^2 + |\Delta^0|^2) - \mu v^2 \Re\Delta^0. \tag{2.82}$$

This potential has its minimum when the (2,1) component of the $\Delta$ matrix is equal to $\mu v^2/2m_\Delta = v_\Delta/2$. Thus, when this triplet acquire vev, the interaction between the triplet and left handed neutrinos term becomes

$$\mathcal{L}_{\Delta\nu} = i\frac{kv_\Delta}{2}\nu_L^T\sigma^2\nu_L + h.c. \tag{2.83}$$

which is a Majorana term where $m_\nu = kv_\Delta$. If we consider different flavors of neutrinos, the only difference is that we will have a coupling matrix $k_{ij}$. If we make the natural assumption that $\mu$ and $m_\Delta$ are of the same order of magnitude, then we will have that neutrino masses will be suppressed with respect to the Higgs vev by a large mass $m_\Delta$. Both new particles from type I and II seesaws can be introduced together in the SM, producing again small neutrino masses.

#### Type-III seesaw

The same approach considered for the type-I seesaw can be used to generate neutrino masses including in the SM a right handed fermionic triplet, namely $\vec{\Sigma} = (\Sigma^1, \Sigma^2, \Sigma^3)$, with null hypercharge. In the charge basis, we can define three fields which are $\Sigma^0 = \Sigma^3$ and $\Sigma^\pm = (\Sigma^2 \mp \Sigma^1)/\sqrt{2}$. The lagrangian in this case contains a new Yukawa-like term that can be written as

$$\mathcal{L}_\Sigma = -\bar{L}_L Y_\Sigma^\dagger[\vec{\tau} \cdot \Sigma]\Phi^c + h.c. \tag{2.84}$$

where $\tau$ are the group generators and $Y_\Sigma$ is a complex matrix. Allowing the lepton number violation, we can build the Majorana mass term for the new fermion triplet as

$$\mathcal{L}_{\Sigma,Maj} = -\frac{1}{2}\bar{\vec{\Sigma}}M_\Sigma\vec{\Sigma}^c + h.c. \tag{2.85}$$

where again $M_\Sigma$ is a symmetric matrix. After the SSB, we obtain a mass term for neutrinos which is very similar to the type-I seesaw

$$\mathcal{L}_{mass} = \frac{1}{2}\begin{pmatrix}\bar{\nu}_R & \bar{N}_R\end{pmatrix}\begin{pmatrix}0 & M_D^T \\ M_D & M_\Sigma\end{pmatrix}\begin{pmatrix}\nu_L \\ N_L\end{pmatrix} + h.c. \tag{2.86}$$

where the Dirac mass matrix is defined as $M_D = vY_\Sigma/\sqrt{2}$ while the flavour neutrino fields, in the usual basis in which the charged lepton matrix is diagonal, are the following

$$N = \Sigma^0 + (\Sigma^0)^c \quad \nu = \nu_L + \nu_L^c\,. \tag{2.87}$$

Differently from the type-I seesaw, in this case we obtain also a contribution to the charged lepton mass matrix, which however can be neglected using the hypothesis that the charged $\Sigma$ fields have very large Majorana masses compared to the charged lepton masses. After the neutrino mass matrix diagonalization, we obtain again naturally small masses which, up to higher order terms are

$$\tilde{\mathcal{M}}_\nu \sim -M_D^T M_\Sigma^{-1} M_D\,. \tag{2.88}$$

**The seesaw mechanisms in an effective field theory approach**

It is worth to mention that, if we consider the possible dimension 5 operators in the SM lagrangian in effective field theory (EFT), regardless of the UV completion, there is one operator, the *Weinberg operator*, which may be able to give small masses to neutrinos:

$$\mathcal{L}_5 = \frac{c_{\alpha\beta}}{\Lambda^2} L_\alpha L_\beta \Phi\Phi \tag{2.89}$$

where $\Phi$ is the Higgs field, $L$ is the lepton $SU(2)_L$ doublet, $c_{\alpha\beta}$ are coefficients and $\Lambda$ is the energy scale at which EFT is no longer valid. Starting from the four doublets in the operator we need to build a singlet under $SU(2)_L$; in order to do so, there are four possibility for the contractions

$$\mathcal{O}_1 = [(LL)_1(\Phi\Phi)_1]_1 \tag{2.90}$$
$$\mathcal{O}_2 = [(L\Phi)_1(L\Phi)_1]_1 \tag{2.91}$$
$$\mathcal{O}_3 = [(LL)_3(\Phi\Phi)_3]_1 \tag{2.92}$$
$$\mathcal{O}_4 = [(L\Phi)_3(L\Phi)_3]_1\,. \tag{2.93}$$

The first one $\mathcal{O}_1$ is zero, since the singlet built with two identical fields $\Phi$ vanishes. On the other hand, in all the other three cases after the SSB it appears a mass term for neutrinos in the lagrangian

$$\mathcal{L}_m = \frac{c_{\alpha\beta}v^2}{\Lambda^2}\nu_\alpha\nu_\beta\,. \tag{2.94}$$

This term, if $\Lambda$ is big enough, can naturally be small. Let us now discuss one by one which may be the new physics origin of $\mathcal{O}_2$, $\mathcal{O}_3$ and $\mathcal{O}_4$.

- $\mathcal{O}_2$ is a four-fermion operator that can arise if an heavy fermion propagator that connects two fermion-scalar-fermion verteces is integrated out. Considering the $SU(2)_L$ contractions in $\mathcal{O}_2$, this heavy fermion must be a singlet. We have thus recovered the *type-I seesaw*, in which a heavy fermion singlet (right handed neutrinos) is added to the SM.

- $\mathcal{O}_3$, on the other hand, can arise if an heavy scalar propagator that connect two scalar-scalar-scalar verteces is integrated out. From the $SU(2)_L$ structure it is clear that we need a new scalar triplet, recovering the *type-II seesaw*.

- $\mathcal{O}_4$, finally, has a similar structure to $\mathcal{O}_2$, but with two triplets contractions. Thus, we need in this case a new fermion triplet just like the *type-III seesaw*.

We have thus demonstrated in a general way how the simplest models which can generate small neutrino mass in the SM starting from the standard particle fields and adding only one heavy $SU(2)_L$ multiplet are the seesaw ones.

# Chapter 3

# Neutrino oscillations beyond the standard model

The Standard Model is, as already discussed, the most successful physics theory so far. However, it still fails in explaining some phenomena. There are different very well known criticisms in the Standard Model. Some of them are more evident, like the absence of a Dark Matter particle [208] or the neutrino masses. Other problems are related to the *naturalness* of the theory, namely the fact that we expect that free parameters having the same theoretical origin should not to be very different; among them, we have the strong-CP problem or the flavor problem [38, 40, 41, 209, 210]. Finally, while the SM is able to unify the electromagnetic and the weak forces at a some energy scales, it fails to do the same with the strong force; moreover, it turned to be very tricky to include gravity in the particle physics framework, since this process introduces formal tensions between the general relativity and the standard model of particles.
All these aspects, together with some anomalous measurements in the quark and charged lepton sectors [48, 52, 211–225], suggest that there should exist some extensions of the Standard Model which could solve the theoretical and experimental problems without modifying drastically the astonishing predictions of the SM. High precision accelerator experiments failed to find any evident new physics up to the TeV energy scale; however, current and next generation neutrino experiments are expected to provide very clean environment to search for new physics. Indeed, even though the neutrino sector remains the least known sector of the SM, currently we know most of the neutrino properties (like the oscillation parameters) with a few percents uncertainties. Thus, precision neutrino measurements will soon compete with hadrons and charged leptons ones for the BSM (Beyond Standard Model) searches. We will now briefly describe some of the models that could be probed with neutrino experiment [226, 227]. After that, we will go into the details of a few of them.

**Sterile neutrinos** Long-standing anomalies [62, 64, 117, 228–233] in some oscillation experiments (see Sec. 3.1) have suggested that there may exist at least one additional neutrino flavor which is *sterile*, i.e. do not undergo weak interactions. Anomalous oscillation data suggest that the mass splitting related to such neutrino must be much bigger than the other ones, namely $\Delta m^2 \sim 1\ eV^2$; for this reason, the sterile-driven oscillation are very fast and can be observed at very short baselines. The presence of a fourth flavor modify all the oscillation probabilities and for this reason both $\nu_\mu \to \nu_e$ and $\nu_\mu \to \nu_\mu$ channels at accelerator experiments, as well as $\nu_e \to \nu_e$ transition at reactor experiments and $\beta$-beams can be used to probe such a model.

**Non Standard Interactions (NSI)** Non standard neutrino interactions (NSIs) [77, 234–236] are a general and largely studied effective field theory framework (even though UV completion models exists, see [188, 237–242]) in which we can parameterize new physics in the neutrino sector. In particular, they allow to introduce new interactions between neutrinos and matter particles, mediated by vector, scalar or other spin structures particles [243, 244]. The most studied case is the vector one; in this case neutrinos can undergo new interactions their production, propagation or detection. Many different experiments can probe NSIs, including long baseline experiments, in which the matter propagation is important, or scattering experiments.

**Non-unitarity** Different neutrino mass models predict the presence of additional heavy fermions (see type-I seesaw) which in principle would act like an additional neutrino flavor [245–248]. For this reason, in such models the neutrino mixing matrix is bigger than the usual $3 \times 3$ PMNS matrix. Thus, the matrix we measure with oscillation experiment is a submatrix of a bigger one and no longer has to be unitary (see Sec. 3.4). The effect of the unitarity breaking can be sizeable [249–254] and can be measured using different neutrino oscillation experiments.

**Neutrino decays** In the SM neutrinos are stable particles. Moreover, considering their very small mass and the fact that they couple to other particles only via weak interactions, there are no kinematically allowed decays in the standard model. However, many new physics models introduce very light particles (Majorons [255–257]) which in principle could couple to neutrinos and allow their decay [258–261]. Terrestrial experiments are able to bound the neutrino lifetime (see Sec. 3.3); however, the strongest constraints on the neutrino decays come from cosmology [262].

**Lorentz invariance violation** The violation of the Lorentz symmetry (or CPT) is present in some BSM models, like string theory [263]. In these cases, a non-trivial spacetime dependence of the theory vacuum leads to an apparent violation of the Lorentz symmetry. In neutrino experiments, such violations could cause modifications of the oscillation probabilities, like time or direction dependent effects, energy dependence of the mass splittings or neutrino-antineutrino mixing [264–268]. It is possible to parameterize the effect of the Lorentz violation introducing a new field that, coupling to neutrinos, brings into the game new possible CPT-odd and CPT-even interactions. The former at the lowest-order modify the probabilities in a NSI-like fashion [269, 270], while the latter introduce richer phenomenology. For neutrino oscillation analysis in the context of the Lorenz violation see [271–293].

**Large extra dimensions** Some neutrino mass models imply that righ-handed neutrinos propagate in extra dimensions and interact with active neutrinos that acquire Dirac Mass [294]. After the compactification of the large extra dimensions, the so-called *Kaluza-Klein* modes generate an infinite number of sterile neutrinos in the bulk. The sterile-active mixing modify the oscillation probabilities which can depend on the new neutrino masses and the compactification radius [295–304].

**Neutrino tridents** Neutrino trident production is a rare weak process in which a neutrino scatters on an heavy nucleus producing a pair of charged leptons [305–312]. Some measurements have already been carried out [313–315], but still there is room for new measurements which could give hints of the presence of new physics. Indeed, a class of $Z'$ models modify the dimuon trident cross-section [316, 317]. An excellent environment where to search for an anomalous number of trident events will be the Near Detectors of future long baseline experiments [318, 319].

**Heavy Neutral Leptons** Heavy Neutral Leptons (HNL), or heavy sterile neutrinos, other than being related to the generation of neutrino masses, could play a role as a dark matter component and as responsible of matter-antimatter asymmetry [184, 320–325]. Also in this case, Near Detectors could be crucial in the HNL detection [326–328]: indeed, such particles produced through rare meson decays, could reach the near detector decaying into SM particles. Other than direct searches, hints of their presence could be found looking at the mixing with active neutrinos.

**Ultra-light Dark Matter** Ultra-light scalar fields are present in different extensions of the standard model. When such particles couple to neutrinos, the neutrino oscillation probabilities may change in time, due to the vacuum expectation value of the new field [329–336]. Moreover, invoking the neutrino interactions with background particles, also the matter effects may result to be modified with a non-trivial energy dependence [337]. The very rich phenomenology related to the presence of light particles has been widely studied in different neutrino experiments and has also been used to explain anomalies in oscillation data [338].

**Quantum decoherence** Quantum fluctuations in the gravitational field due to micro black holes may cause the loss of the quantum coherence [339–343]. If pure states may evolve in incoherent states, the quantum theory should be modified. The reduction of the coherence between two states $i$ and $j$ in this model is proportional to an exponential factor $e^{-\gamma_{ij}L}$ which grows with the baseline [344]. The $\gamma_{ij}$ parameters can be function of the energy $\gamma_{ij} = \gamma_{ij}^0 (E/GeV)^n$ where $n$ is an integer. A given experiment is sensitive to decoherence when $\gamma_{ij} L \sim 1$. In the literature, models with $n < 0$ have been studied [345]; however, positive values are more interesting since some string-theory models predict $n > 0$ [340–343]. LBL experiments with high energy fluxes [346–348], as well as atmospheric [298, 344, 349] or astrophysical neutrinos [185, 350–354] can explore vast regions of the parameters space.

## 3.1 A closer look to the 3+1 sterile neutrino model

The history of the sterile neutrino searches is very rich because, since the first oscillation experiments, some hints of the presence of a new sterile neutrino appeared. We know from the $Z$ boson decays that the active light neutrino species must be 3 at a great confidence level [355–358]. However, there are no particle physics measurements that can limit the number of sterile species other than neutrino oscillations. If new neutrinos are much heavier than the active ones, it is rather difficult to observe oscillations, since they would be very fast and would appear as averaged out at any baseline. In this case we expect that the main phenomenological implication would be the non-unitarity of the $3 \times 3$ PMNS matrix (see Sec. 3.4). However, if the sterile neutrinos have a mass which is comparable with that of active flavors, then we may be able to see some oscillation effects. Even though many models have been explored in literature [295, 296, 359–367], the simplest one is the so-called *3+1 sterile neutrino model*, in which we include only a new sterile state. In this case, the full $4 \times 4$ mixing matrix can be written in terms of 6 mixing angles and 3 phases. Thus, in total, considering also the new independent mass splitting $\Delta m^2_{41}$, we have 6 new parameters. For this reason, the oscillation probabilities results more complicated. Moreover, taking into account the fact that sterile neutrinos do not couple with matter, we can no longer neglect the NC matter potential; this can cause the presence of new matter resonances absent in the 3-neutrino framework. In the following subsections we will briefly describe the anomalies which favors the 3+1 model, as well as the current limits on the new parameters. Moreover, we will mention some models in which light sterile neutrinos are included.

### 3.1.1 Anomalies in the oscillation data

The first experimental evidence for the existence of neutrinos came from the observation of the antineutrino flux from nuclear reactors. Even though only very precise medium and long

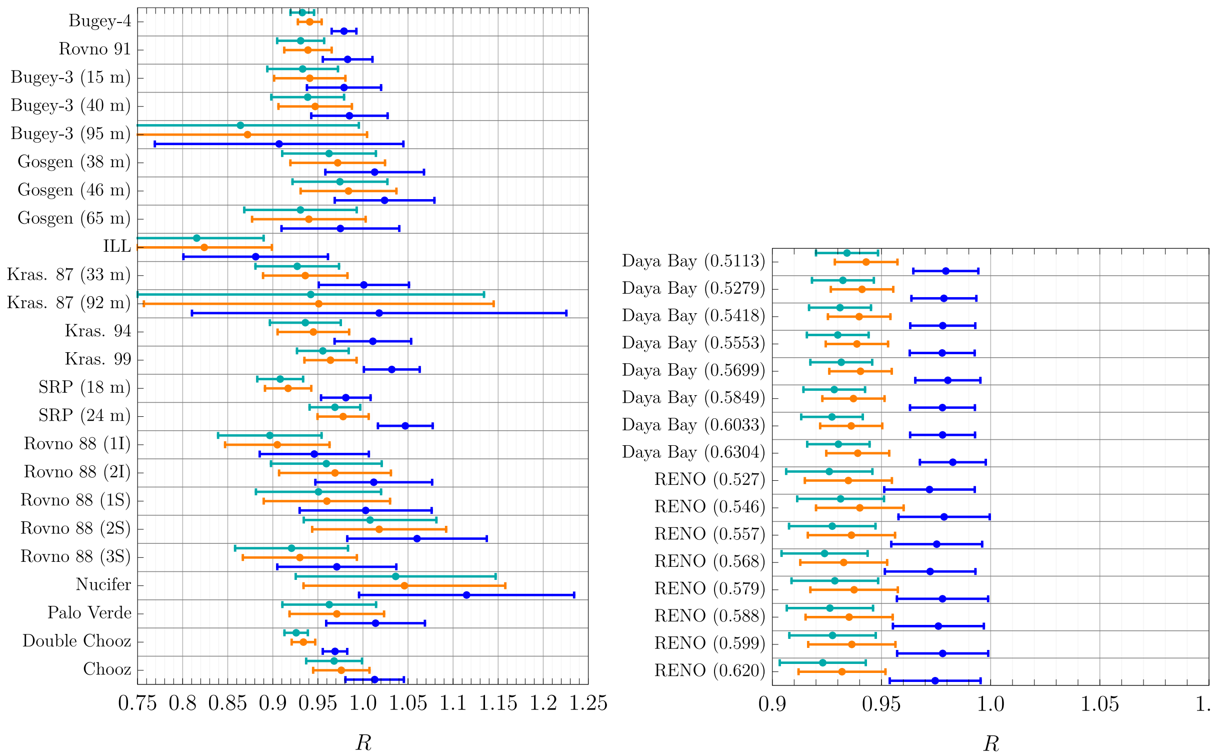


Figure 3.1: Ratio between the observed number of events and the predicted one (R) for different short (left panel) and medium (right panel) reactor experiments. Orange lines have been obtained using the Huber-Muller (HM) flux prediction [388, 389], the green lines using the Hayen-Kostensalo-Severijns-Suhonen (HKSS) flux prediction [387], while the blue ones using the *ab-initio* calculations [390]. Figures taken from [117].

baseline experiments like RENO [368], Daya Bay [369] and KamLAND [121] were able to measure oscillation parameters, a large number of short baseline (few meters) experiments were built in the last 50 years [233, 370–386]. In such experiments we expect that neutrinos have no time to oscillate and the number of observed neutrinos should be in agreement with the theoretical flux predictions. However, the latest flux calculations [387–390] could not reproduce the data from reactor experiments: most of the experiments observed less events than expected. This disagreement is known as *reactor anti-neutrino anomaly* and has a total significance of about $3\sigma$ [117, 228, 391].

Flux calculations could still hide some criticisms[1]. Indeed, as shown in Fig. 3.1, depending on the model used for the flux prediction, the anomaly significance can be drastically reduced. Some recent experiments like Daya Bay and RENO have developed some methods to measure the antineutrino fluxes coming from the different fuel isotopes separately [396–402]; the results seem to point in the direction of wrong flux predictions but there are still different aspects that need to be considered [117]. In order to separate the possible theoretical uncertainties in the flux predictions from the presence of new physics, the Neutrino-4 experiment has been built so to be able to measure the number of neutrino events at different baselines. Recent results from this experiment claimed a $4.6\sigma$ anomaly [233]. However, this result has been criticized [117, 403] and needs further analysis.

The reactor anomaly became more interesting in the 1990s when two gallium solar experiments, namely GALLEX and SAGE [61, 63] monitored the neutrino flux coming from intense radioactive sources during their calibration. Four measurements have been performed and all of them observed a number of events which was below the expectations; the combined significance of the

[1]Many experiments which were able to measure the antineutrino spectra observed also the so-called *5 MeV bump* that still requires more effort to be explained [392–395]

*gallium anomaly* is around $3\sigma$ [232, 404, 405].
Finally, at the end of the last century, a completely different experiment, LSND [136], observed a third anomaly [229]. In this case, muon neutrinos were produced from stopped pions decays and were observed in a liquid scintillator detector after travelling roughly 30 meters. Considering the experiment design, the neutrino flux was almost free from $\bar{\nu}_e$ contamination. Nonetheless, a significant ($3\sigma$) electron antineutrino excess compared to the estimated background was observed in the detector. In the last two decades, no satisfactory explanations in terms of systematic errors or SM uncertainties have been found, even though different hypothesis were explored in the literature [359–364]. The MiniBooNE [138] experiment at Fermilab was designed to reproduce the LSND results independently. In this case, pions decayed in flight and produced a neutrino beam observed by a Cherenkov detector located 541 meters from the source. MiniBooNE confirmed the *short baseline anomaly* observing an excess of $4.8\sigma$ [230, 231, 406]. In this case the estimation of the backgrounds is more complicated than in the LSND case; indeed in MiniBooNE one need to carefully consider the possible contribution of the hadronic resonances or of the presence of neutral pions decaying in the detectors [407]. All these possibilities were explored by the MiniBooNE collaboration, but the anomaly still remains significant [231].

### 3.1.2 Sterile neutrinos phenomenology

The computation of the oscillation probabilities in the 3+1 model follows exactly the same procedure used in the standard oscillation framework. In order to try to solve the reactor and gallium anomalies with the sterile hypothesis, we can imagine that sterile oscillations (in this case $\bar{\nu}_e \to \bar{\nu}_s$, where $\nu_s$ is the sterile state) occur at very short baselines. This means that $\Delta m^2_{41} \gg \Delta m^2_{31}$. Thus, in the experiments conditions ($\Delta m^2_{21} L/E \ll \Delta m^2_{31} L/E \ll 1$) we can consider the two-flavors approximation to compute the probability which reads

$$P_{ee} \sim 1 - 4|U_{e4}|^2(1-|U_{e4}|^2)\sin^2\left(\frac{\Delta m^2_{41} L}{4E}\right) \tag{3.1}$$

in terms of the PMNS matrix elements. We can also define a sterile oscillation angle for electron disappearance experiments as $\sin^2 2\theta^s_{ee} = 4|U_{\mu 4}|^2(1-|U_{e4}|^2)$. Reactor and gallium anomalies data, together with constraints from other experiments, show a preference for sterile oscillations with $\Delta m^2_{41} \sim 1\ eV^2$ and $|U_{\mu 4}| \sim 10^{-2}$ (see Fig. 3.2).

If we want to explain the LSND and MiniBooNE anomalies with the sterile hypothesis, we need to compute the $\nu_\mu \to \nu_e$ probability in presence of a fourth sterile state. At short baseline, this reads

$$P_{\mu e} \sim 4|U_{\mu 4}|^2|U_{e4}|^2 \sin^2\left(\frac{\Delta m^2_{41} L}{4E}\right) \tag{3.2}$$

for which we can define the effective mixing angle $\sin^2 2\theta^s_{\mu e} = 4|U_{\mu 4}|^2|U_{e4}|^2$. In this case the analysis in terms of matrix elements is more complicated, since there are two different elements appearing in the probability. The best fits from all the electron neutrino appearance are $\Delta m^2_{41} \lesssim 1\ eV^2$ and $\sin^2 2\theta^s_{\mu e} \sim 0.01$ (see Fig. 3.3). It is clear that oscillation driven by eV-scale sterile neutrinos are able to solve all the anomalies considering all the current electron disappearance and appearance data[2]. However, we can notice that, if from electron disappearance data we have that $|U_{e4}|^2 \sim 0.01$, in order to explain the LSND and MiniBooNE excesses, we would need $|U_{\mu 4}|^2 \sim 1$. Thus, the sterile oscillations effect on the muon disappearance probability, which

[2]Notice that, even though sterile oscillations are bigger at short baselines, they can alter the oscillation probabilities also at longer distances. For this reason long baseline experiments are also able to set bounds on sterile parameters.

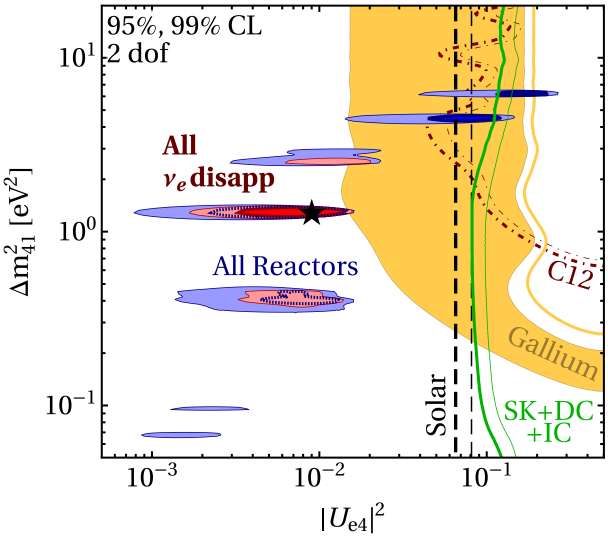


Figure 3.2: Constraints on the 3+1 model due to $\nu_e/\bar{\nu}_e$ disappearance data. The green line represents the limit on $|U_{e4}|$ from atmospheric data of the Super-K, DeepCore and IceCube experiments [105, 130, 408], while the black dashed the limits from solar data. Figure taken from [409].

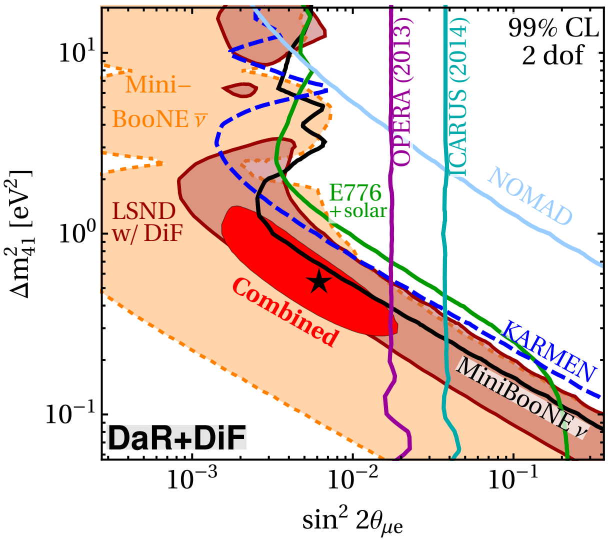


Figure 3.3: Constraints on the 3+1 model due to $\nu_e/\bar{\nu}_e$ appearance data. Limits from other experiments [410–413] are shown. Figure taken from [409].

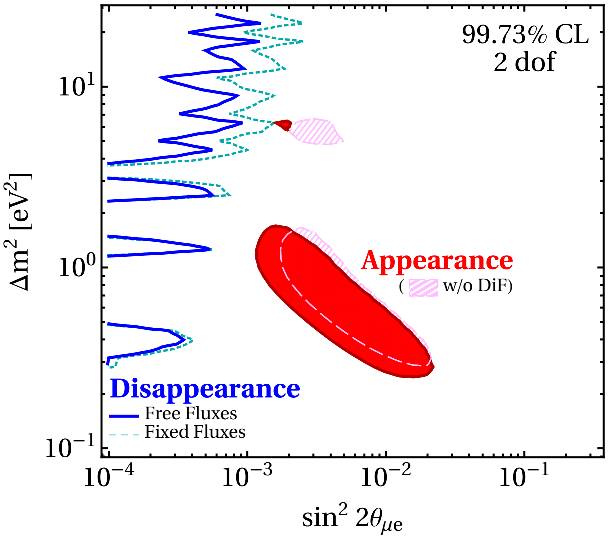


Figure 3.4: Constraints on the 3+1 model due to $\nu_\mu/\bar{\nu}_\mu$ disappearance data. Allowed regions from $\nu_e/\bar{\nu}_e$ appearance searches are shown in red. Figure taken from [409].

reads

$$P_{\mu\mu} \sim 1 - 4|U_{\mu 4}|^2(1 - |U_{\mu 4}|^2)\sin^2\left(\frac{\Delta m^2_{41} L}{4E}\right) \tag{3.3}$$

should not be negligible. This effect has never been observed so far in disappearance experiments (see Fig. 3.4), except for some weak signals from IceCube [414]. This results to the so-called *appearance-disappearance tension*. The future Short Baseline Neutrino (SBN) [415, 416] experiment at Fermilab, composed by three detectors at three different short baselines, is expected to give a final answer to the sterile neutrino issue looking at both muon disappearance and electron appearance channels. First results from the middle detector, namely MicroBooNE [417], showed no $\nu_e$ excess, further reducing the allowed parameters space. However, the sterile explanation for the short baseline experiments is still not completely ruled out.
If we want to measure the non-standard mixing angles, we need to choose a parameterization. Since in the literature different conventions are used, it is complicated to give universal constraints. However, if we chose the parameterization [406, 418, 419]

$$U_{PMNS} = R(\theta_{34})R(\theta_{24})R(\theta_{23},\delta_2)R(\theta_{14})R(\theta_{13},\delta_3)R(\theta_{12},\delta_1) \tag{3.4}$$

where $R$ are the rotation matrices[3], the last column entries are

$$U_{e4} = \sin\theta_{14} \tag{3.5}$$

$$U_{\mu 4} = \cos\theta_{14}\sin\theta_{24} \tag{3.6}$$

$$U_{\tau 4} = \cos\theta_{14}\cos\theta_{24}\sin\theta_{34}\,. \tag{3.7}$$

From these equations, we can obtain the limits on the mixing angles, which are very stringent on $\theta_{14}$, while more loose on $\theta_{24}$ (see recent reviews [117, 409, 415, 420–423]). The limits on $\theta_{34}$, on the other hand, are very difficult to obtain from current experiments, since they mostly come from $\nu_\tau$ oscillations. Future experiments may play a big role in constraining such parameter [16]. The new phases, on the other hand, are not accessible from present data, but they can have an important effect on the $3\times3$ PMNS matrix phase (which in such parameterization is $\delta_3$) determination [424–428]. Currently, as it happens for many neutrino BSM models, cosmology constraints on the new parameters are comparable with the terrestrial ones, but we will not discuss them in details. For more insights on this topic, see [423, 429–431].

[3]Notice that if the $\theta_{i4}$ are zero, the PMNS matrix reduces to the usual $3\times3$ one.

### 3.1.3 Theoretical models which can include light sterile neutrinos

Sterile neutrinos appear in many models used to generate neutrino masses. Indeed, when we introduce a right handed neutrino as a SM singlet, such a particle can be defined as *sterile*. However, as discussed in the previous chapter, in order to have small active neutrino masses, we usually need large masses for the sterile neutrinos. Nevertheless, there exists some models in which at least one of the sterile neutrinos can have an $\mathcal{O}(eV)$ mass.
For instance, motivated by symmetry reasons [432–434], one can try to lower only one ($\mu_s$) of the three sterile Majorana masses in the type-I seesaw model. In this case, after the integration of the two heavy states, the $4 \times 4$ mass matrix reads

$$M_{4\times4} = \begin{pmatrix} -M_D M_M^{-1} M_D^T & M_s \\ M_s^T & \mu_S \end{pmatrix} \tag{3.8}$$

where $M_s$ is a vector whose components are the sterile entries of the Dirac Yukawa matrix, while $\mu_S$ is the Majorana light sterile mass ($\mu_S \ll M_M^1, M_M^2$). Diagonalizing such matrix, we obtain for the active neutrinos

$$M_\nu \sim -M_D M_M^{-1} M_D^T - M_S \mu_S^{-1} M_S^T \tag{3.9}$$

while for the sterile one

$$m_s \sim \mu_s \,. \tag{3.10}$$

Light sterile neutrinos can appear also in the so called *inverse seesaw mechanism* [245, 257, 435]. In this case, we introduce two sets of sterile neutrinos $N$ and $N'$ which carry lepton number. Defining a vector $n = (\nu_e, \nu_\mu, \nu_\tau, N^1, ..., N^n, N'^1, ..., N'^n)$, the neutrino mass term becomes

$$\mathcal{L}_{IS} = -\frac{1}{2} n^T M n = -\frac{1}{2} n^T \begin{pmatrix} 0 & M_D & 0 \\ M_D^T & 0 & M_D' \\ 0 & M_D'^T & \mu \end{pmatrix} n + h.c. \tag{3.11}$$

The $\mu$ matrix, which couples the $N'$ sterile neutrinos with themselves, violates lepton number. Since in the limit $||\mu|| \to 0$ the lepton number becomes a conserved quantity, for naturalness, we can consider the entries of such matrix very small compared to the entries of the other matrices $M_D$ and $M_D'$. It can be showed that, in this limit, some light eigenvalues

$$M_s \sim \frac{||\mu|| \cdot ||M_D'||^2}{||M_D||^2 + ||M_D'||^2} \tag{3.12}$$

appear, and they can play the role of light sterile neutrinos. In this model it can be shown that the mixing between active and sterile neutrinos can also be large, since it is proportional to $||M_D||/||M_D'||$. Other seesaw-like frameworks that could contain light sterile states are the *extended type-I seesaw models* [188] in which a new singlet fermion S is included in addition to the three usual heavy right handed neutrinos. Under some hierarchical assumptions on the Majorana mass matrix related to the S sector, light sterile neutrinos with active-sterile mixing of $\mathcal{O}(0.1)$ can be generated.

## 3.2 A closer look at the Non Standard Interactions

Non Standard Interactions (NSI) have been introduced in the neutrino context since the first discussion about the MSW effect [77, 234, 436–443]. With the NSI formalism, it is possible to describe new physics in a model independent way, introducing four-fermions effective operators which arise in presence of heavy mediator fields. We can distinguish two types of NSI, one that describes charged current interactions and one that describes the neutral current ones. In the oscillation framework, the former can occur at the neutrino production or at neutrino detection, while the latter occur in neutrino propagation. The general NSI lagrangian thus contains the two terms

$$\mathcal{L}_{NC} = -2\sqrt{2}G_F \sum_{f,i,P,\alpha,\beta} \epsilon^{f,P}_{\alpha\beta}(\bar{\nu}_\alpha \mathcal{O}^i P_L \nu_\beta)(\bar{f}\mathcal{O}^i P f) \tag{3.13}$$

$$\mathcal{L}_{CC} = -2\sqrt{2}G_F \sum_{f,i,P,\alpha,\beta} \epsilon^{f,P}_{\alpha\beta}(\bar{\nu}_\alpha \mathcal{O}^i P_L l_\beta)(\bar{f}\mathcal{O}^i P f') \tag{3.14}$$

where $f, f' = e, u, d$ are the matter fermions, $P = P_L, P_R$ are the chirality operators and $\mathcal{O}^i$ are operators that reflect the Lorentz structure of the interactions. The phenomenology of the NSI is extremely rich and, for this reason, they have been used in many context to interpret neutrino oscillation data in an unconventional way. We will not go into the details of all the possible phenomenological implications of NSI, which have been explored in [236, 443] and in the references therein. In this section, however, we will discuss some implications of the vector CC NSI on the neutrino production and detection and of the vector and scalar NC NSI on the neutrino propagation in matter. For discussions on UV complete models which could generate NSI-like phenomenology, see [236–239, 241, 444–447].

### 3.2.1 Source and Detector vector NSI

In the Standard model neutrinos can be produced via different weak processes. In oscillation experiments we usually detect neutrinos coming from nuclear processes (i.e. nuclear fusion reaction in the Sun core) or nuclei, mesons and muons decays. In all these processes, neutrinos are produced in a W boson decay together with the corresponding lepton ($W^+ \to \nu_\alpha l^+_\alpha$ and $W^- \to \bar{\nu}_\alpha l^-_\alpha$). If some new physics is present in Nature, then it may be that when neutrinos are produced, other interactions may occurs. Such interactions can couple neutrinos and leptons of the same flavor or they can violate the lepton numbers conservation coupling particles of different generations. Using the effective field theory formalism, one can include all the possible new physics processes in the neutrino production in the following lagrangian

$$\mathcal{L}^s_{NSI} = \mathcal{L}^s_{V\pm A} + \mathcal{L}^s_{S\pm P} + \mathcal{L}^s_T \tag{3.15}$$

where

$$\mathcal{L}^s_{V\pm A} = \frac{G_F}{\sqrt{2}} \sum_{f,f'} \varepsilon^{s,f,f',V\pm A}_{\alpha\beta}[\bar{\nu}_\beta \gamma^\mu (1-\gamma^5) l_\alpha][\bar{f}'\gamma_\mu(1\pm\gamma^5)f] \tag{3.16}$$

$$\mathcal{L}^s_{S\pm P} = \frac{G_F}{\sqrt{2}} \sum_{f,f'} \varepsilon^{s,f,f',P\pm S}_{\alpha\beta}[\bar{\nu}_\beta (1-\gamma^5) l_\alpha][\bar{f}'(1\pm\gamma^5)f] \tag{3.17}$$

$$\mathcal{L}^s_T = \frac{G_F}{\sqrt{2}} \sum_{f,f'} \varepsilon^{s,f,f',T}_{\alpha\beta}[\bar{\nu}_\beta \sigma^{\mu\nu} l_\alpha][\bar{f}'\sigma_{\mu\nu}f]\,. \tag{3.18}$$

The $\varepsilon^s_{\alpha\beta}$ parameters are the strengths of the interactions and usually are referred as *source NSI parameters*. They are in general complex and for this reason they can be written as $\varepsilon^s_{\alpha\beta} = |\varepsilon^s_{\alpha\beta}|e^{i\phi_{\alpha\beta}}$. The same NSI lagrangian could in principle allow new physics processes also during neutrino detection. In oscillation experiments usually neutrinos are detected through neutrino CC interactions with nuclei. In such processes the neutrino is absorbed and the corresponding lepton is created ($\nu_\alpha N \to N' l^-_\alpha$ or $\bar{\nu}_\alpha N \to N' l^+_\alpha$); when NSI are considered, all lepton flavors in principle could be generated by all incident neutrino flavors, enriching drastically the number

of possible neutrino interactions. All these new physics processes can be again parameterized using nine complex $\varepsilon^d_{\alpha\beta}$ parameters , called *detector NSI parameters*.
Source and detector NSI can introduce in the neutrino phenomenology a very large number of new physics degrees of freedom. Indeed, if we want to separate the vector, axial, scalar, pseudoscalar and tensor contributions and we want to consider different couplings for each matter particle, namely electron, protons and neutrons, we have in the most general case hundreds of new parameters. However, there are some considerations which could be done in order to reduce the number of parameters. For instance, in most of neutrino experiments, the neutrino production and detection involves decays of $u$ quarks into $d$ quarks or vice-versa. For this reason, the only important NSI parameters are the ones for which $f = u$ and $f' = d$. Moreover, $\tau$ neutrino production is very rare in accelerator experiments and impossible for reactor or solar experiments; thus, the source NSI parameters for which $\alpha = \tau$ can be neglected. At the same time, reactor experiments usually only detect electron neutrinos; for this reason all the detector NSI for which $\beta \neq e$ can be put to zero in these cases. Other considerations involving the allowed and forbidden Lorentz structures in a given neutrino production or detection process can be done; see [443] for some discussions about this topic.
From the oscillation phenomenology point of view, it is however convenient to encode all the possible Lorentz structures in the same parameters, for which we drop all the superscripts except the ones which refers to either the source (s) and detector (d) NSIs. Thus, in order to obtain the oscillation probabilities, we can consider that in the neutrino production we do not have a pure flavor eigenstate, but a mixed state that depends on the source NSI parameters

$$|\nu^s_\alpha\rangle = |\nu_\alpha\rangle + \sum_{\beta=e,\mu,\tau} \varepsilon^s_{\alpha\beta}\, |\nu_\beta\rangle \ . \tag{3.19}$$

At the same time, when a neutrino is observed, the detector is sensitive to the combination

$$\langle\nu^d_\beta| = \langle\nu_\beta| + \sum_{\alpha=e,\mu\,\tau} \varepsilon^d_{\alpha\beta}\, \langle\nu_\alpha| \ . \tag{3.20}$$

Notice that in the source NSI parameters the first index refers to the charged lepton flavor while the second to the neutrino flavor; for the detector NSI it is the opposite. Moreover, the NSI matrices in this case have no reasons to be unitary, and for this reason the $|\nu^s_\beta\rangle$ and $\langle\nu^d_\alpha|$ states are not orthonormal. In this context some approximations can be done. In some studies, for instance [443, 448–452] the approximation $\varepsilon^s_{\alpha\beta} = \varepsilon^d_{\beta\alpha}$ has been adopted considering that the detection and production processes are very similar at the fundamental level; in particular this happens if we consider that the interactions only have the structure (V-A)(V-A) [443]. If not specified, we will not use this approximation, keeping our discussion completely general without relying on any consideration about the particular production and detection interactions in a given experiment. The computation of the oscillation probabilities can be done in the following way

$$\begin{aligned} P_{\alpha\beta} &= |\, \langle\nu^d_\beta|\, e^{-iHL}\, |\nu^s_\alpha\rangle\, |^2 = & (3.21)\\ &= |(1+\varepsilon^d)_{\gamma\beta}(e^{-iHL}_{\gamma\delta}(1+\varepsilon^s)_{\alpha\delta}|^2 = & (3.22)\\ &= |[(1+\varepsilon^d)^T e^{-iHL}(1+\varepsilon^s)^T]_{\beta\alpha}|^2 & (3.23)\end{aligned}$$

where H is the usual neutrino Hamiltonian and $\varepsilon^s$ and $\varepsilon^d$ are the matrices whose elements are the NSI couplings. The oscillation probabilities with source and detector NSI are very complicated due to the large number of parameters involved (see for instance [443] for approximated formulae). It is interesting to notice that $\nu_\mu \to \nu_e$ probability mostly depends on $\varepsilon^{s,d}_{\mu e}$ and $\varepsilon^d_{\tau e}$, while the $\nu_\mu \to \nu_\mu$ probability depends on $\varepsilon^{s,d}_{\mu\mu}$, $\varepsilon^s_{\mu\tau}$ and $\varepsilon^d_{\tau\mu}$. All the phases relative to these parameters appear in the probability; for this reason, one of the effects of source and detector

NSI is to worsen the sensitivity to the PMNS phase $\delta_{CP}$.
Bounds from oscillation and non-oscillation experiments on source and detector NSI have been discussed in [20, 236, 443, 448–450, 450–452, 452–465]. In [448], in particular, it is possible to find a detailed description of different approaches one can use to set bounds con CC NSI. In particular, some interesting conclusions that the authors made are the following

- The vector component of the NSI can modify the beta-decay rate. Comparing the CKM matrix component $V_{ud}$ extracted from beta-decays and the same extracted from other hadronic processes which are not affected by NSI, we can set limits on $\varepsilon^{s,d,V}_{e\alpha}$ and $\varepsilon^{s,d,V}_{ee}$.

- Lepton universality measurements can set limits on the axial component of all the source and detector parameters. Indeed, NSI can modify the relative decay rates of charged pions and $\tau$ leptons into pions.

- As already discussed, neutrino oscillation depends on the source and detector parameters. Looking at very small baseline oscillation rates, since the NSI induce zero-distance effects on the probabilities, one can set bounds on different source and detector couplings. We will talk about this topic in details in Sec. 6.2.

- The presence of charged current NSI may induce flavor-changing charged leptons interactions at loop level. However, model independent constraints on the NSI parameters cannot be set except for a single case, the one which may change the $\mu^- \to e^-$ conversion, namely $\varepsilon^{s,d,L}_{\mu e}$, where with L we denote the NSI operator that only select left handed particles.

Considering all these effects, it is possible to set 90% CL bounds of $\mathcal{O}(10^{-2})$ for all the source and detector parameters, except for $\varepsilon_{\tau\tau}$ for which the limit is one order of magnitude bigger. CKM and lepton universality measurements can set more stringent bounds $(10^{-3} - 10^{-4})$ but only on only vector or axial component of the couplings. Finally, the loop level constraints on muon transition into electron can set and incredibly strong bounds of $1.8 \times 10^{-6}$ on $\varepsilon^{s,d,L}_{\mu e}$.
We want to remark that, given the definition of the NSI couplings, they can be linked to the new physics scale; indeed, if NSI are mediated by a new particles whose mass is $M_{NSI}$, then, considering that the effective lagrangian terms are written in terms of the electroweak scale ($G_F$), we expect that $\varepsilon \sim M_W^2/M_{NSI}^2$ [466]. Using this consideration, with present bounds we can only say that, for source and detector NSI, $M_{NSI} > TeV$.

### 3.2.2 Propagation vector NSI

Let us now consider how to treat NC-like NSI. In this case, we have neutrinos in both initial and final states. Such interactions can occur between neutrinos and matter particles, namely electrons and quarks, while neutrinos propagate in a matter medium. If we stick to only $V \pm A$ interactions, the lagrangian is in this case

$$\mathcal{L}^m_{NSI} = \frac{G_F}{\sqrt{2}} \sum_f \varepsilon^{m,f,V\pm A}_{\alpha\beta} [\bar{\nu}_\alpha \gamma^\mu (1-\gamma^5)\nu_\beta][\bar{f}\gamma^\mu(1\pm\gamma^5)f] + h.c.. \tag{3.24}$$

These operators are the same as the lagrangian terms we obtain when we consider the matter potential which affect neutrino oscillations. For this reason, in the hamiltonian formalism, the effect of this kind of NSI is to modify the matter potential oscillation term in the following way

$$V \begin{pmatrix} 1 & 0 & 0 \\ 0 & 0 & 0 \\ 0 & 0 & 0 \end{pmatrix} \longrightarrow V \begin{pmatrix} 1+\varepsilon_{ee} & \varepsilon_{e\mu} & \varepsilon_{e\tau} \\ \varepsilon^*_{e\mu} & \varepsilon_{\mu\mu} & \varepsilon_{\mu\tau} \\ \varepsilon^*_{e\tau} & \varepsilon^*_{\mu\tau} & \varepsilon_{\tau\tau} \end{pmatrix} \tag{3.25}$$

where $V = 2\sqrt{2}G_F N_e E$, $N_e$ is the electron number density and E is the neutrino energy[4]. We want to remark that the $\varepsilon_{\alpha\beta}$ parameters that appear in the matter matrix at the Hamiltonian level are not exactly the ones which appear in eq. (3.24) at lagrangian level. Indeed, when we write the matter potential matrix, we do so considering the mean electron density; for this reason, the hamiltonian an lagrangian parameters satisfy the following relation [236]

$$\varepsilon_{\alpha\beta} = \sum_{f=e,u,d} \frac{N_f}{N_e} \varepsilon^{m,f}_{\alpha\beta} \tag{3.26}$$

The fact that at the lagrangian level there can exist two terms which are hermitian conjugates, assure that the propagation NSI matrix is an Hermitian matrix. For this reason, we expect the three diagonal parameters (known as non-universal, since they can provide flavor universality breaking) to be real, while the three independent non-diagonal parameters (known as flavor-changing) can be complex and they carry a phase. Even though the independent $\varepsilon_{\alpha\beta}$ are 9, only 8 are testable by oscillations. Indeed, we can subtract an identity matrix proportional to one of the diagonal parameters without changing the probabilities. Since scattering experiments can put very tight bounds on $\varepsilon_{\mu\mu}$ [448, 455], usually for oscillation purposes this parameter is subtracted out, making the diagonal part of the NSI matrix $V(1+\varepsilon_{ee}-\varepsilon_{\mu\mu}, 0, \varepsilon_{\tau\tau}-\varepsilon_{\mu\mu}) = V(1+\varepsilon'_{ee}, 0, \varepsilon'_{\tau\tau})$. It is interesting to notice that the presence of NSI can cause an exact degeneracy: a model without NSI is exactly equivalent to a model with $\varepsilon'_{ee} = -2$ and opposite mass ordering. Another degeneracy arises since the CPT invariance of the vacuum Hamiltonian can be translated into a symmetry of the probabilities when the following transformations are performed: $\Delta m^2_{31} \to -\Delta m^2_{32}$, $\theta_{12} \to \pi/2 - \theta_{12}$ and $\delta_{CP} \to \pi - \delta_{CP}$. Even though this degeneracy is completely broken in presence of matter (indeed, as discussed previously, solar experiment can univocally determine $\theta_{12}$) the NSI can recover this degeneracy if matter density is constant and $\varepsilon'_{ee} \to -\varepsilon'_{ee} - 2$, $\varepsilon'_{\tau\tau} \to -\varepsilon'_{\tau\tau}$ and $\varepsilon_{\alpha\beta} \to -\varepsilon^*_{\alpha\beta}$. Thus, in principle the NSI can introduce a second-octant solution for $\theta_{12}$ which is called *LMA-Dark* solution [467–473]. Finally, Non Standard Interactions can increase the $\theta_{23}$ octant degeneracy increasing the number of parameter sets for which the probabilities are numerically the same [236, 474].

Using a global analysis on current oscillation data and fixing the ordering to normal, the 90% CL bounds on the NSI parameters are at the level of $10^{-1}$ for $|\varepsilon_{e\mu}|$, $|\varepsilon_{e\tau}|$, $\varepsilon'_{ee}$ and $\varepsilon'_{\tau\tau}$, while are one order of magnitude smaller in the $|\varepsilon_{\mu\tau}|$ case (see [475]) since this last parameter appear at leading order in the muon neutrino disappearance probability. There are no current bounds on the phases, however some future experiments are expected to exclude some portions of the their parameters space [475–477].

In Figs. 3.5 and 3.6 results of the global fit for the LIGHT-NO ($\theta_{12} < \pi/4$ and $\Delta m^2_{31} > 0$) and DARK-IO ($\theta_{12} > \pi/4$ and $\Delta m^2_{31} < 0$) solutions respectively. It is worth to mention that the best fit for $|\varepsilon_{e\mu}|$ is not zero, but roughly 0.06; however this result has not a great statistical significance. Moreover, the bounds in the two quasi degenerate solutions are very similar. However, the LMA-Dark solution seem to fit T2K long baseline data but on the other hand is completely disfavored considering solar neutrino data, as already mentioned [475].

### 3.2.3 Propagation scalar NSI

We have so far considered the effect of NSI induced by ordinary matter on neutrino oscillations focusing on vector currents, which may be mediated by a vector mediator [478–481]. However, neutrinos may also couple to scalar fields. Such couplings should be considered even more

[4]From now on, we will drop the superscript $m$ from the NSI couplings when we refer to the propagation NSI. Indeed, this type of NSI is the most studied being the one with the less stringent non-oscillation constraints. In specific models, however, the strengths of source, detector and propagation NSI are predicted to be the same [236, 443].

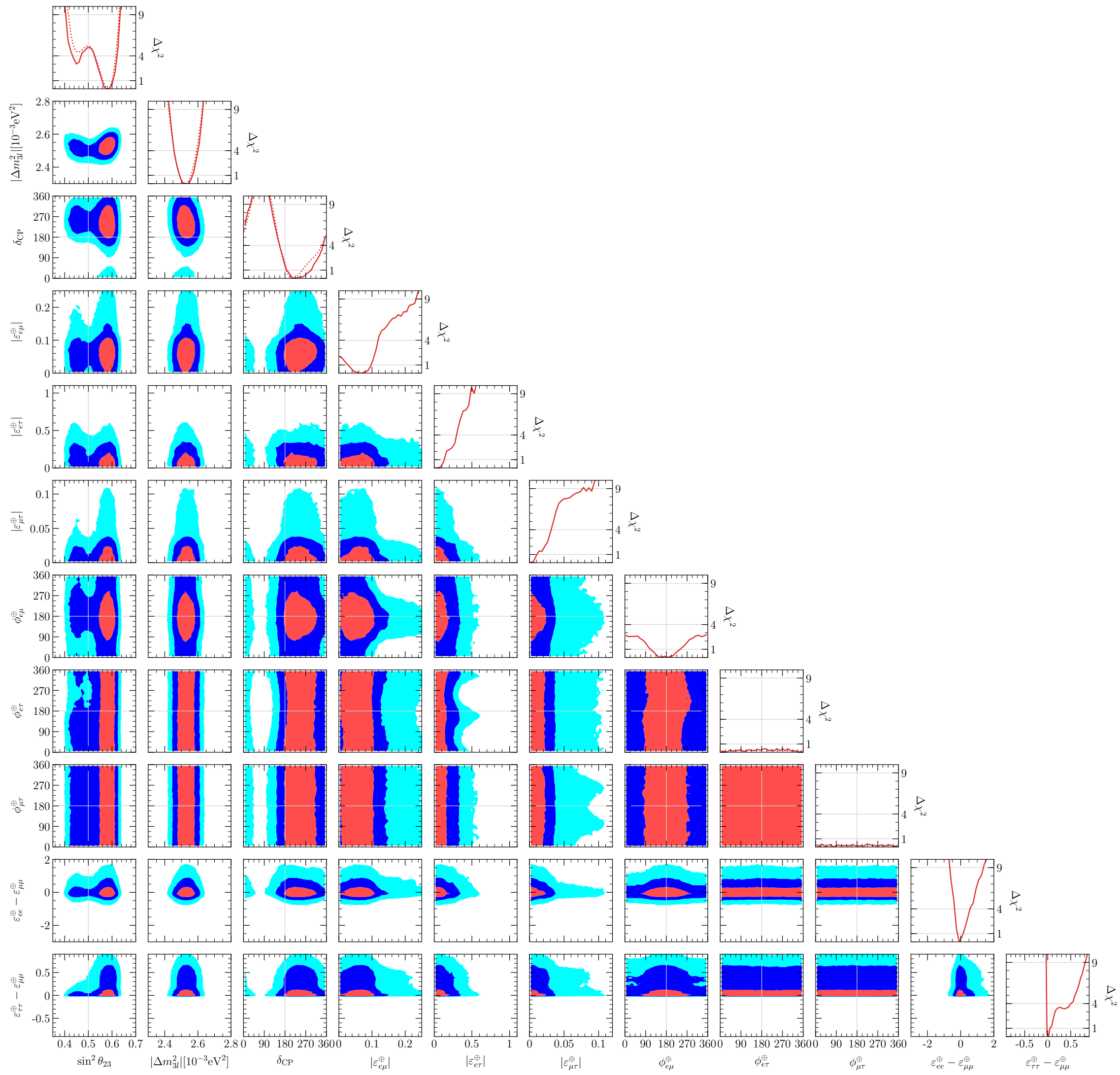

Figure 3.5: Global analysis of solar, atmospheric, reactor and accelerator oscillation experiments in the LIGHT ($\theta_{12} < \pi/4$) side of the parameter space and for Normal Ordering of the neutrino states. For the $\chi^2$ analysis, a marginalization in respect with the undisplayed parameters has been performed. The different contours correspond to the allowed regions at 68%, 95% and 99% CL. Figure from [475].

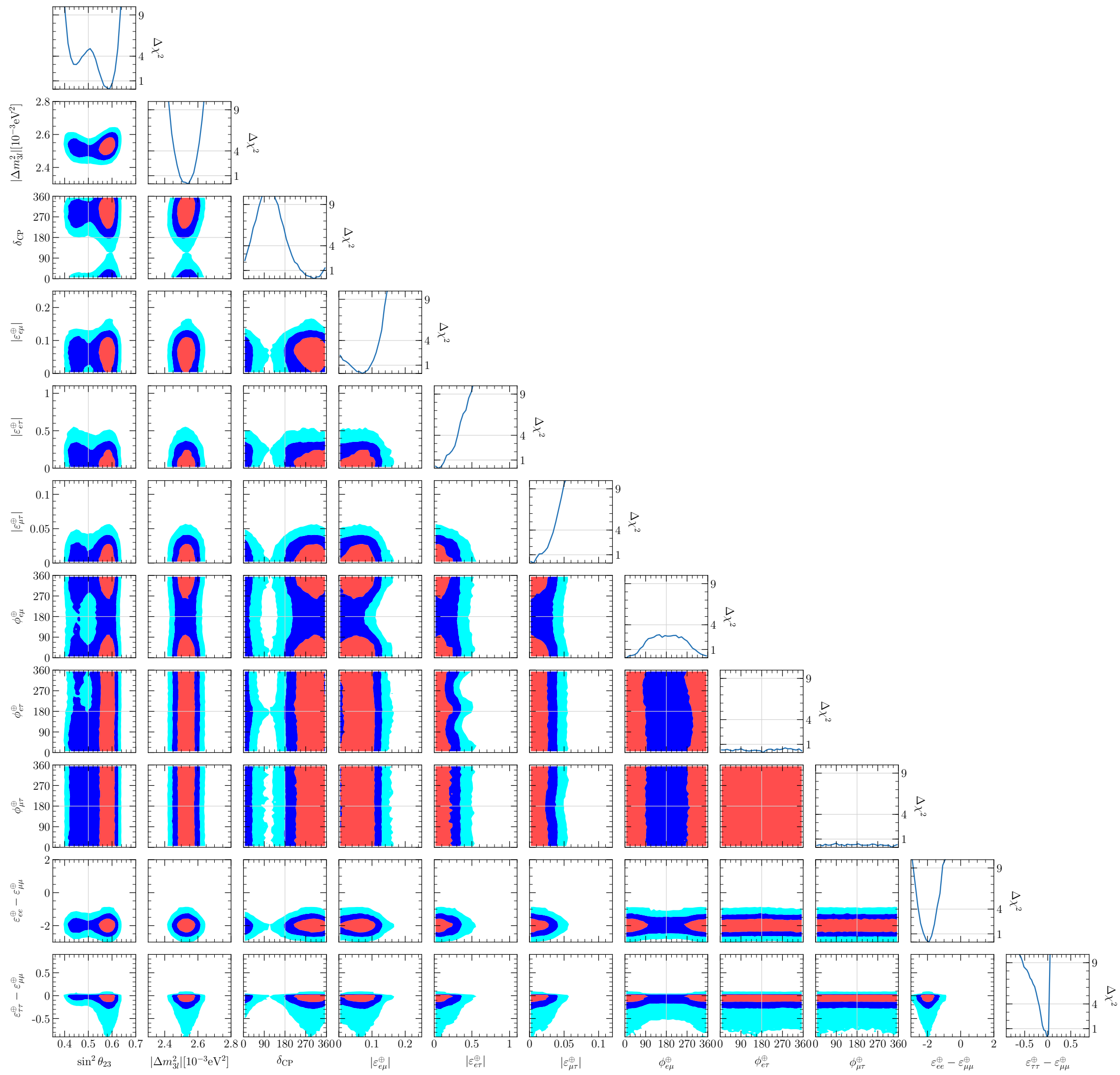

Figure 3.6: Same as Fig. 3.5 but for the DARK solution ($\theta_{12} > \pi/4$) in Inverted Ordering. Figure from [475].

natural, since natural mechanisms for neutrinos to acquire masses may come from the presence of a scalar particle with a non-vanishing vacuum expectation value [243]. It is therefore interesting to explore the phenomenology of scalar NSI. The effect of this type of NSI has been studied in the context of neutrinos propagating in some dark matter media [329, 331, 333, 482–486]; however, we will show that there is a model-independent way to take into account such interactions in neutrino oscillation considering the ordinary matter density. In this case, the lagrangian four fermions effective term can be written as

$$\mathcal{L}_{scalar NSI} = \frac{y_f Y_{\alpha\beta}}{m_\phi^2}[\bar{\nu}_\alpha \nu_\beta][\bar{f} f] \tag{3.27}$$

where $m_\phi$ is the scalar mediator mass, $y_f$ its coupling with the environmental fermion and $Y_{\alpha\beta}$[5] its coupling with neutrinos. This lagrangian term cannot be converted to a vector current one [487, 488]; for this reason, differently from the vector NSI, we cannot expect that scalar NSI modify the standard neutrino matter potential. On the other hand, in the nonrelativistic limit, the matter fermions spinors reduces to $u_f = (\xi, \xi)^T$ where $\xi_+ = (1, 0)^T$ and $\xi_- = (0, 1)^T$ for the two spin polarizations. Thus, $\bar{u}_f u_f = 2\xi^\dagger \xi = n_f$, where $n_f$ is the number density of a given fermion. In this framework, the term in eq. (3.27) can be written as $\sum_f n_f y_f Y_{\alpha\beta}/m_\phi^2\,[\bar{\nu}_\beta \nu_\alpha]$, which is a correction to the neutrino mass term. Defining $\delta M = \sum_f n_f y_f Y/m_\phi^2$, the effective mass matrix which appears in the neutrino oscillation Hamiltonian is modified to

$$M^2 \longrightarrow (M + \delta M)(M + \delta M)^\dagger \,. \tag{3.28}$$

Since the scalar NSI modify the mass term instead of the matter potential, we expect such interactions to produce a different phenomenology in neutrino oscillations. If the mediator mass is light enough, $\delta M$ can survive current constraints obtained from different leptons and neutrinos observables [489–495]. As usual, we can diagonalize the neutrino mass matrix through the PMNS matrix $U_\nu$. However, when such rotation is performed, we cannot rotate away all the unphysical phases in the scalar NSI contribution $\delta M$. We can parameterize after such rotation, in a complete model-independent way, the scalar NSI correction to the mass term in the following way [243]

$$\tilde{M} = \sqrt{\Delta m_{31}^2}\begin{pmatrix} \eta_{ee} & \eta_{e\mu} & \eta_{e\tau} \\ \eta_{e\mu}^* & \eta_{\mu\mu} & \eta_{\mu\tau} \\ \eta_{e\tau}^* & \eta_{\mu\tau}^* & \eta_{\tau\tau} \end{pmatrix} \tag{3.29}$$

where $\eta_{\alpha\beta}$ are dimensionless complex parameters (only the diagonal ones must be real in order to preserve the Hermiticity of the Hamiltonian matrix) and their phases come from both the NSI couplings and the unphysical phases which appear after the diagonalization. The latter are not the only standard neutrino parameters which become measurable only in presence of scalar NSI. Indeed, in absence of new interactions, we only have $M^2$ as mass term in the Hamiltonian; from this matrix we can subtract one of the absolute masses $m_i^2$ without changing the probabilities. This make the oscillations sensitive only to the mass splittings. When $\eta_{\alpha\beta} \neq 0$, on the other hand, we cannot perform the subtraction anymore, since the full mass matrix $(M + \delta M)(M + \delta M)^\dagger$ is no longer diagonal. For this reason, differently from the vector NSI case, the scalar NSI introduce a dependence of the oscillation probabilities on the absolute neutrino mass scale. Moreover, the scalar NSI do not conserve chirality [243, 438, 496].
Considering the scalar NSI Hamiltonian, it seems that the genuine mass term and the scalar NSI ones have exactly the same effect on neutrino oscillation. Thus, oscillations which seem to be driven by a neutrino mass splitting, may be driven only by scalar NSI; there is however an important difference. Indeed, while mass splittings can cause oscillations in vacuum, scalar NSI cannot, since in the definition of the $\eta$-s there is an implicit dependence on the matter

[5] For a real scalar, $Y$ must be an Hermitian matrix.

density $n_f$. In general, it is hard to distinguish the true mass splittings from the scalar NSI induced ones; one of the strategies one can adopt is to look for oscillations at two different matter densities. In this way, the effective measured mass splittings should be different, since the scalar NSI-induced modifications may be different in the two cases [243]. For instance, the presence of a non-zero diagonal term in the scalar NSI matrix could explain the discrepancy of the $\Delta m^2_{21}$ mass splitting measurements of KamLAND and SNO [123, 497] considering that in the SNO case the matter density is bigger. Recent Borexino data [498] seems to favor nonzero scalar NSI. Also atmospheric experiments can be affected by such new interactions, since, depending on the direction of neutrinos, the matter potential is different. Moreover, it has been shown [499] that scalar NSI may also alter the sensitivity of accelerator long baseline experiment to the CP-violating phase $\delta$.

## 3.3 A closer look at Neutrino Decay

In the Standard Model neutrinos are stable particles since, being massless and interacting only via weak interactions [13], there are no particles which may be produced in an hypothetical decay. Even if we consider that neutrinos are massive, we know that their masses must be very small, and their decay remains impossible. However, as widely discussed, in order to generate neutrino masses, we need to introduce new physics processes in the SM. Such process may be responsible of their decay. For instance, neutrino masses can arise from Yukawa couplings between right-handed neutrinos and the Higgs field. If we need a mechanism that generates the right-handed neutrino masses, we can introduce a coupling with a scalar singlet (*Majoron*) that takes a non-vanishing vacuum expectation value and in most of the models, being a Goldstone boson, is massless [255, 500–504]. In presence of such scalar massless particle which couple to neutrinos, we do have a possibility for the neutrino decay. Indeed, in this case, we can build the following lagrangian terms

$$\mathcal{L}_{\nu S} = \frac{(g_s)_{ij}}{2}\bar{\nu}_i\nu_j S + i\frac{(g_p)_{ij}}{2}\bar{\nu}_i\gamma_5\nu_j S \tag{3.30}$$

where S is the Majoron fields and $g_s$ ($g_p$) are scalar (pseudoscalar) couplings. In presence of such terms, the heaviest neutrino states can decay in the following way

$$\nu_i \to \nu_j + S\,. \tag{3.31}$$

Moreover, if neutrinos are Majorana particles, we can have both helicity conserving ($\nu \to \nu + S$ and $\bar{\nu} \to \bar{\nu} + S$) and flipping ($\nu \to \bar{\nu} + S$ and $\bar{\nu} \to \nu + S$) decays. In principle, we can distinguish two types of neutrino decays:

- The neutrino in the final state is an active state, namely one of the other two SM neutrinos. In this case we talk about *visible decay* and the final neutrino can be detected. Since the decay product will have lower energies than the parent neutrino, one of the typical signatures of such decay is an increase of low-energy events at the detector.

- The final state is completely invisible since the produced neutrino is a sterile state. In this case the phenomenology is simpler since we only expect less events at the neutrino detector. This model is known as *invisible decay* model.

Solar [497, 505–512] and supernovae [513–515] neutrinos observations have been able to put strong bounds con the $\nu_1$ ($\tau_1/m_1 > 6 \times 10^{-5}\, s/eV$[6]) and $\nu_2$ ($\tau_2/m_2 > 7 \times 10^{-4}\, s/eV$) lifetimes in the invisible hypothesis. On the other hand, the $\nu_3$ invisible decay lifetime [260, 516] is

[6]In this case $\tau$ is the lifetime in the center of mass frame and $m$ is the neutrino mass eigenstate.

much more difficult to bound ($\tau_3/m_3 > 3 \times 10^{-10}\, s/eV$ at 90% from a current global fit [517]) since it can be measured at atmospheric or accelerator experiments which have relatively small baselines[7]. Using only long baseline data (MINOS and T2K), the bound is reduced by two orders of magnitude [524]. Thus, being the less known, from now on we will only consider the lifetime of the third eigenstate, which in NO is the heaviest. Moreover, we will consider the Majoron to be massless.
In the invisible decay case, the neutrino vacuum Hamiltonian is modified in a very simple way by the presence of the decay width $\Gamma_3 = m_3/(\tau_3 E)$ in the following way [260]

$$H = U^r \begin{pmatrix} 0 & 0 & 0 \\ 0 & \frac{\Delta m_{21}^2}{2E} & 0 \\ 0 & 0 & \frac{\Delta m_{31}^2}{2E} - i\frac{\Gamma_3}{2} \end{pmatrix} (U^r)^\dagger \tag{3.32}$$

where $r$ refers to the neutrino helicity we are considering. The probabilities are thus computed just replacing the atmospheric mass spitting with $\Delta m_{31}^2 - i\Gamma_3 E$. The presence of the imaginary term produce an exponential dumping of some of the probability terms. If the neutrino lifetime is very short ($\Gamma_3 \to \infty$), then such terms become negligible and the oscillation probabilities do not depend anymore on L/E. In presence of matter, we just need to include the matter potential into the neutrino Hamiltonian (note that here we are considering that the sterile neutrino which is produced in the invisible decay does not mix with the active ones). Due to the very simple phenomenology, different studies have been done in order to give bounds on the invisible decay parameter. It is worth to mention that terrestrial bounds on the invisible decay are not competitive to the cosmology ones, which can be up to 15 orders of magnitude more stringent [262, 525–534]; however, such bounds strongly depends on the cosmological model and for this reason it is still interesting to study the neutrino decay at oscillation experiments.

If the decay is visible, on the other hand, we can define the differential probability that a neutrino $\nu_\alpha$ with energy $E_\alpha$ and helicity $r$ oscillate to a neutrino $\nu_\beta$ with energy $E_\beta$ and helicity $s$ as [260]

$$\frac{dP_{\nu_\alpha^r \to \nu_\beta^s}}{dE_\beta} = P^{inv}_{\nu_\alpha^r \to \nu_\beta^s}(E_\alpha)\delta(E_\alpha - E_\beta)\delta_{rs} + \Delta P^{vis}_{\nu_\alpha^r \to \nu_\beta^s}(E_\alpha, E_\beta) \tag{3.33}$$

where the first term is the probability computed in the invisible decay model; the second one, namely the visible decay correction, can be obtained in the following way

$$\Delta P^{vis}_{\nu_\alpha^r \to \nu_\beta^s}(E_\alpha, E_\beta) = \int_0^L |A_{\nu_\alpha^r \to \nu_\beta^s}(E_\alpha, E_\beta)|^2 dL' \tag{3.34}$$

where $A$ is the transition amplitude, L is the experiment baseline and L' is the distance at which the decay occurs. The transition amplitude in this case is proportional to the square root of the normalized energy distribution of the neutrino decay

$$W_{3j}^{rs} = \frac{1}{\Gamma_{3j}^{rs}} \frac{d\Gamma_{3j}^{rs}(E_\alpha, E_\beta)}{dE_\beta} \tag{3.35}$$

where $\Gamma_{3j}^{rs}$ are the $\nu_3^r \to \nu_j^s$ decay widths. Thus, in this model, the new parameters that may be probed at oscillation experiments are all possible combinations of the decay amplitudes and decay energy distribution. The fact that we observe a spectral distortion, due to the dependence of the probabilities to both energies $E_\alpha$ and $E_\beta$ makes the $\tau_3/m_3$ bounds more stringent in the

[7]In principle astrophysical neutrinos at IceCube may bound the $\nu_3$ lifetime, but the large uncertainties on the initial flux make this measurements difficult [518–521]. See [522, 523] for recent neutrino decay applications in IceCube measurements.

visible decay case than in the invisible decay one [258, 507, 535]. For instance, using MINOS and T2K data, if $\nu_3$ decays visibly we get $\tau_3/m_3 > 1.5 \times 10^{-11}\, s/eV$ [259]. However, due to the fact that there are more new parameters in the game, such bounds depends on the hypothesis on the scalar and pseudo-scalar couplings [260].

## 3.4 A closer look at Non-unitarity

Neutrino masses, as widely discussed, are the motivation for many SM extensions. Neutral heavy leptons (NHL) arise in several of such extensions, among the others the type-I seesaw. Their phenomenology, depending on their nature and on the gauge structure of the new physics model, can be very rich. For instance, they can have relevant implications in cosmology, accelerator direct searches, lepton flavor violation process, neutrinoless double beta decays.
However, even if they are too heavy to be produced in current experiments or if the new physics processes they induce are too rare, their presence can be indirectly probed with neutrino oscillations. Indeed, every time we introduce new neutral leptons, they can mix with SM neutrinos. Thus, the PMNS matrix, in presence of new physics, may be larger than the usual $3 \times 3$ one [248]. If new particles are much heavier than the 3 usual neutrinos, their oscillations are too fast to be resolved and their major observable effect is to break the unitarity of the $3 \times 3$ mixing matrix, given that only the full matrix must satisfy the unitarity conditions.

### 3.4.1 Non-unitarity formalism and non-oscillation experiments

A general $3 \times 3$ mixing matrix, without any unitarity constraints, requires 9 additional real parameters to be parameterized. One of the most convenient choice for the Non-Unitary mixing matrix parameterization, is the so-called *lower-triangular parameterization.* In this case, the PMNS matrix is written as [203, 249, 536]

$$N = (1 + \alpha)U \tag{3.36}$$

where U is the $3 \times 3$ unitary PMNS matrix and

$$\alpha = \begin{pmatrix} \alpha_{11} & 0 & 0 \\ \alpha_{21} & \alpha_{22} & 0 \\ \alpha_{31} & \alpha_{32} & \alpha_{33} \end{pmatrix} . \tag{3.37}$$

As usual, the three diagonal parameters are real, while the three off-diagonal ones are complex and carry new phases. Due to the zeros in the first two rows of the $\alpha$ matrix, the non-standard parameters which are important in the neutrino oscillations which are usually studied in accelerator, atmospheric, solar and reactor experiments are $\alpha_{11}$, $\alpha_{22}$ and $\alpha_{21}$ (that appear at the leading order respectively in the $\nu_e \to \nu_e$, $\nu_\mu \to \nu_\mu$ and $\nu_\mu \to \nu_e$ probabilities). The other parameters may be probed using $\nu_\tau$ appearance or looking at the matter induced probability terms. Talking about the matter effects, the fact that the PMNS matrix is no longer unitary does not allow us to subtract the NC matter potential to the Hamiltonian matrix as a multiple of the unit matrix. For this reason, in the probabilities two matter potentials appear, which are related to both CC and NC interactions with enviromental fermions.
In the hypothesis that the Non-Unitarity comes from the presence of HNL, the $\alpha_{ij}$ parameters can be written in terms of complex sines ($\xi_{ij} = e^{-i\phi_{ij}} \sin\theta_{ij}$, where $\phi_{ij}$ are the CP violating phases) and cosines ($c_{ij} = \cos\theta_{ij}$) of the mixing angles [203, 537–539]. In presence of $n-3$ new HLN, the three diagonal parameters are

$$1 + \alpha_{11} = c_{1n} c_{1n-1} c_{1n-2} \ldots c_{14}, \tag{3.38}$$

$$1 + \alpha_{22} = c_{2n} c_{2n-1} c_{2n-2} \ldots c_{24}, \tag{3.39}$$

$$1 + \alpha_{33} = c_{3n} c_{3n-1} c_{3n-2} \ldots c_{34} \tag{3.40}$$

while the three off diagonal ones can be written in a more complicated way, as shown in [249]. However, using such equations, one can derive some relations between off-diagonal and diagonal parameters[8], namely

$$|\alpha_{ij}| < \sqrt{(1+\alpha_{ii})^2(1+\alpha_{jj})^2} \tag{3.41}$$

called *triangular relations* [253].

Bounds on non-unitarity parameters can be extracted, in the HNL hypothesis, using lepton universality constraints [249, 540]. Indeed, new neutral leptons can enter in the muon and beta decays amplitude modifying in different ways the effective Fermi constants and breaking the unitarity constraints of the first row of the CKM matrix [13, 184, 539, 541–546]. From these measurements one obtain that $-2\alpha_{22} - \alpha_{22}^2 - |\alpha_{21}|^2 < 0.0005$ at $1\sigma$. From pion decay branching ratios [547, 548], it is possible to extract other bounds, for instance $-2\alpha_{11} - \alpha_{11}^2 < 0.0130$ at 90% CL. If neutrinos are Majorana, bounds con $\alpha_{11}$ may be set by neutrinoss double beta decays experiments [203, 549]. Other model-dependent bounds are discussed in [249, 253].

### 3.4.2 Non-Unitarity and neutrino oscillations

The breaking of the unitarity of the PMNS matrix can certainly change the oscillation probabilities. In this case the flavor transitions will depend not only on the standard mixing parameters, but also on the new $\alpha$ parameters. This would introduce new phenomenological features of the oscillations. For instance, the breaking of the PMNS unitarity induces also the breaking of the probabilities unitarity: $\sum_\beta P_{\alpha\beta} \neq 1$. Moreover, in this case we have the so-called *zero-distance effect*, namely $P_{\alpha\beta}(L=0) \neq \delta_{\alpha\beta}$. This can be interpreted, if the non-unitarity is caused by the presence of new heavy neutral states, as the effect of averaged out very fast oscillations, which occur at very short baseline.

Thus, from experiments with $L \sim 0$, we can extract bounds on $\alpha_{11}$, $\alpha_{22}$ and $\alpha_{21}$ looking at $\nu_e \to \nu_e$, $\nu_\mu \to \nu_\mu$ and $\nu_\mu \to \nu_e$ oscillation data, respectively. At 90% CL, one gets $\alpha_{11} \sim 10^{-3}$, $\alpha_{22} \sim 10^{-4}$ and $\alpha_{21} \sim 10^{-3}$ [80, 253, 411, 550, 551]. Also long baseline experiments data can be used to set bounds on Non-Unitarity parameters using CC and NC data [551, 552]; however, in this case, it is crucial to be able to know the flux precisely without the beam monitoring of a Near Detector, which would be as well affected by non-unitarity via zero-distance effects. We will discuss this point later.

Another interesting method that has been used to set unitarity bounds on the PMNS matrix consists on the study of the leptonic unitarity triangles[9]. Indeed, the unitarity relations $\sum_i U_{\alpha i}U^*_{\beta i} = 0$ and $\sum_\alpha U_{\alpha i}U^*_{\alpha j} = 0$ define closed triangles in the complex planes. If we consider the following parameters

$$\rho_{xy} + i\eta_{xy} = -\frac{U_{x\beta}U^*_{y\beta}}{U_{x\gamma}U^*_{y\gamma}} \;\; or \;\; -\frac{U_{\alpha x}U^*_{\alpha y}}{U_{\delta x}U^*_{\delta y}}\,, \tag{3.42}$$

in the $(\rho_{xy}, \eta_{xy})$ planes, these triangles have two fixed vertices, namely the origin and (1,0) and a third vertex which depends on the experimental value of the mixing matrix entries. The Non-Unitarity of the PMNS matrix should cause the opening of the unitarity triangles. A complete analysis using this approach can be found in [555, 556].

[8] Notice from eq. 3.40 that in the hypothesis that the unitarity breaking come from the presence of new heavy states, $\alpha_{ii} < 0$.

[9] Unitarity triangles are widely used in the context of the CKM matrix, see [13, 90, 553, 554] and references therein.

## 3.5 Equivalence of the oscillation phenomenology in different BSM models

We discussed different BSM models which modify the neutrino oscillation Hamiltonian matrix. Such matrix, being a simple $3 \times 3$ Hermitian matrix, has a relatively small number of degrees of freedom. Thus, it has been studied the possibility to find connections between new physics parameters of different models [254]. In particular, among the models we discussed in details, it has been shown the phenomenological equivalence of the 3+1, Non-unitarity and NSI models.
Let us first consider the equivalence between the 3+1 model and Non-unitarity model. In this case, we can chose for instance (neglecting the CP violating phases), the PMNS matrix parameterization

$$U_{PMNS} = R(\theta_{34})R(\theta_{24})R(\theta_{14})R(\theta_{23})R(\theta_{13})R(\theta_{12})\,. \tag{3.43}$$

Doing so, we can write, in the 3 active neutrino sector, the PMNS matrix as

$$U'_{PMNS} = NU^{3\nu}_{PMNS} \tag{3.44}$$

where $U^{3\nu}_{PMNS}$ is the usual PMNS matrix and $N$ is the $3{\times}3$ sector of the matrix $R(\theta_{34})R(\theta_{24})R(\theta_{14})$. Such matrix, in this particular parameterization can be written as

$$N = \begin{pmatrix} \cos\theta_{14} & 0 & 0 \\ -\sin\theta_{14}\sin\theta_{24} & \cos\theta_{24} & 0 \\ -\cos\theta_{24}\sin\theta_{14}\sin\theta_{34} & -\sin\theta_{24}\sin\theta_{34} & \cos\theta_{34} \end{pmatrix} \tag{3.45}$$

which is a lower triangular matrix, just like the non-unitarity matrix previously discussed. Thus, we obtain the following relations between Non-unitarity and 3+1 parameters

$$1+\alpha_{11} = \cos\theta_{14} \tag{3.46}$$
$$1+\alpha_{22} = \cos\theta_{24} \tag{3.47}$$
$$1+\alpha_{33} = \cos\theta_{34} \tag{3.48}$$
$$\alpha_{21} = -\sin\theta_{14}\sin\theta_{24} \tag{3.49}$$
$$\alpha_{31} = -\cos\theta_{24}\sin\theta_{14}\sin\theta_{34} \tag{3.50}$$
$$\alpha_{32} = -\sin\theta_{24}\sin\theta_{34} \tag{3.51}$$

which in the diagonal sector correspond to eq. (3.40) for n=1. It is worth to mention that the two models have the same phenomenology only if sterile neutrino oscillations can be averaged out. If not, the new oscillation frequency driven by $\Delta m^2_{41}$ would modify the probabilities.
Considering source and detector NSI, we pointed out that the oscillation probability can be directly computed squaring the quantity $(1+\varepsilon^d)Ue^{-iHL}U^\dagger(1+\varepsilon^s)$. It is evident that we can map the NSI parameters to the Non-unitarity (and thus to the 3+1) ones using the relations[10]

$$\varepsilon^{s*}_{\beta\alpha} = \varepsilon^d_{\alpha\beta} = \alpha_{\alpha\beta}\,. \tag{3.52}$$

Finally, let us consider the propagation vector NSI. In this case it is more complicated to find a direct correspondence. However, in the Non-unitary case, the matter effect matrix can be written as

$$N^\dagger \begin{pmatrix} V_{CC}+V_{NC} & 0 & 0 \\ 0 & V_{NC} & 0 \\ 0 & 0 & V_{NC} \end{pmatrix} N \tag{3.53}$$

[10]In our previous discussions, we used flavor indices for the NSI parameters and numerical indices for Non-unitarity parameters. Here, with $\alpha_{\alpha\beta}$ we denote $\alpha_{ij}$ where $e=1$, $\mu=2$, $\tau=3$.

where $N = (1+\alpha)U_{PMNS}$. Neglecting higher order terms in $\alpha_{ij}$ and using the approximation that neutron and electron densities are the same, we get

$$-\frac{V_{CC}}{2}U^\dagger \begin{pmatrix} 2-2\alpha_{11} & \alpha_{21}^* & \alpha_{31}^* \\ \alpha_{21} & 2\alpha_{22} & \alpha_{32}^* \\ \alpha_{31}^* & \alpha_{32}^* & 2\alpha_{33} \end{pmatrix} U\,. \tag{3.54}$$

This matrix can be easily mapped to the propagation NSI ones using the relations

$$\varepsilon_{\alpha\alpha} = c_{\alpha\alpha}\alpha_{\alpha\alpha} \tag{3.55}$$

$$\varepsilon_{\alpha\beta} = \frac{1}{2}\alpha_{\beta\alpha}^* \tag{3.56}$$

where $c_{\alpha\alpha} = 1$ for $\alpha = e$, $-1$ otherwise.
The fact that such correspondences exist between BSM parameters allow us to extract bounds on one model knowing bounds on another one. However, it is important to consider that even if the phenomenology seems to be the same for all the models, the physics behind for instance NSI and sterile neutrinos is very different. Indeed, depending on the experiment, we cannot always probe all the models in the same way. In very short baseline experiments we have access to the unitarity violation via zero distance effects, but propagation NSI are not developed yet due to the absence of matter effects. Moreover, in some conditions, if we try to connect 3+1 mixing angles and NSI couplings, we may obtain unphysical solutions, such as $\sin\theta_{i4} > 1$.
It is worth to mention another important correspondence that has been explored in literature: the one between the CPT-odd Lorentz violating parameters and the propagation NSI ones [269, 270]. Only recently it has been recently proposed a way to distinguish between these two models using Earth core passing atmospheric neutrinos [291].

# Chapter 4

# Next Generation Long Baseline Experiments

We discussed how rich the oscillation phenomenology can be, considering also all the possible BSM models that may affect the neutrino oscillation probabilities. However, as already pointed out, current neutrino data are not enough to answer all the open questions in this sector and there are still different observables that need to be determined. For this reason, a certain number of future oscillation experiments have been proposed.
The first next-generation experiment to take data will be the reactor experiment JUNO (Jiangmen Underground Neutrino Observatory) [557], which will be ready to collect neutrino data in the next few years. Such experiment, considered as a follow-up of Daya-Bay, will be placed at a distance of 53 km from different reactor plants in China. Its long baseline (with respect to reactor neutrino energy) will allow JUNO to look at low frequency solar oscillations modulated by high frequency atmospheric oscillations. The great expected energy reconstruction of this experiment will hopefully lead to precise measurements of mixing parameters as well as to the determination of the neutrino mass ordering [558, 559].
After JUNO, in the 2030s, two long baseline experiments will become operative: DUNE (Deep Underground Neutrino Experiment) in the USA [560, 561] and T2HK (Tokai to Hyper-Kamiokande) in Japan [156]. While the former can be considered as a completely new experiment (even though it will share some facilities with the successful NO$\nu$A experiment), the latter will be an upgrade of the T2K experiment. These two experiments are expected to provide a great environment for the study of oscillations in the SM as well as in BSM scenarios. We will later discuss their potential in searching for new physics hints; before that, we will describe in this chapter which are their essential features and which are their expected performances in constraining standard physics parameters.

## 4.1 DUNE (Deep Underground Neutrino Experiment)

The DUNE experiment [14, 560–562], proposed in 2014, whose construction began in 2017, is expected to start taking data by the end of this decade (possibly in 2027). It will consist of a far detector located 1.5 km underground at the Sanford Underground Research Facility (SURF) in South Dakota and a near detector complex [157] located at Fermilab, Illinois. The distance between the two facilities will be roughly 1300 km; for this reason DUNE will be the neutrino experiment with the longest baseline ever built. Both detectors will be exposed to the world's most intense neutrino beam, which is originated at Fermilab. Its primary science goals are

- Neutrino oscillation measurements using $\nu_\mu$ and $\bar{\nu}_\mu$ beams from Fermilab. These include the measurement of the CP phase of the PMNS matrix (the proposed goal is to reach $3\sigma$

sensitivity for the 75% of the possible values of the phase), the determination of the mass ordering and a precise measurement of $\theta_{23}$, which will allow to solve the octant degeneracy.

- Search for proton decay in several modes.
- Detection of the $\nu_e$ flux from a core-collapse supernova within our galaxy.

However, the experimental setup will allow DUNE to have a very rich ancillary science program. Such program includes the study of BSM physics in the oscillation context, the detection of atmospheric neutrinos, the searches for dark matter and neutron-antineutron oscillation and the measurements of neutrino cross sections with a focus on the nuclear effects.

### 4.1.1 DUNE Detectors

Extensive preliminary studies suggested that for the main DUNE goals, a 1300 km baseline was well-optimized for neutrino oscillation physics. Considering that the beam facility was already present at Fermilab for the NO$\nu$A experiment, the Homestake mine in South Dakota, where the SURF is located, has been chosen as far site. In order to attenuate the cosmic rays background, the far detector should have been built sufficiently underground.
The Liquid Argon Time Projection Chamber (LArTPC) technology [563] will be adopted by DUNE. These kind of detectors provide a good scalability, an high-performance event imaging as well as calorimetry and particle identification capabilities. Such features are very important for an experiment in which the neutrino beam has a wide energy range (see following subsection). We will now briefly describe the main features of the far and the near detectors.

#### DUNE Far Detector

The DUNE Far Detector (FD) will consist of four LArTPC modules, each contained in a cryostat filled with 17.5 kt of liquid Argon; each module has a fiducial mass of at least 10 kt. Thus, the total far detector mass is of about 40 kt. The DUNE collaboration considered two possible LArTPC technologies.

- *Single-phase*: in this case, the ionization charges are drifted horizontally and read out on wires contained in the liquid argon. Such technology has already been used for the first LArTPC detector, namely ICARUS [142] and for the SBN (Short Baseline Neutrino Project) [416] detectors: SBND and MicroBooNE. However, for a large detector like the DUNE one, the electronics requirements in single phase are very stringent.
- *Dual-phase*: the dual-phase technology is less established but in principle offers some advantages. In this case, the ionization charges are drifted in the LAr and transferred into a layer of gas above the liquid. Here, electron multiplier devices amplify the charges. The improved charge gain in the gas phase reduces the requirements on the electronics. However, a dual-phase detector needs an higher voltage, allowing on the other hand an increased drift length.

Two DUNE prototypes, ProtoDUNE-SP and ProtoDUNE-DP are currently running at CERN. Each detector is one-twentieth of the expected size of the DUNE FD [564, 565].
Very recent studies based on the performances of the two ProtoDUNE detectors, observed that the gain from the gaseous phase of the dual phase technology may not be needed. For this reason, the first FD module has been chosen to be a single-phase detector [566]. For the second module, a third possibility is being currently studied: the *Vertical Drift technology* [567–570]. A Vertical Drift single-phase detector may benefit from the advantages of the dual-phase design while eliminating the complexity due to the liquid-gas interface. In particular, such a detector, compared to a standard horizontal drift single-phase detector, maximizes the active volume, has a simpler installation and suffers from less mechanical deformations.

**DUNE Near Detector complex**

For long baseline neutrino experiments the presence of a Near Detector (ND) can be crucial. Indeed, if we analyze the data considering the ratio between the number of the events at the FD and at the ND, we can reduce many sources of uncertainties. For instance, the ND can be used to estimate the neutrino flux close to the beam source. In this way one can have a better understanding of the expected flux composition at the FD. Moreover, if the ND is a rescaled replica of the FD, most of the systematic uncertainties due to the detector are canceled out when the ratio between the number of events at the two baselines is computed. Other than that, since the ND is exposed at a very high intensity flux, it can be used to perform physics measurements, such as cross sections or BSM oscillation studies.
The DUNE Near Detector complex, located at a distance of 574 metres from the beam source, will be made up of three components [157]:

- *ArgonCube*: the main detector, a smaller replica of the FD LAr-TPC. Its fiducial mass will be at least 50 tons; some references take into account 67 tons. Its main purposes are the experimental control for the FD as well as the flux composition and spectrum determinations. This detector can be moved in different off-axis positions in order to better understand the neutrino beam. Such capability is reffered to as DUNE-PRISM (DUNE Precision Reaction-Independent Spectrum Measurement). ArgonCube can also be used to probe BSM models which allow oscillations also at very short baselines.

- *Multipurpose detector (MPD)*: an high-pressure gasseous argon TPC (HPgTPC) with a fiducial mass of approximately 1 ton. This detector will be placed inside a magnetic field, differently from the LArTPC-s. For this reason MPD can recognize the charge of the particles. It can be used as experimental control for ArgonCube and the FD, but also to measure exclusive final states with low momentum threshold. This last feature makes this detector very useful for BSM searches not in the neutrino sector. MPD can also be moved off-axis together with ArgonCube thanks to DUNE-PRIMS.

- *System for on-Axis Neutrino Detection (SAND)*: this detector, which always remains in the same position, will provide a constant and continuous on-axis flux determination.

### 4.1.2 Neutrino fluxes, event rates and detectors' performances

The current generation of long-baseline neutrino experiments (NO$\nu$A and T2K) used narrow-band beams in order to study neutrino oscillations. Moreover, such experiments have their FD located off-axis. This essentially means that the beam is not exactly focused to the Far Detector. The main advantage is the low background rate in $\nu_e$ appearance and $\nu_\mu$ disappearance channels from misidentified NC interactions of high-energy neutrinos. However, this comes at a cost of flux and spectral information with respect to an on-axis configuration [571, 572]. DUNE has as its basic concept the use of a wide-band on-axis beam, which allows to scan over a wide L/E ratios and assures an high event statistics. The background mitigation is granted by the highly-performant detector technology.

**Beam Facility and Neutrino Fluxes**

The neutrino flux is generated by the collision of a proton beam on a fixed target. After the protons interactions, a certain number of mesons, mostly pions, are created and focused in a decay tunnel. While travelling in such tunnel, mesons decay producing neutrinos (mainly $\nu_\mu$ with small $\nu_e$ contamination due to the rare pions electronic decays and kaons decays) and other particles, like leptons or other hadrons. These last particles are absorbed or deviated away by a magnetic field: the only remaining particles are the neutrinos which are now relatively focused

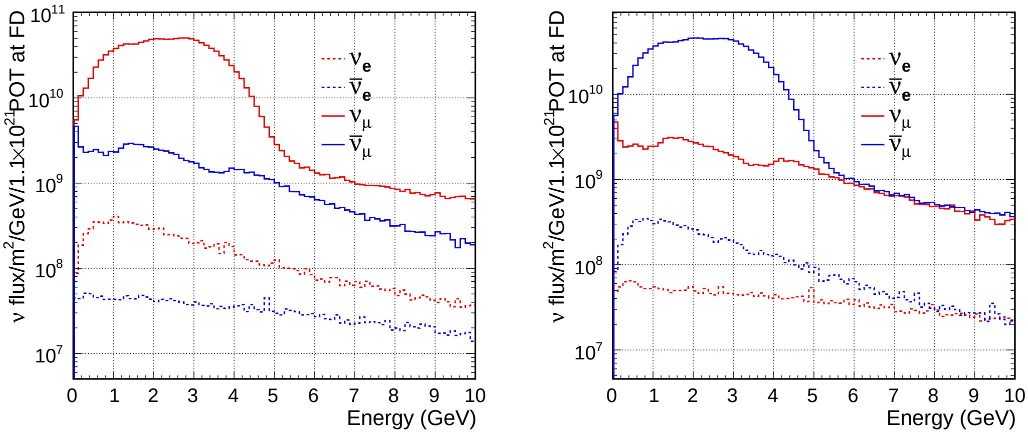


Figure 4.1: Neutrino fluxes at the DUNE FD in neutrino (left) and antineutrino (right) modes. Figure taken from [561].

in a beam and sent to the Near and Far detectors complexes.
In the DUNE experiment, many configurations are being studied. However, the last DUNE Technical Design Report (TDR) [560, 561] takes into account 1.2 MW of 120 GeV primary protons[1] sent to a 2.2 m long graphite target. This corresponds to $1.1 \times 10^{21}$ POT/year (protons on target per year) and a total exposure of 480 kt·MW·yrs. Then, the hadrons produced by proton interactions are focused by magnetic horns: when positive (negative) charged hadrons are selected, DUNE runs in $\nu$-mode ($\bar{\nu}$-mode), namely the neutrino flux will be mostly composed by $\nu_\mu$ ($\bar{\nu}_\mu$). Since the negative hadrons produced by proton interactions are less than the positive ones, we expect the antineutrino flux to be less intense than the neutrino one.
In Fig. 4.1 we show the initial non-oscillated neutrino fluxes at the far detector taken from the DUNE TDR [561]. It is clear that in both neutrino and antineutrino modes, the flux is peaked around 2.5 GeV. This is what we need in order to have the largest statistics at the first atmospheric peak ($\Delta m^2_{31} L/4E \sim \pi/2$). However, the flux is only reduced of a factor of 4 in the broad range [0-5] GeV. This clearly shows the meaning of broad-band beam experiment: we have an important neutrino flux for a wide range of L/E ratios and we can even observe oscillations at the second atmospheric maximum, which comes at around 0.88 GeV. In each mode, the wrong-sign neutrinos ($\bar{\nu}_\mu$ in neutrino mode and $\nu_\mu$ in antineutrino mode) represent a non-negligible fraction of the total neutrino flux. This has to be taken into account since the DUNE LArTPC FD will not be able to distinguish the sign of the lepton produced by the neutrino interaction. On the other hand, the electron neutrino beam contamination is only a subdominant fraction of the flux ($\sim 1\%$ at the beam peak). Fig. 4.2 shows the $\nu_e$ and $\nu_\mu$ spectra expected at the far detector after oscillation given the initial fluxes described above and the parameters best fits in NO from [152]. The DUNE running time considered here is 3.5 years in neutrino and 3.5 years in antineutrino modes. The DUNE running time is divided by the collaboration in different stages: one year with 20 kt, two years with 30 kt and the rest with the total 40 kt of fiducial mass; after 6 year, the beam is also upgraded up to 2.4 MW[2]. For each oscillation channels also the background events are shown. These are

- For the $\nu_e$ *appearance channel*, the $\nu_e$ and $\bar{\nu}_e$ CC events due to the electron neutrino beam contamination as well as misidentified NC, $\nu_\tau$ CC and $\nu_\mu$ CC events.
- For the $\nu_\mu$ *disappearance channel*, the misidentified NC, $\nu_\tau$ CC and $\nu_e$ CC events.

[1]In earlier studies also 80 GeV protons have been considered [14, 562].
[2]When not specified, we do not adopt such running staging.

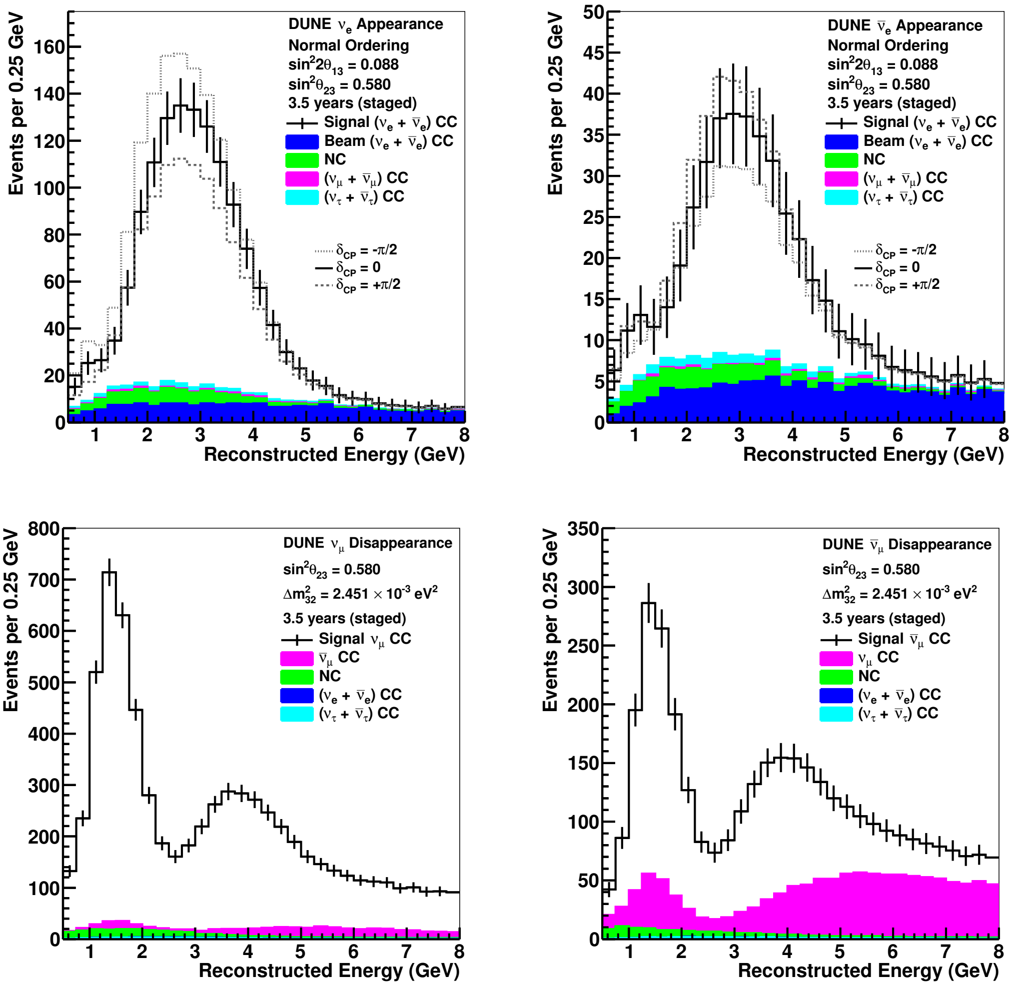


Figure 4.2: $\nu_e$ (top left), $\bar{\nu}_e$ (top right), $\nu_\mu$ (bottom left) and $\bar{\nu}_\mu$ (bottom right) fluxes at the Far Detector considering neutrino oscillations with best fit parameters [152] in NO. The total running time in this case is 3.5+3.5 years staged. Figure taken from [561].

| | Expected events (3.5 years staged) |
|---|---|
| **$\nu$ mode** | |
| $\nu_e$ Signal NO (IO) | 1092 (497) |
| $\bar{\nu}_e$ Signal NO (IO) | 18 (31) |
| Total Signal NO (IO) | 1110 (528) |
| Beam $\nu_e + \bar{\nu}_e$ CC background | 190 |
| NC background | 81 |
| $\nu_\tau + \bar{\nu}_\tau$ CC background | 32 |
| $\nu_\mu + \bar{\nu}_\mu$ CC background | 14 |
| Total background | 317 |
| **$\bar{\nu}$ mode** | |
| $\nu_e$ Signal NO (IO) | 76 (36) |
| $\bar{\nu}_e$ Signal NO (IO) | 224 (470) |
| Total Signal NO (IO) | 300 (506) |
| Beam $\nu_e + \bar{\nu}_e$ CC background | 117 |
| NC background | 38 |
| $\nu_\tau + \bar{\nu}_\tau$ CC background | 20 |
| $\nu_\mu + \bar{\nu}_\mu$ CC background | 5 |
| Total background | 180 |

Table 4.1: Integrated rates of selected $\nu_e$ and $\bar{\nu}_e$ events signal and backgrounds. For backgrounds NO has been assumed. $\delta_{CP}$ has been fixed to 0. Table from [561].

| | Expected events (3.5 years staged) |
|---|---|
| **$\nu$ mode** | |
| $\nu_\mu$ Signal | 6200 |
| $\bar{\nu}_\mu$ Signal | 389 |
| Total Signal | 6589 |
| NC background | 200 |
| $\nu_\tau + \bar{\nu}_\tau$ CC background | 46 |
| $\nu_e + \bar{\nu}_e$ CC background | 8 |
| Total background | 254 |
| **$\bar{\nu}$ mode** | |
| $\nu_\mu$ Signal | 2303 |
| $\bar{\nu}_\mu$ Signal | 1129 |
| Total Signal | 3432 |
| NC background | 101 |
| $\nu_\tau + \bar{\nu}_\tau$ CC background | 27 |
| $\nu_e + \bar{\nu}_e$ CC background | 2 |
| Total background | 130 |

Table 4.2: Integrated rates of selected $\nu_\mu$ and $\bar{\nu}_\mu$ events signal and backgrounds. $\delta_{CP}$ has been fixed to 0. Table from [561].

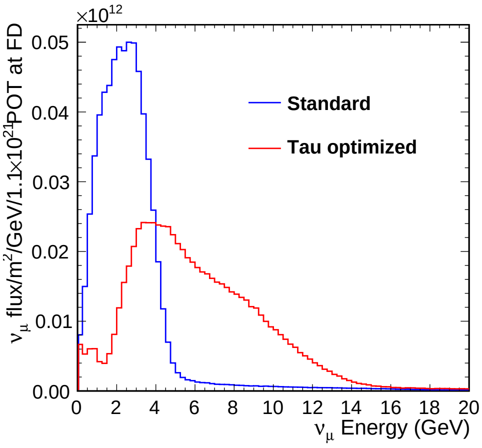


Figure 4.3: Standard neutrino flux optimized for $\delta_{CP}$ determination (blue line) vs high-energy flux optimized for the $\nu_\tau$ searches (red line). Figure from [561]. We show here only the flux in neutrino mode. For the same in antineutrino mode see [16].

In Tabs. 4.1 and 4.2 the total expected number of signal and background events are reported. Now we can discuss together the tables and the figures. First of all, in the appearance channel, we expect, roughly 1100 signal events in $\nu$-mode and 300 in $\bar{\nu}$-mode in the Normal Ordering hypothesis. If we consider the Inverted Ordering, we expect roughly 500 events in both cases. The total background rate is 300 events in the $\nu$-mode and 180 $\bar{\nu}$-mode. From fig. 4.2 we can see that, in NO, around the oscillation maximum, the number of background events is 7 (5) times smaller than the number of signal events in neutrino (antineutrino) modes. Thus, the backgrounds become very important only below 1.5 GeV and above 5 GeV.
In the disappearance channel, where the mass ordering has not a considerable impact, we expect 6600 signal events in neutrino mode and 3400 in antineutrino mode. The number of background events are respectively roughly 200 and 150. Thus, the backgrounds are even less important in this channel. In Fig. 4.2 we observe that the disappearance spectra have two peaks, which correspond to the atmospheric oscillation minima, around 1.5 GeV and 4 GeV. Around the first oscillation maximum (2.5 GeV), on the other hand, we have a minimum in the spectra. The number of background events is negligible. On the other hand, the wrong sign events, which can be considered as signal since the DUNE detector cannot distinguish the lepton charge, are negligible in neutrino mode, while very important, in particular for $E > 3$ GeV in antineutrino mode.

It is worth to mention that the flux peaked at 2.5 GeV is not the only one which has been proposed by the DUNE collaboration. Indeed, an high-energy flux, peaked at around 5 GeV (Fig. 4.3) with a considerable high-energy tail, is under consideration. This flux would allow DUNE to collect many $\nu_\tau$ events, which come from $\nu_\mu \to \nu_\tau$ oscillations. Indeed, $\nu_\tau$ CC interactions have a very high energy threshold (3.1 GeV) and with the usual neutrino flux we expect DUNE to be able to observe only a few tens events (see Sec. 4.1.4). Studying $\nu_\tau$-s may be very interesting since so far only the DONUT and OPERA experiments were able to detect few of them [7, 149, 573].

### Efficiencies and Energy resolutions

As already mentioned, the DUNE experiment, as usual for long-baseline experiments, will mostly study the electron appearance and the muon disappearance channels. For the first one, the detector observes $\nu_e$ CC interactions with nuclei. In such processes, an electron is generated, which creates an electromagnetic shower, which leaves a particular signature in the LArTPC. On the other hand, in order to collect disappearance events, the detector observes $\nu_\mu$ CC interactions

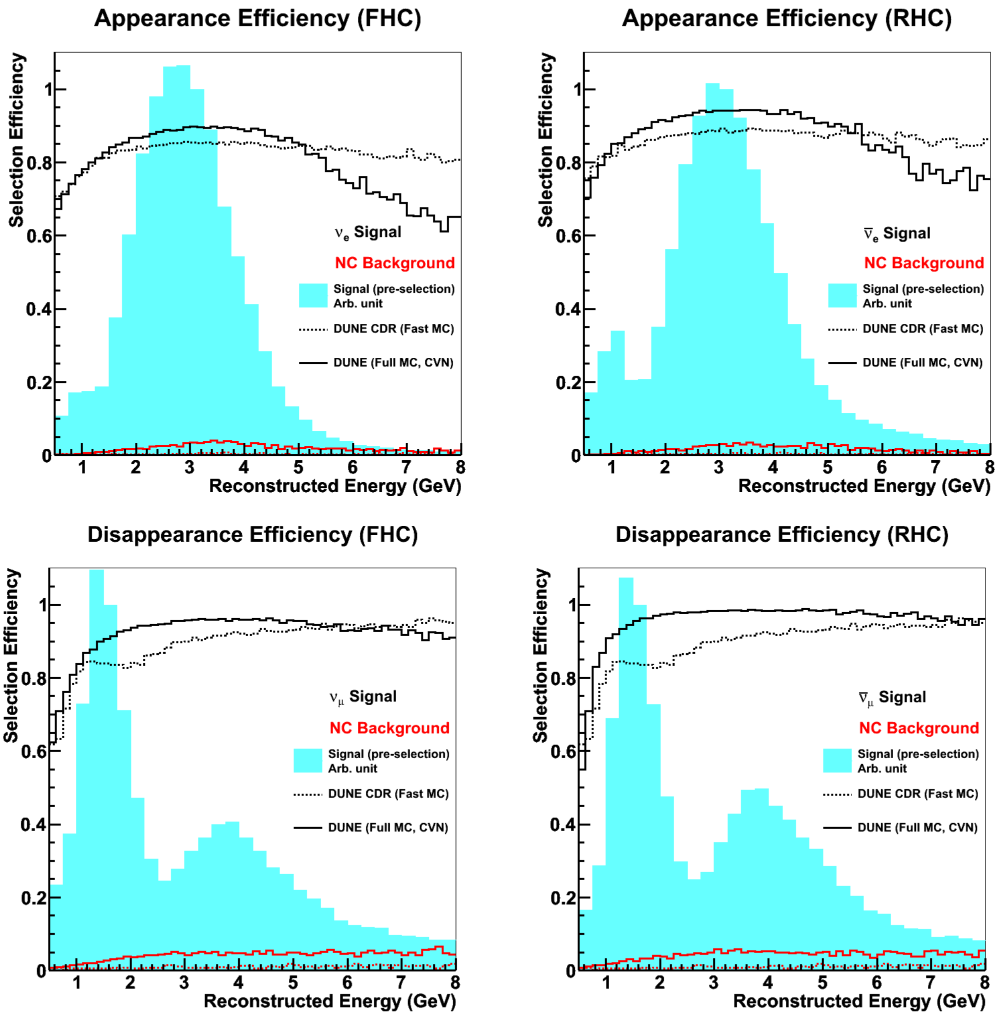


Figure 4.4: Selection efficiency in neutrino and antineutrino mode for the appearance (top panels) and disappearance (bottom panels). The selected events are the ones for which the probability to be a $\nu_e$ ($\nu_\mu$) event is greater than 85% (50%). Figures taken from [561].

| **Particle type** | Detection Threshold | Energy resolution | Angular resolution |
|---|---|---|---|
| $\mu$ | 30 MeV | Contained tracks: track length<br>Exiting tracks: 30% | 1° |
| $\pi$ | 100 MeV | $\mu$-like contained tracks: track length<br>$\pi$-like contained tracks: 5%<br>Showering or exiting tracks: 30% | 1° |
| $e/\gamma$ | 30 MeV | $2\% \oplus 15\%/\sqrt{E}[GeV]$ | 1° |
| p | 50 MeV | p<400 MeV/c: 10%<br>p>400 MeV/c: $5\% \oplus 30\%/\sqrt{E}\,[GeV]$ | 5° |
| n | 50 MeV | $40\%/\sqrt{E}\,[GeV]$ | 5° |
| other | 50 MeV | $5\% \oplus 30\%/\sqrt{E}\,[GeV]$ | 5° |

Table 4.3: Energy and spatial resolution for particles in the DUNE detector [14].

with nuclei, where a muon is generated. This particle, having a long lifetime and being at its ionization minimum when the energy is $\mathcal{O}(GeV)$, does not create a shower, but a long single trace exiting the detector.
Thus, the LArTPC, which has a very good imaging capability, performs very well in distinguishing the two types of events. In Fig. 4.4 we show the selection efficiency in the appearance and disappearance channels in neutrino (FHC, Forward Horn Current) mode and antineutrino (RHC, Reverse Horn Current) modes in function of the reconstructed neutrino energy. For the appearance channel, the efficiency is expected to be maximum at the spectrum peak, and it is about 85% in both FHC and RHC modes. It is clear that the background rejection capability of DUNE is very good since only a few percents of the total number of background events is expected to be selected. In the disappearance channel, the selection efficiencies reaches a plateau around 95% for neutrino energies above 2 GeV.
For the DUNE energy resolution, we need to consider that LArTPCs also act as calorimeters; thus, we expect that the FD will be performing in reconstructing the neutrino energies. In Tab. 4.3 we summarize the DUNE energy and angular resolutions for several particles, as well as the detection threshold. More refined simulations were able to produce migration matrices so to better evaluate the probability that, given a true event energy, the experiment reconstructs a certain energy value [561]. With these it is possible to summarize the energy response of the detectors; for this reason, they have been used in order to obtain all the results shown in the following sections.

### Systematic uncertainties

The systematic uncertainties estimations is a very complicated task, which has been extensively studied by the DUNE collaboration (see Ref. [561] and references therein for detailed discussion about all the possible source of systematics). In general, we can divide them in three categories. The *flux uncertainties* arise primarily due to the hadrons produced off the target and to the uncertainties in the design parameters of the beamline. These are highly correlated across energy bins and neutrino flavors. Nowadays they are estimated to be at the level of 8%, but future hadron production measurements should improve this number. Moreover, flux uncertainties could be drastically reduced by ND flux measurements.
The *interactions uncertainties* are related to the cross section estimations. These uncertainties have many sources, which span from the initial and final state uncertainties, to the multinucleon hard scattering contribution to the total cross section. As in the previous case, interactions uncertainties may be reduced by further theoretical and experimental studies and can be partially

| $\nu_e$ **appearance channel** | | |
|---|---|---|
| Signal | $\nu_e$ and $\bar{\nu}_e$ CC events from $\nu_\mu$ oscillations | 2% sys |
| Backgrounds | Beam $\nu_e$ and $\bar{\nu}_e$ CC events | 5% sys |
| | Misidentified $\nu_\mu$ and $\bar{\nu}_\mu$ CC events | 5% sys |
| | Misidentified $\nu_\tau$ and $\bar{\nu}_\tau$ CC events | 20% sys |
| | Misidentified NC events | 10% sys |
| $\nu_\mu$ **disappearance channel** | | |
| Signal | $\nu_\mu$ and $\bar{\nu}_\mu$ CC events | 5% sys |
| Backgrounds | Misidentified $\nu_\tau$ and $\bar{\nu}_\tau$ CC events | 20% sys |
| | Misidentified NC events | 10% sys |

Table 4.4: Backgrounds and signal systematic uncertainties proposed by the collaboration for the DUNE simulations [562, 574].

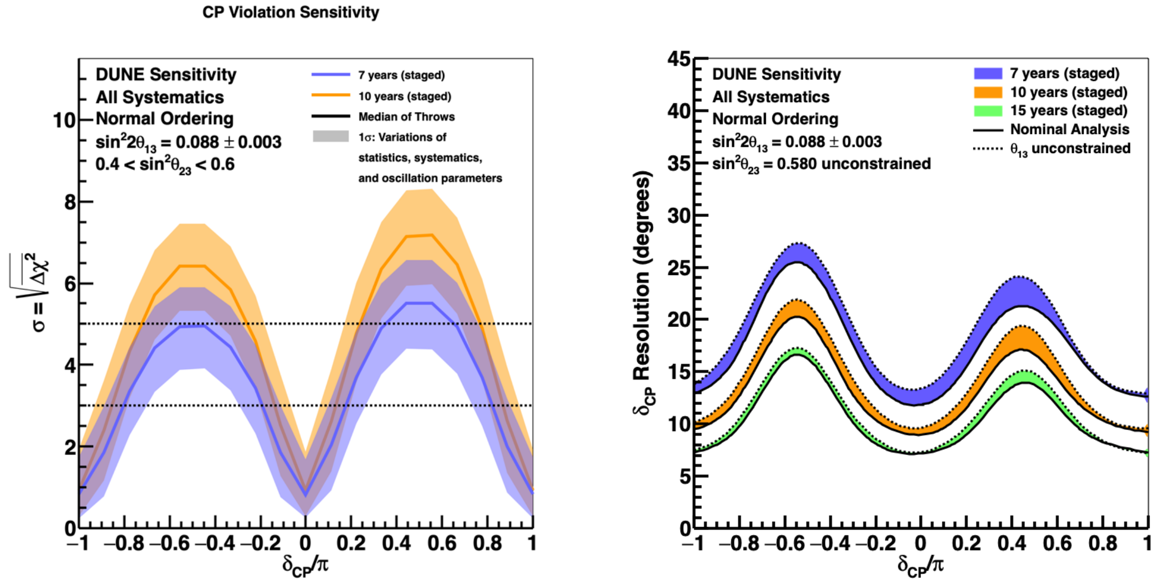


Figure 4.5: DUNE $\delta_{CP}$ sensitivity and precision as a function of the true phase value. Figures taken from [561].

simplified if measurements are performed at both ND and FD.
The *detector uncertainties* come from wrong energy reconstruction, as well as from acceptance and efficiencies misunderstanding. Again, since near and far detectors share the same technology, these uncertainties can be reduced.
The total systematic uncertainties estimated for DUNE considering the impact of the Near Detector as well as the expected improving of our knowledge of the neutrino sector, are listed in Tab. 4.4. For the $\nu_e$ appearance and $\nu_\mu$ disappearance signals, the DUNE collaboration considers respectively 2% and 5% of normalization error.

### 4.1.3 Sensitivity to oscillation parameters

In this subsection we will briefly show which are the expected DUNE capabilities in measuring some neutrino oscillation parameters. Results mentioned here have been taken from the latest DUNE TDR.
In Fig. 4.5 (left panel) we show the expected sensitivity to $\delta_{CP}$ using the staged DUNE running already described for a total exposure of 7 (3.5+3.5) and 10 (5+5) years. The $\Delta\chi^2$ function is defined as

$$\Delta\chi^2_{\delta_{CP}} = \chi^2(\delta_{CP}) - \chi^2(\delta_{CP} = 0, \pi)\,. \tag{4.1}$$

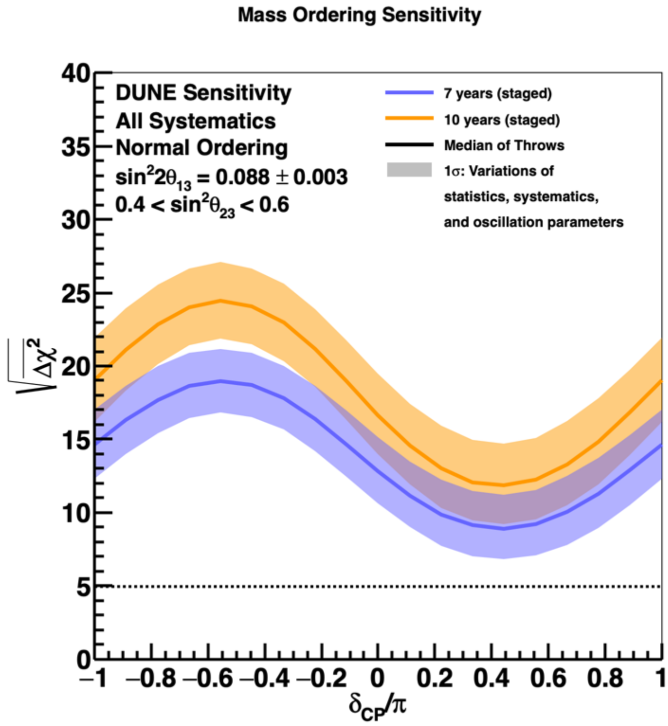


Figure 4.6: DUNE mass hierarchy sensitivity as a function of the true phase value. The true ordering has been taken as Normal. Figure taken from [561].

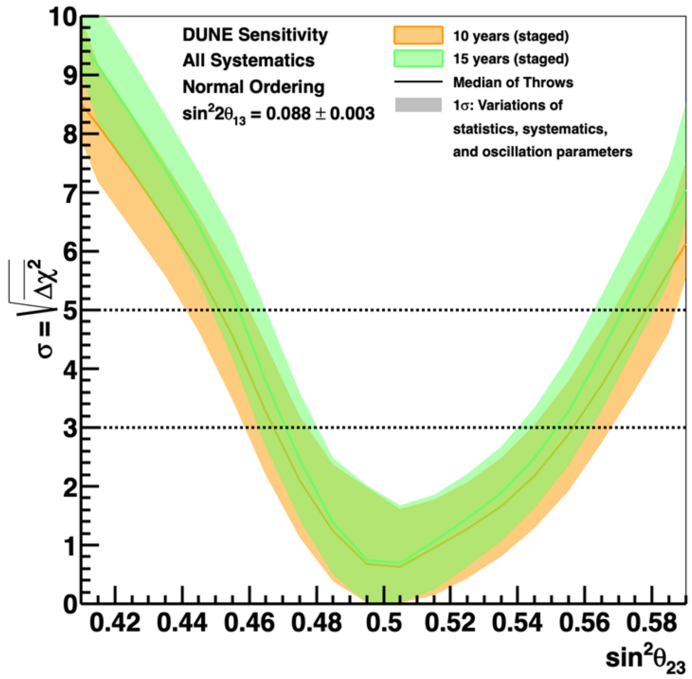


Figure 4.7: Atmospheric angle octant sensitivity of the DUNE experiment. Figure taken from [561].

| Physics Goal | Exposure (staged years) |
|---|---|
| $5\sigma$ Mass Ordering ($\delta_{CP} = -\pi/2$) | 1 |
| $5\sigma$ Mass Ordering (any $\delta_{CP}$) | 2 |
| $3\sigma$ CP Violation ($\delta_{CP} = -\pi/2$) | 3 |
| $3\sigma$ CP Violation (50% of $\delta_{CP}$ values) | 5 |
| $5\sigma$ CP Violation ($\delta_{CP} = -\pi/2$) | 7 |
| $5\sigma$ CP Violation (50% of $\delta_{CP}$ values) | 10 |
| $3\sigma$ CP Violation (75% of $\delta_{CP}$ values) | 13 |
| $\delta_{CP}$ Resolution of 10° ($\delta_{CP} = 0$) | 8 |
| $\delta_{CP}$ Resolution of 20° ($\delta_{CP} = -\pi/2$) | 12 |
| $\sin^2 2\theta_{13}$ Resolution of 0.004 | 15 |

Table 4.5: Exposure in staged years after which the DUNE experiment will reach certain physics goals. The true value for $\theta_{23}$ has been chosen so that $\sin^2\theta_{23} = 0.58$ (the timing shown here is very sensitive to the atmospheric angle true value). Figure taken from [561].

We can observe that the oscillation parameters variation (in particular the $\theta_{23}$ variation, as we will discuss later) have a huge impact on the sensitivity. Indeed, for the 7 years configuration, $5\sigma$ ($\sqrt{\Delta\chi^2} = 5$ for the Wilk's theorem [575, 576]) median sensitivity is reached only for positive values of $\delta_{CP}$ in the range [0.3-0.7]$\pi$, but such interval can drastically change varying the parameters. On the other hand, the $3\sigma$ sensitivity, which is considered to be the main goal for DUNE, may be reached even with 7 years running for more than 50% of the possible phase values. In the right panel of Fig. 4.5 we show the $\delta_{CP}$ resolution which may be reached by DUNE, defined as the $1\sigma$ uncertainty. In this case the minimum uncertainty, namely 13° for 7 years, is reached for CP conserving values of $\delta_{CP}$, 0 and $\pi$. On the other hand, if the CP violation is maximum, the uncertainty will be between 21° and 27°.
The neutrino mass hierarchy, on the contrary, will be determined by DUNE at a very high statistical significance for any value of $\delta_{CP}$, as shown in Fig. 4.6. The $\Delta\chi^2$ function is defined here as

$$\Delta\chi^2 = \chi^2_{NO} - \chi^2_{IO} \tag{4.2}$$

The maximum (minimum) sensitivity is reached for the negative (positive) maximal value of the PMNS matrix phase [96]. The DUNE experiment should also be able to establish the $\theta_{23}$ octant. Indeed, as shown in Fig. 4.7, where

$$\Delta\chi^2_{\theta_{23}} = \chi^2(\theta_{23}) - \chi^2(\pi/2 - \theta_{23})\,, \tag{4.3}$$

after 10 years of staged data taking, DUNE will distinguish the atmospheric angle octant at $3\sigma$ if $\sin^2\theta_{23} < 0.46$ or $\sin^2\theta_{23} < 0.56$ ($\theta_{23} \in [0.24 - 0.26]\pi$). We will discuss later how the presence of matter effects will negatively affect the capability of DUNE to measure $\theta_{23}$ if its true value is close enough to $\pi/4$ (see Sec. 5.2). The measurements of $\Delta m^2_{31}$ and $\theta_{13}$ performed by DUNE are also expected to be extremely precise [14, 561]. We quote in Tab. 4.5 after how many years of staged running DUNE will reach some physics milestones regarding the mass hierarchy, the CP violation and the $\theta_{13}$ measurement for $\sin^2\theta_{23} = 0.58$.

### 4.1.4 The $\nu_\tau$ channel

The tau neutrino is the last fermion to be discovered so far. Indeed, only in 2000 the DONUT experiment [7] was able to see this particle. The reason why $\nu_\tau$-s are so difficult to observe is that their CC interactions, as already mentioned, have a relatively high energy threshold (3.1 GeV) with respect to the usual detectable neutrinos. Thus, even if in long baseline experiments we study atmospheric oscillations, which are dominated by the $\nu_\mu \to \nu_\tau$ transition, we usually look

for the disappearance of muon neutrinos instead of the appearance of taus. Only the OPERA [149, 573] experiment[3], where a 17 GeV peaked neutrino beam was employed, has been able to detect $\nu_\tau$-s in the context of neutrino oscillations.
Even in presence of enough energetic neutrinos, however, the $\nu_\tau$ detection results to be very challenging; if $\nu_e$ CC and $\nu_\mu$ CC interactions produce stable or long-living particles, $\nu_\tau$ CC interactions produce the very short living $\tau$ leptons which, at neutrino beam energies, decay very close to the interaction vertex. The charged decay products can be electrons (18%), muons (18%) or hardons (64%). These particles can leave traces in the detector and their identification may in principle lead to the possibility of the $\nu_\tau$ detection.
DUNE, considering its high energy flux tail and its very good imaging capability, should be

| $\nu$ **mode** | | $\bar{\nu}$ **mode** | |
|---|---|---|---|
| $\nu_\tau$ Signal | 277 | $\nu_\tau$ Signal | 68 |
| $\bar{\nu}_\tau$ Signal | 26 | $\bar{\nu}_\tau$ Signal | 85 |
| Total Signal | 303 | Total Signal | 153 |
| $\nu_e + \bar{\nu}_e$ CC Bkg (beam) | 333 + 38 | $\nu_e + \bar{\nu}_e$ CC Bkg (beam) | 117 + 104 |
| $\nu_e + \bar{\nu}_e$ CC Bkg (oscillation) | 1753 + 12 | $\nu_e + \bar{\nu}_e$ CC Bkg (oscillation) | 90 + 188 |

Table 4.6: Expected total number of events after oscillation at the 40-kt far detector for Signals and Backgrounds (Bkg) obtained using no selection efficiencies hypothesis in the case of the standard flux and for Normal Hierarchy (NH). $\delta_{CP} = 215°$ is assumed [578]. The events correspond to DUNE running for a total of 7 years (3.5 years in neutrino mode and 3.5 years in anti-neutrino mode).

| $\nu$ **mode** | | $\bar{\nu}$ **mode** | |
|---|---|---|---|
| $\nu_\tau$ Signal | 2673 | $\nu_\tau$ Signal | 98 |
| $\bar{\nu}_\tau$ Signal | 34 | $\bar{\nu}_\tau$ Signal | 983 |
| Total Signal | 2707 | Total Signal | 1081 |
| $\nu_e + \bar{\nu}_e$ CC Bkg (beam) | 688 + 63 | $\nu_e + \bar{\nu}_e$ CC Bkg (beam) | 176 + 177 |
| $\nu_e + \bar{\nu}_e$ CC Bkg (oscillation) | 1958 + 11 | $\nu_e$ CC Bkg (oscillation) | 76 + 324 |

Table 4.7: Same as table 4.6 but for the optimized flux.

able to identify a few $\nu_\tau$ events. These events may come from the identification of the $\tau$ hadronic [579] or electronic [16] decays. In the former case, the most important source of background should be misidentified NC events, where hadrons are produced. On the other hand, in the latter case, the background events mainly come from $\nu_e$ CC interactions[4]. The studies of the physics potentials of the $\nu_\tau$ appearance channel at DUNE produced many results in the last years [16, 18–21, 555, 579, 582–585]; a review about the perspectives about the $\tau$ neutrino physics at DUNE and other experiments can be found here [586].
In [16], we showed that in DUNE roughly 450 $\nu_\tau$ and $\bar{\nu}_\tau$ events are expected; this number can be increased of almost a factor of 10 if an high energy flux will be used for the same amount of time (see Tabs. 4.6 and 4.7). To this number one should apply the selection efficiencies, which depend on the decay mode we are considering and on the detector efficiency. In Fig. 4.8 we show the potentials of the DUNE Far Detector in constraining $\theta_{23}$, $\theta_{13}$ and $\Delta m^2_{31}$ using the $\nu_\tau$ appearance channel with subsequent electron decay in different hypothesis on the selection efficiency (100% and 30% of electron events, respectively 18% and 6% of the total events)

[3]High energy neutrino candidates have been recently observed by neutrino telescopes [577].
[4]The performances of LArTPCs in the $\nu_\tau$ detection have been studied in the context of the first LArTPC ever built, the ICARUS detector, in [142, 580, 581].

and on the signal over background ratio (18.6 and 2.45). These choices have been taken from the LArTPC detector of the ICARUS experiment predictions [580, 581]. We estimated the systematic uncertainties related to this channel to be at the level of 20%, much larger than the other channels' ones; this is so mainly because reconstructing the $\nu_\tau$ interaction topology is much difficult, and because we do not have many information about the $\nu_\tau$ CC cross section. It is clear that the performances of this channel are not comparable to the other channel's ones. These results can be improved with the high-energy flux (in Fig. 4.9 we show the results in this case with an aggressive 10% systematics hypothesis) but still very large portions of the parameters space ($\theta_{23} \in [30-60]^\circ$, $\theta_{13} < 20^\circ$ and $\Delta m^2_{31} \in [2.3-2.8] \times 10^{-3}\, eV^2$) are allowed. This essentially means that this new transition channel will not be able to substantially improve the standard oscillation parameters measurements. In Fig. 4.10 we show a comparison between the performances of each channel, considering a running time of 3.5+3.5 years with the standard flux, where it is clear that the performances of the $\nu_\tau$ appearance channels are poor in constraining standard oscillation parameters. Similar results have been obtained in [579] using the events in which the $\tau$ leptons decay in hadrons. They estimate that 30% of the hadronically decaying $\tau$ leptons (20% of the total $\nu_\tau$ sample) may be observed at DUNE. The main backgrounds in this case are misidentified NC events.
However, the $\nu_\tau$ sample at DUNE could be useful not only to study the properties of this particle, like the interaction cross section, but also to study BSM physics [16, 18–21, 555, 579, 582–586], as we will discuss later on.

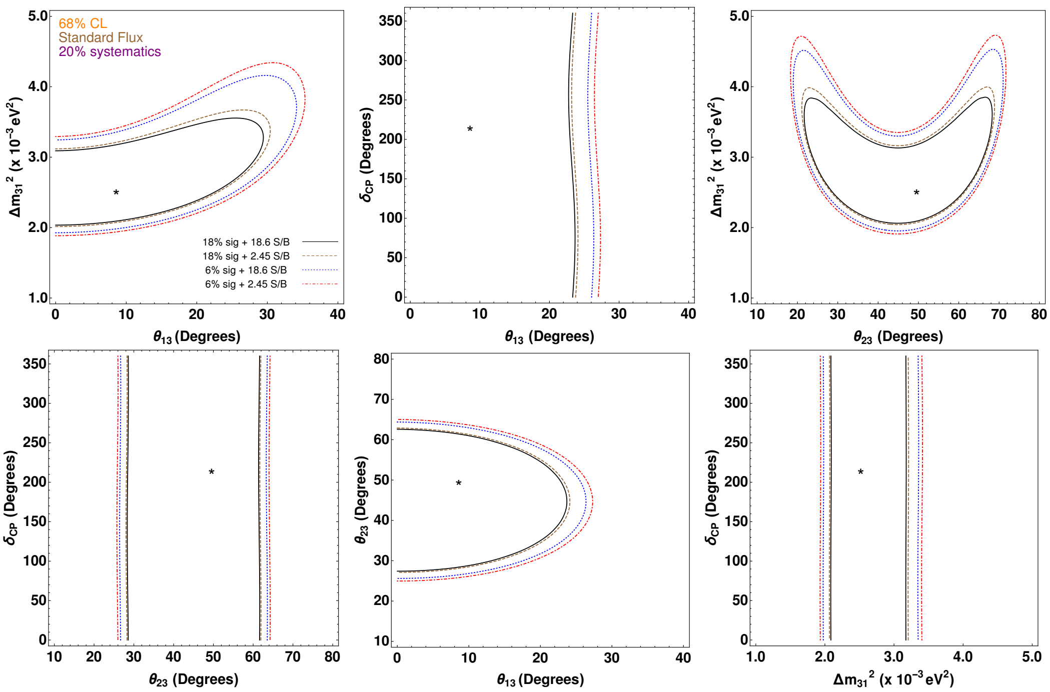

Figure 4.8: Correlations among oscillation parameters using only $\nu_\tau$ appearance channel with the DUNE standard flux and 20% systematics. The curves show the allowed parameters space regions at 68% confidence level with different efficiencies and S/B (signal/background) ratios.

## 4.2 Hyper-Kamiokande (HK)

In 2013, the T2K experiment in Japan established $\nu_\mu \to \nu_e$ oscillation at $7.3\sigma$ [587], opening, together with the NO$\nu$A measurements, the road towards the CP violation determination in neutrino experiment. The T2K success lead in 2015 to the proposal of an experiment upgrade, which is known as Hyper-Kamiokande (HK) [156, 159]. Hyper-K, which will use all the already

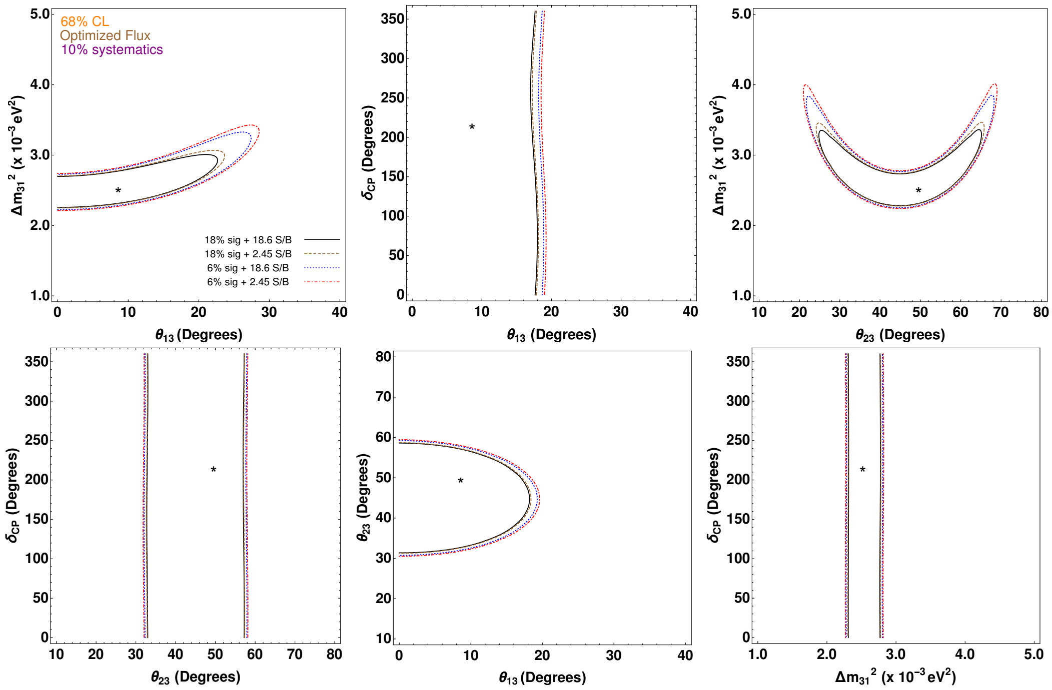


Figure 4.9: Same as Fig. 4.8 but with the $\tau$-optimized flux and 10% systematics.

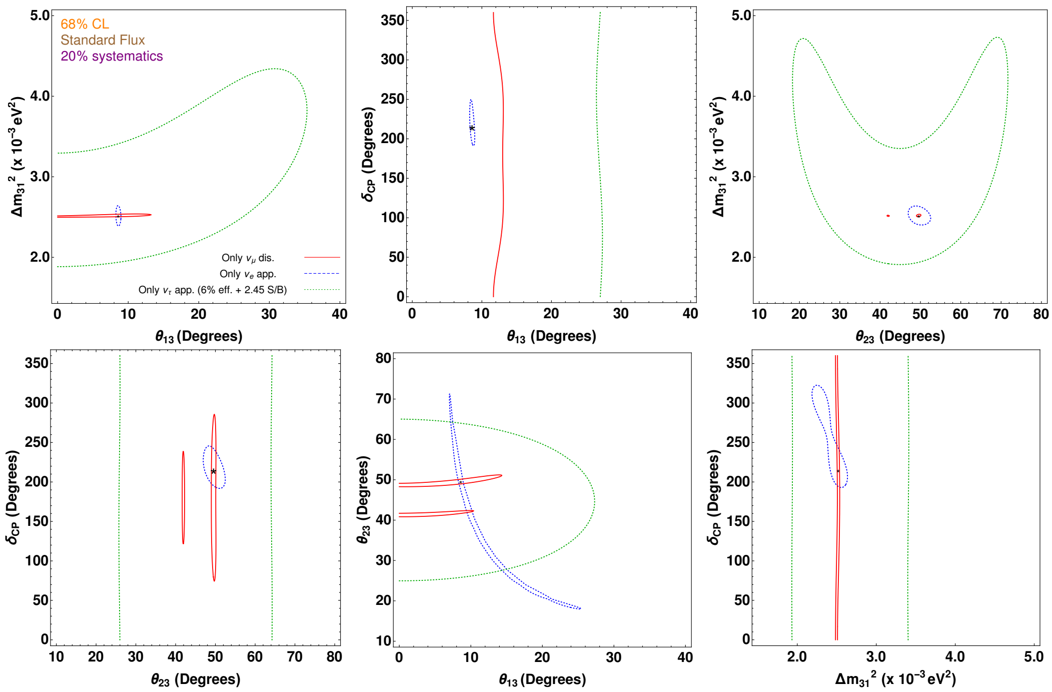


Figure 4.10: Correlations among oscillation parameters using separately $\nu_\mu$ disappearance (red solid line), $\nu_e$ appearance (blue dashed line) and $\nu_\tau$ appearance channels (6%, 2.45 S/B and 20% systematics, green dotted line) with the DUNE standard flux. The curve shows the allowed parameters space regions at 68% confidence level. The star represent the best fit point.

well-proven technologies tested at T2K, will be an highly performing long baseline neutrino experiment, which in principle will be able to observe also proton decays, atmospheric, solar and supernovae neutrinos. The construction has been approved in 2019 and the begininning of data taking is planned for 2027, the same year as DUNE.

### 4.2.1 HK Detectors

The HK facilities will be placed at J-PARC (proton accelerator and Near Detector Complex) and in the Kamioka mines where, 8 km south from the T2K far detector, the HK far detector will be built. The distance between the neutrino source and the main detector will be 295 km. This distance needs 0.6 GeV neutrinos in order to sit at the first atmospheric oscillation maximum. It is interesting to notice that in this case, even though we measure the same oscillation features, HK has a much smaller baseline compared to DUNE. This will drastically reduce the matter effects, which can negatively affect the $\delta_{CP}$ measurements, but on the other hand will not allow to observe high energy neutrinos.

#### HK Far Detector

The T2K detector, known as Super-K, is a huge water Cherenkov detector. The Hyper-K detector, will be built using the same technologies, but its fiducial mass will be almost 9 times larger, namely 187 kt. The enormous Hyper-K water tank[5] proposed dimensions are 60m of height and 73 m of diameter. The detector will be placed 650 m underground and it will be surrounded by almost $10^5$ photon multiplier. These devices will be able to catch the Cherenkov light produced by charged particles generated in neutrino interactions. Differently from the DUNE LArTPC, which is going to observes particle traces, the HK Cherenkov detector will see light rings, which depending on the particle and on its energy will have different features. This type of detector, being filled with purified water and not with Liquid Argon can reach bigger dimensions. However, some features of the detector are relatively worse in the water Cherenkov detectors. The high transparency of the water is crucial for the HK detector: this feature allow us to be able to observe most of the Cherenkov light produced in the detector. At the same time, the transparency assure that the number of impurities (like the Radon nuclei) which can produce background events are extremely low. One option that is being explored for the HK Far Detector is the Gadolinium addition in water. This element is highly performing in capturing thermal neutrons. Since the neutron capture produce a well known light signature (which has been used since the first neutrino detection experiments), the Gadolinium doping may be very useful for several reasons [588–592]. For instance, it can help in distinguishing neutrinos from antineutrinos since the interactions of the latter produce more neutrons. Moreover, the doping can improve the energy determination or the NC background reduction. It is worth to mention that the Gadolinium nuclei should not compromise the water transparency.

#### HK Near Detectors

The HK Near detector complex consists in a few detectors, each having a crucial role in the experiment. Indeed, they should be able to reduce systematic uncertainties and determine the neutrino beam properties like the $\nu_e$ and the wrong-sign $\nu_\mu$ contamination. Moreover, they should be able to measure other interactions features like the neutron multiplicity.
The first Near Detector will be an improvement of the T2K *ND280 detector*. ND280 will be a 4.3 tons 2.5° off-axis detector placed 280 m far from the neutrino source. Differently from the HK Far Detector, it will be composed by a Time Projection Chamber (TPC) tracker[6] surrounded by a neutral pions detector, an electromagnetic calorimeter and a muon detector. The flux determination made by this Near Detector will reduce the systematic uncertainties on flux and cross section of a factor of 3 [156]. However, being ND280 a different detector with respect to the FD, it will not be able to reduce the detector systematic uncertainties.
At the same ND280 distance, the on-axis *INGRID* detector will be built using 16 iron-scintillator

[5] A configuration with two identical tanks is also under consideration [156, 159].
[6] The target nuclei have not been decided yet. However, the current T2K ND280 uses water [593].

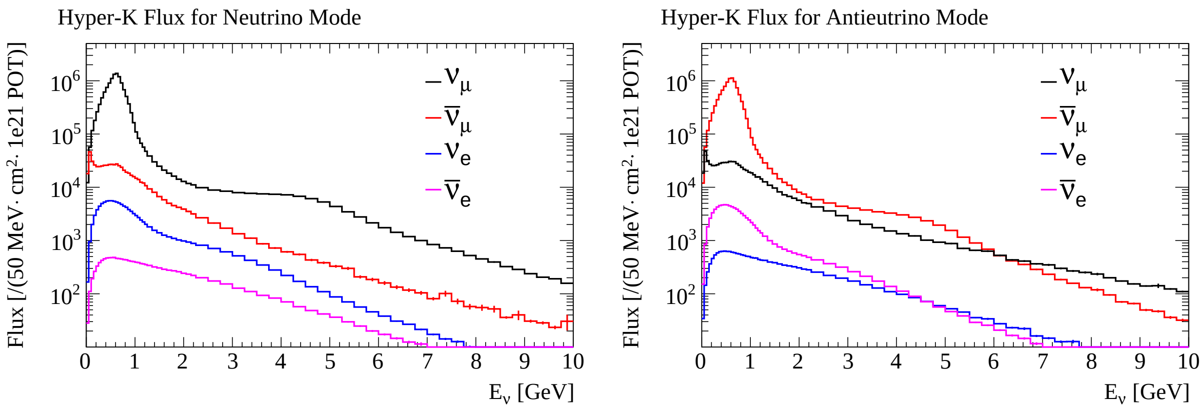


Figure 4.11: Neutrino spectra composition at Hyper-Kamiokande without oscillations in neutrino (left panel) and antineutrino (right panel) mode. Figure from [156].

| | | signal | | BG | | | | | | Total |
|---|---|---|---|---|---|---|---|---|---|---|
| | | $\nu_\mu \to \nu_e$ | $\overline{\nu}_\mu \to \overline{\nu}_e$ | $\nu_\mu$ CC | $\overline{\nu}_\mu$ CC | $\nu_e$ CC | $\overline{\nu}_e$ CC | NC | BG Total | |
| $\nu$ mode | Events | 1643 | 15 | 7 | 0 | 248 | 11 | 134 | 400 | 2058 |
| | Eff.(%) | 63.6 | 47.3 | 0.1 | 0.0 | 24.5 | 12.6 | 1.4 | 1.6 | — |
| $\bar{\nu}$ mode | Events | 206 | 1183 | 2 | 2 | 101 | 216 | 196 | 517 | 1906 |
| | Eff. (%) | 45.0 | 70.8 | 0.03 | 0.02 | 13.5 | 30.8 | 1.6 | 1.6 | — |

Table 4.8: Expected number of $\nu_e/\overline{\nu}_e$ signal and backgrounds events and efficiencies at HK. Normal mass hierarchy with $\sin^2 2\theta_{13} = 0.1$ and $\delta_{CP} = 0$ are assumed. Table from [156].

modules in a cross pattern. Its primary purpose will be to constrain precisely the neutrino beam direction.
The third 1 kt HK Near Detector, called *IWCD (Intermediate Water Cherenkov Detector)* is going to be placed off-axis, around 1-2 km from the neutrino source. Since IWCD will use the same technology of the Far Detector, being a water Cherenkov Detector, it will help in reducing the detector uncertainties at the FD. Such detector will be complementary to ND280, that, on the other hand, should be capable of tracking particles which are below the Cherenkov light production threshold, performing more precise measurements. The two main IWCD features will be the capabality to be moved at different off-axis angles and the Gadolinium doping.

### 4.2.2 Neutrino fluxes, event rates and detectors' performances

The accelerator neutrinos detected by Hyper-Kamiokande will be produced at the Japan Proton Accelerator Research Complex (J-PARC). All the accelerator facilities and the ND complex will be located there. Differently from the DUNE experiment and just like the previous experiment T2K, HK is going to adopt the well-known strategy based on a narrow-band 2.5° off-axis neutrino beam. As already mentioned, this type of beam assures a reduction of the NC background to both disappearance and appearance channel. This is crucial for a water Cherenkov detector, where the event reconstruction is more difficult with respect to a tracker. However, having an off-axis detector reduces the total number of neutrinos; moreover, the narrow beam does not allow to study the oscillation at different L/E ratios.

#### Beam Facility and Neutrino Fluxes

The T2HK experiment has a much smaller baseline than DUNE. For this reason, in order to study oscillations at the first atmospheric oscillation maximum, it needs neutrino with an energy

| | | $\nu_\mu$CCQE | $\nu_\mu$CC non-QE | $\overline{\nu}_\mu$CCQE | $\overline{\nu}_\mu$CC non-QE | $\nu_e + \overline{\nu}_e$ CC | NC | $\nu_\mu \to \nu_e$ | total |
|---|---|---|---|---|---|---|---|---|---|
| $\nu$ mode | Events | 6043 | 2981 | 348 | 194 | 6 | 480 | 29 | 10080 |
| | Eff. (%) | 91.0 | 20.7 | 95.6 | 53.5 | 0.5 | 8.8 | 1.1 | — |
| $\bar{\nu}$ mode | Events | 2699 | 2354 | 6099 | 1961 | 7 | 603 | 4 | 13726 |
| | Eff. (%) | 88.0 | 20.1 | 95.4 | 54.8 | 0.4 | 8.8 | 0.7 | — |

Table 4.9: Same as Tab. 4.8, but for the disappearance channel. Th number of events here is divided in Quasi-Elastic (QE) events and non-Quasi Elastic (non-QE) events. Table from [156].

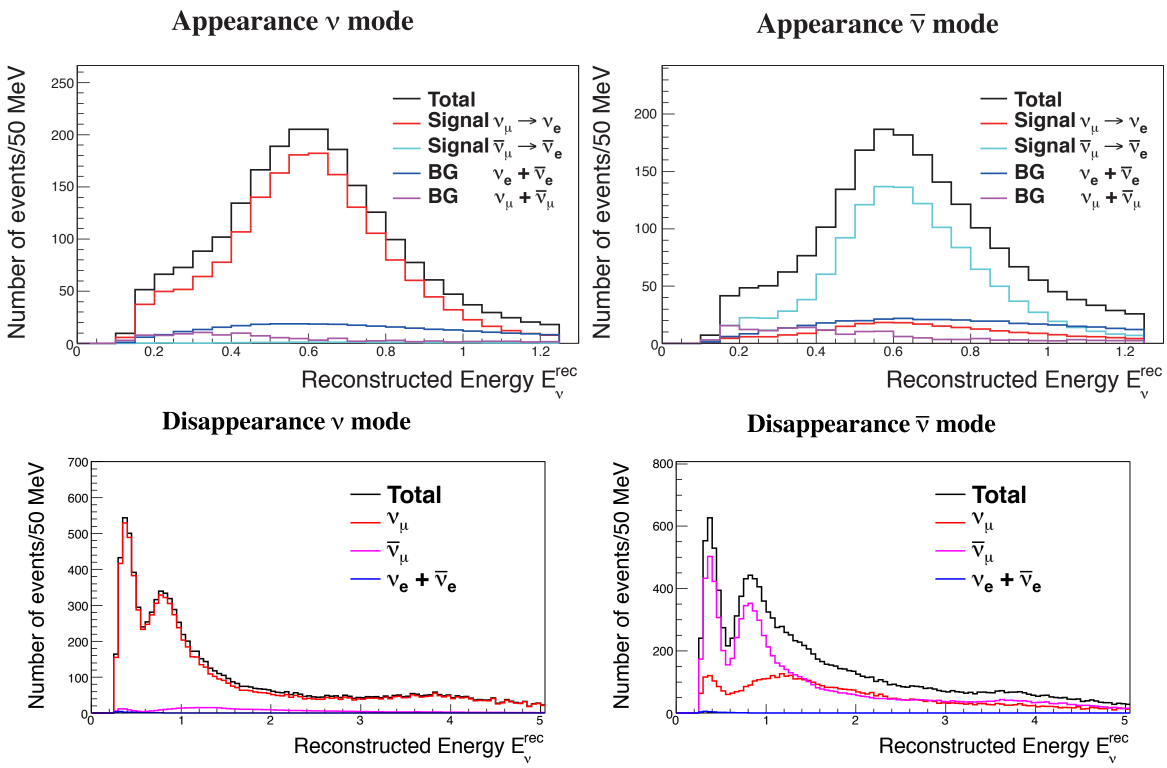


Figure 4.12: Far Detector HK neutrino spectra after oscillations in neutrino (left panels) and antineutrino mode (right panels). Top panels refer to the appearance channel while bottom ones to the disappearance channel. Oscillation parameters in NO have been taken from [578], while $\delta_{CP} = 0$. Figures from [156].

of about 0.6 GeV. For this purpose, at J-PARC, 30 GeV protons will be sent to a 91 cm long graphite target. The beam power will be 1.3 MW, that corresponds to $2.7\times10^{21}$ POT/year. The total expected experiment exposure will be 2431 kt·MW·years, five times the DUNE one. Like in the DUNE experiments, magnets will be able to select the charge of the mesons produced in the proton interactions. This will create neutrino or antineutrino enhanced beams. After a decay tunnel, an absorber should stop all the particles but the neutrinos, which will be mainly $\nu_\mu$. At the T2HK energies, the $\nu_e$ beam contamination is expected to be less than 1% and it should mainly come from muon decays. The 2.5° off-axis location of the detector takes advantage of the pion decay kinematics that produces a narrow band beam peaked at 600 MeV, which is the desired energy. Neutrino fluxes are shown in Fig. 4.11. It is evident how the beam is much less broad than the DUNE one. On the other hand, the compositions of the DUNE and T2HK fluxes are very similar.
In [156] it is possible to find a detailed discussion about all the possible analysis that may be performed at Hyper-Kamiokande. For accelerator neutrino oscillation purposes, the Japanese experiment will be, as already mentioned, very powerful in studying the $\nu_e$ appearance and the $\nu_\mu$ disappearance. For the former, taking into account only neutrino CC interactions with oxygen nuclei, the events candidates should satisfy the following criteria: the reconstructed ring is an electron-like (fuzzy) ring, the visible energy is greater than 100 MeV, the reconstructed energy is less than 1.25 GeV and the event is not compatible with a $\pi^0$ decay. The irreducible background to this channel is made of $\nu_e \to \nu_e$ events from the beam contamination as well as misidentified $\nu_\mu$ and NC events. The total number of signal events is 1600 in $\nu$-mode (2.5 years) and 1400 in $\bar{\nu}$-mode (7.5 years)[7]. On the other hand, the total number of background events is expected to be 400 in $\nu$ mode and 500 in $\bar{\nu}$ mode (see Tab. 4.8 for details). The resulting events spectrum at the far detector, considering the best fits for oscillation parameters, NO and $\delta_{CP} = 0$ is shown in Fig. 4.12 (top panels).
For the $\nu_\mu$ disappearance events, the criteria are a muon-like Cherenkov ring, reconstructed energy greater than 200 MeV/c and at most one decay electron associated to the event. Irreducible backgrounds are misidentified $\nu_e$ and NC events. The total number of expected events are 9500 in $\nu$ mode and 13000 in $\bar{\nu}$ mode (mostly Quasi-Elastic), with 500 and 600 background events, respectively (see Tab. 4.9). Top panels of Fig. 4.12 show the resulting neutrino spectrum for the disappearance channel at the far detector. It is possible to see how, due to the narrow beam, the double peaked shape observed in DUNE is less pronounced even though the total number of events is larger.

**Efficiencies and Energy resolutions**

The narrow-band T2HK beam allows us to neglect the energy dependence of the detector efficiency. We summarize the selection efficiencies at the Far Detector in Tabs. 4.8 and 4.9. It is clear that for the $\nu_e$ appearance channel, the T2HK experiment should reach 64% (71%) signal efficiency in $\nu$ ($\bar{\nu}$) mode. The wrong-sign signal efficiency should be around 45%. The great background rejection capabilities will reduce the selection efficiency of the misidentified events up to 1.6% in both modes; the component which is difficult to reject the most is, obviously, the one related to the $\nu_e$ events from the flux contamination. For the disappearance channel, the T2HK collaboration distinguish the various types of interactions. For the CC-quasi elastic (CCQE) interactions, the selection efficiency is around 90% (95%) for $\nu_\mu$ ($\bar{\nu}_\mu$). The efficiency after all the kinematics and energetic cuts for the non-QE interactions is around 21% for muon neutrinos and 50% for muon antineutrinos. In this case, the remaining background events are only a very small fraction of the total non-$\nu_\mu$ CC events.
The energy resolution functions suggested by the collaboration are, for the electron appearance

[7]The running time ratio 1 : 3 has been chosen by the collaboration in order to have a similar number of events in both modes.

| Appearance channel | Normalization Error | Calibration Error |
|---|---|---|
| $\nu_e$ ($\bar{\nu}_e$) Signal | 5% | 5% |
| Intrinsic $\nu_e$ ($\bar{\nu}_e$), misidentified $\nu_\mu$ ($\bar{\nu}_\mu$) and NC Backgrounds | 10% | 5% |
| **Disappearance channel** | | |
| $\nu_\mu$ ($\bar{\nu}_\mu$) Signal | 3.5% | 5% |
| Misidentified $\nu_e$ ($\bar{\nu}_e$) and NC Backgrounds | 10% | 5% |

Table 4.10: Proposed systematics for the HK experiment [15]. See [156, 597] for other possible less conservative hypothesis.

channel [156]

$$\nu - mode \quad \longrightarrow \quad \sigma(E) = 12\%E + 7\%\sqrt{E} \tag{4.4}$$

$$\bar{\nu} - mode \quad \longrightarrow \quad \sigma(E) = 12\%E + 9\% \tag{4.5}$$

where the term proportional to $E$ encodes the instrumental effects, the one proportional to $\sqrt{E}$ reflects the statistical fluctuations and the constant term is due to the redout electronic noise. For the disappearance channel, on the other hand, we have, for both modes [156]

$$\sigma(E) = 6\%\sqrt{E} + 6\%\,. \tag{4.6}$$

**Systematic uncertainties**

The T2HK collaboration based their estimation of the systematic uncertainties on the T2K experiment results [594, 595]. The main sources of systematics, as for DUNE, are the flux and cross section uncertainties as well as near and far detectors response uncertainties.
In order to reduce the *flux prediction* systematics, measurements about the proton beam, the horn field, the beam-line alignment and the hadron production are needed. These uncertainties are the dominant source of systematics. The presence of a Near Detector can reduce the impact of the flux uncertainties, but still the near-to-far flux extrapolation have a residual 0.5% fractional error.
The *interaction model* uncertainties can come from the poor knowledge of the neutrino cross sections. The nuclear model, for instance, can increase the total uncertainty up to 20%; this number can be reduced of a factor of 10 using the Near Detector constraints. For this purpose, the presence of IWCD is very useful.
The *detector uncertainties* in T2K have been estimated using atmospheric neutrinos as a control sample. Thus, the error reduction is limited by statistics. However, since Hyper-Kamiokande is expected to collect a much larger number of atmospheric events, we expect to have a better knowledge of the detector performances.
Discussion about correlation between errors in different types of events can be found in [159, 596]. The total systematics suggested by the T2HK collaboration are listed in Tab. 4.10. In particular, we expect 5% normalization error for the $\nu_e$ appearance signal and 3.5% normalization error for $\nu_\mu$ disappearance signal. The collaboration also proposes 5% energy calibration error. It is worth to mention that, compared to DUNE, the T2HK experiment is expected to behave better, in terms of systematics, in the disappearance channel and worse in the appearance channel. This is mainly because the huge dimension of the Hyper-K water Cherenkov detector allow to observe more precisely long-living particles events, while the DUNE imaging capabilities allow to better reconstruct the more complicated electromagnetic showers produced by $\nu_e$ CC events.

### 4.2.3 Sensitivity to oscillation parameters

Let us now discuss briefly the perfomarnces of T2HK in the determination of the PMNS phase, the mass hierarchy and the atmospheric angle octant. The $\Delta\chi^2$ analysis described here are the

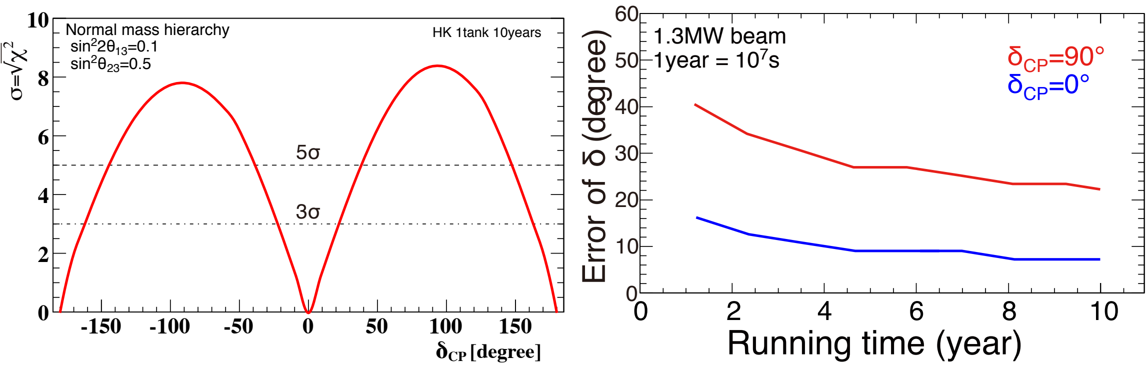


Figure 4.13: Left panel: $\delta_{CP}$ T2HK sensitivity after 10 (2.5+7.5) running years. Oscillation best fits are taken from [578], ordering fixed to Normal and $\theta_{23} = \pi/4$. Right panel: reachable error on $\delta_{CP}$ as a function of the running time (neutrino-antineutrino modes ratio is fixed to 1:3). Figures taken from [156].

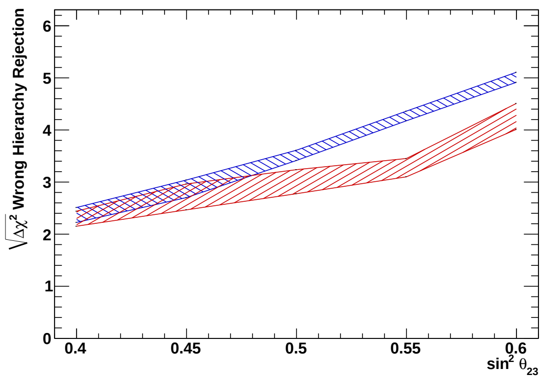


Figure 4.14: Mass Hierarchy determination for true NO (red) and IO (blue) as a function of the true $\theta_{23}$ value. The $\delta_{CP}$ effect is shown as band width. Figure from [156].

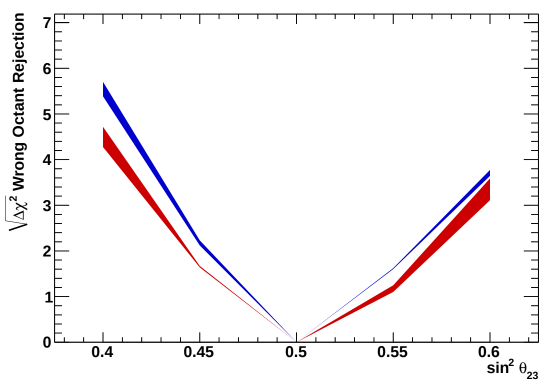


Figure 4.15: Sensitivity to the $\theta_{23}$ octant of the HK experiment for NO (red) and IO (blue). The bands show the effect of varying the phase $\delta_{CP}$. Figure from [156].

| Detector Location | Signal | Wrong-sign Signal | Intrinsic $\nu_e$, $\bar{\nu}_e$ | NC | CC $\nu_\mu$,$\bar{\nu}_\mu$ | Total |
|---|---|---|---|---|---|---|
| OAA, L | Neutrino Mode | | | | | |
| 2.5°, 1100 km | 87.9 | 1.7 | 28.3 | 12.5 | 1.7 | 132.2 |
| 2.0°, 1100 km | 122.6 | 2.0 | 33.8 | 21.4 | 2.4 | 182.3 |
| 1.5°, 1100 km | 140.6 | 2.4 | 39.1 | 39.1 | 3.7 | 224.8 |
| OAA, L | Antineutrino Mode | | | | | |
| 2.5°, 1100 km | 89.8 | 15.5 | 39.4 | 14.3 | 0.8 | 159.8 |
| 2.0°, 1100 km | 131.5 | 19.8 | 46.3 | 23.4 | 1.1 | 222.1 |
| 1.5°, 1100 km | 159.1 | 23.9 | 54.3 | 39.5 | 1.7 | 278.5 |

Table 4.11: Expected number of $\nu_e$ and $\bar{\nu}_e$ candidate events at different proposed locations for the second Korean Detector. Normal mass ordering with $\sin^2\theta_{13} = 0.0219$ and $\delta_{cp} = 0$ are assumed. The first column refers to different off-axis angle (OAA) and baseline (L) combinations. Table from [15].

same as the DUNE ones.
Using a 10 years (2.5+7.5) experiment running, as showed in left panel of Fig. 4.13, T2HK should be able to reach $5\sigma$ sensitivity for wide range of possible $\delta_{CP}$ values[8], namely $[-135, -40]°$ and $[40, 145]°$. Comparing these intervals to the DUNE ones, T2HK is expected to perform better; however, this highly depends on the $\theta_{23}$ true value, as we will discuss in the following chapter. The better T2HK performances can come from smaller matter effects, since the matter potential can induce a larger fake CP violation in DUNE [598–600]. The error on $\delta_{CP}$ is also expected to be similar to the DUNE one, after 6 years of T2HK running time (Fig. 4.13, right panel).
About the mass hierarchy determination (see Fig. 4.14), the T2HK measurements are not expected to discover the sign of the atmospheric mass splitting at high confidence level for any true value of the oscillation parameters, differently from DUNE. This is mainly because of the smaller matter effects, which in DUNE enhance the probability terms sensitive to the mass hierarchy and the narrower T2HK neutrino beam, which does not allow for a full spectral analysis. Moreover, the true value of the atmospheric angle may have a huge impact on such measurement. The addition of the atmospheric neutrino sample to the accelerator one, may drastically improve the mass hierarchy sensitivity [156]. On the other hand, the $\theta_{23}$ octant determination capabilities are expected to be very similar to the DUNE ones (see Fig. 4.15).
It is clear that, from the standard oscillations point of view, DUNE and T2HK will independently determine most of the neutrino oscillation unknown. However, as we will show later, the complementarity between the two experiments can play an important role for both standard and BSM physics measurements.

### 4.2.4 Second oscillation maximum physics: T2HKK

For the T2HK experiment, the main strategy which has been investigated is to build two identical 260 kton water Cherenkov detectors [159]. For the second detector, different locations are under investigation. One of the most promising choices benefits of the fact that South Korea is $\sim$1100 km far from the J-PARC facility [15, 156]. This distance correspond to the one needed to study oscillations at the second atmospheric oscillation maximum for 0.6 GeV neutrinos. Even though the neutrino beam in Korea would not be as intense as in Japan, a second detector placed at the second oscillation maximum should further enhances the physics capabilities related to neutrino oscillations [15, 156, 160, 601, 602]. Let us for instance consider the $\nu_e$ appearance probability in presence of matter in the atmospheric regime, neglecting higher order terms in the small solar

[8] As true values for the oscillation parameters, T2HK collaboration used $\sin^2 2\theta_{13} = 0.1$ and $\sin^2\theta_{23} = 0.5$ [15, 156].

| Detector Location | Signal | Wrong-sign Signal | NC | CC-$\nu_e$,$\bar{\nu}_e$ | Total |
|---|---|---|---|---|---|
| OAA, L | Neutrino Mode | | | | |
| 2.5°, 1100 km | 1275.0 | 32.7 | 58.5 | 1.9 | 1368.1 |
| 2.0°, 1100 km | 2047.2 | 42.8 | 107.7 | 2.5 | 2200.2 |
| 1.5°, 1100 km | 3652.0 | 55.4 | 210.4 | 2.9 | 3920.7 |
| OAA, L | Antineutrino Mode | | | | |
| 2.5°, 1100 km | 1119.5 | 300.6 | 61.9 | 2.0 | 1484.0 |
| 2.0°, 1100 km | 1888.5 | 390.0 | 102.6 | 2.4 | 2384.4 |
| 1.5°, 1100 km | 3579.2 | 490.8 | 185.1 | 2.8 | 4257.9 |

Table 4.12: Same as Tab. 4.11 but for disappearance channel.

splitting [15]

$$\begin{aligned}
P(\nu_\mu \to \nu_e) \quad \sim \quad & \sin^2\theta_{23}\sin^2 2\theta_{13}\frac{\sin^2(\Delta_{31}-aL)}{(\Delta_{31}-aL)^2}\Delta_{31}^2 + \qquad (4.7)\\
& +\sin 2\theta_{23}\sin 2\theta_{13}\sin 2\theta_{12}\cos\theta_{13}\frac{\sin(\Delta_{31}-aL)}{\Delta_{31}-aL}\Delta_{31}\frac{\sin(aL)}{aL}\Delta_{21}\cos\Delta_{32}\cos\delta + \\
& -\sin 2\theta_{23}\sin 2\theta_{13}\sin 2\theta_{12}\cos\theta_{13}\frac{\sin(\Delta_{31}-aL)}{\Delta_{31}-aL}\Delta_{31}\frac{\sin(aL)}{aL}\Delta_{21}\cos\Delta_{32}\sin\delta + \\
& +\cos^2\theta_{13}\cos^2\theta_{23}\sin^2 2\theta_{12}\frac{\sin^2(aL)}{(aL)^2}\Delta_{21}^2
\end{aligned}$$

where $\Delta_{ij} = \Delta m_{ij}^2 L/4E$ and $a = G_F N_e/\sqrt{2}$ is the matter potential. For antineutrino probabilities, $a$ changes its sign, as well as $\delta_{CP}$. It is clear that the oscillation phase, which in vacuum is $\Delta_{31}$, is shifted by the quantity $aL$; thus, at a fixed energy, the second and the third terms are enhanced when the baseline is bigger. This makes the oscillations at the second oscillation maximum more sensitive to both the mass hierarchy and the CP-violating phase. For this reason, the matter effects, which at the first oscillation maximum induce a fake CP-violation that can reduce the sensitivity to $\delta_{CP}$ at the second oscillation maximum, enhancing the subleading terms in the probabilities, can improve the phase measurements.
The resulting neutrino-antineutrino oscillation asymmetry is therefore bigger in correspondence of the second maximum, and this can partially compensate the larger statistical uncertainties we may have at a longer baseline (see event tables 4.11 and 4.12 for different locations of the Korean detector). However, many complications [15], such as the fact that the second oscillation maximum is narrower than the first one, do not allow a stand-alone detector in Korea to have the same performances of Hyper-Kamiokande in Japan. On the other hand, the combination of the two detectors placed at the two oscillation maxima can improve significantly the performances of the whole T2HK experiment. From now on, we will refer to the T2HK detector in Japan equivalently as JD (Japanese detector) or T2HK; conversely, the Korean detector will indicated as KD or T2HKK (Tokai to Hyper-Kamiokande to Korea). In Fig. 4.16 we show the mass ordering sensitivity (with maximal $\theta_{23}$) for five different configurations: JD only, two copies of JD in the same place and JD+KD with the Korean detector at an off-axis angle of 2.5°, 2.0° and 1.5°. It is evident that the presence of KD will improve significantly the T2HK capability to discover the mass hierarchy for most of the values of $\delta_{CP}$, reaching the same DUNE performances. In Fig. 4.17, the sensitivity to $\delta_{CP}$ is also shown for the same experimental configurations. When the mass ordering is fixed, the presence of the a second detector, independently from its location, will improve the sensitivity to the CP violation. This suggests that at the second oscillation maximum location, the improvement of the $\delta_{CP}$ effect completely balance the reduction of the

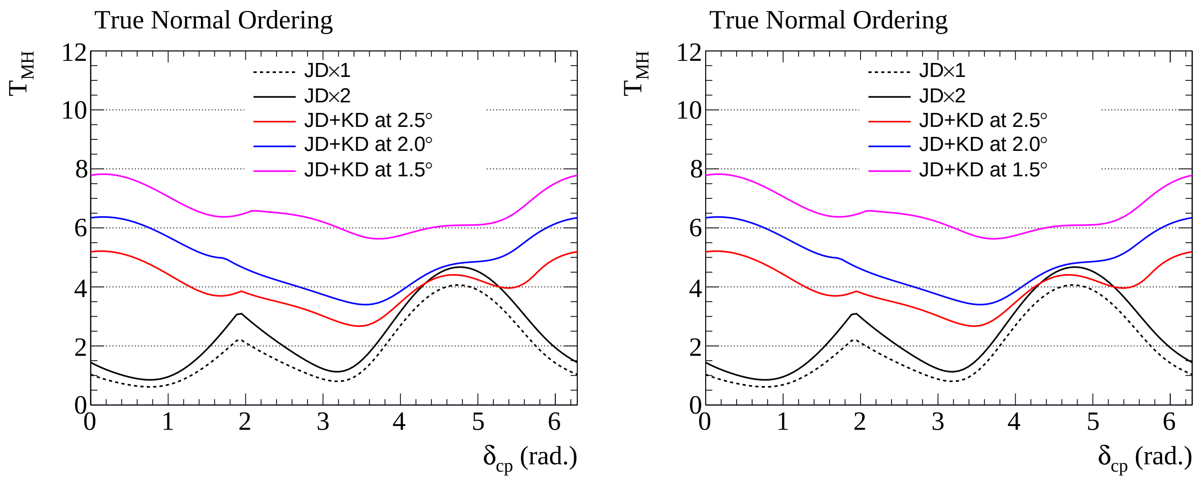


Figure 4.16: Mass Hierarchy sensitivity T2HK (JD) only and different combinations of two detectors. With JDx2 we refer to the possibility of having two identical detectors close to each other in Japan. Figures from [15].

number of the events. On the other hand, if we marginalize over the mass hierarchy (we perform the fit with both $\Delta m^2_{31} > 0$ and $\Delta m^2_{31} < 0$), the Korean detector drastically improves the sensitivity for $\delta_{CP} \in [0, \pi]$ if the true ordering is normal and for $\Delta_{CP} \in [-\pi, 0]$ when the true ordering is inverted. All these results suggest that the most convenient location for the second T2HK detector should be in Korea. From now on, we will consider in our following results the 2.5° off-axis location for KD[9] for the sake of simplicity, being this the same JD off-axis angle. However, we must consider that, as shown in the previous figures, other off-axis angle choices may improve the experimental performances.

[9]In this case, the detector would be build under the Minjuji mountain.

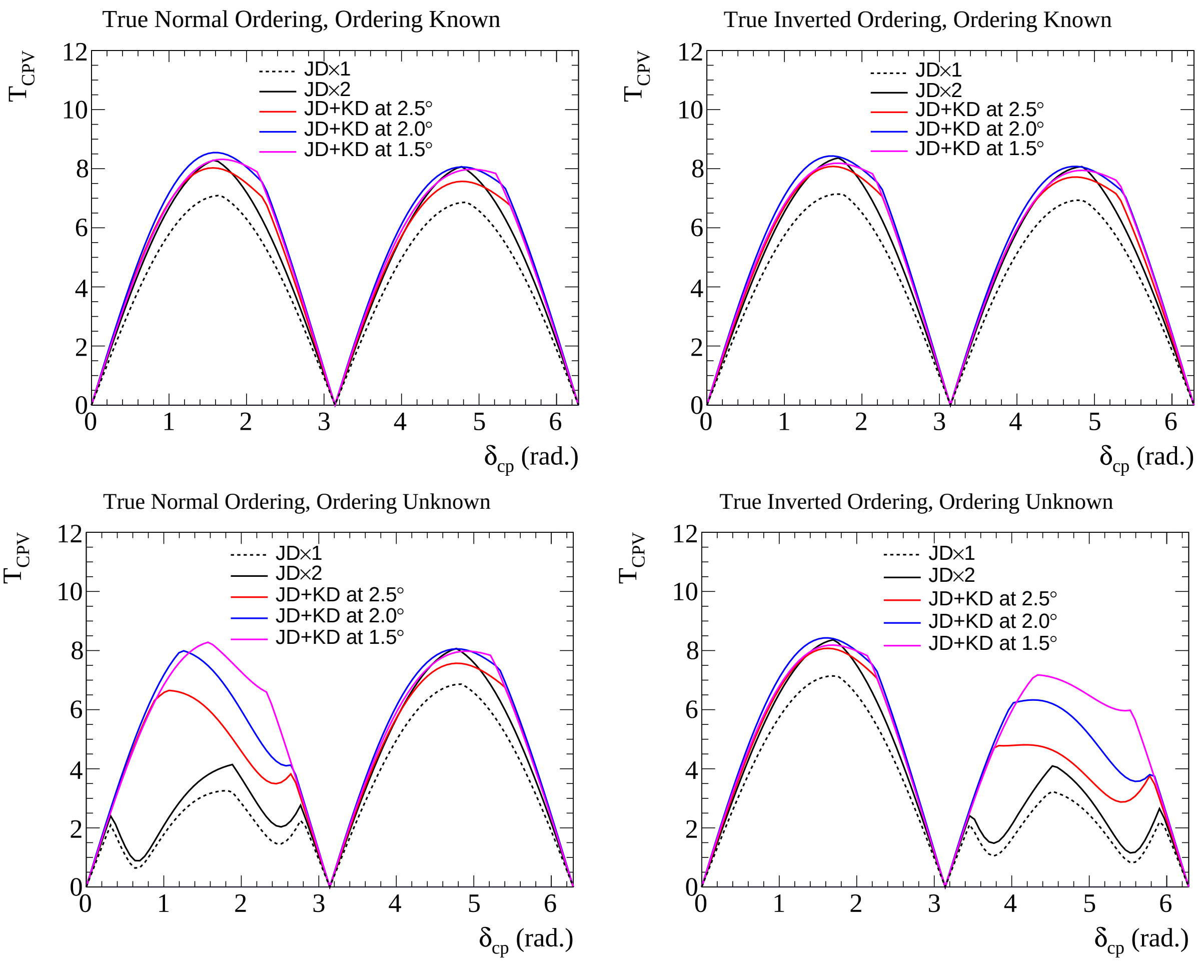


Figure 4.17: CP violation sensitivity $T_{CPV}$ (in unity of $\sigma$-s), for different combinations of detector locations. In the top panels the hierarchy is assumed to be fixed (left NO, right IO); in the bottom, a marginalization over the mass ordering is performed. Figures from [15].

# Chapter 5

# Complementarity between future long baseline experiments

| Characteristics | DUNE | JD/KD |
|---|---|---|
| Baseline (km) | 1285 | 295 (1100) |
| Beam | extension of NuMI beam | JHF beam |
| Beam Type | wide-band, on-axis | narrow-band, 2.5° off-axis |
| Beam Power | 1.2 MW | 1.3 MW |
| Proton Energy | 120 GeV | 80 GeV |
| P·O·T·/year | $1.1 \times 10^{21}$ | $2.7 \times 10^{21}$ |
| Exposure (kt·MW·yrs) | 480 | 2431 |
| Flux peaks at (GeV) | 2.5 | 0.6 |
| $P_{\mu e}$ $1^{st}$ ( $2^{nd}$) max. (GeV) | 2.6 ( 0.9) | 0.6 (0.6) |
| Detector mass (kt) | 40, LArTPC | 187 each, water cherenkov |
| run-time ($\nu + \bar{\nu}$ ) yrs | 5 + 5 | 2.5 + 7.5 |
| Sig. Norm. Err. (App.) | 2% | 5% |
| Sig. Norm. Err. (Disapp.) | 5% | 3.5% |
| Binned events matched with | [574] | [15] |

Table 5.1: Charateristic features of long-baseline experiments.

DUNE and T2HK, which represent the next generation of long-baseline experiment, despite being similar from the point of view of their concept, are very different experiments. In Tab. 5.1 their main features are summarized. DUNE will see higher energy neutrinos travelling for 1300 km, while T2HK will study oscillations at a shorter baseline and lower energies, without being affected strongly by matter effects. Moreover, DUNE will be an on-axis broad band beam experiment, while T2HK will be an off-axis narrow band beam experiment. For this reason, even though they are both meant to determine the oscillation unknowns, the two experiments will have different performances. However, due to their differences, the combination of their data may contain more information than the single experiment ones. In this chapter, we will discuss two examples in which the complementarity between DUNE and T2HK can improve the performances of the two experiments taken one at a time. Before showing the numerical results, we will first discuss the software that has been used to perform the experiments simulations.

## 5.1 The GLoBES software and the oscillation analysis at LBL experiments

Before discussing the main results of this manuscripts, which have been obtained by a full simulation of the future LBL experiments, we want to briefly describe a very useful tool that can be used in order to simulate long baseline experiments. This is the GLoBES (General Long Baseline Experiment Simulator) software, developed since 2004 [603, 604]. It is very useful to simulate and analyze neutrino oscillation at LBL or reactor experiments using a complete three flavor description of the probabilities. The definition of the experiment can be done in a specific abstract language, the AEDL (Abstract Experiment Definition Language), which allows to easily describe the experimental features of a given experiment. One can split the description of a neutrino experiments in three parts: source, oscillation and detection.
About the *source*, the GLoBES software can simulate experiments which have stationary point sources. Moreover, the best description is obtained for experiments that have only one single point like source. However, some approximated simulations can be obtained in the case of reactor experiments using several distant reactor blocks (i.e. Daya Bay [369]). The geometrical effect of a source distribution, on the other hand, are not implemented in the software; for this reason, atmospheric or solar experiments cannot be simulated properly. Also time-dependent sources like supernovae are not covered by GLoBES.
The description of the *oscillation* is very simple; the software numerically diagonalize the Hamiltonian matrix in matter and propagates the neutrino transition amplitudes. This method is called evolution operator method [605]. For the probability computation, the matter density profile is divided into layers of constant matter; however, since the uncertainty on the matter density can be included in the simulation, usually it is enough to consider a single layer with an average density.
The *detection* of the neutrinos, on the other hand, is much more complicated to evaluate. Indeed, in this case many detector features have to be considered at the same time. The basic assumption of a detector description is the linearity, namely the fact that two neutrino events never interfere with each other. Then, another basic concept is that the true neutrino energy and the true neutrino flavor are reconstructed by the detector: they cannot be directly observed, but the observation of secondary particles translates into a distribution of possible energy or flavor values[1]. The features of this distribution depends on the detector performances, which are encoded in the experiment efficiencies and resolutions given as an input. Of course, these quantities must be obtained by a full detector simulation outside GLoBES.
The full experiment definition is obtained using some abstraction levels (see Fig. 5.1). The first is the *channel*, which basically is the link between the oscillation physics and the detection properties of a given oscillation pattern (i.e. $\nu_\mu$ disappearance, $\nu_e$ appearance...). In particular, it maps a specific flavor produced at the neutrino source into a reconstructed neutrino flavor in the detector.
With different channels we can build a *rule*. The rule is a description of what the experiment actually sees when searching for a certain type of neutrino events. Indeed, it contains one or more *signal* and *background* oscillation channels normalized to their efficiencies. In each rule, the GLoBES software implements the signal and background normalization and calibration systematic errors separately. At the rule level, the total number of observed events is computed by the software; this number can be used to perform a $\chi^2$ analysis. The sum of all the $\chi^2$ computed for all the rules defines the *experiment*, which is the final simulation level.

[1] Neutrino reconstructed energy and flavor are the only observables considered in a neutrino event in GLoBES.

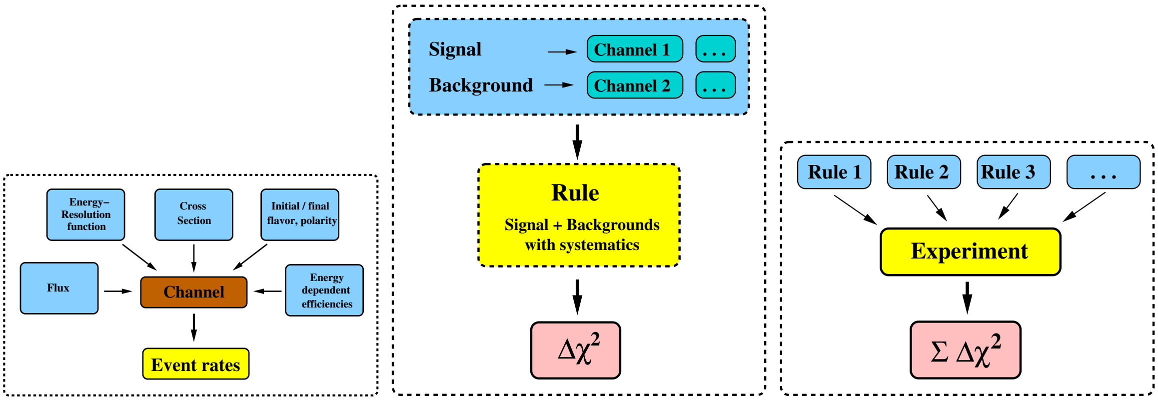


Figure 5.1: Schematic view of the most important GLoBES components: channel, rule and experiment. Figure from [603].

### 5.1.1 The computation of the number of events

The number of events spectra in function of the reconstructed energy $E'$ can be computed by the GLoBES software. The event rate is given by[2]

$$\begin{aligned} \frac{dn_\beta^{IT}}{dE'} =& N \int_0^\infty \int_0^\infty dE d\widehat{E}\ \Phi_\alpha(E) \times \\ & \frac{1}{L^2} P_{(\nu_\alpha \to \nu_\beta)}(E, L, \rho; \theta_{23}, \theta_{13}, \theta_{12}, \Delta m^2_{31}, \Delta m^2_{21}, \delta_{CP}) \times \\ & \sigma_\beta^{IT}(E) k_\beta^{IT}(E - \widehat{E}) \times T_\beta(\widehat{E}) V_\beta(\widehat{E} - E') \end{aligned} \tag{5.1}$$

where we can recognize four different contributions.

- The first one is the production term: it depends on the flux of $\nu_\alpha$, where $\alpha$ is the initial flavor. The energy E is the true incident neutrino energy, which is not directly accessible to the experiment.
- The second term is the propagation term. It depends on $1/L^2$, where L is the baseline of the experiment, and on the oscillation probability from the initial flavor $\alpha$ to the final one $\beta$. $\rho$ is the matter density.
- The third term is the interaction term. $\sigma_\beta^{IT}$ is the total cross section for $\nu_\beta$ and for the IT interaction type. $k_\beta^{IT}$ is the energy distribution of the particle produced in the interaction, namely the one that is detected. $\widehat{E}$ is the energy of such a particle.
- The last term is the detection term. It depends on a threshold function $T_\beta$ and on a energy resolution function $V_\beta$, both features of the detector. The energy $E'$ is the reconstructed neutrino energy, namely the one measured by the experiment.

Given this formula, it is clear that, as inputs, the GLoBES software needs several information. In particular, the initial flux $\Phi_\alpha(E)$ as a function of the true energy and of the neutrino flavor, which have to be computed in a full MonteCarlo simulation, must be specified in the simulation. Then, in order to numerically compute the probabilities, the needed inputs are the experiment baseline $L$, the oscillation parameters and the matter density (or the matter densities if we consider neutrinos passing through several layers). For the interaction term computation, on

[2]We include here also a normalization factor $N$ which may be useful in some experimental configurations and encodes for instance information about detector mass, and beam power.

the other hand, we need to know the interaction cross section; finally, the detection term encodes the detector responses, which can be contained in the so called *smearing matrices*. The detector efficiencies can be included at this level, if they are energy dependent[3] or at the rule level if they can be treated as an overall number.

Notice that given its simplicity, the GLoBES software can be used also to simulate neutrino oscillation in presence of new physics; in this case, it only needs to be modified at the probability level.

### 5.1.2 The systematics implementation and the $\chi^2$ function definition

The systematic uncertainties implementation is one of the most delicate issue in GLoBES. By default, the software supports four types of systematical errors: signal and background normalization error and signal and background tilt or energy calibration energy. The tilt (T) error is implemented as a linear distortion of the spectrum around the center, while the calibration (C) is considered like a stretching of the reconstructed energy scale.
In order to include the systematics, GLoBES uses the *pull-method* [606–608]. In this case, nuisance parameters $\zeta_i$ are introduces, so that the signal and background event rates in each energy bin $i$ are scaled in the following way

$$s(\zeta_1) = (1+\zeta_1)s_i \;\; b_i(\zeta_2) = (1+\zeta_2)b_i \,. \tag{5.2}$$

The $\chi^2$ function, which can be used to fit simulated data with a given theory, includes the systematics in this fashion

$$\chi^2(\vec{\lambda}) = \min_{\{\zeta_i\}} \left( \chi^2(\vec{\lambda}, \zeta_1, ...\zeta_k) + \sum_{j=1}^{k} \frac{\zeta_j^2}{\sigma_{\zeta_j}^2} \right) \tag{5.3}$$

where $\chi^2(\lambda, \zeta_1...\zeta_k)$ is the usual Poissonian[4] $\chi^2$ function, which depends on the oscillation parameters vector $\vec{\lambda}$ and the nuisance parameters. Added to the $\chi^2$ we find the *Gaussian penalties* $\zeta_j^2/\sigma_{\zeta_j}^2$ where $\sigma$ are the actual systematics indicated in the GLoBES code. As an example, for a simple background free measurement, with only normalization errors, the $\chi^2$ definition, in the Poissonian case, can be written by

$$\chi^2(\vec{\lambda}, a) = \sum_{i=1}^{n} 2 \left( (1+a)T_i - O_i + O_i \log \frac{O_i}{(1+a)T_i} \right) + \frac{a^2}{\sigma_a^2} \tag{5.4}$$

where $\sigma_a$ is the normalization error, $n$ is the number of energy bins, $O_i$ are the observed rates and $T_i$ are the theoretical ones we are using for the fit. The $\chi^2$ value will be thus obtained not only minimizing on the theory input values, but also on the nuisance parameter $a$. The $\chi^2$ function, however, can be also defined with user-defined systematics; for this reason, the complexity of the GLoBES software allows us to better control with a simple software all the sources of errors. Whenever we include a prior on the oscillation parameters, take for instance a Gaussian prior on $\theta_{13}$ from reactor experiments, the $\chi^2$ is modified in the following way

$$\chi^2_{pull}(\vec{\lambda}) \to \chi^2_{pull}(\vec{\lambda}) + \frac{\theta_{13} - \theta_{13}^0}{\sigma_{\theta_{13}}^2} \tag{5.5}$$

where $\theta_{13}^0$ is the central value for the input and $\sigma_{\theta_{13}}$ is the $1\sigma$ Gaussian error; if the error on a given parameter is not Gaussian, custom error functions can be implemented..

[3]Energy dependent efficiencies are fundamental for broad band beam where a spectral analysis can be performed.

[4]For large number of events, the Poissonian definition coincides with the usual Gaussian one, which we will use in following chapters for simplicity.

## 5.2 The DUNE-T2HK complementarity and the CP coverage

As widely discussed, one of the main goals of the future LBL experiments will be to determine the PMNS phase $\delta_{CP}$. The DUNE collaboration [561] suggested as milestone for the next generation experiment, the reach of 75% $3\sigma$ CP coverage; this means that a great result for the future LBL experiment would be to have at least a $3\sigma$ sensitivity for the 75% of the possible $\delta_{CP}$ values. The reach of this goal, however, strongly depends on the true value of the atmospheric angle, which has a strong impact on the CP violation determination and has not been determined yet with a satisfactory precision by other experiments. Indeed, current measurements allow at $3\sigma$ all the values of $\theta_{23}$ between $40°$ and $60°$ ($\sin^2\theta_{23} \in [0.4, 0.6]$)[5].
Let us now consider what happens at the probability level. At long-baseline (LBL) experiments, we mostly probe the $\nu_\mu(\bar{\nu}_\mu) \to \nu_\mu(\bar{\nu}_\mu)$ disappearance and the $\nu_\mu(\bar{\nu}_\mu) \to \nu_e(\bar{\nu}_e)$ appearance channels. Following the approach in Ref. [161], we can further simplify the appearance probability expression in Ref. [94] that considers series expansion up to the second order term in $\alpha$ and $\sin\theta_{13}$ as follows

$$P_{\mu e} \approx N \sin^2\theta_{23} + O \sin 2\theta_{23} \cos(\Delta + \delta_{\rm CP})\,, \tag{5.6}$$

where,

$$N = 4\sin^2\theta_{13} \frac{\sin^2[(\hat{A}-1)\Delta]}{(\hat{A}-1)^2}\,, \tag{5.7}$$

$$O = 2\alpha \sin\theta_{13} \sin 2\theta_{12} \frac{\sin \hat{A}\Delta}{\hat{A}} \frac{\sin[(\hat{A}-1)\Delta]}{\hat{A}-1}\,. \tag{5.8}$$

This grouping of terms allows us to visualize the dependence on the atmospheric mixing angle ($\theta_{23}$). In the above equations, $\Delta = \Delta m^2_{31} L/4E$, $\alpha = \Delta m^2_{21}/\Delta m^2_{31}$, and $\hat{A} = A/\Delta m^2_{31}$, wherein $A = 2\sqrt{2} G_F N_e E = 7.6 \times 10^{-5} \times \rho$ (g/cm$^3$) $\times E$ (GeV). From eq. (5.6), we observe that the CP-violating term contains $\sin 2\theta_{23}$ and thus is insensitive to the octant of the atmospheric angle [96, 164, 165, 609–611]. Moreover, changing from neutrino to antineutrino mode notably $\hat{A}$ changes its signs, thus leading to matter-induced or fake (extrinsic) CP violation [598–600]. This will have a dominant contribution as it is present in the coefficient of the leading term N (refer to eq. (5.7)). While the presence of the Dirac CP phase in the sub-leading term gives rise to the genuine (intrinsic) CPV (refer to eq. (5.8)).
One useful observable to probe CPV in oscillation experiments is to note the difference between neutrino and antineutrino probabilities. The quantity which is strongly correlated to the sensitivity in $\delta_{\rm CP}$ is the CP asymmetry [612–615].
The CP asymmetry in the appearance channel is defined as

$$\mathcal{A}^{\mu e}_{\rm CP} = \frac{P_{\mu e} - \bar{P}_{\mu e}}{P_{\mu e} + \bar{P}_{\mu e}}\,. \tag{5.9}$$

Different expansions have been done to understand the behavior of such an asymmetry in terms of mixing angles [21]. However, if we want to outline the role of the atmospheric mixing angle in the $\delta_{\rm CP}$ sensitivity, we can fix the other mixing angles to their best-fit values ($\sin\theta_{13} \sim 1/7$ and $\sin\theta_{12} \sim 1/\sqrt{3}$) and expand $\hat{A}$ up to the first order since the matter parameter is small at the future LBL experiments under consideration. The resulting asymmetry can be written as follows:

$$\mathcal{A}^{\mu e}_{\rm CP} = [\mathcal{A}^{\mu e}_{\rm CP}]_{\rm vac} + \hat{A}[\mathcal{A}^{\mu e}_{\rm CP}]_{\rm mat} + \mathcal{O}(\hat{A}^2)\,, \tag{5.10}$$

[5] Depending on the global fit and on the used dataset, upper or lower octant values are preferred [111–113].

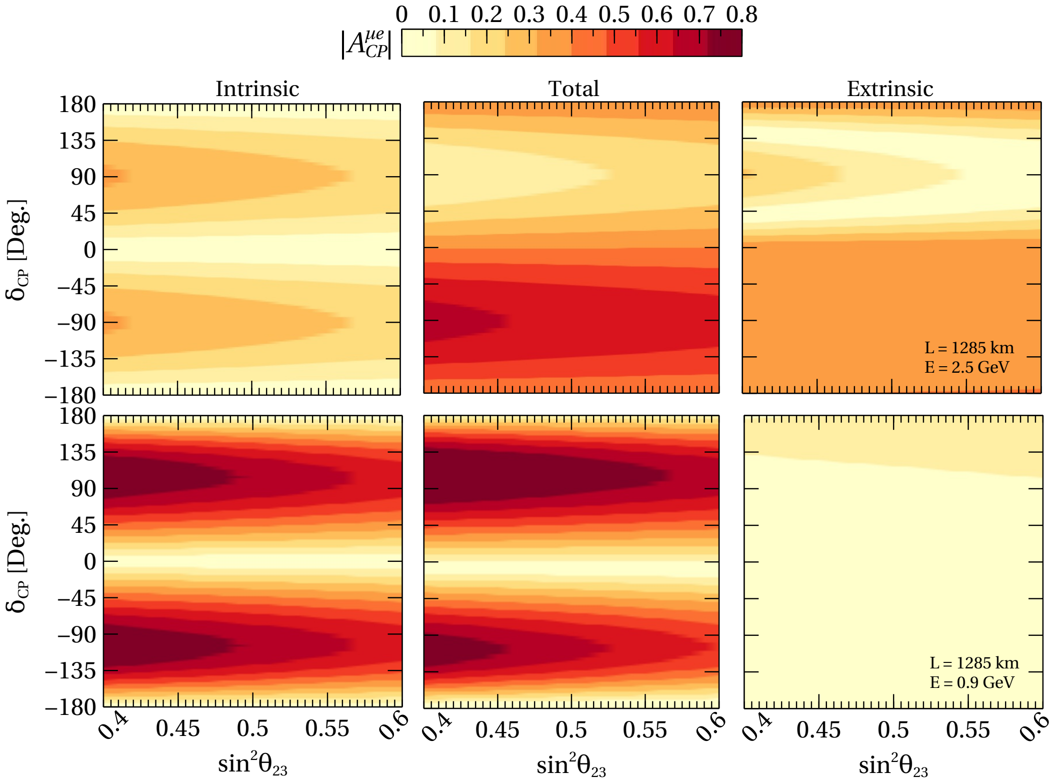


Figure 5.2: The Absolute CP asymmetry ($|\mathcal{A}_{\rm CP}^{\mu e}|$) as a function of $\delta_{\rm CP}$ and $\sin^2\theta_{23}$ for first oscillation maximum ($L$ = 1285 km, $E$ = 2.5 GeV) and second oscillation maximum ($L$ = 1285 km, $E$ = 0.9 GeV) in DUNE are shown in the top and bottom panels, respectively. The left and middle panels in both top and bottom plots are obtained in a vacuum (intrinsic or genuine $\mathcal{A}_{\rm CP}^{\mu e}$) and finite matter density (both intrinsic and extrinsic $\mathcal{A}_{\rm CP}^{\mu e}$) scenarios, respectively. While the right panel represents the difference between the first two (only extrinsic or fake $\mathcal{A}_{\rm CP}^{\mu e}$). Best-fit values of the other oscillation parameters are taken from Ref. [113]. NO is assumed.

where

$$[\mathcal{A}_{\rm CP}^{\mu e}]_{\rm vac} = \frac{-28\alpha\Delta\cos\theta_{23}\sin\delta_{\rm CP}\sin\Delta}{3\sqrt{2}\sin\theta_{23}\sin\Delta + 28\alpha\Delta\cos\theta_{23}\cos\delta_{\rm CP}\cos\Delta} \tag{5.11}$$

$$[\mathcal{A}_{\rm CP}^{\mu e}]_{\rm mat} = -\sin^2\theta_{23}(\Delta\cos\Delta - \sin\Delta)\frac{126\alpha\Delta\cos\theta_{23}\cos\delta_{\rm CP}\cos\Delta + 18\sin^2\theta_{23}\sin\Delta}{(3\sin^2\theta_{23}\sin\Delta + 7\sqrt{2}\alpha\cos\delta_{\rm CP}\cos\Delta\sin^2(2\theta_{23}))^2} \tag{5.12}$$

It is clear that, when the value of $\theta_{23}$ increases, the denominator of both the contributing term in eq. (5.11) and eq. (5.12) increases. For this reason, the absolute value of the asymmetry becomes smaller, and we expect less CP violation sensitivity. So, at the first oscillation maximum, $(\Delta = \pi/2)$[6] the asymmetry reduces to:

$$\mathcal{A}_{\rm CP}^{\mu e} \sim -\frac{7}{3}\alpha\sqrt{2}\pi\cot\theta_{23}\sin\delta_{\rm CP} + 2\hat{A}\,, \tag{5.13}$$

whose modulus decreases with an increase in $\theta_{23}$. Notice that the genuine CP contribution has the opposite sign to the fake or matter-induced contribution. Thus, there exists some combination of $\theta_{23}$ and $0^\circ < \delta_{\rm CP} < 180^\circ$, such that the asymmetry vanishes. It is interesting to note that the vacuum contribution becomes three times larger when considering the second oscillation maximum $(\Delta = 3\pi/2)$. Therefore, observing the CP violation at such L/E combinations can give much more sensitivity to $\delta_{\rm CP}$ [160, 601, 602]. The exact numerical behavior of the CP asymmetry in the appearance channel ($|\mathcal{A}_{\rm CP}^{\mu e}|$) is shown in Figs. 5.2 for ($L$ = 1285 km, $E$ = 2.5 GeV), ($L$ = 1285 km, $E$ = 0.9 GeV) which corresponds to the first and second oscillation maxima in DUNE.

[6] To be maximally sensitive to the oscillation probability, we must have $\Delta = (2n+1)\frac{\pi}{2}$, where $n = 0, 1, 2, \ldots$

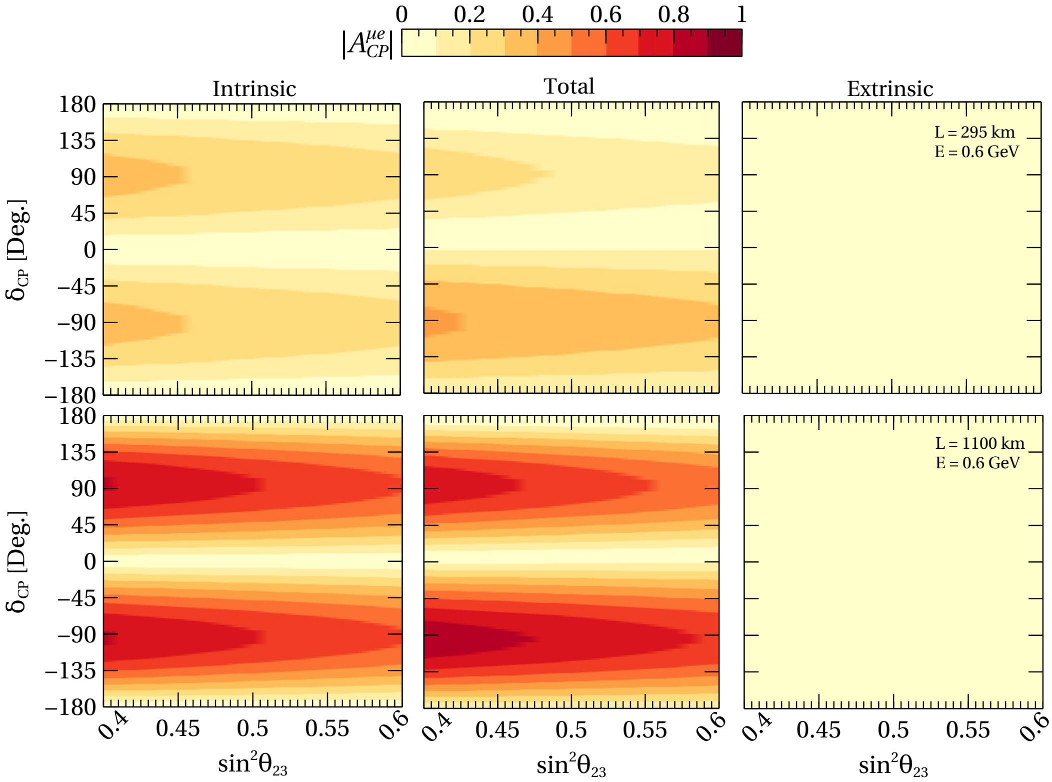


Figure 5.3: $|\mathcal{A}^{\mu e}_{\rm CP}|$ as a function of $\delta_{\rm CP}$ and $\sin^2\theta_{23}$ for first oscillation maxima in JD ($L$ = 295 km, $E$ = 0.6 GeV) and second oscillation maxima in KD ($L$ = 1100 km, $E$ = 0.6 GeV) assuming NO are shown in the top and bottom panels, respectively. The left and middle panels in both top and bottom are obtained in a vacuum (intrinsic or genuine $\mathcal{A}^{\mu e}_{\rm CP}$) and finite matter density (both intrinsic and extrinsic $\mathcal{A}^{\mu e}_{\rm CP}$) scenarios, respectively. While the right panel represents the difference between the first two (only extrinsic or fake $\mathcal{A}^{\mu e}_{\rm CP}$). Best-fit values of the other oscillation parameters are taken from Ref. [113].

For each $L/E$ combination, we show three panels: in the left column, we show the vacuum or $\delta_{\rm CP}$-induced contribution (intrinsic). In the central panel, we illustrate the total asymmetry, and in the right column, we display the contribution due to the matter effects (extrinsic). In all the panels, we only plot the absolute value of the asymmetries since the most important aspect is to stress the difference between the asymmetries in the CP-violating cases with the CP-conserving ones. For the top left panel in Fig. 5.2, we observe that the intrinsic contribution is the same in both maximal CP-violating values of $\delta_{\rm CP}$ (90 and -90°). Moreover, keeping the CP phase fixed to any value, the asymmetry reduces when we increase the value of $\theta_{23}$ from lower octant (LO) to higher octant (HO) (as expected from eq. (5.11) and eq. (5.12)). Contrastingly, the extrinsic CP asymmetry (top right panel), which occurs solely due to the matter effect, is asymmetric, being larger for favorable $\delta_{\rm CP}$ in NO (negative half plane) and smaller for unfavorable $\delta_{\rm CP}$ in NO (positive half plane). Therefore, the total asymmetry (middle panel) is no longer the same for the maximal cp-violating values of $\delta_{\rm CP}$. Further, due to contribution from $\hat{A}$, the intrinsic $|\mathcal{A}^{\mu e}_{\rm CP}|$, which was zero at CP-conserving values ($\delta_{\rm CP} = 0°, 180°$), now has a finite value. Hence, from the top middle panel, it is clear that the asymmetries in CP-violating cases tend to shift closer to the CP-conserving value when $\theta_{23}$ increases. For the bottom row, where we plot the CP asymmetry at the second oscillation maxima ($E = 0.9$ GeV), the matter effect becomes smaller, and the intrinsic component completely dominates the total asymmetry. Similarly, in Fig. 5.3, we plot the CP asymmetry for the T2HK (JD) setup with $L$ = 295 km and $E$ = 0.6 GeV at the first oscillation maxima (top row) and T2HKK with $L$ = 1100 km and $E$ = 0.6 GeV at the second oscillation maxima (bottom row). The top panel does not observe any significant

contribution due to matter ($L = 295$ km). Thus we can expect the J-PARC based experiments to provide a cleaner environment for the measurements of $\delta_{\rm CP}$, even though the values reached by the asymmetries in these cases are not as large as the DUNE one. On the other hand, the bottom panels of Fig. 5.3, which correspond to the second oscillation maximum $L/E$ choice for T2HKK, behaves just like the bottom panels in Fig. 5.2.
One interesting aspect that has an important role on the $\delta_{CP}$ determination, is the fact that also in the disappearance channel the asymmetry is different from zero in presence of matter effects. For this reason, also the disappearance channel may have an impact on the measurement of the PMNS phase. Following the same convention, as discussed in Ref. [161], we write the disappearance probability as

$$P_{\mu\mu} \approx 1 - M \sin^2(2\theta_{23}) - N \sin^2\theta_{23} - R \sin 2\theta_{23} + T \sin 4\theta_{23} \,, \tag{5.14}$$

where:

$$\begin{aligned} M &= \sin^2\Delta - \alpha\cos^2\theta_{12}\Delta\sin 2\Delta + \\ &\quad + \frac{2}{\hat{A}-1}\sin^2\theta_{13}\left(\sin\Delta\cos(\hat{A}\Delta)\frac{\sin[(\hat{A}-1)\Delta]}{\hat{A}-1} - \frac{\hat{A}}{2}\Delta\sin 2\Delta\right) \,, \end{aligned} \tag{5.15}$$

$$R = 2\alpha\sin\theta_{13}\sin 2\theta_{12}\cos\delta_{\rm CP}\cos\Delta\frac{\sin\hat{A}\Delta}{\hat{A}}\frac{\sin[(\hat{A}-1)\Delta]}{\hat{A}-1} \,, \tag{5.16}$$

$$T = \frac{1}{\hat{A}-1}\alpha\sin\theta_{13}\sin 2\theta_{12}\cos\delta_{\rm CP}\sin\Delta\left(\hat{A}\sin\Delta - \frac{\sin\hat{A}\Delta}{\hat{A}}\cos[(\hat{A}-1)\Delta]\right) \,. \tag{5.17}$$

and N has already been defined in eq. (5.7). The detailed analytical discussion of fake CP asymmetry in the disappearance channel results in a cumbersome expression. However, for first oscillation minima ($\Delta = \pi/2$) and using the approximated numerical values of the solar and the reactor mixing angles ($\sin\theta_{12} = 1/\sqrt{3}$ and $\sin\theta_{13} = 1/7$), one can calculate the CP asymmetry in the $\nu_\mu \to \nu_\mu$ disappearance channel, defined as

$$\mathcal{A}_{\rm CP}^{\mu\mu} = \frac{P_{\mu\mu} - \bar{P}_{\mu\mu}}{P_{\mu\mu} + \bar{P}_{\mu\mu}} \,, \tag{5.18}$$

neglecting the higher order terms, obtaining

$$\mathcal{A}_{\rm CP}^{\mu\mu} \sim \hat{A}\frac{24\sin^2\theta_{23} + 7\sqrt{2}(\pi^2-4)\alpha\cos\delta_{\rm CP}\sin 2\theta_{23}}{6 + 141\cos 2\theta_{23}} \,. \tag{5.19}$$

This asymmetry increases with the increase in $\theta_{23}$ until the expansion breaks at $\cos 2\theta_{23} = -6/141$. This occurs for $\sin^2\theta_{23} > 0.5$ (HO). While after this value, the magnitude in asymmetry starts decreasing with the increase in $\theta_{23}$. In Fig. 5.4 we exhibit the absolute value of the disappearance asymmetry ($|\mathcal{A}_{\rm CP}^{\mu\mu}|$) for ($L = 1285$ km, $E = 2.5$ GeV) and ($L = 295$ km, $E = 0.6$ GeV) that also corresponds to DUNE and JD at their respective first oscillation maxima energy. We do not show the plots corresponding to the second oscillation maxima since the fake CP asymmetry in disappearance is solely due to the interaction with the Earth matter potential, whose effect becomes minimal in such conditions. It can be noticed that JD, bearing a relatively small baseline (L = 295 km) and for this reason suffering for very small matter effects, exhibits very minute fake asymmetry even at first oscillation maximum, as shown in the right panel of Fig. 5.4. On the other hand, DUNE has a larger baseline ($L = 1285$ km), thus exhibiting consequential $|\mathcal{A}_{\rm CP}^{\mu\mu}|$ that reaches values as large as $\approx 0.6$ (see left panel in Fig. 5.4), which is almost comparable to the total $|\mathcal{A}_{\rm CP}^{\mu e}|$ ($\approx 0.8$ ) (see top middle panel in Fig. 5.2). We observe that $|\mathcal{A}_{\rm CP}^{\mu\mu}|$ is minimal at the two extremes of octant of $\theta_{23}$ for any value of $\delta_{\rm CP}$. The asymmetry gradually increases while proceeding towards the MM from either side for almost all $\delta_{\rm CP}$. However, $|\mathcal{A}_{\rm CP}^{\mu\mu}|$ manifests two maxima around $\delta_{\rm CP} = 0°$, one each in the two octants: LO ($\sin^2\theta_{23} \approx 0.49$) and HO ($\sin^2\theta_{23} \approx 0.52$). As discussed previously in the analysis of eq. (5.19), we observe a critical point in HO in the figure as well, around which the nature of $\mathcal{A}_{\rm CP}^{\mu\mu}$ changes; in that point, while our expansion breaks, the full asymmetry $\mathcal{A}_{\rm CP}^{\mu\mu} \approx 0$ due to higher order terms that we neglected in our expansion. This nature of fake $\mathcal{A}_{\rm CP}^{\mu\mu}$ is crucial in our result. Given all

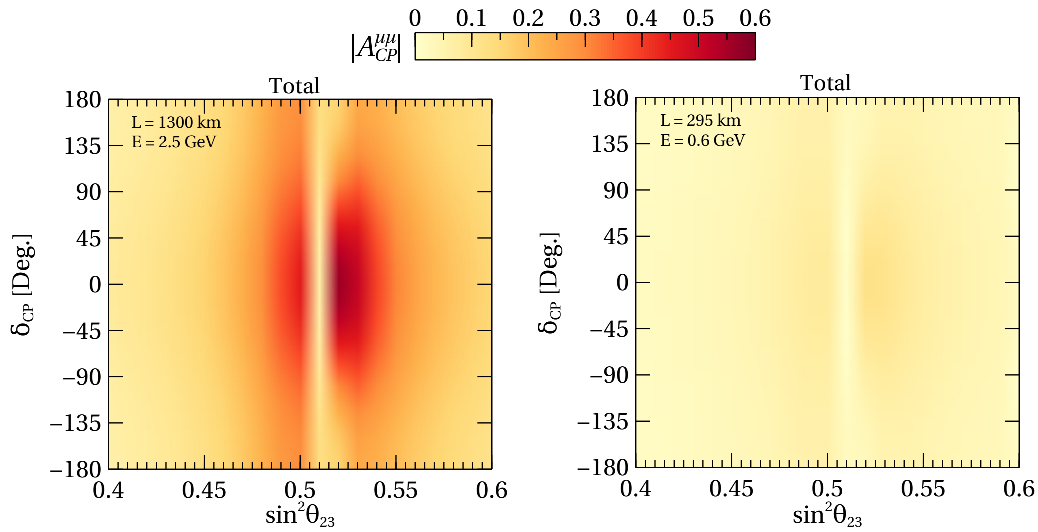


Figure 5.4: The asymmetry $|\mathcal{A}_{\rm CP}^{\mu\mu}|$ as a function of $\delta_{\rm CP}$ and $\sin^2\theta_{23}$ assuming NO for first oscillation maxima in DUNE ($L = 1285$ km, $E = 2.5$ GeV) and JD ($L = 295$ km, $E = 0.6$ GeV) is shown in the left and right panels, respectively. The best-fit values of the other oscillation parameters are taken from Ref. [113].

these discussions, we expect that the CP sensitivity, and consequently the CP coverage, are mainly driven by the electron appearance channel, as it is well known in the literature [616]. The fact that the related asymmetry decreases with $\theta_{23}$ let us expect that the coverage decreases when the atmospheric angle increases. However, we should take into account another issue: we do not know exactly the value of $\theta_{23}$, which should be determined, together with the PMNS phase, at LBL experiments. For this reason, we expect that, while fitting the T2HK and DUNE data, we would need to marginalize over the current allowed range for $\theta_{23}$, which at $3\sigma$, as already mentioned, is rather large and contains, in NO, all the values between 40° and 60°. In the marginalization process, it may occur that, given the couple of true values ($\theta_{23}$,$\delta_{CP}$), it exists a degenerate couple ($\bar\theta_{23}$,$\bar\delta_{CP}$) for which

$$P_{\mu e}(\theta_{23}, \delta_{\rm CP}) \;=\; P_{\mu e}(\bar\theta_{23}, \bar\delta_{\rm CP})\,, \tag{5.20}$$
$$\bar P_{\mu e}(\theta_{23}, \delta_{\rm CP}) \;=\; \bar P_{\mu e}(\bar\theta_{23}, \bar\delta_{\rm CP})\,. \tag{5.21}$$

Using the above expressions (eq. (5.6)) for the probability, we obtain that, for $\theta_{23} = 45°$, $\sin\theta_{13} = 1/7$, and $\sin\theta_{12} = 1/\sqrt{3}$,

$$P_{\mu e}(\pi/4, \delta_{\rm CP}) = \frac{2\sin[(A-1)\Delta]^2}{49(A-1)^2} + \frac{4\sqrt{2}\alpha\cos(\delta_{\rm CP}+\Delta)\sin[(A-1)\Delta]\sin(A\Delta)}{21A(A-1)}\,. \tag{5.22}$$

Assuming that the degenerate atmospheric angle is not too far from the maximal value, we define it as $\bar\theta_{23} = \pi/4 + x$. Now, considering terms only up to the first order in $x$ we obtain:

$$P_{\mu e}(\pi/4 + x, \bar\delta_{\rm CP}) = P_{\mu e}(\pi/4, \bar\delta_{\rm CP}) + \frac{4x\sin[(A-1)\Delta]^2}{49(A-1)^2}\,. \tag{5.23}$$

For the above scenario, the system of equations in eq. (5.20) and eq. (5.21) reduces to the following two equations-

$$\frac{\sqrt{2}\alpha\sin(A\Delta)}{3A}[\cos(\Delta-\delta_{\rm CP})-\cos(\Delta-\bar{\delta}_{\rm CP})]=x\frac{\sin[(A-1)\Delta]}{7(A-1)} \tag{5.24a}$$

$$\frac{\cos(\Delta+\delta_{\rm CP})-\cos(\Delta+\bar{\delta}_{\rm CP})}{\cos(\Delta-\delta_{\rm CP})-\cos(\Delta-\bar{\delta}_{\rm CP})}=\frac{\sin[(A-1)\Delta]}{\sin[(A+1)\Delta]}\frac{1+A}{A-1}\,. \tag{5.24b}$$

It is clear that, in vacuum ($A \to 0$), the only solution is $x = 0$ and $\bar{\delta}_{CP} = \delta_{CP}$; on the other hand, when the matter effect is non-negligible, it is possible to find solutions in which, for instance, $\delta_{CP} = 0, \pi$, while $\bar{\delta}_{CP}$ has a value that violates CP. This degeneracy is thus important and can affect the CP coverage for DUNE, in which the long baseline increases the effect of the matter potential. On the other hand, the $\theta_{23}$-$\delta_{CP}$ has almost no effect on T2HK for which $A \sim 0$.
However, there is a way for DUNE to reduce the effect of such degeneracy. If the analysis is performed using both appearance and disappearance data, the degenerate solution is valid only if it solves also the two equations

$$P_{\mu\mu}(\theta_{23},\delta_{\rm CP}) = P_{\mu\mu}(\bar{\theta}_{23},\bar{\delta}_{\rm CP}) \tag{5.25}$$
$$\bar{P}_{\mu\mu}(\theta_{23},\delta_{\rm CP}) = \bar{P}_{\mu\mu}(\bar{\theta}_{23},\bar{\delta}_{\rm CP}). \tag{5.26}$$

This is unlikely to happen, since the disappearance probability has only a mild dependence on the PMNS phase. Thus, when a full analysis is performed, the disappearance channel provides an almost $\delta_{CP}$-independent measurement of $\theta_{23}$ that breaks the degeneracy in the appearance channel, which is now able to measure better the PMNS phase. There is an important exception: when the true value of the atmospheric angle is around its maximal value, the matter effects enhance the $\delta_{CP}$ dependence of the disappearance probability (see Fig. 5.4). In this case, it is no longer possible to provide a $\delta_{CP}$-independent measurement of $\theta_{23}$ and the appearance degeneracy cannot be broken.
All the discussed effects are clearly shown in Fig. 5.5, where we show for DUNE and T2HK the CP coverage as a function of $\theta_{23}$ in three cases:

- The dotted line has been obtained fixing the atmospheric angle in the fit to its true value; in this case we know from external inputs which is exactly the value of $\theta_{23}$
- The dashed curve has been obtained marginalizing $\theta_{23}$ over its current $3\sigma$ allowed range using only the appearance channel
- The solid curve shows the case in which in the marginalized fit, we include also the disappearance channel.

In all simulations, the other mixing parameters have been fixed to their best fit values (shown in Tab. 5.2). Firstly, the general decreasing tendency of the coverage when $\theta_{23}$ increases is clear for both experiments. Looking at the single experiments, in the T2HK (JD) case, the three blue lines almost overlap. This happens because, in absence of matter effects, neither the marginalization nor the disappearance channel has any impact on the coverage, since in this case the appearance channel alone completely drives the sensitivity. At DUNE, on the other hand, the marginalization has an important role which can be drastically reduced by the disappearance channel, through which, as already mentioned, it is possible to measure the atmospheric angle precisely. However, around the maximal mixing, the disappearance channel becomes less important for our purposes, since the measure of $\theta_{23}$ is now $\delta_{CP}$ dependent and therefore we observe a dip in the coverage.

| $\sin^2\theta_{12}$ | $\sin^2\theta_{23}$ | $\sin^2\theta_{13}$ | $\Delta m^2_{31}$ (eV$^2$) $\times 10^{-3}$ | $\Delta m^2_{21}$ (eV$^2$) $\times 10^{-5}$ | $\delta_{CP}$ (°) | Mass Ordering |
|---|---|---|---|---|---|---|
| 0.303 | 0.455 | 0.0223 | 2.522 | 7.36 | - 43 | Normal |
| [0.263 : 0.345] | [0.4 : 0.6] | [0.0204 : 0.0244] | [2.436 : 2.605] | [6.93 : 7.93] | [-175 : 139] | (NO) |

Table 5.2: The benchmark values of the oscillation parameters (refer to the second row) and their respective $3\sigma$ uncertain ranges (refer to the third row) from [113]. In our study, we only use the $3\sigma$ allowed range of $\sin^2\theta_{23}$ when a marginalization is performed.

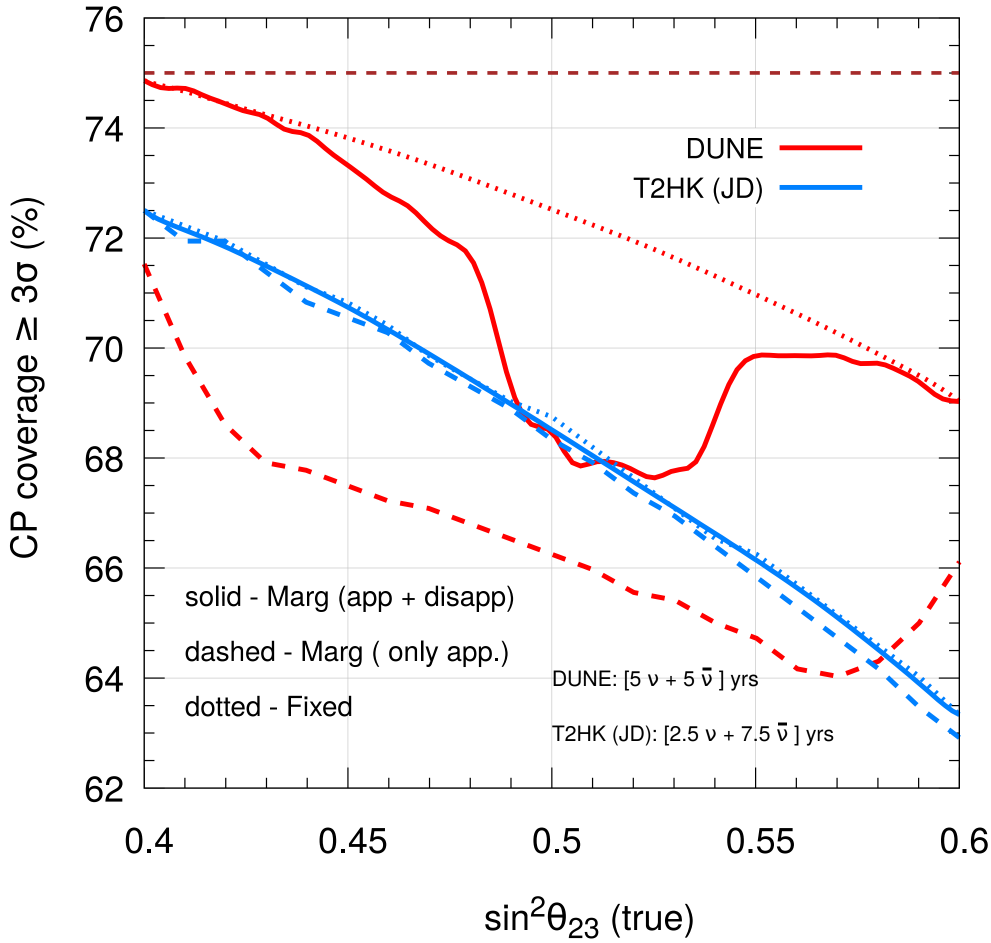


Figure 5.5: CP coverage as a function of true $\sin^2\theta_{23}$ assuming NO. The solid curves considers all possible contributions from both appearance and disappearance channels in establishing the CP coverage when marginalized over $\sin^2\theta_{23}$ in our theory. The dashed curves are obtained by considering contribution from only the appearance channel after marginalizing over $\sin^2\theta_{23}$. The dotted curves correspond to CP coverage by fixing identical $\sin^2\theta_{23}$ in both data and theory (fixed-parameter scenario). The curves red and blue are for DUNE and JD, respectively.

### 5.2.1 Reaching the 75% CP coverage milestone

In our simulations, in which we fix all the oscillation parameters to their best values and we marginalize over the atmospheric angle only, it is clear from Fig. 5.5 that neither T2HK, nor DUNE are able to reach 75% coverage using their nominal values for the systematics, the running time and the exposure (Tab. 5.1). Moreover, it is possible to notice that the DUNE coverage is always better than the JD one when we marginalize over the atmospheric angle and we use also disappearance data, except for the $\theta_{23}$ values around 45°. This is mainly due because of the

lower appearance systematic uncertainties in DUNE (2%) with respect to T2HK (5%).
We can now ask ourselves what happens if we combine DUNE and T2HK data, or if we consider also the possibility of the second T2HK detector in Korea (KD). We show in Fig. 5.6 the CP coverage results as a function of the $\theta_{23}$ true value, considering the full appearance+disappearance analysis in the marginalized case. We observe that the combination of at least two experiments makes CP coverage for the entire canvas of $\sin^2\theta_{23}$ above 75%. This points out that the complementarity between DUNE and JD or JD and KD can help attain a better CP coverage irrespective of the $\sin^2\theta_{23}$ value in Nature. Thus, if we are concerned about only CP coverage, there may be no remarkable advantages in adding a second detector to T2HK as DUNE + JD attains a better CP coverage than JD + KD combined. In all the setups, there is a general trend of CP coverage decreasing as we increase $\sin^2\theta_{23}$ in our data; the reason for that can be found in the behavior of the appearance asymmetry, as previously discussed. In the DUNE+JD case, the $3\sigma$ CP coverage decreases from 82% to 77% when $\theta_{23}$ increases from 40° ($\sin^2\theta_{23} = 0.4$) to 60° ($\sin^2\theta_{23} = 0.6$), while in the JD+KD case it decreases from 80% to 76% for the same.

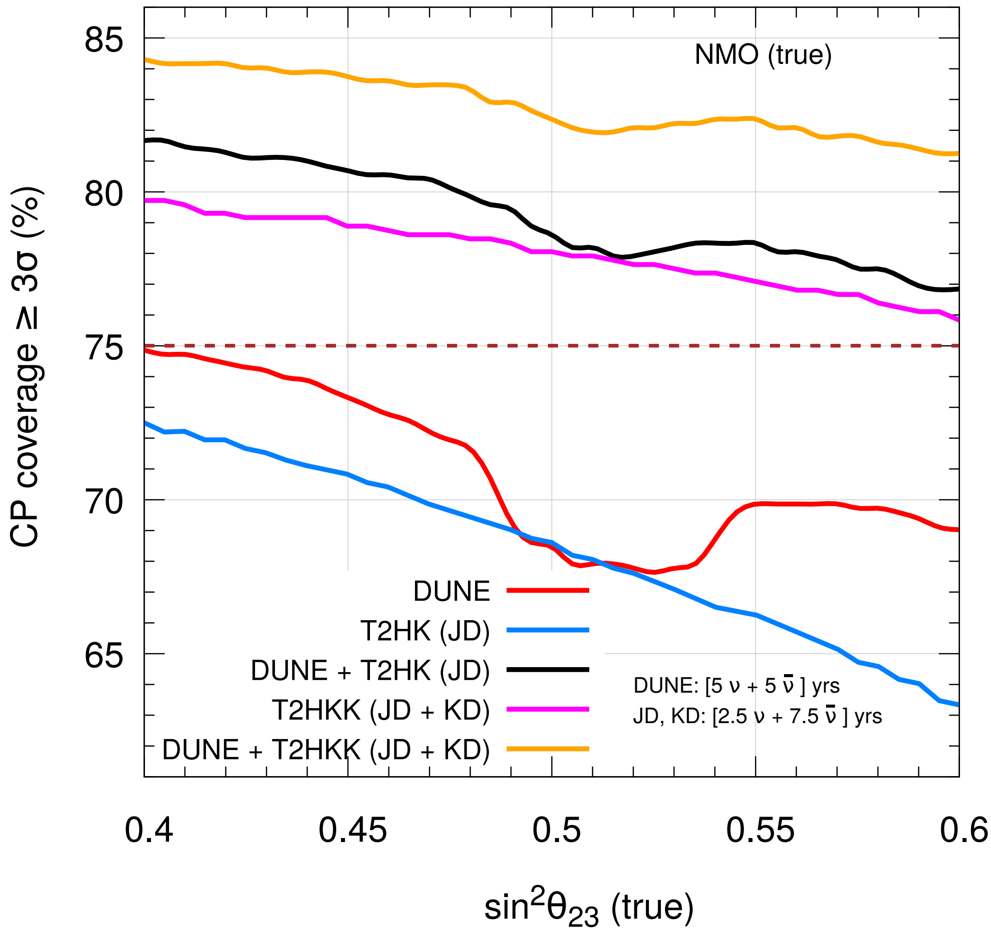


Figure 5.6: Percentage of true $\delta_{\mathrm{CP}}$ which can effectively establish CPV with a sensitivity of at least $3\sigma$ C.L. as a function of true $\sin^2\theta_{23}$. The curves represent the CP coverage when marginalizing over the uncertain range of $\sin^2\theta_{23}$ as mentioned in Table 5.2. The curves: red, blue, black, magenta, and orange are for DUNE, JD, DUNE + JD, JD + KD, and DUNE + JD + KD neutrino oscillation experiments, respectively. We assume true NO, benchmark exposure, and the nominal run-time as mentioned in Table 5.1.

It is interesting to see if the complementarity between the two different experiments may allow us to reach the coverage milestone also after a fraction of the running time or if the systematics are larger than those predicted by the collaborations. In Fig. 5.7, we show how the CP cov-

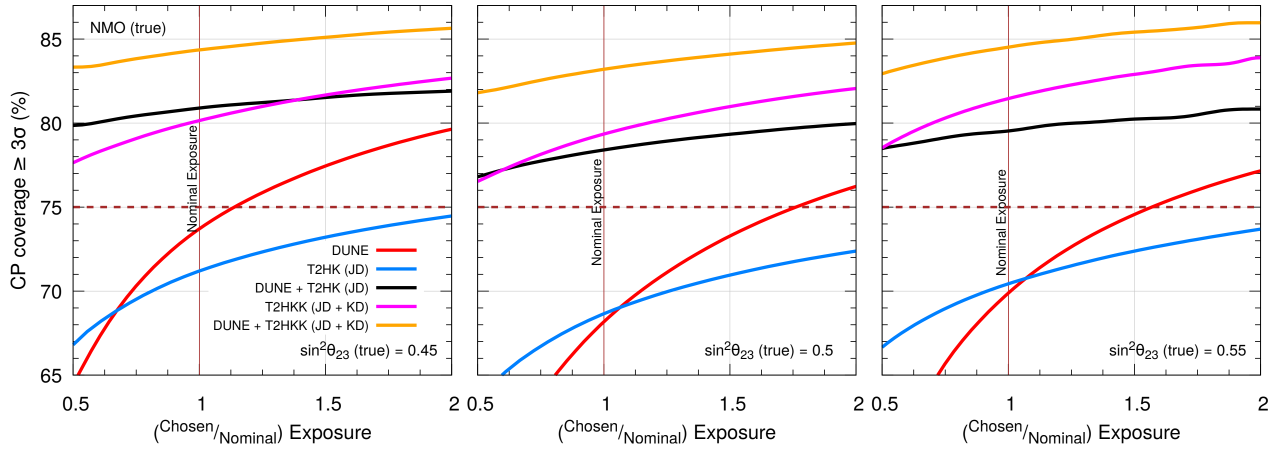


Figure 5.7: The CP coverage as a function of scaled exposures assuming true NO for true $\sin^2\theta_{23} = 0.45$ (LO, left panel), 0.5 (MM, middle panel), and 0.55 (HO, right panel). Here, we define scaled exposure as the ratio of assumed exposure with the nominal exposure of each experiment. Thus, (chosen/nominal exposure) = 1 is the benchmark exposure of the considered experiment. The solid curves are obtained by marginalizing over $\theta_{23}$ in our theory. The curves: red, blue, black, magenta, and orange are for DUNE, JD, DUNE + JD, JD + KD, and DUNE + JD + KD neutrino oscillation experiments, respectively.

erage is influenced by the change in total exposure of the experiments for $\sin^2\theta_{23} = 0.45$ (left panel), 0.5 (middle panel), and 0.55 (right panel). The curves are shown for DUNE (red), JD (blue), DUNE + JD (black), JD + KD (magenta), and DUNE + JD + KD (orange). We obtain these by marginalizing the atmospheric angle. Looking first at the performances of the single experiments, we observe that by keeping the true value for $\sin^2\theta_{23}$ fixed in LO and doubling the exposure from the nominal value of 2431 (480) kt·MW·yrs in JD (DUNE), the coverage increases from 74% to 79% in DUNE and from 71% to 75% in JD. On the other hand, if the exposure is reduced up to half the nominal value, the CP coverage drastically reduces for both experiments. It is worth mentioning that DUNE has better performances than JD on comparing both the experiments with their 70% of exposure. Even though going from LO to MM we observe a similar trend of increasing CP coverage with exposure, the maximum reachable coverage is now reduced (76% for DUNE, 72% for JD). Moreover, JD performs better than DUNE in this scenario at the nominal exposures. This happens due to strong $\theta_{23} - \delta_{\rm CP}$ degeneracy in DUNE near MM, which results in the reduction of CP coverage as compared to JD. In the HO case, coverage worsens further for JD (maximum coverage 70%), but not for DUNE, which now suffers less from the $\theta_{23} - \delta_{\rm CP}$ degeneracy in the non-maximal case. We have checked that, following the previous results, if we fix the value of $\sin^2\theta_{23}$ then the DUNE performance considerably increases in MM, while it slightly improves in the HO case. Coming back at our discussion about the complementarity between DUNE and T2HK (JD). we observe that the combination between the two experiments datasets enhances our result to much more than 75% coverage even if we consider half the exposure in both DUNE and JD for any value of $\theta_{23}$. As discussed earlier, the addition of KD to JD also increases the CP coverage for any value of true $\sin^2\theta_{23}$. Also, under the nominal exposure, the combination of DUNE, JD, and KD achieves CP coverage always above $\sim 80\%$ irrespective of the values of $\theta_{23}$. On the other hand, in Fig. 5.8, we illustrate the effect of the systematic uncertainties in the appearance channel for various setups on the CP coverage when marginalized over $\sin^2\theta_{23}$. It is clear that the JD curve has a steeper slope than the DUNE; however, one must remember that the nominal uncertainties in JD (5%) are higher than that of DUNE (2%). Recently the T2K collaboration [617] has been considering conservative uncertain-

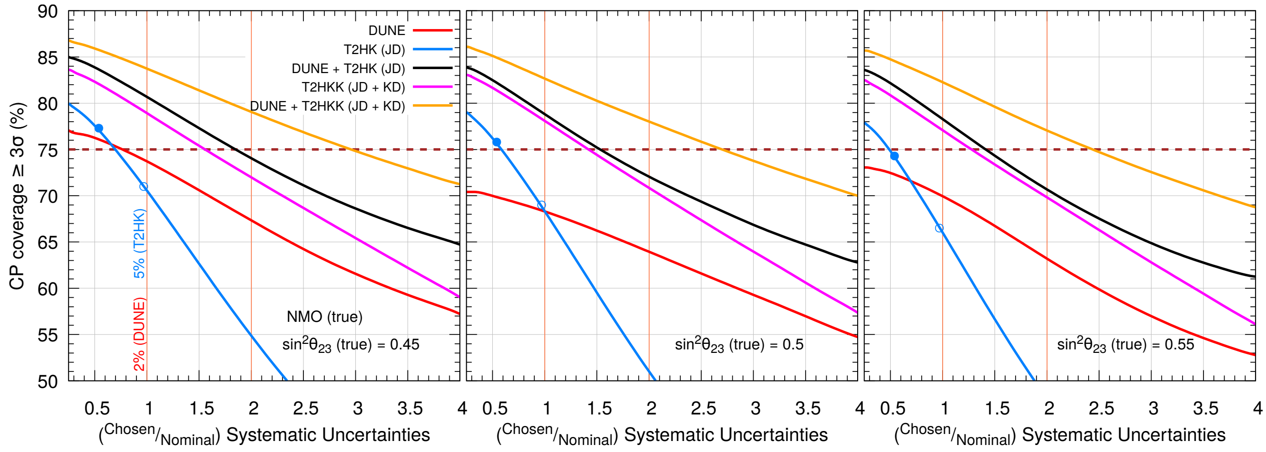


Figure 5.8: CP coverage as a function of scaled systematic uncertainties in $\nu_\mu \to \nu_e$ assuming NO is portrayed wherein, 1 represents the benchmark-systematic uncertainty for DUNE as 2% while for both JD and KD it refers to 5%. In the left, middle, and right panels we show the CP coverage by considering true $\sin^2\theta_{23} = 0.45$ (LO), 0.5 (MM), and 0.55 (HO) when marginalized over the uncertain range of $\sin^2\theta_{23}$ in our theory, respectively. The curves: red, blue, black, magenta, and orange are for DUNE, JD, DUNE + JD, JD + KD, and DUNE + JD + KD neutrino oscillation experiments, respectively. The blue colored filled and unfilled circles in the figure depict the CP coverage corresponding to 2.7% and 4.9% systematic uncertainties, respectively.

ties in the $\nu_e$ appearance systematics of about 4.9%, which they further expect to improve to about 2.7% by the time T2HK starts taking data [597]. These two possibilities have been shown in Fig. 5.8 (refer to blue unfilled and filled circles). Thus, comparing now the CP coverage obtained with the expected T2HK systematics of 2.7% (filled blue circles) and the nominal in DUNE (2%), we observe that T2HK outperforms DUNE for all three possible choices of $\theta_{23}$. We have also checked that in DUNE, the impact of the marginalization becomes negligible when systematics are higher than 5%, so the scenario is completely systematics dominated. Thus even if we consider half the nominal systematics (2.5%) for each value of the $\sin^2\theta_{23}$ (true), DUNE fails to reach the landmark of 75% CP coverage in both the MM and the HO cases, while JD does (notice that, for equal systematics JD always has better performances than DUNE due to its larger statistics). . If the real systematics turns out to be about 1.5 times higher than their nominal values in both DUNE and T2HK experiments, combining them is the only option to achieve 75% of CP coverage in all the three possible choices of $\theta_{23}$: 0.45, 0.5, and 0.55. Also, with the second proposed detector KD, when included in the analysis, we achieve our goal easily even if systematics are increased by a factor of 2.5 for all the three possible choices of $\theta_{23}$.
Another interesting factor to be taken into account is the fraction of total running time in which the experiments run in antineutrino mode. For DUNE and T2HK, we find two completely different approaches. In DUNE, the collaboration proposes 5 years in neutrino and 5 years in antineutrino modes. In this way we have a time-balanced running. However, being the antineutrino flux lower than the neutrino one, with this configuration we expect that the number of DUNE events in neutrino mode will be much higher than the number of events in antineutrino mode. The T2HK collaboration, on the other hand, proposes to run in antineutrino mode for a time which is 3 times bigger than the neutrino mode running time (2.5+7.5 years). In this way, being the antineutrino flux approximately 1/3 of the neutrino one, one expects roughly the same number of neutrino and antineutrino events. We show this in Tab. 5.3 where we compute the number of DUNE and T2HK events for different choices of $\theta_{23}$ and $\delta_{CP}$. We also show here

| Exp. \ Param. | $\theta_{23}$ | $\delta_{\rm CP}= 0°$ $(\nu_e,\, \bar{\nu}_e,\, \mathcal{N}^{\mu e}_{\rm CP})$ | $\delta_{\rm CP} = 90°$ $(\nu_e,\, \bar{\nu}_e,\, \mathcal{N}^{\mu e}_{\rm CP})$ | $\delta_{\rm CP} = -90°$ $(\nu_e,\, \bar{\nu}_e,\, \mathcal{N}^{\mu e}_{\rm CP})$ |
|---|---|---|---|---|
| DUNE | 40° | 1274, 354, *0.56* | 965, 398, *0.41* | 1611, 270, *0.71* |
| | 45° | 1526, 417, *0.57* | 1213, 462, *0.44* | 1869, 332, *0.69* |
| | 50° | 1779, 480, *0.57* | 1471, 524, *0.47* | 2117, 396, *0.68* |
| JD | 40° | 1242, 920, *0.14* | 875, 1191, *-0.15* | 1622, 618, *0.45* |
| | 45° | 1489,1098, *0.15* | 1116, 1373, *-0.1* | 1875, 790, *0.4* |
| | 50° | 1736, 1275, *0.15* | 1369, 1546, *-0.06* | 2117, 972, *0.37* |

Table 5.3: Total $\nu_e$ appearance event rates in $\nu$, $\bar{\nu}$ modes, and $\mathcal{N}^{\mu e}_{\rm CP}$ (see eq. (5.27)) for DUNE (JD) corresponding to different sets for $\delta_{\rm CP} : 0°, 90°, -90°$ and $\theta_{23} : 40°, 45°$, and $50°$ are shown in the second (third) set of rows, respectively.

the integrated asymmetry, namely

$$\mathcal{N}^{\mu e}_{\rm CP} = \frac{N_{\mu e} - \bar{N}_{\mu e}}{N_{\mu e} + \bar{N}_{\mu e}} \tag{5.27}$$

where $N_{\mu e}$ ($\bar{N}_{\mu e}$) is the number of events in the neutrino (antineutrino) mode, with the aim of demonstrating that also at the events number level the asymmetry decreases for high values of the atmospheric angle.

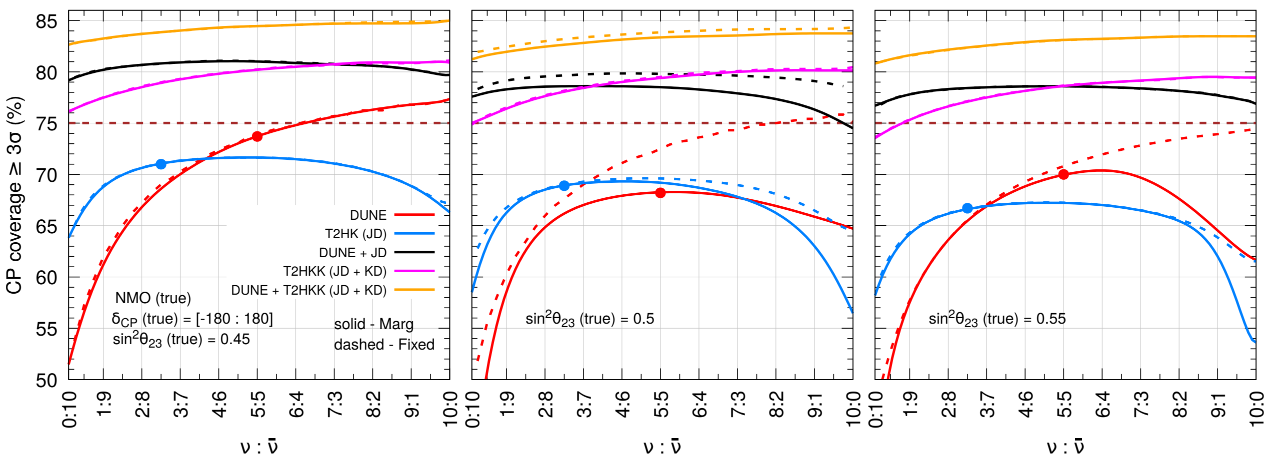


Figure 5.9: CP coverage as a function of ratio of the run-time in neutrino and antineutrino ($\nu : \bar{\nu}$) modes. The left, middle, and right panels represent CP coverage with true $\sin^2\theta_{23} = 0.45$ (LO), 0.5 (MM), and 0.55 (HO), respectively. The dashed lines are obtained by considering identical $\sin^2\theta_{23}$ in both data and theory, while the solid lines show CP coverage when marginalized over $\theta_{23}$ in the theory. The curves: red, blue, black, magenta, and orange are for DUNE, JD, DUNE + JD, JD + KD, and DUNE + JD + KD neutrino oscillation experiments, respectively. The red and blue dots depict the CP coverage for nominal run-time in DUNE [5 $\nu$ + 5 $\bar{\nu}$] years and T2HK [2.5 $\nu$ + 7.5 $\bar{\nu}$] years, respectively. We assume true NO.

In Fig. 5.9, we represent how the ratio between neutrino and antineutrino run-time affects the coverage for all the considered setups and the usual three choices of $\sin^2\theta_{23}$ (true) (LO, MM, and HO). We distinctly show two possible scenarios: first by fixing the same set of oscillation parameters in both data and theory (dashed curves) and second by marginalizing $\sin^2\theta_{23}$ (solid curves) in our theory and fixing all other parameters to our best-fit from Table 5.2. In the

LO case, while the nominal choice for JD [2.5 + 7.5] turns out to be the best, DUNE has no advantage of running in antineutrino mode. Instead, we observe that the best coverage (77%) for DUNE is acquired when only neutrino mode is employed for the full 10 years of run-time. The reason is simply due to the $\delta_{\rm CP}$ independent measurement of $\sin^2\theta_{23}$ by the disappearance channel in LO. Once the atmospheric angle is constrained by disappearance, the appearance channel benefits more from the increment in statistics by following [10 + 0] years instead of a balanced number of neutrino and antineutrino events, because of the small DUNE systematics (2%). In the maximal mixing case, the JD remains almost the same; contrastingly for DUNE, the subdued abilities of the disappearance channel in the marginalized $\theta_{23}$ scenario are overcome by the balanced run-time of [5 + 5] years, achieving the best coverage of 68%. While the HO case is intermediate: the best coverage in DUNE is neither obtained by the balanced [5 + 5] years nor with the highest number of events in [10 + 0] years, but the [6.5 + 3.5] years scenario. This can be understood from our previous discussions. We observe that $\sin^2\theta_{23}$ (true) = 0.55 is still in the dip region (refer solid red in Fig. 5.5) but not completely, thus disappearance is not able to constrain $\sin^2\theta_{23}$ in the fit much and so we can see the effect of $\theta_{23}-\delta_{\rm CP}$ degeneracy that requires both neutrino and antineutrino modes to resolve.
However, the complementarity between the experiments plays a crucial role irrespective of $\sin^2\theta_{23}$ in Nature. On combining DUNE and JD or adding KD, the coverage becomes almost insensitive of the choices in run-time and undisputedly reaches 75% in all the cases.

## 5.3 Complementarity and BSM: the Non-Unitarity case

So far we have discussed how the two future long baseline experiments may be used together to perform the desired measurement of the CP-violating PMNS matrix phase. However, the complementarity between DUNE and T2HK can be fundamental also in the context of BSM models. We present here a detailed discussion about the capabilities of the future LBL in constraining the full new physics parameters space in the Non-Unitarity case (see Sec. 3.4).
We already discussed how to parameterize a Non-Unitary PMNS matrix. One possibility consists of factorizing the deviation from unitarity into a matrix $\alpha$ in such a way that the non-unitary neutrino mixing matrix $N$ is expressed as[7]:

$$N = (I+\alpha)\, U_{PMNS}\,, \tag{5.28}$$

where the matrix $\alpha$ has a lower triangular structure and contains nine free parameters organized as follows:

$$\alpha = \begin{pmatrix} \alpha_{11} & 0 & 0 \\ |\alpha_{21}|e^{i\phi_{21}} & \alpha_{22} & 0 \\ |\alpha_{31}|e^{i\phi_{31}} & |\alpha_{32}|e^{i\phi_{32}} & \alpha_{33} \end{pmatrix}\,. \tag{5.29}$$

This parameterization simplifies the oscillation probabilities and let the parameter $\alpha_{ij}$ to be the main source of non-unitarity for the oscillation channel $\nu_i \to \nu_j$ $(i,j=e,\mu,\tau)$. Bounds on the $\alpha_{ij}$ parameters have been recently computed, among others, in Ref. [551] and reported for convenience in Table 5.4. These results have been obtained using data from the short-baseline experiments NOMAD and NuTeV, and the long-baseline experiments MINOS/MINOS+, T2K, and NO$\nu$A. For the off-diagonal Non-Unitarity Neutrino mixing (NUNM) parameters, the authors also used the triangular inequalities[8]: $\alpha_{ij} \leq \sqrt{1-(1+\alpha_{ii})^2}\sqrt{1-(1+\alpha_{jj})^2}$ [253], which

[7]We choose the convention in which the matrix $\alpha$, which invokes non-unitarity, is added to the identity matrix. Note that other phenomenological studies adopt the relation $N=(1-\alpha)\,U_{PMNS}$ [254]. Our results can be compared to the others just changing the sign in front of the diagonal elements.

[8]Note that, in this model, the diagonal parameters can only be negative.

| $\alpha_{11}$ | $\alpha_{22}$ | $\alpha_{33}$ | $\|\alpha_{21}\|$ | $\|\alpha_{31}\|$ | $\|\alpha_{32}\|$ |
|---|---|---|---|---|---|
| $< 0.031$ | $< 0.005$ | $< 0.110$ | $< 0.013$ | $< 0.033$ | $< 0.009$ |

Table 5.4: 90% confidence level (C.L.) limits on the NUNM parameters using data from various short-baseline and long-baseline experiments, as obtained from the Ref. [551].

appear due to the assumption that the standard 3×3 active neutrino mixing matrix is a non-unitary sub-matrix of a larger unitary mixing matrix. In the following discussion, we do not take into account these inequalities with the aim of studying the capability of long-baseline experiments in constraining NUNM parameters in a complete model-independent fashion. Taking into account the expression in eq. (5.28), the complete effective neutrino propagation Hamiltonian in the mass-eigenstate is:

$$H = \frac{1}{2E_\nu}\left[\begin{pmatrix} 0 & 0 & 0 \\ 0 & \Delta m^2_{21} & 0 \\ 0 & 0 & \Delta m^2_{31} \end{pmatrix} + N^\dagger \begin{pmatrix} a_e + a_n & 0 & 0 \\ 0 & a_n & 0 \\ 0 & 0 & a_n \end{pmatrix} N\right]. \tag{5.30}$$

As usual, the matter potential parameters are given by $a_e = 2\sqrt{2}E_\nu G_F N_e$ and $a_n = -\sqrt{2}E_\nu G_F N_n$ where, $N_e$ and $N_n$ are the electron and the neutron number densities, respectively. Note that in this framework, the neutral current (NC) matter potential is necessary since the non-unitarity of the matrix $N$ does not allow the subtraction of an identity matrix proportional to $a_n$. From the Schroedinger equation, the transition probability at a given baseline $L$ is obtained from the following expression:

$$P_{\alpha\beta} = |(N e^{-iHL} N^\dagger)_{\beta\alpha}|^2. \tag{5.31}$$

The relevant probabilities for long-baseline experiments are the $\nu_\mu \to \nu_e$ appearance and $\nu_\mu \to \nu_\mu$ disappearance channels. In order to get approximate analytical expressions for the transition probabilities, we observe that the vacuum approximation cannot be sufficiently precise in experiments like DUNE, since the matter effects can modify the appearance probability up to about 10%. For this reason, we derive approximate analytical expressions in the presence of matter. We use perturbation theory in the small expansion parameters ($r$, $s$, and $a$) defined as follows:

$$\sin\theta_{13} = \frac{r}{\sqrt{2}}, \qquad \sin\theta_{12} = \frac{1}{\sqrt{3}}(1+s), \qquad \sin\theta_{23} = \frac{1}{\sqrt{2}}(1+a), \tag{5.32}$$

where, $r$, $s$, and $a$ represent the deviation from the tri-bimaximal mixing values of the neutrino mixing parameters, namely, $\sin\theta_{13} = 0$, $\sin\theta_{23} = 1/\sqrt{2}$, and $\sin\theta_{12} = 1/\sqrt{3}$ [618, 619]. Given the recent global fit of neutrino oscillation data, we can assume that $r, s, a \sim \mathcal{O}(0.1)$ and we can expand them up to the second order [111–113, 620]. To further simplify the notation, we also introduce $\Delta_{31} = \Delta m^2_{31} L/4E_\nu$, $\Delta_e = a_e L/4E_\nu$ and $\Delta_n = a_n L/4E_\nu$; at the DUNE peak energy, namely, $E_\nu = 2.5$ GeV, $\Delta_e \sim 0.36$ and $\Delta_n \sim 0.18$, we can further expand in the small matter potentials up to the first order. Note that for the other experimental facilities discussed in this paper, this approximation is even better; in fact, for the Tokai to Hyper-Kamiokande (T2HK) setup with a far detector in Japan (JD), at beam energy of $E_\nu = 0.6$ GeV, we have $\Delta_e \sim 0.08$ and $\Delta_n \sim 0.04$, while with a second in Korea (KD) at a distance of 1100 km from the source with same energy, we get $\Delta_e \sim 0.30$ and $\Delta_n \sim 0.15$. Also, we use one mass scale dominance (OMSD) approximation ($\Delta_{31} >> \Delta_{21}$, where $\Delta_{21} = \Delta m^2_{21} L/4E_\nu$) in our derivation; this is a valid approximation in the atmospheric regime ($\Delta_{31} \sim \pi/2$).

In the case of the $\nu_\mu \to \nu_e$ appearance probability, we thus obtain:

$$\begin{aligned}
P_{\mu e} \;=\;& \left(\frac{r^2}{\Delta_{31}}\right) \sin\Delta_{31}\left[(\Delta_{31}+2\Delta_e)\sin\Delta_{31} - 2\Delta_{31}\Delta_e\cos\Delta_{31}\right] + \\
& \left(\frac{2|\alpha_{31}|r}{\Delta_{31}}\right) \Delta_n \sin\Delta_{31}\left[\cos(\delta_{\rm CP}-\phi_{31})\sin\Delta_{31} - \Delta_{31}\cos(\delta_{\rm CP}+\Delta_{31}-\phi_{31})\right] + \\
& \left(\frac{|\alpha_{21}|r}{\Delta_{31}}\right) \{\sin\Delta_{31}\left[2\Delta_{31}(\Delta_e+\Delta_n)\cos(\delta_{\rm CP}+\Delta_{31}-\phi_{21}) - \Delta_n\sin(\delta_{\rm CP}-\Delta_{31}-\phi_{21})\right] + \\
& \sin(\delta_{\rm CP}+\Delta_{31}-\phi_{21})\left[(-2\Delta_{31}-2\Delta_e+\Delta_n)\sin\Delta_{31} + 2\Delta_{31}\Delta_e\cos\Delta_{31}\right]\} + \\
& \left(\frac{|\alpha_{21}||\alpha_{31}|}{\Delta_{31}}\right) \Delta_n\left[-2\Delta_{31}\sin(\phi_{21}-\phi_{31}) + \cos(2\Delta_{31}-\phi_{21}+\phi_{31}) - \cos(\phi_{21}-\phi_{31})\right] + \\
& \left(\frac{|\alpha_{21}|^2}{\Delta_{31}}\right) \left[\Delta_{31} - \Delta_n(1-\cos 2\Delta_{31})\right] . \qquad (5.33)
\end{aligned}$$

From the above expression, it is clear that the $\nu_\mu \to \nu_e$ appearance probability strongly depends on $|\alpha_{21}|$ and $|\alpha_{31}|$. The parameter $|\alpha_{21}|$ survives in the vacuum case while $|\alpha_{31}|$ always appears with the matter potential $\Delta_n$. This essentially means that an experiment in which the matter effect is not negligible is able to put strong bounds also to $|\alpha_{31}|$ which, otherwise, would not be accessible by $P_{\mu e}$. Note that due to the loss of unitarity property of the neutrino mixing, some terms remain non-zero in $\nu_\mu \to \nu_e$ appearance probability expression even when the neutrino propagation length $L$ is zero, which is known as zero-distance effect:

$$P_{\mu e}^{L=0} \;\sim\; |\alpha_{21}|^2 . \qquad (5.34)$$

So, it is clear that even the near detectors (ND) of long-baseline experiments could contribute to the bounds of non-unitarity parameters. Finally, we point out that the vacuum limit of eq. (5.33) assumes a particularly simple expression:

$$P_{\mu e}^{vac} \;=\; |\alpha_{21}|^2 + r^2\sin^2\Delta_{31} - 2|\alpha_{21}|r\sin\Delta_{31}\sin(\delta_{\rm CP}+\Delta_{31}-\phi_{21}) , \qquad (5.35)$$

which, in the limit of vanishing solar mass difference, agrees with the results presented in Ref. [249].

In order to assess the modifications in the $\nu_\mu \to \nu_e$ appearance probabilities caused by the presence of non-unitary neutrino mixing, in Fig. 5.10, we show the exact $\nu_\mu \to \nu_e$ appearance probabilities as a function of energy. In the extreme left column, we consider a baseline of 1300 km for DUNE. In the middle column, we show the results for the JD baseline of 295 km. In the extreme right column, we deal with the KD setup having a baseline of 1100 km. Note that for both JD and KD, we consider the neutrino energy range of 0 to 1.5 GeV having a peak around 0.6 GeV. In every rows, we switch-on one off-diagonal NUNM parameters at a time, while maintaining the others to zero. The effect of $|\alpha_{21}|$ is shown in the top panels, $|\alpha_{31}|$ in the middle panels, and $|\alpha_{32}|$ in the bottom panels. In each panel, the solid black curves correspond to the probabilities in the unitary neutrino mixing (UNM) case, while the colored curves correspond to the NUNM cases with four benchmark values of the phases associated with each off-diagonal NUNM parameters, as reported in the legend. As we can see, the impact of the NUNM parameter $|\alpha_{21}|$ (top panels) is comparatively larger than the other two off-diagonal NUNM parameters $|\alpha_{31}|$ and $|\alpha_{32}|$ even though the strength of the $|\alpha_{21}|$ is much smaller than the other two. This feature is more clear for JD in the middle columns. In fact, from the approximated analytical expression of $\nu_\mu \to \nu_e$ appearance probability in Eqs. 5.33 and 5.35, we see that only terms containing $|\alpha_{21}|$ survive in vacuum, while the effect of $|\alpha_{31}|$ and $|\alpha_{32}|$ is linked to $\Delta_e$ and $\Delta_n$ which are very small at the considered baseline. This is not the case for DUNE ($L \simeq 1300$ km) where, given the largest baseline under consideration, $\Delta_e$ and $\Delta_n$ are no longer negligible and the impact of $|\alpha_{31}|$ and $|\alpha_{32}|$ on $P_{\mu e}$ is of the same order as $|\alpha_{21}|$.

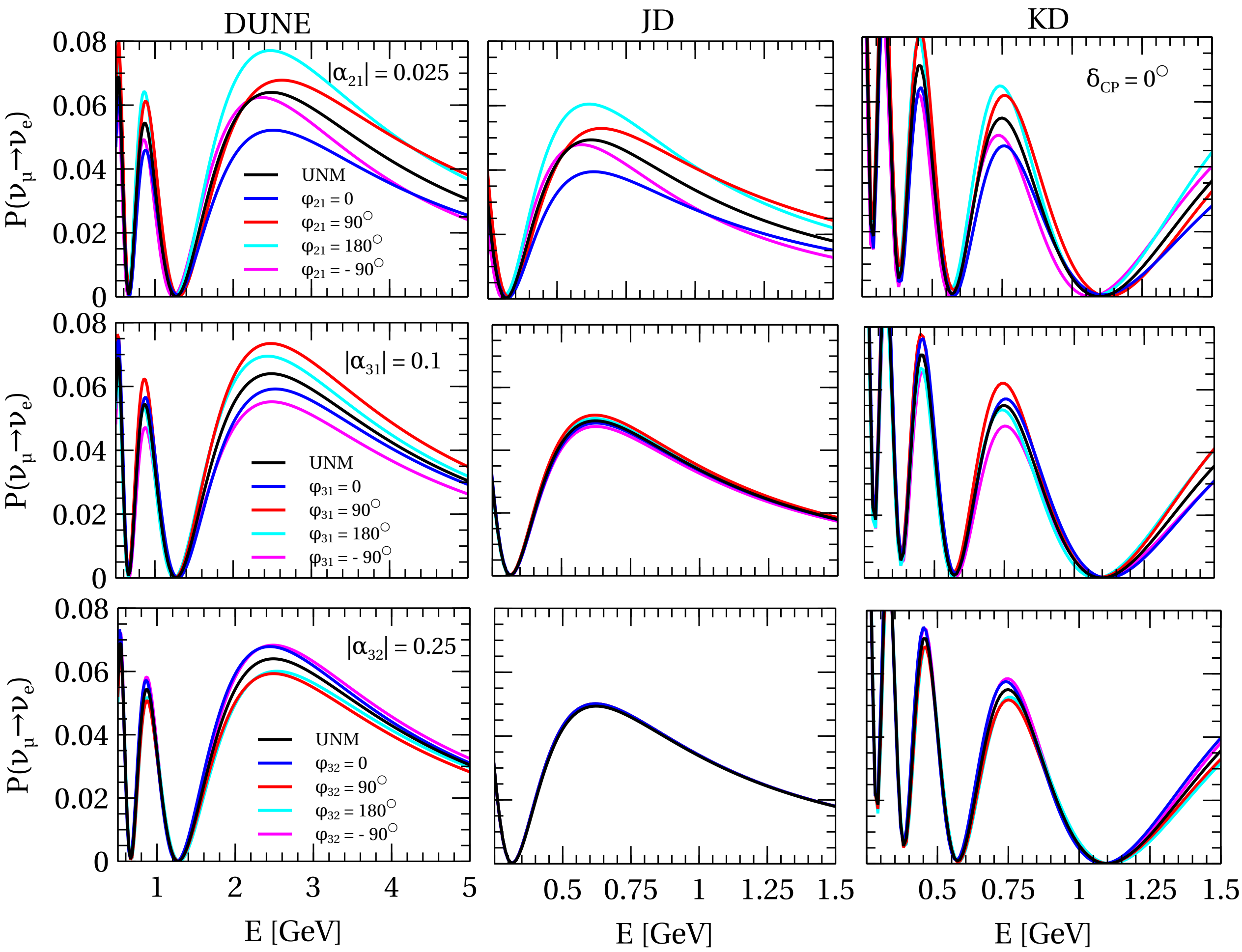


Figure 5.10: $\nu_\mu \to \nu_e$ appearance probability as a function of energy in the presence of off-diagonal NUNM parameters. Left, middle, and right columns correspond to the baselines of 1300 km (DUNE), 295 km (JD), and 1100 km (KD), respectively. The four colored curves correspond to four benchmark values of the phases associated with off-diagonal NUNM parameters: 0°, 90°, 180°, and −90°. We consider $\delta_{\rm CP} = 0°$ and $\sin^2\theta_{23} = 0.5$. The values of the other oscillation parameters are taken from Table 5.2.

For the $\nu_\mu \to \nu_\mu$ disappearance channel, we get:

$$
\begin{aligned}
P_{\mu\mu} \;=\;& \cos^2\Delta_{31}(1+4\alpha_{22}) - 2|\alpha_{32}|\Delta_n \sin 2\Delta_{31}\cos\phi_{32} + 4a^2\sin^2\Delta_{31} + \\
& 2|\alpha_{21}|^2\cos\Delta_{31}\left[2\sin\Delta_{31}(\Delta_e+\Delta_n)+\cos\Delta_{31}\right] + 6\alpha_{22}^2\cos^2\Delta_{31} - \\
& 2|\alpha_{21}|r\sin(2\Delta_{31})(\Delta_e+\Delta_n)\cos(\delta_{\rm CP}-\phi_{21}) + \\
& \left(\frac{8a}{\Delta_{31}}\right)(\alpha_{22}-\alpha_{33})\Delta_n\sin\Delta_{31}(\sin\Delta_{31}-\Delta_{31}\cos\Delta_{31}) \\
& -2|\alpha_{21}||\alpha_{31}|\Delta_n\sin 2\Delta_{31}\cos(\phi_{21}-\phi_{31}) - 8\alpha_{22}|\alpha_{32}|\Delta_n\sin 2\Delta_{31}\cos\phi_{32} \\
& -2|\alpha_{32}|\alpha_{33}\Delta_n\sin 2\Delta_{31}\cos\phi_{32}\,, \qquad (5.36)
\end{aligned}
$$

from which we learn that all the NUNM parameters $\alpha_{ij}$ but $\alpha_{11}$ enter into the probability expression. Also, in this case, we get the zero-distance expression of the $\nu_\mu \to \nu_\mu$ survival

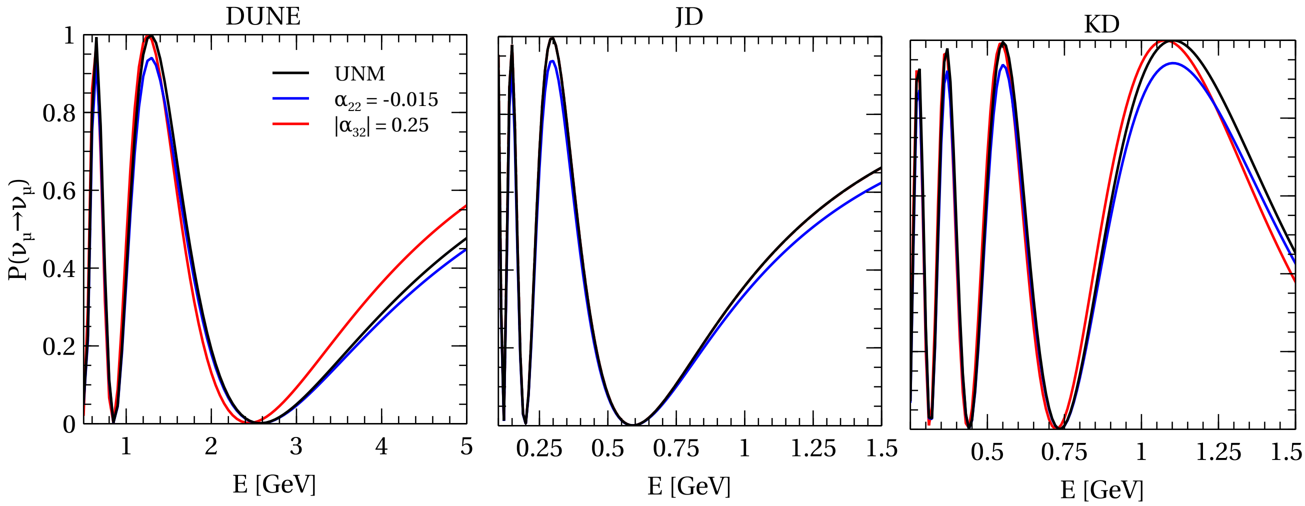


Figure 5.11: $\nu_\mu \to \nu_\mu$ disappearance probabilities as a function of neutrino energy in the presence of the NUNM parameters $\alpha_{22}$ and $|\alpha_{32}|$ assuming $\phi_{32} = 0$ one at a time. Left, middle, and right columns correspond to the baselines of 1300 km (DUNE), 295 km (JD), and 1100 km (KD), respectively. We consider $\delta_{\rm CP} = 0°$ and $\sin^2\theta_{23} = 0.5$. The values of the other oscillation parameters are taken from Table 5.2.

probability, given by:

$$P_{\mu\mu}^{L=0} \sim 1 + 2|\alpha_{21}|^2 + 6\alpha_{22}^2 + 4\alpha_{22}\,, \tag{5.37}$$

and the vacuum approximation (also in agreement with Ref. [249] in the limit of vanishing $\Delta m_{21}^2$):

$$P_{\mu\mu}^{vac} = \cos^2\Delta_{31}\left(1 + 2|\alpha_{21}|^2 + 4\alpha_{22} + 6\alpha_{22}^2\right) + 4a^2\sin^2\Delta_{31}\,. \tag{5.38}$$

In Fig. 5.11, we show the exact $\nu_\mu \to \nu_\mu$ oscillation probabilities as a function of energy for the baseline lengths corresponding to DUNE (left panel), JD (middle panel), and KD (right panel) setups. In each panel, the black solid curves correspond to the UNM case, while the red and blue curves show the presence of $\alpha_{22}$ and $\alpha_{32}$, respectively with strength reported in the legend[9], one at a time. The impact of these two NUNM parameters can be understood from our approximated analytical expressions in eq. (5.36). When matter effects are negligible (for example, in the middle panel of Fig. 5.11), we expect that the parameter $\alpha_{22}$ dominates the deviation from UNM since it appears already at first order in $P_{\mu\mu}$. This remains true when matter parameters are switched-on; the relevant difference compared to the vacuum case relies on the fact that also $|\alpha_{32}|$ enter at first order, although suppressed by $\Delta_n$. Thus, we expect that for DUNE and KD, one can see deviation from the UNM predictions, as visible in Fig. 5.11. Note that the impact of $\alpha_{32}$ is amplified by the larger benchmark value compared to the choice for $\alpha_{22}$.
At the number of events level, we summarize for some benchmark values of the NUNM parameters the expected rates at DUNE, JD and KD, considering for DUNE a running time of 3.5+3.5 years in Tabs. 5.5 and 5.6. The impact of NUNM parameters on the number of events is fully in agreement with our analytical discussions. First of all, as shown in eq. (5.33), the appearance channel is mainly influenced by $|\alpha_{21}|$, even in vacuum. This reflects in an enhancement of the number of events by roughly 5% in both JD and DUNE. On the other hand, the NUNM parameters $|\alpha_{31}|$ and $\alpha_{33}$ are also relevant but they are coupled to the matter potentials, so we expect

[9]Even though the analytical expression of $P_{\mu\mu}$ reported in eq. (5.36) shows the presence of other NUNM parameters, we have numerically checked that they do not have any significant impact.

| | $\nu_e$ appearance | | | $\bar{\nu_e}$ appearance | | |
|---|---|---|---|---|---|---|
| | DUNE | JD | KD | DUNE | JD | KD |
| UNM | 1259 | 1836 | 169 | 221 | 767 | 31 |
| NUNM | DUNE | JD | KD | DUNE | JD | KD |
| $\lvert\alpha_{21}\rvert$ (= 0.025) | 1328 | 1893 | 169 | 232 | 756 | 29 |
| $\lvert\alpha_{31}\rvert$ (= 0.1) | 1420 | 1893 | 187 | 264 | 754 | 30 |
| $\lvert\alpha_{32}\rvert$ (= 0.25) | 1300 | 1855 | 172 | 213 | 756 | 30 |
| $\alpha_{11}$ (= -0.02) | 1203 | 1761 | 162 | 214 | 738 | 29 |
| $\alpha_{22}$ (= -0.015) | 1223 | 1782 | 164 | 215 | 744 | 30 |
| $\alpha_{33}$ (= -0.15) | 1208 | 1817 | 168 | 227 | 779 | 30 |

Table 5.5: Comparison of the total signal rate for the $\nu_e$ and $\bar{\nu_e}$ appearance channels in DUNE, JD, and KD setups in UNM case as well as in presence of various NUNM parameters. The relevant features of these facilities are given in Table 5.1. The values of the standard oscillation parameters used to calculate event rate are quoted in Table 5.2. The phases associated with the off-diagonal NUNM parameters are considered to be zero.

| | $\nu_\mu$ disappearance | | | $\bar{\nu_\mu}$ disappearance | | |
|---|---|---|---|---|---|---|
| | DUNE | JD | KD | DUNE | JD | KD |
| UNM | 10359 | 9064 | 1266 | 6034 | 8625 | 1144 |
| NUNM | DUNE | JD | KD | DUNE | JD | KD |
| $\lvert\alpha_{21}\rvert$ (= 0.025) | 10371 | 9074 | 1264 | 6045 | 8640 | 1149 |
| $\lvert\alpha_{31}\rvert$ (= 0.1) | 10351 | 9062 | 1261 | 6035 | 8627 | 1168 |
| $\lvert\alpha_{32}\rvert$ (= 0.25) | 10978 | 9203 | 1255 | 6005 | 8467 | 1158 |
| $\alpha_{11}$ (= -0.02) | 10359 | 9064 | 1266 | 6034 | 8625 | 1145 |
| $\alpha_{22}$ (= -0.015) | 9748 | 8531 | 1192 | 5681 | 8120 | 1077 |
| $\alpha_{33}$ (= -0.15) | 10406 | 9077 | 1268 | 6040 | 8619 | 1145 |

Table 5.6: Comparison of the total signal rate for the $\nu_\mu$ and $\bar{\nu_\mu}$ disappearance channels in DUNE, JD, and KD setups in UNM case as well as in presence of various NUNM parameters. The relevant features of these facilities are given in Table 5.1. The values of the standard oscillation parameters used to calculate event rate are quoted in Table 5.2. The phases associated with the off-diagonal NUNM parameters are considered to be zero.

them to be relevant primarily for DUNE, where matter effects are more important: in fact, $|\alpha_{31}|$ causes an increase in the number of events up to 10%, while $\alpha_{33}$ provokes a small but visible reduction of the order of 4%. Finally, some impact on the number of signal events is also given by $\alpha_{11}$, even though it only appears at higher orders in our perturbative expansion and has not been displayed (but it present in the vacuum probabilities reported in Ref. [249]). Note that the number of $\nu_e$ and $\bar{\nu}_e$ events in KD is only slightly influenced by the NUNM parameters due to fact that the experiment works close to the second oscillation maximum of the atmospheric oscillation ($\nu_\mu \to \nu_\tau$), where the $\nu_\mu \to \nu_e$ appearance probability approached one of its minima and the effects of new physics are suppressed.

For the disappearance channel, the parameter $\alpha_{22}$, which enters at the first perturbative order in eq. (5.36), produces a reduction of about 6% in the number of events for all three detectors. This can be roughly understood from the fact that the standard disappearance probability is multiplied by $4\alpha_{22} = 0.06$, which causes a reduction by a similar factor in the number of events. The other relevant NUNM parameter is $|\alpha_{32}|$ which, being coupled to matter potential in eq. (5.36), can cause a $\sim 6\%$ increase of events especially in DUNE. The other parameters at their benchmark values only have a negligible impact on the number of disappearance events.

### 5.3.1 Constraining all the NUNM parameters at the Far Detectors

In this subsection, we present our numerical results showing the expected constraints on the six NUNM parameters ($\alpha_{ij}$) that DUNE, JD, KD, and JD+KD setups can place. We study the NUNM parameters by fixing the mixing angles $\theta_{12}$, $\theta_{13}$, and two mass-squared differences $\Delta m^2_{21}$, and $\Delta m^2_{31}$ both in data and theory at their best fit values as given in Table 5.2. We check that the marginalization over the atmospheric mass-squared difference $\Delta m^2_{31}$ does not have any significant effect on our analysis. On the other hand, the only notable effect of the marginalization over the reactor mixing angle $\theta_{13}$ (which has a very small experimental uncertainty of 3%), is the worsening of the $\alpha_{11}$ bound at the level of 15%. This is due to the fact that there is a correlation between these two parameters, which appear in a term proportional to $\alpha_{11}^2 \sin^2 2\theta_{13}$ in the $\nu_\mu \to \nu_e$ transition probability as shown in Ref. [249]. Finally, we marginalized $\theta_{23}$ in its current $3\sigma$ allowed range [113], which is approximately [40°, 50°] and the CP phase $\delta_{\rm CP}$ in its entire possible range [−180°, 180°]. We keep both these parameters with true values as in Table 5.2. Moreover, we consider one NUNM parameter at a time, *i.e.*, when a parameter is taken into account the others are considered to be zero. Finally, the phases associated with each off-diagonal NUNM parameters are marginalized over the entire possible range from −180° to 180°. The statistical significance with which we can constrain the NUNM parameters ($\alpha_{ij}$) in a given experiment is defined as

$$\Delta\chi^2 = \min_{(\theta_{23},\,\delta_{\rm CP},\,\phi_{ij},\,\lambda_1,\,\lambda_2)} \left[\chi^2(\alpha_{ij} \neq 0) - \chi^2(\alpha_{ij} = 0)\right] , \tag{5.39}$$

where, $\chi^2(\alpha_{ij} \neq 0)$ and $\chi^2(\alpha_{ij} = 0)$ are calculated by fitting the prospective data assuming NUNM ($\alpha_{ij} \neq 0$) and UNM ($\alpha_{ij} = 0$). Note that $\chi^2(\alpha_{ij} = 0) \approx 0$ because the statistical fluctuations are suppressed to obtain the median sensitivity of a given experiment in the frequentist approach [621]. While estimating the constraints, we marginalize over the most uncertain oscillation parameters ($\theta_{23}$, $\delta_{\rm CP}$) and the phases associated with the off-diagonal NUNM parameters ($\phi_{ij}$) in the fit. We also minimize over the systematic pulls on signal ($\lambda_1$) and background ($\lambda_2$).

In Fig. 5.12, we plot the $\Delta\chi^2$ function for the six NUNM parameters analyzed in our paper considering only the far detectors in a given setup. Upper (lower) panels show the results for the diagonal (off-diagonal) NUNM parameters. The red curves in each panel refer to the sensitivities obtained for the DUNE setup considering a total of 336 kt-MW-yrs exposure, corresponding to a total 7 years of data collection with equal run-time in neutrino and antineutrino modes. The green curves show the results for JD for which we consider a total exposure of 2431 kt-MW-yrs with 10 years of total run-time (2.5 years in neutrino mode and 7.5 years in antineutrino mode). The magenta curves correspond to KD assuming the same exposure. We also estimate the results for JD+KD as shown by the blue curves. From the upper left panel, we observe that DUNE and JD+KD place similar constraints on $\alpha_{11}$. The sensitivity to this parameter comes from two contributions: the intrinsic $\nu_e$ beam contamination disappearance background and the $\nu_e$ appearance. For both contribuiting channels, DUNE has better systematics and JD+KD more statistics. As a result, limits on $\alpha_{11}$ are found to be almost the same for the two setups. However, for $\alpha_{22}$ (upper middle panel), JD+KD has significantly better sensitivity compared to DUNE setup. This is because $\alpha_{22}$ is mainly constrained by the disappearance channels, which due to the large statistics, is primarily limited by the systematic uncertainties. Since the normalization error for this channel is 3.5% (5%) for JD+KD (DUNE), it is clear that JD+KD can put better limit than DUNE. We have checked that if we consider the same amount of systematic uncertainties for both the setups, DUNE shows slightly better sensitivity than T2HKK. For $|\alpha_{21}|$, DUNE and JD+KD have comparable sensitivities (see lower left panel). The slightly better limit on $|\alpha_{21}|$ achieved in the case of JD+KD as compared to DUNE, is due to the fact that JD+KD has larger statistics in the appearance channels. For the other three parameters $|\alpha_{31}|$, $|\alpha_{32}|$ and $\alpha_{33}$, which enter the $\nu_\mu \to \nu_e$ appearance channel through matter

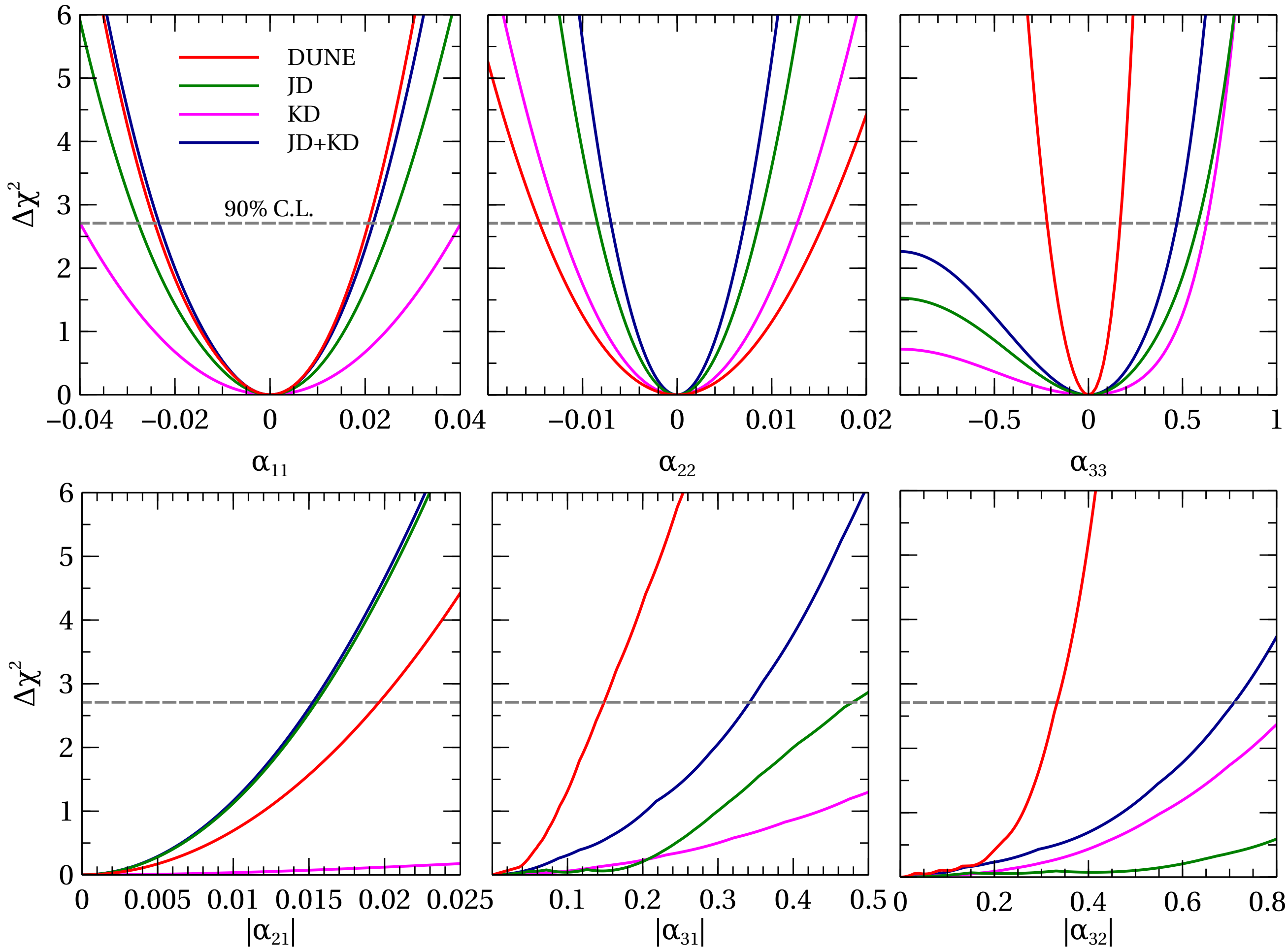


Figure 5.12: Expected limits on the NUNM parameters from DUNE (red curves), JD (green curves), KD (magenta curves), and JD+KD (blue curves). The upper (lower) panels are for the diagonal (off-diagonal) NUNM parameters one at a time. True values of $\theta_{23}$ and $\delta_{\rm CP}$ are $45°$ and $-90°$, respectively. For the diagonal NUNM parameters, we marginalize over $\theta_{23}$ in the range $[40°, 50°]$ and $\delta_{\rm CP}$ in the range $[-180°, 180°]$ in the fit. For the off-diagonal NUNM parameters, apart from $\theta_{23}$ and $\delta_{\rm CP}$, we also marginalize over the associated NUNM phases in the range of $-180°$ to $180°$.

parameters $\Delta_e$ and $\Delta_n$ (see eq. (5.33)), DUNE outperforms JD+KD setups because of its large matter effects.

| | DUNE | JD | KD | JD+KD | JD+KD+DUNE | T2K+NO$\nu$A |
|---|---|---|---|---|---|---|
| $\alpha_{11}$ | [-0.020, 0.020] | [-0.025, 0.025] | [-0.040, 0.040] | [-0.022, 0.022] | [-0.017, 0.017] | [-0.06, 0.06] |
| $\alpha_{22}$ | [-0.014, 0.014] | [-0.0087, 0.0087] | [-0.013, 0.013] | [-0.007, 0.007] | [-0.006, 0.006] | [-0.02, 0.02] |
| $\alpha_{33}$ | [-0.2, 0.17] | $< 0.6$ | $< 0.63$ | $< 0.476$ | [-0.17, 0.17] | $< 0.64$ |
| $\|\alpha_{21}\|$ | $< 0.022$ | $< 0.015$ | $< 0.10$ | $< 0.016$ | $< 0.012$ | $< 0.06$ |
| $\|\alpha_{31}\|$ | $< 0.15$ | $< 0.48$ | $< 0.70$ | $< 0.34$ | $< 0.11$ | $< 2.20$ |
| $\|\alpha_{32}\|$ | $< 0.33$ | $< 1.2$ | $< 0.85$ | $< 0.71$ | $< 0.27$ | $< 1.4$ |

Table 5.7: Bounds on the NUNM parameters at 90% C.L. (1 d.o.f.) using DUNE (second column), JD (third column), KD (fourth column), and JD+KD (fifth column). Sixth column shows the results for the combination of DUNE and JD+KD. Last column depicts results using the full exposure of T2K and NO$\nu$A.

We summarize our results in Table 5.7, where we give the bounds on the six NUNM parame-

| Parameter | DUNE (3.5 yrs+3.5 yrs) | DUNE (5 yrs+5 yrs) |
|---|---|---|
| $\alpha_{11}$ | [-0.020, 0.020] | [-0.020, 0.018] |
| $\alpha_{22}$ | [-0.014, 0.014] | [-0.013, 0.013] |
| $\alpha_{33}$ | [-0.2, 0.17] | [-0.19, 0.15] |
| $\|\alpha_{21}\|$ | $< 0.022$ | $< 0.016$ |
| $\|\alpha_{31}\|$ | $< 0.15$ | $< 0.12$ |
| $\|\alpha_{32}\|$ | $< 0.33$ | $< 0.31$ |

Table 5.8: 90% C.L. (1 d.o.f.) limits on the NUNM parameters considering two different exposures of DUNE: total run-time of 7 years (see second column) and 10 years (see third column) equally divided in neutrino and antineutrino modes.

ters at 90% C.L. for the various long-baseline experimental setups discussed so far. As clear from our previous discussion, the expected constraints on NUNM parameters from DUNE is better than the other two experiments JD and KD (and their combination) except for the parameters $\alpha_{22}$ and $|\alpha_{21}|$, where JD has better sensitivity than DUNE. Finally, in the sixth column of the Table, we give the final constraints on the NUNM parameters by combining the expected results from DUNE and JD+KD setups. As we have anticipated, the bounds experience a general improvements by $\sim$ 20%, with the precise magnitude depending on the parameter under consideration. For a comparison with the ongoing long-baseline experiments, we also add the expected constraints from the combination of the T2K and NO$\nu$A setup in the last column. For T2K, we consider a total exposure of 84.4 kt-MW-yrs with 22.5 kt detector mass, 750 kW proton beam power, 5 years run-time (2.5 years each for neutrino and antineutrino mode). For NO$\nu$A, the considered exposure is 58.8 kt-MW-yrs with 14 kt detector mass, 700 kW proton beam power, and 6 years for total run-time (3 years each for neutrino and antineutrino modes). Also, due to the limited statistics, we observe that the expected constraints from T2K+NO$\nu$A setup is worse than the DUNE or JD+KD setup.

Note that the if some information coming from Near Detector measurements (e.g. the initial neutrino flux) are used to analyze Far Detector data, constraints on $\alpha_{22}$ and $\alpha_{11}$ could be deteriorated (see Sec. 5.3.2). However, our approach in which the far detector data alone are considered, is in principle valid also for the diagonal parameters $\alpha_{11}$ and $\alpha_{22}$ if the initial fluxes of both experiments can be determined without relying on the ND data. For instance, theoretical data and simulations could be used to predict the neutrino flux. Moreover, as it happened for the flux determination at MINOS/MINOS+, one could obtain the neutrino flux using only hadronic data, which are not affected by oscillations [622]. In such cases, the systematic uncertainties used in our simulations may be too optimistic. Nevertheless, we verified that for $\alpha_{22}$ and $\alpha_{11}$ our bounds are mostly dictated by systematics; hence, for example, a doubling of the systematics will roughly cause a doubling of the upper limits. We compare now our results summarized in Table 5.7 with the bounds reported in Table 5.4[10]. We observe that the bound we achieve from the DUNE+JD+KD (DUNE+T2HKK) setup for the diagonal $\alpha_{11}$ is $\sim$80% better than the bound quoted in Ref. [551]. In the $\alpha_{22}$ case, the two results are comparable, with a slightly better limit when the global neutrino data analysis is performed. For the remaining diagonal parameter $\alpha_{33}$, NC data from MINOS/MINOS+ give a 60% stronger bound [551] compared to the one expected from the DUNE+JD+KD setup. As for $\alpha_{21}$, the authors of the Ref. [551] make use of the triangular inequality as well as the data from the short-baseline experiments; this allows to constrain the mentioned parameter very tightly. However, due to the large statistics and good systematics of DUNE and JD+KD setups, we can achieve an almost similar bound

[10]In order to get their results, the authors of Ref. [253] left free the standard oscillation parameters $\theta_{23}$, $\delta_{\rm CP}$, and $\Delta m^2_{31}$ and the NUNM parameters $\alpha_{11}$, $\alpha_{21}$, $\alpha_{22}$. Conversely, in our work we marginalize over $\delta_{\rm CP}$ and $\theta_{23}$ only, but we have checked that the marginalization over $\Delta m^2_{31}$ does not have any significant impact.

| Parameter | Other $\alpha_{ij}$'s zero | Other $\alpha_{ij}$'s free |
|---|---|---|
| $\alpha_{11}$ | [-0.017, 0.017] | [-0.02, 0.02] |
| $\alpha_{22}$ | [-0.006, 0.006] | [-0.006, 0.006] |
| $\alpha_{33}$ | [-0.20, 0.17] | [-0.35, 0.33] |
| $\lvert\alpha_{21}\rvert$ | $< 0.012$ | $< 0.017$ |
| $\lvert\alpha_{31}\rvert$ | $< 0.11$ | $< 0.18$ |
| $\lvert\alpha_{32}\rvert$ | $< 0.27$ | $< 0.40$ |

Table 5.9: 90% C.L.(1 d.o.f.) limits on various NUNM parameters. Second column shows the constraints considering only one NUNM parameter at a time, while other NUNM parameters are assumed to be zero in the fit. Third column depicts the bounds on a given NUNM parameter when all other NUNM parameters and the phases associated with the off-diagonal parameters are kept free in the fit. True values of the standard oscillation parameters are taken from Table 5.2. We marginalize over $\theta_{23}$ and $\delta_{\rm CP}$ in the fit (see text for details).

without using any external hypothesis on the relations between the $\alpha_{ij}$. On the other hand, constraints on $\alpha_{31}$ and $\alpha_{32}$ in Table 5.4 are substantially better than the ones we obtain from DUNE+JD+KD setup. Also, in these cases, the triangular inequalities which link them to the diagonal NUNM parameters play an important role, together with the short-baseline experiments limits on the $\nu_\tau$ appearance. However, it is important to stress that all our results are obtained in a complete model independent fashion, relying only on the expected data from DUNE and T2HKK. We checked that for our best setup, namely DUNE+T2HKK, the only bound which would benefit using the inequalities in a considerable way is the $|\alpha_{32}|$, but only if the near detector normalization is not taken into account. The poor limits obtained for $\alpha_{33}$ and the already strong ones for $|\alpha_{21}|$ do not allow improvements for the other parameter's bounds.

As already pointed out in the previous subsection in the context of the CP coverage, the DUNE collaboration [574] exploited the possibility of increasing the exposure of the experiment from 336 kt-MW-yrs to 480 kt-MW-yrs (corresponding to an increase of the data taking time from 7 years to 10 years with 5 years in neutrino mode and 5 years in antineutrino mode). In Table 5.8, we compare our previous constraints from the DUNE experiment, Table 5.7, with those obtained in the $(5+5)$ years configuration. We observe that the constraints on all six NUNM parameters improve by small amount except for $|\alpha_{21}|$, which shows a significant improvement. This happens because the higher run-time increases statistics of the $\nu_\mu \to \nu_e$ appearance channel, which is the one driving the $\alpha_{21}$ sensitivity. On the other hand, the $\nu_\mu \to \nu_\mu$ disappearance channel is almost already saturated by systematics after 3.5 years + 3.5 years of running. This leads to only small improvements on the other NUNM parameters sensitivities.

For sake of completeness, we show in Tab. 5.9 the limits that the combination of DUNE, JD and KD would be able to put if a full marginalization over the NUNM parameter space is performed. It is clear that the three most constrained parameters $\alpha_{11}$, $\alpha_{22}$ and $|\alpha_{21}|$ do not suffer much the marginalization, while the bounds on the other three are considerably worsened. This happens because in $\nu_\mu$ disappearance and $\nu_e$ appearance channels, $|\alpha_{31}|$, $|\alpha_{32}|$ and $\alpha_{33}$ often appear multiplied to other NUNM parameters.

Our discussion on the Non-Unitarity has a very important outcome: DUNE and T2HK, in this context, have very different performances: T2HK can put stringent bounds, due to the higher statistics, to the parameters which affect the most the probabilities, namely $\alpha_{22}$ and $|\alpha_{21}|$. On the other hand, DUNE, should be able to bound the other parameters due to the matter effects. This means that with the combination of the two experiments dataset, we may be able for the first time a full model independent set of bounds on all the NUNM parameters.

### 5.3.2 NUNM and the Near Detectors

Near detectors (ND), as already widely discussed in Ch. 4 are a fundamental component for long-baseline neutrino experiments. Indeed, a detector placed very close to the beam source (from hundreds of meters to a few kilometers) is able to monitor the neutrino beam, measuring the flavor composition, and the total number of neutrinos emitted from the source. Near detectors are not expected to improve any of the standard oscillation parameter measurements, since at such short distances, oscillations do not develop for neutrinos with energies in the GeV range. However, in some new physics scenarios, in which, oscillation probabilities contain zero-distance terms, near detectors can be used to constrain non-standard parameters in a very straightforward way. This is the case of the non-unitarity framework under discussion where, as already pointed out, at vanishing distances we have zero-distance terms in case $\nu_\mu \to \nu_e$ appearance channel: $P_{\mu e}^{L=0} \sim |\alpha_{21}|^2$, and $\nu_\mu \to \nu_\mu$ disappearance channel: $P_{\mu\mu}^{L=0} \sim 1 + 2|\alpha_{21}|^2 + 6\alpha_{22}^2 + 4\alpha_{22}$ . Thus, we can expect that T2HKK and DUNE near detectors would be able to constrain two parameters $|\alpha_{21}|$ and $\alpha_{22}$ from $\nu_\mu \to \nu_e$ appearance and $\nu_\mu \to \nu_\mu$ disappearance channel, respectively, but also $\alpha_{11}$ considering the $\nu_e$ beam contamination, since it can be showed that [18]

$$P_{ee}^{L=0} \sim 1 + 4\alpha_{11} + 6\alpha_{11}^2 \,. \tag{5.40}$$

So, in this section, we analytically infer the order of magnitude of bounds implied by ND measurements. Let us consider the total number of events of a given channel as [20]:

$$N = N_0 P_{\alpha\beta}(\alpha_{ij}) \,, \tag{5.41}$$

where, the normalization factor $N_0$ includes all the detector properties. For an oscillation channel $\nu_\alpha \to \nu_\beta$, $N_0$ can be defined as (see Ch. 5.1):

$$N_0 \;=\; \int_{E_\nu} dE_\nu \, \sigma_\beta(E_\nu) \, \frac{d\phi_\alpha}{dE_\nu}(E_\nu) \, \varepsilon_\beta(E_\nu) \,, \tag{5.42}$$

where, $\sigma_\beta$ denotes the production cross-section of the $\beta$ lepton, $\varepsilon_\beta$ represents the detector efficiency, and $\phi_\alpha$ stands for the initial neutrino flux of flavor $\alpha$. If we want to put bounds on new physics parameters, we can use a simple $\chi^2$ test with a gaussian $\chi^2$ defined as

$$\chi^2 = \frac{(N_{obs} - N_{fit})^2}{\sigma^2} \,, \tag{5.43}$$

where, $\sigma$ represents the uncertainty on the number of events; in this case, neglecting the backgrounds, we get:

$$\chi^2 = \frac{N_0^2}{\sigma^2} \left[ \delta_{\alpha\beta} - P_{\alpha\beta}(\alpha_{ij}^{fit}) \right]^2 \,. \tag{5.44}$$

For the $\nu_\mu \to \nu_\mu$ disappearance channel, the leading term of the probability is $P_{\mu\mu}^{L=0} = 1 + 4\alpha_{22}$. Therefore, the $\chi^2$ assumes the form:

$$\chi^2 = \frac{16 N_0^2 \alpha_{22}^2}{\sigma^2}. \tag{5.45}$$

At a chosen confidence level, represented by a cut at $\chi_0^2$, it is possible to exclude the region satisfying:

$$|\alpha_{22}| > \frac{\sqrt{\chi_0^2}\sigma}{4N_0}. \tag{5.46}$$

Since the disappearance channel is expected to produce a huge number of events at the near detector, one can consider the uncertainty to be dominated by systematic errors $\sigma_{sys}$. Thus, it

| Expt. | $\alpha_{11}$ | | $\alpha_{22}$ | |
|---|---|---|---|---|
| | w/o norm | w/ norm | w/o norm | w/ norm |
| DUNE | [-0.02, 0.02] | [-0.043, 0.034] | $[-0.014, 0.014]$ | [-0.036, 0.048] |
| JD+KD | $[-0.022, 0.022]$ | [-0.048, 0.040] | $[-0.007, 0.007]$ | [-0.038, 0.050] |
| DUNE+JD+KD | $[-0.017, 0.017]$ | [-0.036, 0.026] | $[-0.006, 0.006]$ | [-0.026, 0.039] |

Table 5.10: 90% C.L. (1 d.o.f.) limits on the NUNM parameters $\alpha_{11}$ and $\alpha_{22}$ for the two setups, DUNE, JD+KD, and combination of them. Second and fourth column correspond to the constraints assuming only far detector. Third and fifth columns correspond to the constraints using the FD and ND correlation (or with normalization factor in the probability).

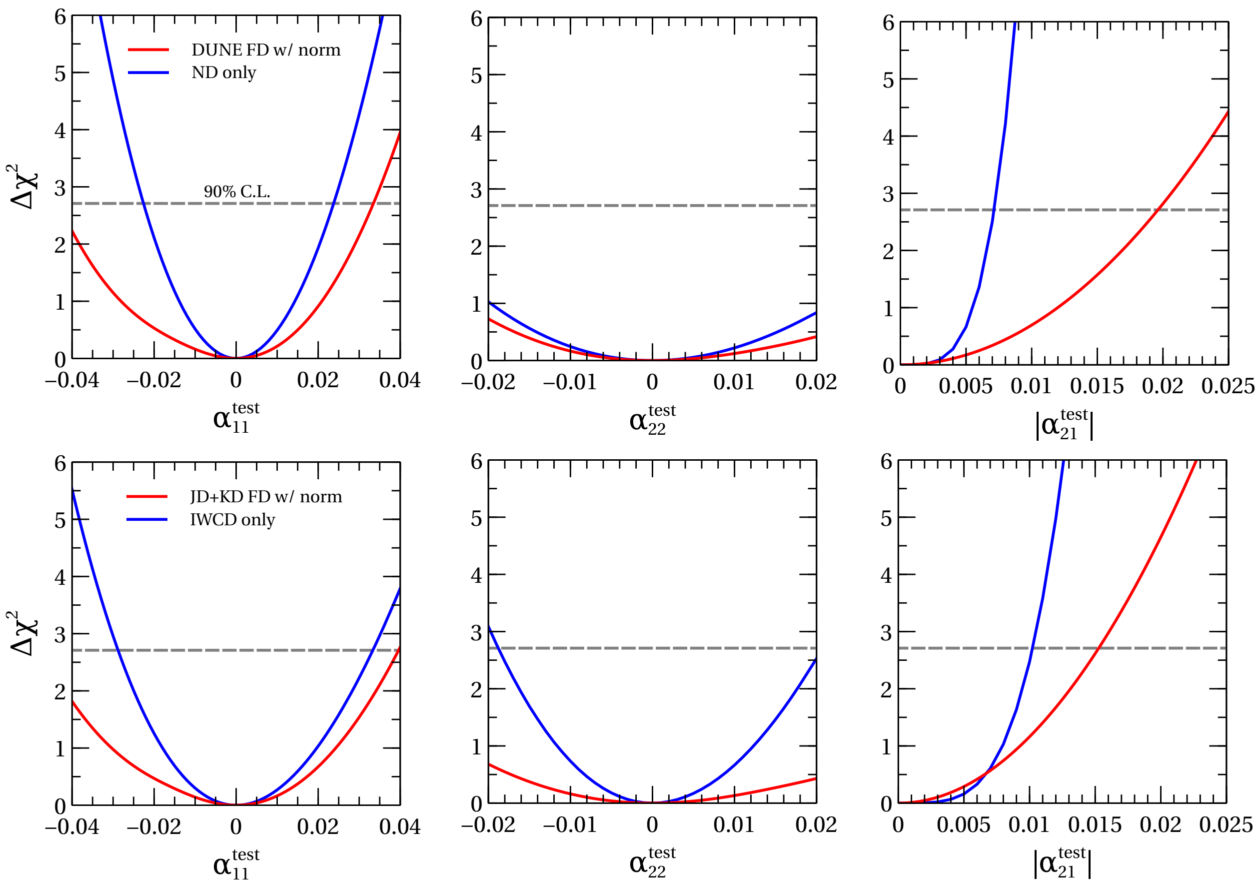


Figure 5.13: Upper panels show the improvements in the sensitivities to $\alpha_{11}$, $\alpha_{22}$, and $|\alpha_{21}|$ due to the presence of 67 tons LArTPC near detector placed at distance of 574 meters from the neutrino source for DUNE. Lower panels portray the same for JD+KD having a 1 kt water Cherenkov near detector placed at a distance of 1 km from J-PARC. The blue curves show the performance with only near detectors. The red curves represent the combined sensitivities due to both near and far detectors. True values of the standard oscillation parameters are taken from Table 5.2. We obtain our resultsamount of non-unitarity is even marginalizing over $\delta_{\rm CP}$ in the range $[-180°, 180°]$ and $\theta_{23}$ in the range $[40°, 50°]$ in the fit. We also marginalize over the associated phase $\phi_{21}$ in the range $[-180°, 180°]$ for the off-diagonal NUNM parameter $|\alpha_{21}|$.

is possible to approximate $\sigma \sim N_0\sigma_{sys}$, where $N_0$ represents the number of events in absence of zero-distance effects, being the disappearance probability in that case equal to 1. This allows to simplify eq. (5.46) as follows:

$$|\alpha_{22}| > \frac{\sqrt{\chi_0^2}\sigma_{sys}}{4}\,, \tag{5.47}$$

which tells us that, neglecting backgrounds effects, the near detector limits would be of the order of the chosen systematic uncertainty. A similar approach can be used for the $\nu_e \to \nu_e$ oscillation channel, which arises from the $\nu_e$ beam contamination, obtaining an inequality for $|\alpha_{11}|$ of the similar form:

$$|\alpha_{11}| > \frac{\sqrt{\chi_0^2}\sigma_{sys}^{\nu_e}}{4}\,, \tag{5.48}$$

where $\sigma_{sys}^{\nu_e}$ refers to the systematic uncertainty on the $\nu_e \to \nu_e$ transition.
For the appearance channel, the zero-distance probability reads $P_{\mu e}^{L=0} = |\alpha_{21}|^2$; the $\chi^2$ function can therefore be written as:

$$\chi^2 = \frac{N_0^2|\alpha_{21}|^4}{\sigma^2}\,, \tag{5.49}$$

and the excluded region is expected to be determined by the following relation:

$$|\alpha_{21}| < \sqrt[4]{\frac{\chi_0^2\sigma^2}{N_0^2}}\,. \tag{5.50}$$

Since the number of events at the near detector is in principle very small (being only caused by new physics), the uncertainty is dominated by statistics. Thus, given a certain number of observed events, $\sigma \sim \sqrt{N_{obs}}$ and the excluded values of $|\alpha_{21}|$ reduced to:

$$|\alpha_{21}| < \sqrt[4]{\frac{\chi_0^2 N_{obs}}{N_0^2}}\,, \tag{5.51}$$

suggesting that the bounds are very sensitive to the number of events and to the running time of the experiment.

Both DUNE and T2HKK, as discussed previously, will have near detectors [157, 623, 624] which may play a crucial role to probe various new physics scenarios including the possibility of non-unitarity of the PMNS matrix which is the main thrust of this work. In our analysis, for DUNE, we consider a 67 tons LArTPC near detector placed at a baseline of 574 meters from Fermilab [157]. For JD+KD, we consider a 1 kt water Cherenkov near detector located at a baseline of 1 km from J-PARC which is known as IWCD [625, 626]. In order to simulate their responses, we scale the far detector fluxes for ND baselines and take into account their fiducial masses. We follow a very conservative approach as far as the systematic uncertainties at the near detectors are concerned. We multiply the FD systematic uncertainties by a factor of three and consider them as inputs for the ND. In DUNE near detector, we expect $\mathcal{O}(10^7)$ $\nu_\mu$ and $\bar{\nu}_\mu$ events, which provide bounds on $\alpha_{22}$. DUNE can place stringent constraints on $\alpha_{11}$ and $\alpha_{21}$ using $\mathcal{O}(10^6)$ $\nu_e$ and $\bar{\nu}_e$ events at ND, which stem from both intrinsic $\nu_e$ ($\bar{\nu}_e$) beam contamination and via $\nu_\mu \to \nu_e$ ($\bar{\nu}_\mu \to \bar{\nu}_e$) appearance caused due to zero-distance effect. For the NDs, we consider their appropriate baselines, fiducial masses, and systematic uncertainties which we assume to be larger than the systematic uncertainties considered for the FDs.

Before discussing the limits that the Near Detectors could be able to set using their own data, we want to quantify the effect of the ND flux measurements on the Far Detector constraints. Indeed, if the initial neutrino flux is monitored at the near site and then extrapolated to the far site, the probability which could be inferred at the FD is the effective probability defined as

$$P_{\alpha\beta}^{\text{eff}} = \frac{P_{\alpha\beta}}{P_{\alpha\alpha}^{L=0}}. \tag{5.52}$$

| Parameter | DUNE (ND) | DUNE (FD+ND) | JD+KD (IWCD) | JD+KD (FD+IWCD) |
|---|---|---|---|---|
| $\alpha_{11}$ | [-0.020, 0.024] | [-0.043, 0.034] | [-0.029, 0.033] | [-0.048, 0.040] |
| $\alpha_{22}$ | [-0.033, 0.037] | [-0.036, 0.048] | [-0.019, 0.020] | [-0.038, 0.050] |
| $\|\alpha_{21}\|$ | $< 0.007$ | $< 0.022$ | $< 0.01$ | $< 0.015$ |

Table 5.11: 90% C.L. (1 d.o.f.) bounds on the NUNM parameters $\alpha_{11}$, $\alpha_{22}$, and $|\alpha_{21}|$ obtained with and without near detectors in DUNE and JD+KD. Note that IWCD is the near detector for JD+KD setup.

The $P_{\alpha\alpha}^{L=0}$ term that appears in the denominator is the initial flavor neutrino survival probability at the source or the zero-distance term which acts as a normalization factor. If we normalize the $\nu_\mu \to \nu_\mu$ survival probability at the far detector using the zero-distance term in eq. (5.37), it is observed that the contribution from $\alpha_{22}$ gets canceled at the leading order. As a result, sensitivity to the parameter $\alpha_{22}$ is worsened for a given setup. The same happens for $\alpha_{11}$, whose contribution in the effective $\nu_e \to \nu_e$ disappearance probability is canceled at the leading order (see [18]). Since the sensitivity to such parameter arises partially due to the intrinsic $\nu_e$ that we have in the beam to begin with, the near detector normalization causes a deterioration of $\alpha_{11}$ limits. In Table 5.10, we show how the constraints on $\alpha_{11}$ and $\alpha_{22}$ would be modified when taking into account the FD and ND correlation for the three setups DUNE, JD+KD, and DUNE+JD+KD. We observe that the bound on $\alpha_{11}$ is increased by a factor of almost two when we consider the correlation between the FD and ND. For $\alpha_{22}$, the bound is deteriorated at least three times compared to the FD case only. We have checked that no other NUNM parameter is affected significantly if we consider the FD and ND correlation. Indeed, the non-diagonal parameters and $\alpha_{33}$ can be constrained using appearance channels (for which we do not have full cancellations in the effective probabilities) or using the interplay with matter effects, which are not developed at the near site.

The bounds obtained using the above-mentioned near detectors are shown in Fig. 5.13 for DUNE and T2HKK together with the results we got using the far detectors data with effective probabilities. For $\alpha_{11}$, the two near detectors can put by themselves bounds better than the one set by the FDs considering the ND normalizations due to the very high statistics and the strong $\alpha_{11}$ dependence of the zero-distance probability. The improvement is roughly a factor of two for DUNE and 60% for T2HKK (see Table 5.11). Note that the obtained limits are in agreement with the predictions deduced from eq. (5.48), once we insert a normalization uncertainty of 6% (15%) for DUNE (JD+KD).

For the second diagonal parameter $\alpha_{22}$ we can observe a similar situation, in which the ND alone can put more stringent bounds than the Far Detector when the normalization is considered, despite of the increased systematics. The improvement can be quantified as rougly 25% in DUNE and a factor of two in T2HKK. Once again, the analytical predictions from eq. (5.48) are sufficiently recovered by the numerical simulations, considering that the near detectors normalization systematics are 15% for DUNE and 10.5% for T2HKK. Notice that the bounds that the far detector alone could set if the near detector data are not taken into account would be considerably better than the near detector ones.

Finally, for the NUNM parameter $|\alpha_{21}|$ the near detectors bounds are considerably better than the far detector ones, thanks to the zero-distance effect outlined in eq. (5.34). In particular, the limits are $\sim 3$ times smaller than the one set by the far detector in the DUNE facility and $\sim 70\%$ smaller in the case of T2HKK. Considering a number of observed events of $\mathcal{O}(10)$, and taking into account that we expect $N_0 \sim 10^6$ per year [157], our analytic estimate for $|\alpha_{21}|$ is comparable with the numerical results.

### 5.3.3 NUNM and $\nu_\tau$ appearance in DUNE

It has been recently pointed out the possibility of collecting a $\nu_\tau$ sample at the DUNE experiment, considering that the high energy tail of the neutrino flux should overcome the $\tau$ lepton production threshold. In presence of Non-Unitarity, also the $\nu_\tau$ appearance probability is modified. In particular we have that, using the expansion already described in this section, the probability reads

$$
\begin{aligned}
P_{\mu\tau} \;=\;& \sin^2\Delta_{31}\left(1+2\alpha_{22}+2\alpha_{33}-4a^2+\alpha_{22}^2+\alpha_{33}^2+4\alpha_{22}\alpha_{33}\right)+\\
& |\alpha_{32}|\sin 2\Delta_{13}\left[2\Delta_n\cos\phi_{32}-\sin\phi_{32}\right]+\\
& \left(\frac{r^2}{\Delta_{31}}\right)\sin(\Delta_{31})\left[2\Delta_{31}\Delta_e\cos\Delta_{31}-\sin\Delta_{31}(\Delta_{31}+2\Delta_e)\right]+\\
& \left(\frac{2}{\Delta_{31}}\right)\left(|\alpha_{21}|^2+|\alpha_{31}|^2\right)\Delta_n\sin\Delta_{31}\left[\sin\Delta_{31}-\Delta_{31}\cos\Delta_{31}\right]+\\
& \left(\frac{|\alpha_{32}|^2}{\Delta_{31}}\right)\left[\Delta_n\sin 2\phi_{32}(\sin 2\Delta_{31}-2\Delta_{31}\cos 2\Delta_{31})+\Delta_{31}\cos^2\Delta_{13}\right]+\\
& \left(\frac{2|\alpha_{21}|r}{\Delta_{31}}\right)\sin\Delta_{31}\left[\sin\Delta_{31}\cos(\delta_{\rm CP}-\phi_{21})(\Delta_{31}+\Delta_e-\Delta_n)-\Delta_{31}\Delta_e\cos(\delta_{\rm CP}+\Delta_{31}-\phi_{21})+\right.\\
& \qquad\left.\Delta_{31}\Delta_n\cos(\delta_{\rm CP}-\Delta_{31}-\phi_{21})\right]+\\
& \left(\frac{2|\alpha_{31}|r}{\Delta_{31}}\right)\left[\sin\Delta_{31}(\sin\Delta_{31}\cos(\delta_{\rm CP}-\phi_{31})(\Delta_{31}+\Delta_e-\Delta_n)-\Delta_{31}\Delta_e\cos(\delta_{\rm CP}-\Delta_{31}-\phi_{31})+\right.\\
& \left.\Delta_{31}\Delta_n\cos(\delta_{\rm CP}+\Delta_{31}-\phi_{31})\right]+\left(\frac{8a}{\Delta_{31}}\right)(\alpha_{22}-\alpha_{33})\,\Delta_n\sin\Delta_{31}(\Delta_{31}\cos\Delta_{31}-\sin\Delta_{31})+\\
& 4a|\alpha_{32}|\sin^2\Delta_{31}\cos\phi_{32}+\\
& \left(\frac{2|\alpha_{21}||\alpha_{31}|}{\Delta_{31}}\right)\sin\Delta_{31}\left[2\Delta_{31}(\Delta_e+\Delta_n)\cos(\Delta_{31}-\phi_{21}+\phi_{31})+2\Delta_n\sin\Delta_{31}\cos(\phi_{21}-\phi_{31})-\right.\\
& \left.\Delta_{31}\sin(\Delta_{31}-\phi_{21}+\phi_{31})\right]+\\
& 4\alpha_{22}|\alpha_{32}|\sin\Delta_{31}\left(\frac{\Delta_n\cos\phi_{32}(\sin\Delta_{31}+2\Delta_{31}\cos\Delta_{31})}{\Delta_{31}}-\cos\Delta_{31}\sin\phi_{32}\right)+\\
& -\left(\frac{2|\alpha_{32}|\alpha_{33}}{\Delta_{31}}\right)\sin\Delta_{31}\left[2\Delta_n\cos\phi_{32}(\sin\Delta_{31}-3\Delta_{31}\cos\Delta_{31})+\Delta_{31}\cos\Delta_{31}\sin\phi_{32}\right]\,. \qquad (5.53)
\end{aligned}
$$

This rather complicated equation, depends at the leading order, without the matter coupling, on the "third generation" parameters $\alpha_{33}$ and $|\alpha_{32}|$. Since these parameters are only weakly constrained by the DUNE experiment using the $\nu_\mu$ disappearance and the $\nu_e$ appearance channels, we may wonder if the inclusion of the $\nu_\tau$ appearance could improve the already discussed NUNM bounds. In fact, introducing the $\nu_\tau$ channel as discussed in Sec. 4.1.4, we obtain the results shown in Fig. 5.14. It turns out that the allowed range of $\alpha_{33}$, which appears only at the second order in the probability, is reduced of $\sim$ 13% by the inclusion of the new oscillation channel, and the new limits are set into the range [-0.16, 0.15] (see Table 5.12). On the other hand, the sensitivity to $|\alpha_{32}|$, which impacts linearly the $\nu_\tau$ appearance probability, is significantly improved: in this case, the new upper bound is roughly 60% smaller than the one set by the standard oscillation channels, namely $|\alpha_{32}| < 0.19$.

### 5.3.4 NUNM and the $\delta_{CP}$ determination

It is well known that the Non-Unitarity model, as well as most of the BSM models that affects neutrino oscillations, introduces new phases in the probabilities. This can affect the measurement of $\delta_{CP}$. Let us consider, for instance, the $\nu_e$ appearance probability in eq. (5.33). The dominant

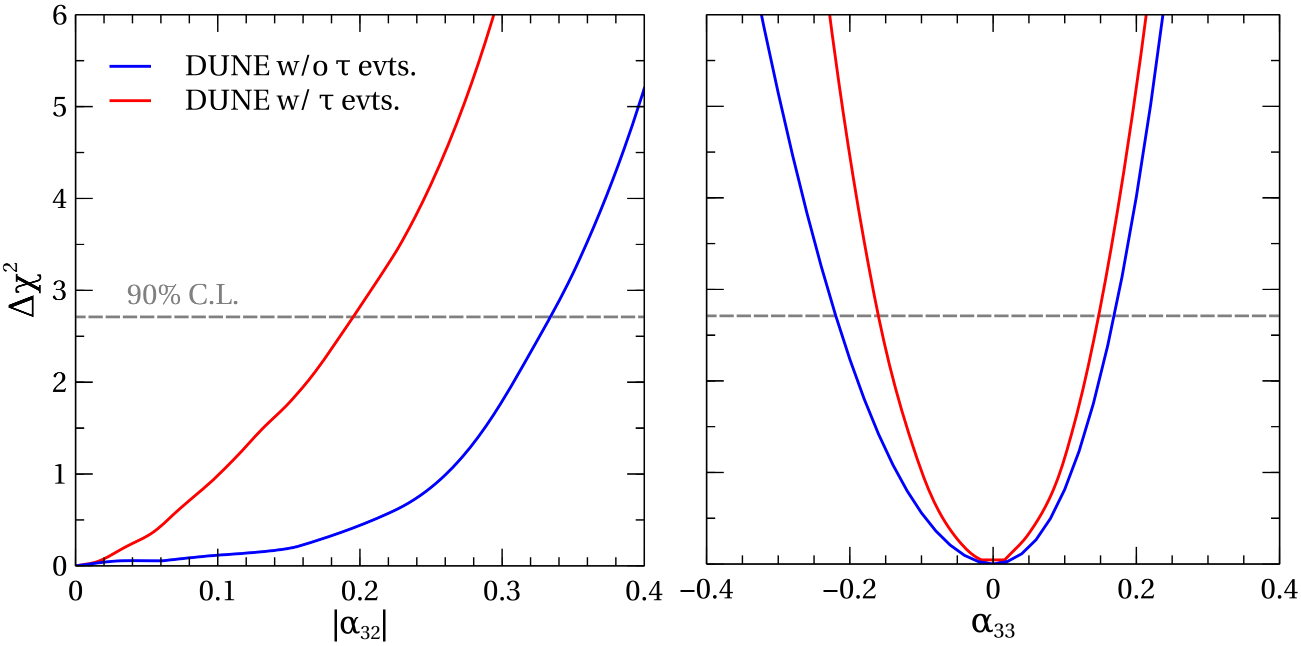


Figure 5.14: Comparison between the DUNE sensitivities on $|\alpha_{32}|$ (left panel) and $\alpha_{33}$ (right panel) when $\nu_\tau$ appearance channel is included in the analysis (red lines) and the case where no $\tau$ events are analyzed (blue lines). True values of the standard oscillation parameters are taken from Table 5.2. All results have been obtained marginalizing over $\delta_{\rm CP}$ in the range $[-180°, 180°]$ and $\theta_{23}$ in the range $[40°, 50°]$. For $|\alpha_{32}|$ (left panel), we also marginalize over $\phi_{32}$ in the range $[-180°, 180°]$.

| Parameter | w/o $\nu_\tau$ appearance | w/ $\nu_\tau$ appearance |
|---|---|---|
| $\alpha_{33}$ | [-0.2, 0.17] | [-0.16, 0.15] |
| $\lvert\alpha_{32}\rvert$ | $< 0.33$ | $< 0.19$ |

Table 5.12: 90% C.L. limits on the NUNM parameters $\alpha_{33}$ and $|\alpha_{32}|$ from the DUNE setup. Second (third) column shows the results without (with) $\tau$ in the analysis.

term which contains a non-standard phase is

$$-2|\alpha_{21}|r\sin\Delta_{31}\sin(\delta_{CP}-\phi_{21}+\Delta_{31}). \tag{5.54}$$

In the hypothesis of a non-vanishing $|\alpha_{21}|$ this term can contribute to the total asymmetry; this contribution will be proportional to $\sin(\delta_{CP}-\phi_{21})$ and for different values of the new phase can affect the sensitivity of a given experiment to $\delta_{CP}$[11]. Not only, this term also changes the precision that an experiment may achieve. If we sit at around the first oscillation maximum, namely $\Delta_{31}=\pi/2+\epsilon$, we can study the derivative of this term, which will give information of its contribution to the reachable uncertainty on the standard CP-violating phase. We obtain, expanding in $\epsilon$ and neglecting $\mathcal{O}(\epsilon^2)$ terms

$$2|\alpha_{21}|r[\epsilon\cos(\delta_{CP}-\phi_{21})-\sin(\delta_{CP}-\phi_{21})]. \tag{5.55}$$

This show us that both modulus and phase of $\alpha_{21}$ affect the precision we can reach with a given experiment. Moreover, it is also clear that the non-standard phase can also be responsible for a shift of the $\delta_{CP}$ value for which we obtain the best precision, namely

$$\bar{\delta}_{CP}=\arctan\epsilon+\phi_{21}+n\pi. \tag{5.56}$$

[11]Notice that this term will affect the probabilities also if we neglect the small $\Delta m^2_{21}$, while the leading term in $\delta_{CP}$ in the standard oscillation framework is always proportional to the small ratio $\Delta m^2_{21}/\Delta m^2_{31}$.

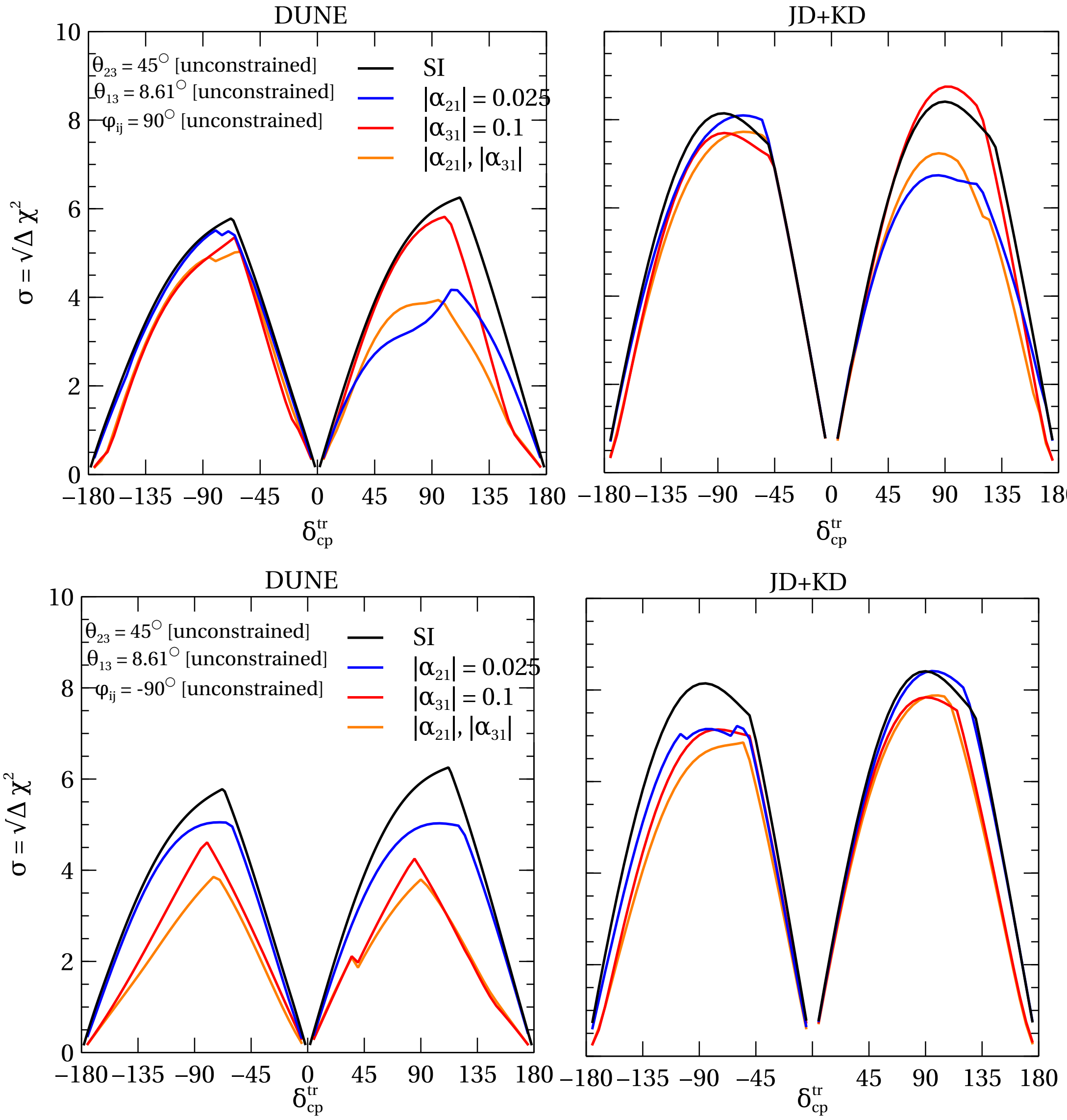


Figure 5.15: $\delta_{CP}$ sensitivity of the DUNE and JD+KD experiments in the standard case (black line) and in presence of NU. In the fit procedure we marginalized over $\theta_{23}$, $\theta_{13}$ and the phase of the NU parameter which was considered to be different from zero. True values for the non-standard phases are 90° (top plots) and −90° (bottom plots)

.

In Fig. 5.15 we show the $\delta_{CP}$ sensitivity at DUNE and T2HKK (JD+KD) when the true values of the new phases (we consider here also $\phi_{31}$) is 90° or 90°. In this analysis we marginalize over $\theta_{23}$, $\theta_{13}$ and the NUNM phases, while we set the new NUNM moduli to $|\alpha_{21}| = 0.025$ and $|\alpha_{31}| = 0.1$. When the true value of the phases are 90° (in particular in the case of $|\alpha_{21}|$), the sensitivities are mostly reduced if the $\delta_{CP}$ true value is positive, while are almost unaffected by new physics if it is negative. The main reason is that when the $\delta_{CP}$ and $\phi_{ij}$ have opposite sign and are maximal, $\sin(\delta_{CP} - \phi_{ij})$ is suppressed, while $\cos(\delta_{CP} - \phi_{ij})$ is maximized but negative. This leads to a reduction in the number of neutrino appearance events due to terms like the one in eq. (5.55).

When on the other hand, the phase true value is −90°, the situation is different. In the DUNE case, the reduction of the sensitivity (25% in the case of $|\alpha_{21}|$ and 30% in the case of $|\alpha_{31}|$) is similar for positive and negative values of the true PMNS phase value. This is due to some terms which appears in the appearance probability only if the solar mass splitting is not neglected,

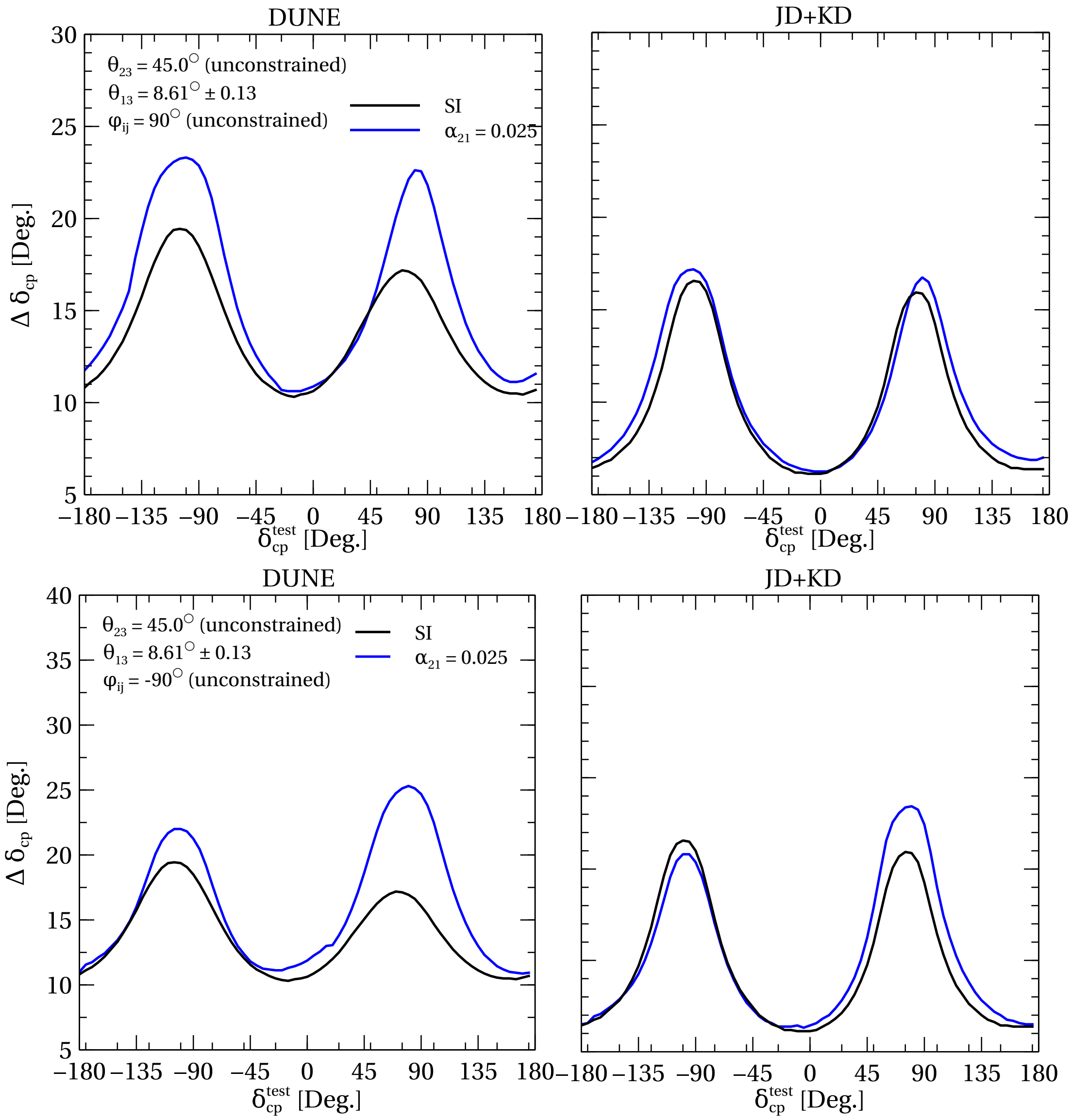


Figure 5.16: $\delta_{CP}$ precision ($1\sigma$) range in the case of standard oscillation and Non-Unitarity. $\theta_{13}$, $\theta_{23}$, and the phases associated with the NUNM parameters are marginalized with the fit. At the top (bottom) panel, true value of the NUNM phases are assumed to be $90°$ ($-90°$) in the simulation.

which are proportional to $\sin \phi_{ij}$ and negative in the case of neutrinos (see for instance Ref. [249]); such terms are responsible to a reduction of the statistics for any value of the true $\delta_{CP}$ phase value. In JD+KD this effect is less visible and the sensitivity results to be reduced of roughly 15% only in the case of positive $\delta_{CP}$ values.
In the context of the precision on the $\delta_{CP}$ measurement, we considered fixed the true values of the phase $\delta_{CP}$ then we fitted the data varying its value in the entire allowed range and eventually we determine the $1\sigma$ uncertainty on the parameter finding the values for which $\Delta\chi^2 = 1$. Since the interval could be asymmetrical, we define

$$\Delta\delta_{CP} = \frac{\delta_{>}^{fit} - \delta_{<}^{fit}}{2} \tag{5.57}$$

where $\delta_{>}^{fit}$ ( $\delta_{<}^{fit}$) is the $\delta_{CP}$ fit value for which $\Delta\chi^2 = 1$ which lies on the right (left) of $\delta_{CP}^{true}$. It is well known [602, 627, 628] that the behaviour of the precision of the phase measurement is the opposite that of the sensitivity. Indeed, the best $\delta_{CP}$ sensitivity is reached when the phase is maximal, while the best $\delta_{CP}$ precision is reached when the phase is CP-conserving. In Fig. 5.16, we show the precision on the $\delta_{CP}$ measurement at DUNE and T2HKK when $|\alpha_{21}| = 0.025$, for $\phi_{21} = 90°, -90°$. According to our analytical prediction of the contribution to the precision due to the leading new physics term, we find that when the new phase is positive, the minimum is shifted to the right, while when negative, it is shifted to the left. Moreover, the precision in this case is worsen of about 20% for DUNE when new physics is present. The worsening is less important for JD+KD, which is more performing also in the NU scenario. The combination of the DUNE and the T2HKK data set has been shown to be able to improve the $\delta_{CP}$ precision in the standard oscillation framework [629]; we expect the same to happen also in presence of BSM phases.

# Chapter 6

# The DUNE experiment: new approaches to the study of BSM models

In this final chapter, we will discuss some new approaches to search for BSM effects in neutrino oscillation at DUNE. In the literature, DUNE simulations have been performed in the context of several BSM models (see references in the next sections). However, its unprecedent experimental features may allow us to develop new strategies to find great limits on the new physics parameters, overcoming the capabilities of the other experiments.

## 6.1 Invisible neutrino decay: the multi-channel analysis

We introduced the invisible decay model in Sec. 3.3. In LBL experiments, it is interesting to consider that the only decaying mass eigenstate is the third one, the heaviest in normal mass ordering (NMO). So far, the terrestrial limits[1] set by current and past LBL experiments are the following [524, 630]

$$\tau_3/m_3 \; > \; 7.8 \times 10^{-13} \text{ s/eV} \;\; (\text{T2K}) \tag{6.1}$$

$$\tau_3/m_3 \; > \; 2.8 \times 10^{-12} \text{ s/eV} \;\; (\text{MINOS}) \tag{6.2}$$

$$\tau_3/m_3 \; > \; 1.5 \times 10^{-12} \text{ s/eV} \;\; (\text{T2K} + \text{NO}\nu\text{A}) \tag{6.3}$$

where $\tau_3$ is the third neutrino lifetime and $m_3$ its mass. On the other hand, a combined analysis of atmospheric and LBL data set the limit [517]

$$\tau_3/m_3 \; > \; 9.3 \times 10^{-12} \text{ s/eV} \;\; (\text{SK} + \text{K2K} + \text{MINOS})\,. \tag{6.4}$$

In the context of the DUNE experiment, the expected bound using the standard analysis based on the $\nu_\mu$ disappearance and $\nu_e$ appearance channels with a 5+5 years exposure is [631]

$$\tau_3/m_3 \; > \; 4.5 \times 10^{-11} \text{ s/eV} \;\; \text{DUNE}\,. \tag{6.5}$$

while other bounds that may be obtained by future experiments can be found in [632–635].
As discussed, in the invisible decay model, a sterile neutrino is involved, but in this case we consider the hypothesis in which this fourth sterile state does not mix with the active states. Thus we can neglect the sterile sector and the Hamiltonian is simply [636]:

$$H = U \left[ \frac{1}{2E} \begin{pmatrix} 0 & 0 & 0 \\ 0 & \Delta m^2_{21} & 0 \\ 0 & 0 & \Delta m^2_{31} \end{pmatrix} - i \frac{1}{2\beta_3 E} \begin{pmatrix} 0 & 0 & 0 \\ 0 & 0 & 0 \\ 0 & 0 & 1 \end{pmatrix} \right] U^\dagger + \begin{pmatrix} A & 0 & 0 \\ 0 & 0 & 0 \\ 0 & 0 & 0 \end{pmatrix} \,, \tag{6.6}$$

[1] For cosmological bounds, see [262, 525–534].

where $\beta_3 = \tau_3/m_3$ and the term $A = 2\sqrt{2}G_F n_e E$ is the neutrino electron scattering in matter, $G_F$ is the Fermi constant, $E$ the energy of the neutrino, and $n_e$ the electron density.

In a long baseline experiment, the impact of the matter potential on the oscillation probabilities depends on the $L/E$ ratio. In the case of a matter density of 4 $g/cm^3$, the comparison of the energy behavior of the oscillation probabilities with and without matter effects (in the standard case of stable neutrinos) for an approximately 1300 km baseline shows the largest difference in the $\nu_e$ appearance probability, where the vacuum case can be roughly 9% smaller for energies around 2 GeV. However, the related effect on the number of events is not so relevant since the integral of the probability between 0.2 and 15 GeV is only 5% bigger in the matter than in the vacuum case; this difference does not change much even when $\beta_3 < \infty$. For this reason, throughout the rest of the paper, matter effects will not be taken into account in the numerical simulations of the rates in DUNE.

We now derive the oscillation probabilities in the case of unstable $\nu_3$ eigenstate. If $\lambda_i$ are the eigenvalues of the Hamiltonian matrix and S is the diagonalizing matrix, the transition amplitude can be obtained in the following way:

$$\langle \nu_\beta | \nu_\alpha \rangle = \sum_i S_{\beta i} S^{-1}_{i\alpha} e^{-i\lambda_i L}\,, \tag{6.7}$$

where $L$ is the distance travelled by the neutrino after its creation. Notice that the hamiltonian $H$ in Eq.(6.6) is non-Hermitian, thus the inverse of S must appear in the amplitude. The expression of the resulting transition probabilities are quite cumbersome, thus we prefer to present the $\nu_\mu \to \nu_f$ oscillation formulae (with $f = e, \mu, \tau$) expanded up to the second order in the parameter $\alpha = \frac{\Delta m^2_{21}}{2E} L$. We separate various terms according to the convention $P_{\mu f} = P^{(0)}_{\mu f} + \alpha P^{(1)}_{\mu f} + \alpha^2 P^{(2)}_{\mu f}$, where the superscripts $(0), (1), (2)$ refer to the respective perturbative order. For the sake of simplicity, we quote here the zeroth-order results only, which capture the main effects of the decay; for higher order expansions, see [19]. For the $\nu_\mu \to \nu_e$ transition we obtain:

$$P^{(0)}_{\mu e} = \sin^2 2\theta_{13} \sin^2\theta_{23} \left[ e^{-\frac{1}{\beta_3}\frac{L}{2E}} \sin^2\left(\frac{\Delta m^2_{31} L}{4E}\right) + \left(\frac{1 - e^{-\frac{1}{\beta_3}\frac{L}{2E}}}{2}\right)^2 \right], \tag{6.8}$$

while for the $\nu_\mu \to \nu_\tau$ appearance we get:

$$P^{(0)}_{\mu\tau} = \cos^4\theta_{13} \sin^2 2\theta_{23} \left[ e^{-\frac{1}{\beta_3}\frac{L}{2E}} \sin^2\left(\frac{\Delta m^2_{31} L}{4E}\right) + \left(\frac{1 - e^{-\frac{1}{\beta_3}\frac{L}{2E}}}{2}\right)^2 \right]. \tag{6.9}$$

Finally, for $\nu_\mu$ disappearance our result reads:

$$\begin{aligned} P^{(0)}_{\mu\mu} =& 1 + 2\left(e^{-\frac{1}{\beta_3}\frac{L}{2E}} - 1\right)\cos^2\theta_{13}\sin^2\theta_{23} + \left(e^{-\frac{1}{\beta_3}\frac{L}{2E}} - 1\right)^2 \cos^4\theta_{13}\sin^4\theta_{23} \\ & - e^{-\frac{1}{\beta_3}\frac{L}{2E}} \left(\cos^4\theta_{13}\sin^2 2\theta_{23} + \sin^2 2\theta_{13}\sin^2\theta_{23}\right) \sin^2\left(\frac{\Delta m^2_{31} L}{4E}\right). \end{aligned} \tag{6.10}$$

We see that the decay parameter has two main roles. On the one hand, it acts as a damping factor, reducing the amplitudes by the quantity $e^{-\frac{1}{\beta_3}\frac{L}{2E}}$. On the other hand, it adds to the probabilities constant terms (i.e., not depending on the mixing angles) that contain the factor $\left(1 - e^{-\frac{1}{\beta_3}\frac{L}{2E}}\right)$. Thus, for small values of the decay parameters, we expect the appearance probabilities no longer to depend on the ratio $L/E$ and to converge to a fixed value (1/4 for both $\nu_\mu \to \nu_e$ and $\nu_\mu \to \nu_\tau$ transitions). In the disappearance channel we observe again the same behaviour for small $\beta_3$ although the constant limiting value is approximated by $P^{(0)}_{\mu\mu} = (1 - \cos^2\theta_{13}\sin^2\theta_{23})^2 \sim 0.21$. The explanation of this effect resides on the fact that, if the decay parameter is small, all neutrinos in the third mass eigenstate decay before reaching the far detector and since at leading order we are neglecting the mass difference between $\nu_1$ and $\nu_2$, the three neutrinos are no longer affected by oscillations. We finally observe that, since the effect of decay is encoded in the damping factor which is common for every transition, all oscillation channels will be equally sensitive to the decay parameter. Thus a collection of events in each channel can be very powerful in constraining $\beta_3$.

Notice that, in the presence of neutrino decay, Eqs. (6.8), (6.9) and (6.10) imply:

$$\sum_{\alpha}^{e,\mu,\tau} P_{\mu\alpha} = 1 + (e^{-\frac{1}{\beta_3}\frac{L}{E}} - 1)\cos^2\theta_{13}\sin^2\theta_{23} \neq 1\,; \tag{6.11}$$

indeed, if $\nu_3$ can decay into a sterile neutrino during its travel, the total number of active neutrinos will decrease when the distance travelled by the particles increases. So we expect that the total number of active neutrinos will decay exponentially from the maximum, obtained when we are close to the neutrino source (small $L$), to an asymptotic value that depends at the leading order on $\theta_{23}$ and $\theta_{13}$ only.

Plots showing the exact dependence in vacuum of $P_{\mu\alpha}$ on $L/E$ between 0 and 1300 km/GeV are reported in Fig.(6.1) for different values of the decay parameter: $\beta_3 = 10^{-10}$ s/eV (blue dashed line), $5 \times 10^{-11}$ s/eV (green dotted line), $10^{-11}$ s/eV (magenta dot-dashed line) and $2 \times 10^{-12}$ s/eV (yellow densely dotted line). These values have been chosen being of the order of the decay parameter limits set by oscillation experiments as discussed above. For the sake of comparison, we also show with red solid lines the behavior in the absence of decay, that is in the standard three neutrino framework. As it can be seen, the main effect of the decay parameter in the $L/E$ region accessible by long baseline experiments like DUNE is a decrease of the probabilities around the atmospheric peak ($L/E \sim 500$ Km/GeV). This reduction is approximately of 1.5% when $\beta_3 = 10^{-10}$ s/eV, 3% when $\beta_3 = 5 \times 10^{-11}$ s/eV, 15% when $\beta_3 = 10^{-11}$ s/eV and 45% when $\beta_3 = 2\times10^{-12}$ s/eV. The flattening of the probabilities previously discussed can be noticed around the valleys, where on the other hand $P_{\mu e}$ and $P_{\mu\tau}$ increase.

### 6.1.1 The inclusion of the NC channel

| Parameter | Central Value | Relative Uncertainty |
|---|---|---|
| $\theta_{12}$ | 33.82° | 2.3% |
| $\theta_{23}$ | 48.3° | 2.2% |
| $\theta_{13}$ | 8.61° | 1.4% |
| $\delta_{CP}$ | 222° | 13% |
| $\Delta m^2_{21}$ | $7.39\times10^{-5}$ eV$^2$ | 2.8% |
| $\Delta m^2_{31}$ | $2.523\times10^{-3}$ eV$^2$ | 1.3% |

Table 6.1: Best fit value and relative uncertainty of neutrino oscillation parameters used in our simulation from a global fit to neutrino oscillation data [578].

We have already mentioned that in [631] the authors performed a DUNE simulation in presence of invisible neutrino decay using the $\nu_\mu$ disapperance and the $\nu_e$ appearance channels. We observed that also the $\nu_\tau$ appearance depends on the decay parameter. Moreover, also the number of Neutral Current events will depend strongly on $\beta_3$, since in this model the total number of active neutrinos is not conserved. In fact, the number of NC events will be proportional to the $\sum_\alpha P_{\mu\alpha}$, which, as showed in eq. 6.11 depends on the decay parameter. For these reasons, we decided to include in our DUNE analysis both the $\nu_\tau$ appearance and the NC channels, in order to study which may be their impact on the $\beta_3$ sensitivity.
The $\nu_\tau$ channel has been included as described in Sec. 4.1.4, while the NC channel has been defined as in [637], namely with an overall 90% signal detection efficiency; since the backgrounds

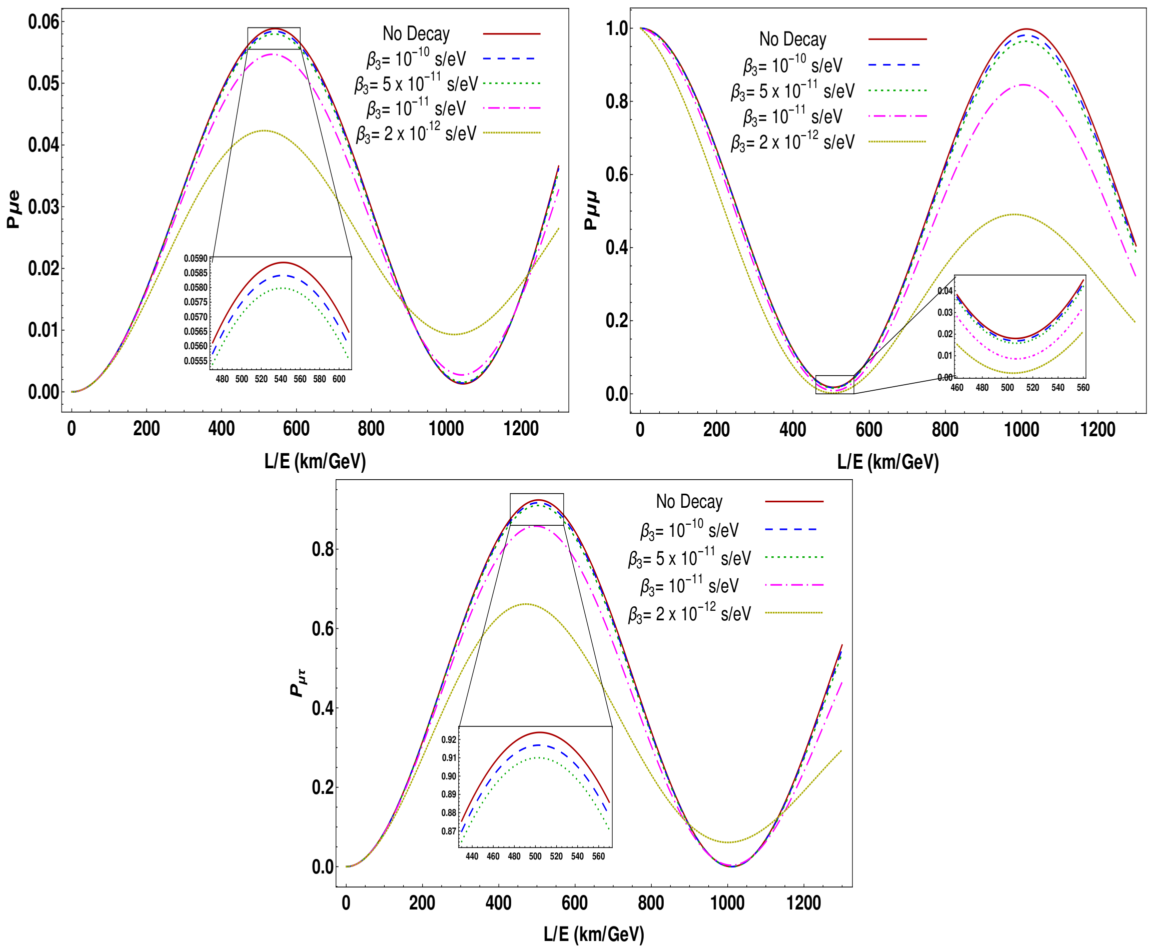


Figure 6.1: Exact $L/E$ dependence in vacuum of $P_{\mu e}$ (top-left panel), $P_{\mu\tau}$ (top-right panel) and $P_{\mu\mu}$ (bottom panel). Different values of the decay parameter are shown: $\beta_3 = 10^{-10}$ s/eV (blue dashed line), $5 \times 10^{-11}$ s/eV (green dotted line), $10^{-11}$ s/eV (magenta dot-dashed line) and $2 \times 10^{-12}$ s/eV (yellow densely dotted line). Red solid lines refers to the behavior of $P_{\mu f}$ in the absence of decay.

come from the mis-identification of charged current events, we add to the background sample a conservative 10% of the $\nu_\mu$ and $\nu_e$ CC events and all the $\nu_\tau$ CC events where the $\tau$ lepton decays hadronically.
In Fig.(6.2) we report our results for the sensitivity to $\beta_3$ when only CC (blue dashed line) and CC+NC events (red solid line) are taken into account. The curves have been obtained with true values of the standard oscillation parameters listed in Tab.(6.1). As fit values, we considered the same central points with their quoted uncertainties. For this analysis we used the full matter Hamiltonian showed in Eq. (5.30).

First of all, we notice that the addition of the NC events will be able to increase the lower bound on $\beta_3$ by roughly 16%. In particular, the lower limit from the CC+NC analysis, $\beta_3 > 5.2 \times 10^{-11}$ s/eV, would be the best world limit set by a single long-baseline experiment. It is worth to mention that the limit set by the CC-only analysis (namely $\beta_3 > 4.4 \times 10^{-11}$ s/eV) is very similar to the one discussed in Ref. [631] where only $\nu_\mu$ disappearance and $\nu_e$ appearance channels (and a longer DUNE running time) were considered. This essentially means that the inclusion of the $\nu_\tau$ events in the analysis provides only a small contribution to the sensitivity, due to the (somehow) limited statistics. This fact can be appreciated in Fig.(6.3), where we split the contributions to the DUNE sensitivity to $\beta_3$ given by the different channels (see the caption for details). We see that the $\nu_\tau$ appearance is sensitive only to very small decay parameters, while the largest contribution comes from the $\nu_\mu \to \nu_\mu$ disappearance channel because, beside

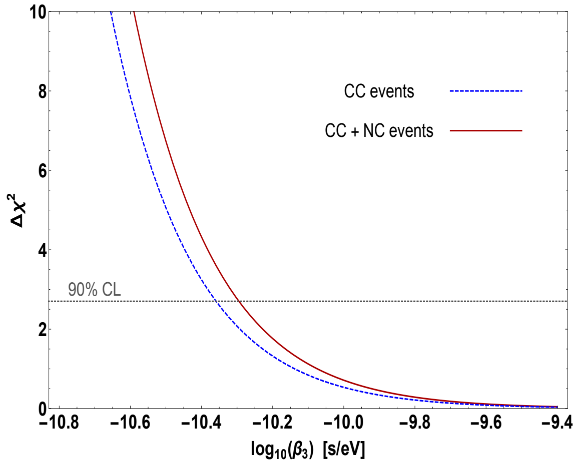


Figure 6.2: DUNE sensitivity to the decay parameter. The blue dashed line has been obtained using only the CC channels, while the red solid one has been obtained adding the NC channel. Here $\Delta\chi^2 = \chi^2 - \chi^2_{min}$.

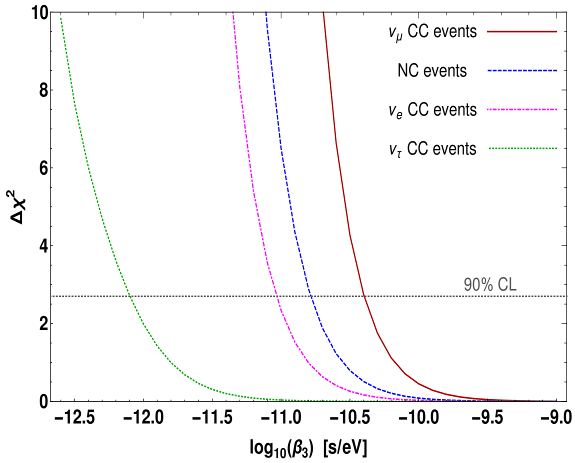


Figure 6.3: Contributions to $\beta_3$ by the different transition channels: red solid line refers to the $\nu_\mu$ CC events, the magenta dot-dashed line to the $\nu_e$ CC events, the green densely-dot-dashed line to the $\nu_e$ CC events while the blue dashed line represents the NC contribution.

providing a larger number of interactions, the variation of the events as $\beta_3$ decrease is larger than in the other channels.

As for a precision measurement of a possibly finite decay parameter, we show in Fig.(6.4) an example in which the true value $\beta_3 = 8.5 \times 10^{-12}\ s/eV$ (best fit obtained by MINOS and T2K data [524]) is assumed; the numerical results highlight that roughly 23% and 20% precision can be achieved, if CC only or CC + NC are considered in the analysis, respectively. Finally, in Tab.(6.2) we collect both the 90% CL bound and the 90% CL error regions that DUNE will be able to set on $\beta_3$. For reference, we also included the results for two more assumptions on the true $\beta_3$ value: $\beta_3 = 1.2 \times 10^{-11}\ s/eV$ (MINOS best fit) and $\beta_3 = 1.6 \times 10^{-12}\ s/eV$ (T2K best fit [524]). We clearly see that the precision we can achieve varies from a maximum of $\sim 30\%$ for $\beta_3 = 1.2 \times 10^{-11}\ s/eV$ to a minimum of $\sim 10\%$ for the smallest $\beta_3$; this is due to the fact that the difference among the values of a given transition probability computed at two different $\beta_3$'s is amplified in the case of small decay parameter.

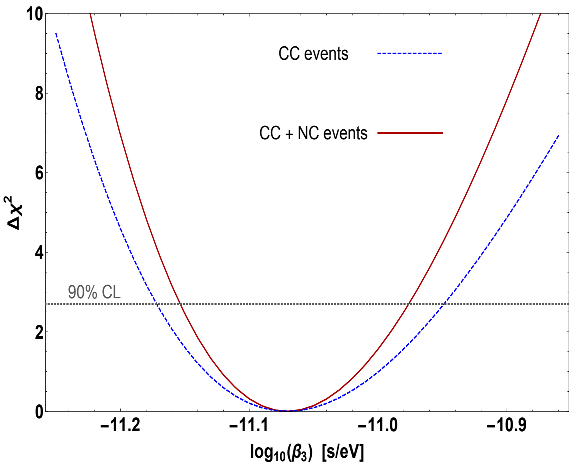


Figure 6.4: $\Delta\chi^2$ as a function of $\beta_3$ obtained with a true value $\beta_3 = 8.5 \times 10^{-12}$ $s/eV$, corresponding to the best fit from MINOS and T2K data analysis [524]. The blue dashed line has been obtained using only the CC channels, while the red solid has been obtained adding the NC channel.

| | ***CC only*** | ***CC+NC*** |
|---|---|---|
| $\beta_3 = \infty$ | $\beta_3 > 4.4 \times 10^{-11}$ s/eV | $\beta_3 > 5.1 \times 10^{-11}$ s/eV |
| $\beta_3 = 1.2 \times 10^{-11}$ s/eV | $\beta_3 \in [0.91 - 1.78] \times 10^{-11}$ s/eV | $\beta_3 \in [0.94 - 1.67] \times 10^{-11}$ s/eV |
| $\beta_3 = 8.5 \times 10^{-12}$ s/eV | $\beta_3 \in [0.65 - 1.12] \times 10^{-11}$ s/eV | $\beta_3 \in [0.70 - 1.05] \times 10^{-11}$ s/eV |
| $\beta_3 = 1.6 \times 10^{-12}$ s/eV | $\beta_3 \in [1.46 - 1.83] \times 10^{-12}$ s/eV | $\beta_3 \in [1.48 - 1.79] \times 10^{-12}$ s/eV |

Table 6.2: 90% CL lower bound ($\beta_3 = \infty$) and ranges on the decay parameter $\beta_3$ that will be set by DUNE when using the CC sample only (second column) or CC+NC events (last column). Several assumptions on a finite $\beta_3$ are reported.

## 6.2 Source and detector NSI: the Near Detector sample

Discussing the source and detector Non Standard Interactions (see Sec. 3.2.1), we pointed out that oscillation experiments, in particular LBL, may not provide the clearest environment where to probe them. Indeed, it is clear that we would need a simultaneous determination of all standard and non standard mixing parameters, including the propagation NSI ones. Selected classes of neutrino experiments, however, have been used to constrain some of the entries of the $\varepsilon^{s,d}$ matrices. This is the case of solar neutrino experiments[2], where 90% confidence level (CL) bounds on $|\varepsilon^d_{ee,\tau\tau}| \sim \mathcal{O}(10^{-1} - 10^{-2})$ [453, 454] are extracted. Also reactor as well as long baseline experiments have been probed to be useful, in particular, to restrict the various $|\varepsilon^{s,d}_{e\alpha}| \sim \mathcal{O}(10^{-2})$ [448, 449]. Although the bounds achieved from non-oscillation experiments on source and detector NSI [236, 455–459] are strong and robust at the level of (generally speaking) percentage, future LBL experiments may improve current oscillation bounds [450–452, 460–465]; in this panorama, DUNE places itself in a relevant position thanks to the capability of improving the NSI bounds, in particular the propagation NSI ones [16, 579, 638–641]. However, as discussed in [642], the DUNE Far Detector (FD) is expected to be less performing in constraining source and detector NSIs. Indeed, the bounds obtained in their analysis with $\varepsilon^m = 0$ and summarized in Tab. 6.3, are just a 10-40% improvement with respect to the existing literature pertinent to long baseline experiments. These constraints are further relaxed when propagation NSI are taken into account into the fit. We can try to (partially) fill the gap, trying to constrain a subset of the $\varepsilon^{s,d}$ matrix elements by means of data that will be collected at the DUNE Near

[2]Notice that the NSI parameters that affect neutrino oscillations are combinations of those entering the Lagrangian describing the interaction processes. We assume here that the quoted bounds directly apply to $\varepsilon^{s,d}$.

| ***Parameter*** | ***DUNE FD 90% CL bounds*** |
|---|---|
| $\lvert\varepsilon^s_{\mu e}\rvert$ | 0.017 |
| $\lvert\varepsilon^s_{\mu\mu}\rvert$ | 0.070 |
| $\lvert\varepsilon^s_{\mu\tau}\rvert$ | 0.009 |
| $\lvert\varepsilon^d_{\mu e}\rvert$ | 0.021 |
| $\lvert\varepsilon^d_{\tau e}\rvert$ | 0.028 |

Table 6.3: 90% CL limits on the source and detector NSI parameters obtained in [642] using the DUNE Far Detector analysis for a total of 10 years of data taking. New phases are unconstrained.

Detector only. Since the ND is not affected by NSI in the same way as the FD [254], we expect on the one side to scrutinize more in details those parameters also accessible at the FD and, on the other hand, to access to a complete new set of parameters on which the DUNE FD is not particularly sensitive. In this context, the role of the ND is promoted as a complementary tool to FD studies [319, 328, 623, 643–648], more than a mere (although important) indicator of fluxes and detection cross sections [649]. It is worth to mention that at the Near Detector, we do not have any flux monitor; for this reason, in order to perform any kind of analysis, we need external inputs like MonteCarlo simulation, theoretical calculations or data from another zero-distance detector whose data are not affected by neutrino oscillation [157, 650, 651].
Let us first discuss the oscillation probabilities at zero distance. The transition probabilities can be simplified to:

$$P_{\alpha\beta} = |[(1+\varepsilon^d)^T(1+\varepsilon^s)^T]_{\beta\alpha}|^2. \tag{6.12}$$

Considering that the oscillation phase $(\Delta m^2_{31}L/4E) \sim \mathcal{O}(10^{-3})$ and the current bounds on $\varepsilon^{s,d}$ are of the order of $10^{-1}-10^{-2}$ [236, 448, 449, 455–459], we expect the approximation in eq.(6.12) to be reliable up to the second order in $\varepsilon$. Parameterizing the new physics complex parameters as $\varepsilon^{s/d}_{\alpha\beta} = |\varepsilon^{s/d}_{\alpha\beta}|e^{i\Phi^{s/d}_{\alpha\beta}}$, the disappearance probabilities ($\alpha=\beta$) read:

$$\begin{aligned}P_{\alpha\alpha} =& 1 + 2|\varepsilon^s_{\alpha\alpha}|\cos\Phi^s_{\alpha\alpha} + 2|\varepsilon^d_{\alpha\alpha}|\cos\Phi^d_{\alpha\alpha} + |\varepsilon^s_{\alpha\alpha}|^2 + |\varepsilon^d_{\alpha\alpha}|^2 + \\ &+ 4|\varepsilon^s_{\alpha\alpha}||\varepsilon^d_{\alpha\alpha}|\cos\Phi^s_{\alpha\alpha}\cos\Phi^d_{\alpha\alpha} + 2\sum_{\beta\neq\alpha}|\varepsilon^s_{\alpha\beta}||\varepsilon^d_{\beta\alpha}|\cos\left(\Phi^s_{\alpha\beta}+\Phi^d_{\beta\alpha}\right),\end{aligned} \tag{6.13}$$

while the appearance probabilities ($\alpha \neq \beta$) are given by:

$$P_{\alpha\beta} = |\varepsilon^s_{\alpha\beta}|^2 + |\varepsilon^d_{\alpha\beta}|^2 + 2|\varepsilon^s_{\alpha\beta}||\varepsilon^d_{\alpha\beta}|\cos\left(\Phi^s_{\alpha\beta} - \Phi^d_{\alpha\beta}\right). \tag{6.14}$$

In the disappearance case, the dependence on the diagonal NSI parameters appears already at the first order and the whole probabilities (including second-order corrections driven by the off-diagonal matrix elements) depend on twelve independent real parameters; in addition, the leading order and the diagonal next-to-leading terms display a complete symmetry under the interchange $s \leftrightarrow d$, so that we expect similar sensitivities to $\varepsilon^{s,d}_{\alpha\alpha}$. The off-diagonal second order corrections are no longer symmetric since two flavor changes are needed to have the same flavor at the source and at the detector.

In the appearance case, the new parameters appear at the second order and only four independent of them are involved. The relevant $P_{\mu e}$ and $P_{\mu\tau}$ are completely symmetric under $s \leftrightarrow d$ because, at short distances, the flavor changing can happen at both source or detector with no fundamental distinction.

The drastic reduction of independent NSI parameters the ND is sensitive to, allows to derive simple rules on how their admitted ranges can be strongly limited compared to the existing literature. Indeed, let us work in the simplified scenario where the experiment counts a certain number $N$ of events when searching for $\nu_\alpha \to \nu_\beta$ oscillations; since the probabilities in eq.(6.12) show no dependence on neutrino energy, baseline, matter potential and standard mixing parameters, $N$ assumes the form:

$$N = N_0 P_{\alpha\beta}(\varepsilon^s, \varepsilon^d)\,, \tag{6.15}$$

where the normalization factor $N_0$ includes all the detector properties and, given an observation mode $\nu_\alpha \to \nu_\beta$, is defined by:

$$N_0^{\alpha\beta} \;=\; \int_{E_\nu} dE_\nu\, \sigma_\beta(E_\nu)\, \frac{d\phi_\alpha}{dE_\nu}(E_\nu)\, \varepsilon_\beta(E_\nu)\,, \tag{6.16}$$

in which $\sigma_\beta$ is the the cross section for producing the lepton $\beta$, $\varepsilon_\beta$ the detector efficiency and $\phi_\alpha$ the initial neutrino flux of flavor $\alpha$. Suppose now that we want to exclude a region of the parameter space using a simple $\chi^2$ function defined as:

$$\chi^2 = \frac{(N_{obs} - N_{fit})^2}{\sigma^2}\,, \tag{6.17}$$

where $\sigma$ represents the statistical uncertainty on the number of events. Assuming vanishing true values of all NSI parameters, the $\chi^2$ function becomes:

$$\chi^2 = \frac{N_0^2}{\sigma^2}[\delta_{\alpha\beta} - P_{\alpha\beta}(\varepsilon^s_{fit}, \varepsilon^d_{fit})]^2\,. \tag{6.18}$$

For appearance analysis, eq.(6.14) allows us to write:

$$\chi^2 = \frac{N_0^2}{\sigma^2}[|\varepsilon^s_{\alpha\beta}|^2 + |\varepsilon^d_{\alpha\beta}|^2 + 2|\varepsilon^s_{\alpha\beta}||\varepsilon^d_{\alpha\beta}|\cos(\Phi^s_{\alpha\beta} - \Phi^d_{\alpha\beta})]^2\,, \tag{6.19}$$

whose minimum can always be found when $\cos\Delta\Phi = -1$. Thus, for every pairs of $(|\varepsilon^s_{\alpha\beta}|, |\varepsilon^d_{\alpha\beta}|)$:

$$\chi^2_{min} = \frac{N_0^2}{\sigma^2}(|\varepsilon^s_{\alpha\beta}| - |\varepsilon^d_{\alpha\beta}|)^4\,. \tag{6.20}$$

Indicating with $\chi^2_{0,\alpha\beta}$ the value corresponding to the cut of the $\chi^2$ at a given CL, we can exclude the region delimited by:

$$||\varepsilon^s_{\alpha\beta}| - |\varepsilon^d_{\alpha\beta}|| > \sqrt[4]{\frac{\chi^2_{0,\alpha\beta}\,\sigma^2}{N_0^2}}\,, \tag{6.21}$$

which is external to a band in the $(|\varepsilon^s_{\alpha\beta}|, |\varepsilon^d_{\alpha\beta}|)$-plane of width

$$\Delta_{\alpha\beta} = \sqrt[4]{\frac{4\chi^2_{0,\alpha\beta}\,\sigma^2}{N_0^2}} \tag{6.22}$$

centered on the line $|\varepsilon^s_{\alpha\beta}| = |\varepsilon^d_{\alpha\beta}|$. Thus, $\Delta_{\alpha\beta}$ provide a measure of the allowed parameter space. Clearly, the excluded region is larger when the uncertainty on the number of events $\sigma$ is smaller and the normalization factor $N_0$ is bigger.

Consider now the disappearance case; neglecting second order terms, the $\chi^2$ function is now:

$$\chi^2 = \frac{4N_0^2}{\sigma^2}(|\varepsilon^s_{\alpha\alpha}|\cos\Phi^s_{\alpha\alpha} + |\varepsilon^d_{\alpha\alpha}|\cos\Phi^d_{\alpha\alpha})^2 = \frac{4N_0^2}{\sigma^2}[\Re(\varepsilon^s_{\alpha\alpha}) + \Re(\varepsilon^d_{\alpha\alpha})]^2\,. \tag{6.23}$$

Following the same procedure as for the appearance case, the excluded region in the $[\Re(\varepsilon^s_{\alpha\alpha}), \Re(\varepsilon^d_{\alpha\alpha})]$-plane is delimited by:

$$|\Re(\varepsilon^s_{\alpha\alpha}) + \Re(\varepsilon^d_{\alpha\alpha})| > \sqrt{\frac{\chi^2_{0,\alpha\alpha}\,\sigma^2}{4N_0^2}}\,, \tag{6.24}$$

where, in this case, the band width is:

$$\Delta_{\alpha\alpha} = \sqrt{\frac{\chi^2_{0,\alpha\alpha}\,\sigma^2}{2N_0^2}} \tag{6.25}$$

with $\chi^2_{0,\alpha\alpha}$ being the desired cut of the $\chi^2$. Notice that, for the same $\sigma$ and $N_0$, we expect the disappearance channels alone to be more performing than the appearance ones. This is essentially motivated by the absence of first order terms in $\varepsilon$ in the appearance probabilities. Notice also that eqs.(6.21) and (6.24) show a perfect symmetry under the interchange of source and detector parameters which, however, could be (partially) disentangled if a multi-channel analysis is performed. For example, the parameter $|\varepsilon^s_{\mu e}|$ appears in the $\nu_\mu \to \nu_e$ oscillation but also as a correction to the $\nu_\mu \to \nu_\mu$ probability, differently from the case of $|\varepsilon^d_{\mu e}|$ which is present in the $\mu \to e$ transition only. Nevertheless, given the relatively small contributions of the second order terms compared to the first order, we expect such corrections to have a negligible impact.

### 6.2.1 The CC Near Detector sample

For the Near Detector simulations, we make the hypothesis that the ND performances are the same as the FD ones. The included channels are the $\nu_e$ and $\nu_\tau$ appearance as well as the $\nu_\mu$ disappearance. The systematics considered in our study will be dominated by cross sections and flux normalization uncertainties. While the former could be in principle improved by future data and calculations, the latter will anyway remain as the dominant source of error because of the hadroproduction processes and uncertainties in the focusing system at the LBNF beam. Differently from similar studies involving the DUNE ND [319, 648][3], where the same systematic uncertainties reported in the DUNE Far Detector GLoBES configuration file have been used, we decided to consider worst systematics since the ND cannot benefit of a (partial) systematic cancellation provided by a detector closer to the neutrino production region. In particular, we took into account an overall systematic normalization uncertainty of 10% for the $\nu_\mu$ disappearance, $\nu_e$ disappearance and $\nu_e$ appearance channels signals and of 25% for the $\nu_\tau$ appearance signal. For the NC background we considered a 15% uncertainty. In our numerical simulations we use exact transition probabilities and we set all NSI true values to zero; we marginalize over all absolute values of the parameters appearing in the probabilities up to the second order (with no priors) and over all relevant phases, which are allowed to vary in the $[0, 2\pi)$ range [4]. Since, as showed in the previous section, the strongest constraints on $\varepsilon^{s,d}_{\alpha\beta}$ can be obtained from the corresponding oscillation probability $P_{\alpha\beta}$, we simulated one transition channel at a time. To make a comparison with the bounds obtainable at the FD (see Tab.(6.3)) we consider $5 + 5$ years of data taking.

In the disappearance sector, the interesting pairs of NSI parameters for the ND are $\left[\Re(\varepsilon^s_{\mu\mu}), \Re(\varepsilon^d_{\mu\mu})\right]$ and $\left[\Re(\varepsilon^s_{ee}), \Re(\varepsilon^d_{ee})\right]$, which are mainly constrained by the $\nu_\mu \to \nu_\mu$ and $\nu_e \to \nu_e$ transitions, respectively. The regions that could be excluded by the DUNE ND are displayed in Fig.(6.5), where we also superimposed the limits set by the FD analysis only[5] [642] (no limits can be put on $\varepsilon^{s,d}_{ee}$). As it is clear from the left panel, the numerical results completely reflect the analytic anticorrelations discussed in eq.(6.24): even though for every value of $\Re(\varepsilon^d_{\mu\mu})$ there is an interval of $\Re(\varepsilon^s_{\mu\mu})$ for which the $\chi^2$ is small, it is nonetheless possible to exclude a sizable portion of the parameter space allowed by FD analysis. Similar considerations can be done on the parameters

[3] In these papers different physics models than NSI are analyzed, less sensitive to systematics.

[4] The standard oscillation parameters are fixed to the central values reported in [578] because they have no effects in our fit.

[5] Horizontal and vertical lines showed in our plots do not represent the results of a correlation analysis at the far detector, but only the sensitivity limits obtained after a full marginalization on the parameter space.

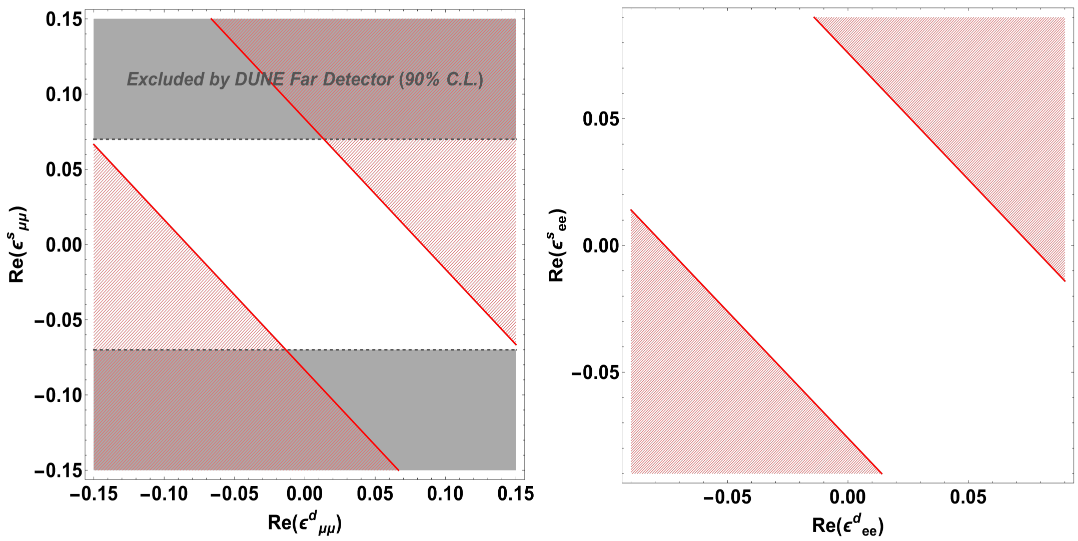


Figure 6.5: 90% CL excluded regions (in red) in the $\left[\Re(\varepsilon^s_{\mu\mu}),\Re(\varepsilon^d_{\mu\mu})\right]$-plane (left panel) and $\left[\Re(\varepsilon^s_{ee}),\Re(\varepsilon^d_{ee})\right]$-plane (right panel) by the DUNE ND. The FD excluded zones are shown with horizontal gray bands.

$\Re(\varepsilon^{s,d}_{ee})$ shown in the right panel, for which the ND is able to rule out a relevant fraction of them, a goal otherwise not possible with the DUNE FD alone.

Given the band width in eq. (6.25), the above considerations can be summarized as follows:

$$\Delta_{\mu\mu} = 0.12 \qquad \Delta_{ee} = 0.11\ . \tag{6.26}$$

Notice that, for 90% CL, $\chi^2_0 = 4.6$ (2 degrees of freedom) and $N_0$ is roughly $10^7$ events per year for the $\nu_\mu \to \nu_\mu$ channel and $10^5$ events per year in the $\nu_e \to \nu_e$ channel. The obtained values of the band are of the same order of the systematics discussed in the previous section, namely 10% for the signal and 15% for the background, and are almost the same for the two channels even though the number of $\nu_\mu$ events is two order of magnitude larger than the number of $\nu_e$ events. This reflects the fact that, for the disappearance channels, we cannot be sensitive to NSI parameters which cause changes to standard oscillation probabilities smaller than the adopted systematic uncertainties. However, even with our realistic assumptions, the result on $\Delta_{\mu\mu}$ permits to exclude parts of the parameter space allowed by the general analysis performed in [448] ($|\varepsilon^s_{\mu\mu}| < 0.068$ and $|\varepsilon^s_{\mu\mu}| < 0.078$). On the other hand, the result on $\Delta_{ee}$ is worse than the one set by reactor experiments like Daya Bay [449] ($|\varepsilon_{ee}| < 2\times10^{-3}$) that have been obtained, we have to outline, under the restrictive assumption $\varepsilon^s = \varepsilon^{d*}$. In the case of the appearance channels, eq.(6.14) highlights that the interesting pairs of parameters are $\left(|\varepsilon^s_{\mu e}|, |\varepsilon^d_{\mu e}|\right)$ and $\left(|\varepsilon^s_{\mu\tau}|, |\varepsilon^d_{\mu\tau}|\right)$. We show the 90% CL excluded regions in Fig.(6.6) where we also displayed the bounds that would be set by the FD. Also in this case, the correlations outlined in eq.(6.21) is recovered and large portions of the parameter spaces can be ruled out, in particular for the $\nu_e$ appearance channel. On the other hand, the small signal to background ratio in the $\nu_\tau$ appearance channel results in a larger band width; thus, the region excluded by the ND but allowed by the FD is delimited by $|\varepsilon^d_{\mu\tau}| > 0.024$. The appearance results are summarized by the following widths:

$$\Delta_{\mu e} = 0.0065 \qquad \Delta_{\mu\tau} = 0.026\,. \tag{6.27}$$

A better background rejection in the $\nu_\tau$ channel could reduce the band width by up to one order of magnitude. An important role in defining the allowed ranges for the appearance parameters $|\varepsilon^{s/d}_{\mu e}|$ and $|\varepsilon^{s/d}_{\mu\tau}|$ is played by the CP violating phases $\Phi^s_{\alpha\beta}$ and $\Phi^d_{\alpha\beta}$. Recalling eq.(6.20), it is clear that the degeneracy that let the $\chi^2$ vanish when the absolute values of detector and source parameters are the same, occurs only when $\Delta\Phi_{\alpha\beta} = \Phi^s_{\alpha\beta} - \Phi^d_{\alpha\beta}$ is very close to $\pi$. For all other

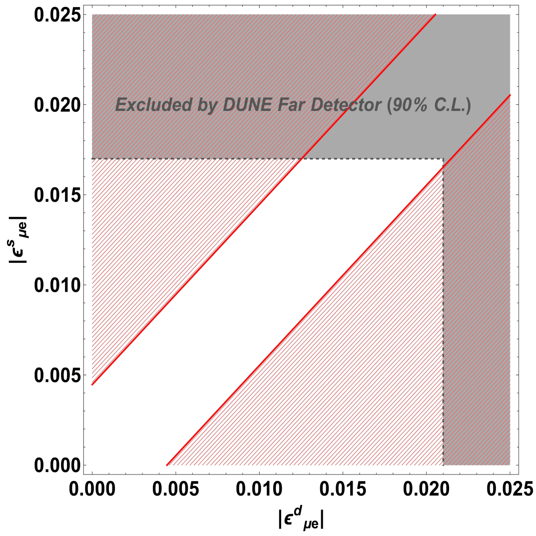


Figure 6.6: Same as Fig.(6.5) but in the $\left(|\varepsilon^s_{\mu e}|, |\varepsilon^d_{\mu e}|\right)$ (left panel) and $\left(|\varepsilon^s_{\mu\tau}|, |\varepsilon^d_{\mu\tau}|\right)$ planes (right panel).

values of the phase difference, the ND could be able to set very stringent 90% CL limits (with a 5+5 years of data taking), namely:

$$|\varepsilon^{s/d}_{\mu e}| < 0.0046 \qquad |\varepsilon^{s/d}_{\mu\tau}| < 0.019\,, \tag{6.28}$$

which are very competitive to the ones set so far by other neutrino oscillation experiments (for instance, $|\varepsilon^{s/d}_{\mu e,\mu\tau}| < \mathcal{O}(10^{-2})$ obtained in [448] and [452]). This is clearly shown in Fig.(6.7) where we present the contours at 90% CL in the $\left(|\varepsilon^{s/d}_{\mu e}|, \cos\Delta\Phi_{\mu e}\right)$ and $\left(|\varepsilon^{s/d}_{\mu\tau}|, \cos\Delta\Phi_{\mu\tau}\right)$-planes, obtained after marginalizing the $\chi^2$ function over all undisplayed parameters.

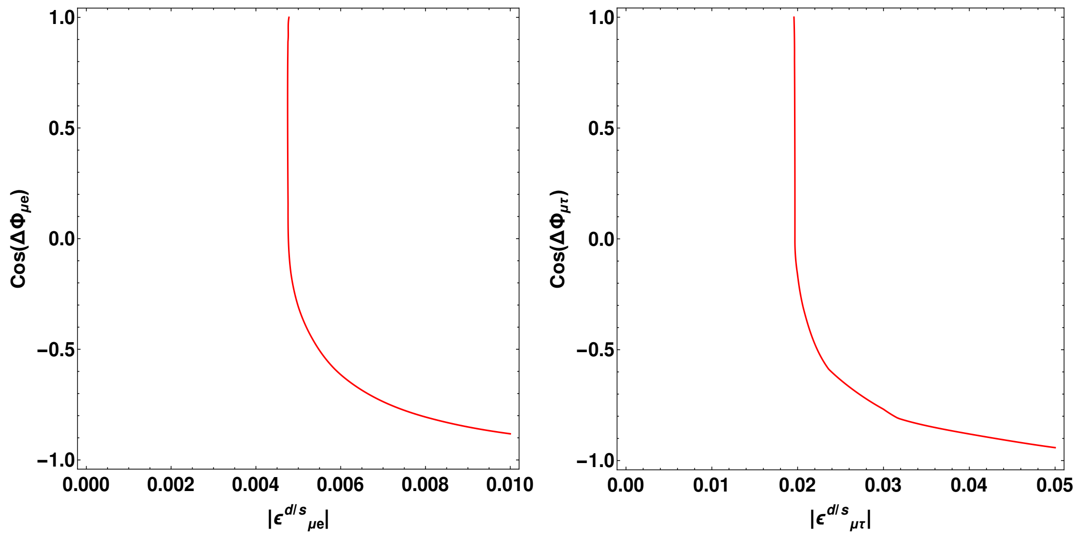

Figure 6.7: Contours at 90% CL in the $\left(|\varepsilon^{s/d}_{\mu e}|, \cos\Delta\Phi_{\mu e}\right)$ (left panel) and $\left(|\varepsilon^{s/d}_{\mu\tau}|, \cos\Delta\Phi_{\mu\tau}\right)$ (right panel) planes obtained by our DUNE ND simulations.

As discussed previously, the choice of the systematic uncertainties is a crucial point in the determination of the limits that the Near Detector could be able to set. In order to understand how much the band widths $\Delta_{\alpha\beta}$ would change in the case of a different choice of systematics, we performed the same simulations for a data taking time of 5+5 years considering three different cases:

- *Case A*: the standard (optimistic) case, namely the one implemented in the DUNE Far Detector GLoBES configuration file. In this case the systematics are 5% for the $\nu_\mu$ disappearance channel, 2% for the $\nu_e$ appearance and disappearance channels and 20% for the $\nu_\tau$ appearance channel. The uncertainty on the NC background has been considered to be 10%.

- *Case B*: the more realistic choice used in the previous section, where we fixed 10% for the $\nu_e$ appearance, $\nu_e$ disappearance and $\nu_\mu$ disappearance, 25% for the $\nu_\tau$ appearance and 15% for the NC background.

- *Case C*: a more pessimistic case in which the systematics are 15% for $\nu_e$ appearance, $\nu_e$ disappearance and $\nu_\mu$ disappearance, 30% for the $\nu_\tau$ appearance and 20% for the NC background.

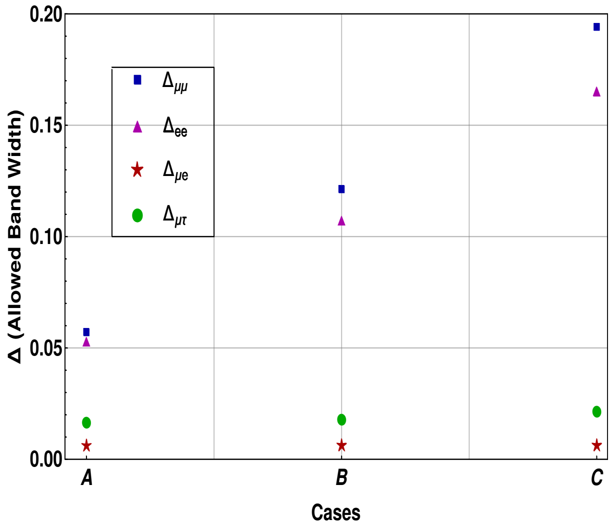


Figure 6.8: Variation of the allowed band widths $\Delta_{\alpha\beta}$ for a data taking time of 5+5 years and four different choice of systematics: optimistic (A), standard (B) and pessimistic (C).

The results of our simulations are reported in Fig.6.8. We clearly see that $\Delta_{ee}$ and $\Delta_{\mu\mu}$ are the parameters which are affected the most by the systematics, as previously discussed. Indeed, being the survival probability at L=0 in the standard model equal to 1, the number of observed events will be, even in presence of the small effect of the NSI, of the same order of magnitude as $N_0$. Thus, when statistical errors are negligible, the definition for the band width (eq.(6.25)) can be simplified to:

$$\Delta_{\alpha\alpha} \sim \sqrt{\frac{\chi^2_{0,\alpha\alpha}}{2}}\sigma_{sys}\,, \tag{6.29}$$

where we used $\sigma \sim N_0\sigma_{sys}$ .
For the appearance parameters, we register a less evident increasing of the band widths passing from the case (A) to (C), since in this case statistic uncertainties are always dominating over systematics. Indeed, for the two appearance channels, $N_0$ is $\sim 10^7$ per year in the $\nu_\mu \to \nu_e$ channel and $\sim 10^6$ per year in the $\nu_\mu \to \nu_\tau$ channel, but the observed number of events is small due to the very short baseline. For a given small number of observed events $N_{obs}$, we have $\sigma^2 = N^2_{obs}\sigma^2_{sys} + N_{obs} \sim N_{obs}$. Thus, the width can be simplified as follows:

$$\Delta_{\alpha\beta} \sim \sqrt[4]{\frac{4\chi^2_{0,\alpha\beta}N_{obs}}{N_0^2}}\,. \tag{6.30}$$

This quantity is roughly independent on the systematics and for $N_{obs} = \mathcal{O}(10)$ is of the order of $10^{-3}$. This number is in agreement with our numerical results for $\Delta_{\mu e}$ while for $\Delta_{\mu\tau}$ the agreement is confined to the case where the NC background (which in addition suffers by the increase of the systematics) is turned off.

We want to outline that we recomputed the various $\Delta_{\alpha\beta}$ also for several positioning of the DUNE ND at different off-axis angles with respect to the beam direction [652] and found a general worsening of the ND performances due to the decreased number of collected events. In fact, spectra distortions of signal and backgrounds cannot improve source and detector NSI analysis since probabilities in this regime do not depend on neutrino energies.

### 6.2.2 Achievable precision on non-vanishing source and detector NSI

The relatively simple strategy we used to find analytic bounds on NSI parameters can also be applied to compute the precision on the measurement of non-vanishing parameters, that is in the case where the true values of the source and detector parameters are non zero. In this case eq.(6.18) becomes:

$$\chi^2 = \frac{N_0^2}{\sigma^2}[\delta_{\alpha\beta} + K_{\alpha\beta} - P_{\alpha\beta}(\varepsilon^s_{fit}, \varepsilon^d_{fit})]^2 \,, \tag{6.31}$$

where $K_{\alpha\beta}$ is defined as the true $P_{\alpha\beta}$ for the appearance channels and $P_{\alpha\alpha} - 1$ for the disappearance channels.

Let us start from the disappearance. Given the structure of the $\chi^2$ function:

$$\chi^2 = \frac{4N_0^2}{\sigma^2}\left[K_{\alpha\alpha}/2 - \Re(\varepsilon^s_{\alpha\alpha}) - \Re(\varepsilon^d_{\alpha\alpha})\right]^2 \,, \tag{6.32}$$

the allowed regions in the $\left[\Re(\varepsilon^s_{\alpha\alpha}), \Re(\varepsilon^d_{\alpha\alpha})\right]$-plane are identified by:

$$\left|\Re(\varepsilon^d_{\alpha\alpha}) + \Re(\varepsilon^s_{\alpha\alpha}) - K_{\alpha\alpha}/2\right| < \sqrt{\frac{\chi^2_{0,\alpha\alpha}\sigma^2}{4N_0^2}} \,. \tag{6.33}$$

This means that the allowed regions around the values of $\Re(\varepsilon^d_{\alpha\alpha})$ and $\Re(\varepsilon^s_{\alpha\alpha})$ chosen by Nature have essentially similar shapes as those presented in Fig.(6.5) but with a band centered on the line $\Re(\varepsilon^d_{\alpha\alpha}) = -\Re(\varepsilon^s_{\alpha\alpha}) + K_{\alpha\alpha}/2$.

In the case of the appearance channel, the $\chi^2$ function reads:

$$\chi^2 = \frac{N_0^2}{\sigma^2}\left[K_{\alpha\beta} - |\varepsilon^s_{\alpha\beta}|^2 - |\varepsilon^d_{\alpha\beta}|^2 - 2|\varepsilon^s_{\alpha\beta}||\varepsilon^d_{\alpha\beta}|\cos\left(\Phi^s_{\alpha\beta} - \Phi^d_{\alpha\beta}\right)\right]^2 . \tag{6.34}$$

The minima of the $\chi^2$ are always in $(\cos\Delta\Phi_{min}) = \left(\frac{K_{\alpha\beta} - |\varepsilon^s_{\alpha\beta}|^2 - |\varepsilon^d_{\alpha\beta}|^2}{2|\varepsilon^s_{\alpha\beta}||\varepsilon^d_{\alpha\beta}|}\right)$; however, when $|(\cos\Delta\Phi_{min})| > 1$, $\Delta\Phi_{min}$ is forced to be either 0 or $\pi$. Fixing the cut of the $\chi^2$ ($\chi_{0,\alpha\beta}$) at a given CL, the allowed regions are delimited by:

$$\begin{aligned} Max\left[0, K_{\alpha\beta} - \sqrt{\frac{\chi^2_{0,\alpha\beta}\sigma^2}{N_0^2}}\right] < \quad \left(|\varepsilon^s_{\alpha\beta}| + |\varepsilon^d_{\alpha\beta}|\right)^2 \quad < K_{\alpha\beta} \\ K_{\alpha\beta} < \quad \left(|\varepsilon^s_{\alpha\beta}| - |\varepsilon^d_{\alpha\beta}|\right)^2 \quad < K_{\alpha\beta} + \sqrt{\frac{\chi^2_{0,\alpha\beta}\sigma^2}{N_0^2}} \,. \end{aligned} \tag{6.35}$$

As an example, we report in Fig.(6.9) the results of our numerical simulations of the precision achievable in the measurement of the NSI parameters whose true values are fixed to $\left[\Re(\varepsilon^d_{\mu\mu}), \Re(\varepsilon^s_{\mu\mu})\right] = (0.01, 0.01)$ (left panel) and $\left(|\varepsilon^d_{\mu\tau}|, |\varepsilon^s_{\mu\tau}|\right) = (0.02, 0.03)$ (right panel).

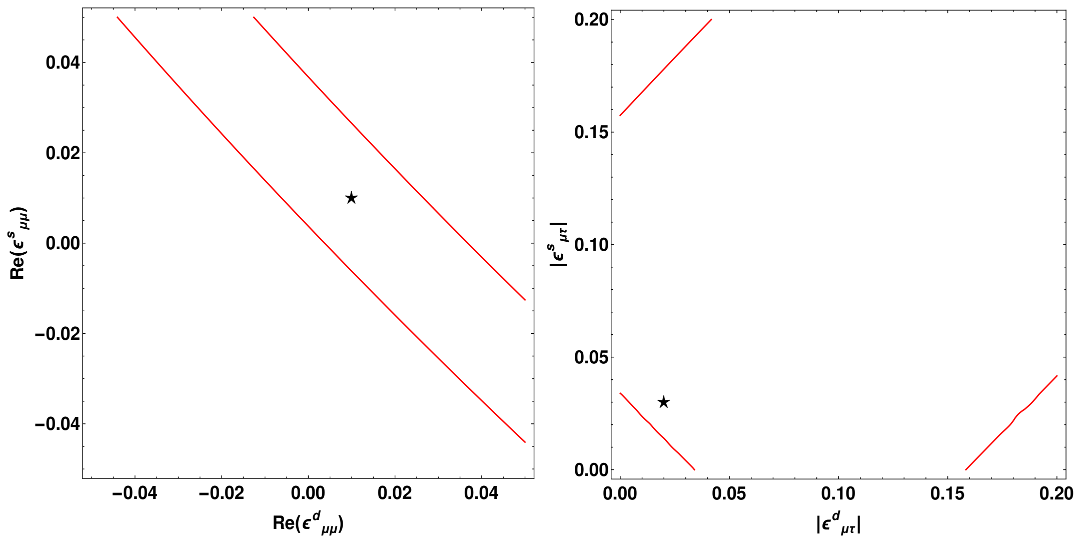


Figure 6.9: 90% CL allowed regions in the measurement of the NSI parameters; true values are fixed to $\left[\Re(\varepsilon^d_{\mu\mu}), \Re(\varepsilon^s_{\mu\mu})\right] = (0.01, 0.01)$ (left panel) and $\left(|\varepsilon^d_{\mu\tau}|, |\varepsilon^s_{\mu\tau}|\right) = (0.02, 0.03)$ (right panel).

As we can see, the allowed regions strictly follow the analytic results reported in eqs.(6.33) and (6.35). In these two examples, data permit to exclude the point (0,0) corresponding to the absence of NSI, but this is not the general case as, for different input values, if $K_{\alpha\beta} < \sqrt{\frac{\chi^2_{0,\alpha\beta}\sigma^2}{N_0^2}}$ or $K_{\alpha\alpha} < \sqrt{\frac{\chi^2_{0,\alpha\alpha}\sigma^2}{N_0^2}}$, the standard oscillation framework cannot be excluded at the desired confidence level.

## 6.3 Hints of new sources of CP violation: the role of the integrated asymmetries

In the previous sections, we discussed some examples in which it is possible to bound new physics models performing a fit on the oscillation data at DUNE. However, we propose here a way to search for hints of the presence of new physics effects, which does not require to perform a fit on the data. In particular, we consider here the effect of the new phases which appear in a given BSM model. We chose for this purpose two cases, the 3+1 sterile neutrino model and the propagation NSI model; however, the analysis may be repeated for any model with new phases. Defining $P(\nu_\alpha \to \nu_\beta)$ as the transition probability from a flavor $\alpha$ to a flavor $\beta$, one can construct the CP-odd asymmetries[6] as:

$$A_{\alpha\beta} \equiv \frac{P(\nu_\alpha \to \nu_\beta) - P(\bar{\nu}_\alpha \to \bar{\nu}_\beta)}{P(\nu_\alpha \to \nu_\beta) + P(\bar{\nu}_\alpha \to \bar{\nu}_\beta)} \,. \tag{6.36}$$

It is well known that matter effects modify the behaviour of the asymmetries as a function of the Standard Model CP phase $\delta$ (see, e.g., [653]): in fact, the passage of neutrinos through matter introduces fake CP-violating effects which allows $A_{\alpha\beta} \neq 0$ even when $\sin\delta = 0$. In principle, to extract genuine CP violating effects, one could defines the subtracted asymmetries as $A^{\rm sub}_{\alpha\beta}(\delta) = A_{\alpha\beta}(\delta) - A_{\alpha\beta}(\delta = 0)$. However, we prefer to deal with more directly measurable

[6]Notice that we already discussed asymmetries in Sec. 5.2. However, since in that case we were interested in the dependence on the atmospheric mixing angle, we used a different expansion to compute them.

quantities and we will use eq.(6.36) which, for non negligible matter effects, are non vanishing when $\delta = 0, \pm\pi$.

To derive the analytic expressions for the asymmetries we use an expansion similar to the one described in Sec. 5.3. In particular, we expand up to the second in the small $\alpha = \Delta m^2_{21}/\Delta m^2_{31}$ ratio [443] and in $r, s$ and $a$, which represent the deviation from the tri-bimaximal mixing values of the neutrino mixing angles $\theta_{13}, \theta_{12}, \theta_{23}$. Moreover, after defining $\Delta_{21} = \Delta m^2_{21} L/4E_\nu$, $\Delta_{31} = \Delta m^2_{31} L/4E_\nu$ and $V_{CC} = A_{CC} L/2\Delta_{31} = 2A_{CC} E_\nu/\Delta m^2_{31}$, we further expand in the small $V_{CC}$ up to the first order.

To start with, let us consider the *vacuum* case; for the $\nu_\mu \to \nu_e$ channel, the leading term of the asymmetry is the following:

$$A^{SM_0}_{\mu e} = -\frac{12}{f_1} r\, \alpha \Delta_{31} \sin\delta \sin^2\Delta_{31}\,, \tag{6.37}$$

where

$$f_1 = 9r^2 \sin^2\Delta_{31} + 4\alpha\Delta_{31}\left(\alpha\Delta_{31} + 3r\cos\delta\cos\Delta_{31}\sin\Delta_{31}\right). \tag{6.38}$$

Being the numerator and the denominator of eq.(6.37) doubly suppressed by small quantities, we expect $A^{SM_0}_{\mu e} \sim \mathcal{O}(1)$.
For the $\nu_\mu \to \nu_\tau$ channel, on the other hand, we find that the leading contribution to the asymmetry is given by a simpler expression:

$$A^{SM_0}_{\mu\tau} = \frac{4}{3} r\alpha\Delta_{31}\sin\delta\,, \tag{6.39}$$

which is clearly smaller than $A_{\mu e}$. Notice also that, differently from $A_{\mu e}$, this asymmetry becomes negative if $\delta > 180°$, as emerging from fits to neutrino oscillation data [111, 112].
A third possible asymmetry, namely $A_{\mu\mu}$, is obviously vanishing in vacuum because of CPT conservation but can assume a relevant role when matter effects are taken into account (as we will discuss later on).

As it is well known, the inclusion of matter effects complicates the analytic expressions of the transition probabilities and, more importantly, that of the asymmetries. In order to deal with readable formulae, we can work in the regime of weak matter potential $V_{CC} \ll 1$ which, as outline before, is a good approximation in the case of DUNE. Thus, we can organize our perturbative expansion as follows:

$$A_{\alpha\beta} = A^{SM_0}_{\alpha\beta} + V_{CC}\, A^{SM_1}_{\alpha\beta} + \mathcal{O}(V^2_{CC})\,, \tag{6.40}$$

where $A^{SM_1}_{\alpha\beta}$ represents the first order correction to the vacuum case $V_{CC} = 0$. Thus, the asymmetries considered in this study acquire the following corrections:

$$\begin{aligned} A^{SM_1}_{\mu e} &= -\frac{6}{f_1} r\left(\Delta_{31}\cos\Delta_{31} - \sin\Delta_{31}\right)\Big[2\alpha\Delta_{31}\cos\delta\cos\Delta_{31} + 3r\sin\Delta_{31} + \\ &- \frac{24}{f_1} r\alpha^2 \sin^2\delta\, \Delta^2_{31}\sin^3\Delta_{31}\Big]\,, && (6.41) \\ A^{SM_1}_{\mu\tau} &= -2r^2\left(1 - \Delta_{31}\cot\Delta_{31}\right) + \frac{8}{27}\alpha^2\Delta^3_{31}\cot\Delta_{31}\,, && (6.42) \\ A^{SM_1}_{\mu\mu} &= \frac{4}{3} r\alpha\Delta_{31}\cos\delta\left(\Delta_{31} - \tan\Delta_{31}\right) - \frac{8}{27}\alpha^2\Delta^3_{31}\tan\Delta_{31}\,. && (6.43) \end{aligned}$$

It is evident that $A_{\mu e}$ increases because a term proportional to $r^2/f_1$ appears, which is of $\mathcal{O}(1)$. Since at the atmospheric peak $\sin\Delta_{31} \gg \cos\Delta_{31}$, the $r^2/f_1$ correction is positive and adds an

$\mathcal{O}(V_{CC})$ contribution to the total $A_{\mu e}$, that at the DUNE peak energy becomes roughly 1/2. On the other hand, $A_{\mu\tau}^{SM_1}$ contains only terms proportional to $V_{CC}r^2$ and $V_{CC}\alpha^2$ which are not balanced by any small denominator. Thus, both contributions set a correction to the vacuum asymmetry. A similar situation arises for $A_{\mu\mu}$, where only terms proportional to $V_{CC}r\alpha$ and $V_{CC}\alpha^2$ appear.

### 6.3.1 Asymmetries in the NSI case

As discussed in Sec. 3.2.2, propagation NSI modify the neutrino oscillation Hamiltonian introducing new parameters in the matter potential term, which becomes

$$A_{CC}\begin{pmatrix} 1+\varepsilon_{ee} & \varepsilon_{e\mu} & \varepsilon_{e\tau} \\ \varepsilon_{e\mu}^* & \varepsilon_{\mu\mu} & \varepsilon_{\mu\tau} \\ \varepsilon_{e\tau}^* & \varepsilon_{\mu\tau}^* & \varepsilon_{\tau\tau} \end{pmatrix}.$$

where the off-diagonal parameters can be written as $\varepsilon_{\alpha\beta} = |\epsilon_{\alpha\beta}|e^{i\delta_{\alpha\beta}}$. We want to remark, as already discussed, that we can always subtract a matrix proportional to the identity without changing the transition probabilities. If we choose to subtract $\varepsilon_{\mu\mu}\mathbb{I}$, only two independent diagonal parameters ($\varepsilon'_{ee} = \varepsilon_{ee} - \varepsilon_{\mu\mu}$ and $\varepsilon'_{\tau\tau} = \varepsilon_{\tau\tau} - \varepsilon_{\mu\mu}$) will appear in the NSI matrix[7]. Coming back to the CP-odd asymmetries, since NSI effects are strongly intertwined with standard matter effects driven by $V_{CC}$, the asymmetries can be cast in a form which generalizes eq.(6.40):

$$A_{\alpha\beta} = A_{\alpha\beta}^{SM_0} + V_{CC}(A_{\alpha\beta}^{SM_1} + A_{\alpha\beta}^{NSI}) + \mathcal{O}(V_{CC}^2)\,, \tag{6.44}$$

where $A_{\alpha\beta}^{SM_{0,1}}$ refers to the pure Standard Model results and all the effects of the NSI are included in the $A_{\alpha\beta}^{NSI}$ term.
Bounds on the magnitude of the NSI couplings have been widely discussed [654]; even though some of them could in principle be of $\mathcal{O}(1)$ and give rise, for example, to degeneracies leading to the so-called LMA-Dark solution [655], we decided nonetheless to consider all $\varepsilon_{\alpha\beta}$'s on the same footing and of the same order of magnitude as the other small standard parameters $a, s, r, \alpha$ and $V_{CC}$. In this way, we are able to catch the leading dependence on NP carried on by the CP asymmetries.

For the $\nu_\mu \to \nu_e$ channel, the leading order NSI contributions can be arranged as follows:

$$A_{\mu e}^{NSI} = \varepsilon_{e\mu} a_{\mu e}^{\varepsilon_{e\mu}} + \varepsilon_{e\tau} a_{\mu e}^{\varepsilon_{e\tau}}\,, \tag{6.45}$$

where the $a's$ functions are given by:

$$\begin{aligned} a_{\mu e}^{\varepsilon_{e\mu}} &= \frac{3}{f_1}\left[6r\cos(\delta-\delta_{e\mu})\sin\Delta_{31}\left(\Delta_{31}\cos\Delta_{31}+\sin\Delta_{31}\right)+\right.\\ &\quad \left. 4\alpha\Delta_{31}\cos\delta_{e\mu}\left(\Delta_{31}+\cos\Delta_{31}\sin\Delta_{31}\right)\right]\\ &- \frac{72}{f_1^2}r\alpha\sin\delta\Delta_{31}^2\sin^4\Delta_{31}\left[3r\sin(\delta-\delta_{e\mu})+2\alpha\sin\delta_{e\mu}\right]\,, \end{aligned} \tag{6.46}$$

$$\begin{aligned} a_{\mu e}^{\varepsilon_{e\tau}} &= \frac{3}{f_1}\left[6r\cos(\delta-\delta_{e\tau})\sin\Delta_{31}\left(-\Delta_{31}\cos\Delta_{31}+\sin\Delta_{31}\right)+\right.\\ &\quad \left. 2\alpha\Delta_{31}\cos\delta_{e\tau}\left(-2\Delta_{31}+\sin 2\Delta_{31}\right)\right]\\ &+ \frac{72}{f_1^2}r\alpha\sin\delta\Delta_{31}^2\sin^4\Delta_{31}\left[3r\sin(\delta-\delta_{e\tau})-2\alpha\sin\delta_{e\tau}\right]\,. \end{aligned} \tag{6.47}$$

[7]Notice that non-oscillation experiments bounds on $\varepsilon_{\mu\mu}$ are very stringent; thus $\varepsilon'_{ee} \sim \varepsilon_{ee}$ and $\varepsilon'_{\tau\tau} \sim \varepsilon_{\tau\tau}$.

For the sake of simplicity, the symbols $\varepsilon_{\alpha\beta}$ with $\alpha \neq \beta$ indicate the moduli of such parameters. The only NP parameters appearing at the considered perturbative level are $\varepsilon_{e\mu}$ and $\varepsilon_{e\tau}$ which, in turn, carry the dependence on the CP phases $\delta_{e\mu}, \delta_{e\tau}$. All in all, the NSI contributions set an $\mathcal{O}(V_{CC})$ correction to $A_{\mu e}^{SM_0}$. We also notice that the largest of the considered terms, namely the ones linear in $r$ in the numerator, have similar expressions in both $a_{\mu e}^{\varepsilon_{e\mu}}$ and in $a_{\mu e}^{\varepsilon_{e\tau}}$, apart from the sign in front of $\cos\Delta_{31}$. This means that, around the atmospheric peak, the phases $\delta_{e\mu}$ and $\delta_{e\tau}$ are equally important even though the magnitude of their impact strongly depends on the value of the standard CP phase $\delta$.

For the asymmetry in the $\mu\tau$-channel, we found the following structure:

$$
\begin{aligned}
A_{\mu\tau}^{NSI} &= 8\varepsilon_{\mu\tau}\cos\delta_{\mu\tau}\Delta_{31}\cot\Delta_{31} + \\
&- \frac{4}{3}\alpha\Delta_{31}^2\left(\varepsilon_{e\mu}\cos\delta_{e\mu} - \varepsilon_{e\tau}\cos\delta_{e\tau} - 4\varepsilon_{\mu\tau}\cos\delta_{\mu\tau}\csc^2\Delta_{31}\right) + \\
&- 2r\left[\varepsilon_{e\mu}\cos(\delta-\delta_{e\mu}) + \varepsilon_{e\tau}\cos(\delta-\delta_{e\tau})\right](1-\Delta_{31}\cot\Delta_{31}) \\
&+ 4a\varepsilon'_{\tau\tau}(1-\Delta_{31}\cot\Delta_{31}) \; .
\end{aligned} \tag{6.48}
$$

In this case, four different NSI parameters enter the leading order corrections, namely $\varepsilon_{\mu\tau}, \varepsilon_{e\tau}, \varepsilon_{e\mu}$ (together with their phases) and $\varepsilon'_{\tau\tau}$. Contrary to the $\mu e$ case, the largest correction to the vacuum expression is given by the first order term $\varepsilon_{\mu\tau}$ in the first line of eq.(6.48), which is not suppressed by any of the standard small parameters $a, r, s$ and $\alpha$. Considering that $A_{\mu\tau}^{SM_0} \sim \mathcal{O}(r\alpha)$, this makes the $\mu\tau$-channel very promising for searching for NP, at least at the probability level where possible complications due to small $\tau$ statistics do not enter. Finally, for the $\mu\mu$ channel, matter effects generate a substantial difference in the propagation of neutrinos versus antineutrinos, which results in the following NSI contributions:

$$
\begin{aligned}
A_{\mu\mu}^{NSI} &= -8\varepsilon_{\mu\tau}\Delta_{31}\cos\delta_{\mu\tau}\tan\Delta_{31} - 4r\varepsilon_{e\mu}\Delta_{31}\cos(\delta-\delta_{e\mu})\tan\Delta_{31} + \\
&+ 4a\varepsilon'_{\tau\tau}(\Delta_{31} - \tan\Delta_{31})\tan\Delta_{31} - \frac{4}{3}\alpha\Delta_{31} \times \\
&\quad \left[\varepsilon_{e\mu}\cos\delta_{e\mu}(\Delta_{31}+\tan\Delta_{31}) - \varepsilon_{e\tau}\cos\delta_{e\tau}(\Delta_{31}-\tan\Delta_{31}) - \right. \\
&\quad \left. 4\Delta_{31}\varepsilon_{\mu\tau}\cos\delta_{\mu\tau}\sec^2\Delta_{31}\right] \; .
\end{aligned} \tag{6.49}
$$

As expected from unitarity relations, we get an opposite linear dependence on $\varepsilon_{\mu\tau}$ but with a coefficient proportional to $\tan\Delta_{31}$ which, close to the atmospheric peak, gives an important correction to $A_{\mu\mu}^{SM_1}$.

### 6.3.2 Asymmetries in the 3+1 case

The next NP scenario under discussion is the so-called *3+1* model (see Sec. 3.1), in which a sterile neutrino state supplements the three standard active neutrinos. Even though the new state cannot interact with the ordinary matter, it can have a role in neutrino oscillations thanks to the mixing with the active partners. The long-standing reactor, gallium and short-baseline anomalies [422] suggested that, if present, the fourth mass eigenstate $m_4$ should have a mass such that $\Delta m_{41}^2 = m_4^2 - m_1^2 \sim \mathcal{O}(1)$ eV$^2$, that is orders of magnitude larger than the solar and the atmospheric mass splittings, thus capable to drive very fast oscillations visible at accordingly small $L/E$. In addition to the new mass splitting $\Delta m_{41}^2$, the PMNS matrix becomes a $4\times 4$ matrix which can be parametrized in terms of 6 angles and 3 phases. Here, we adopt the following multiplication order of the rotation matrices $R(\theta_{ij})$ [406, 418, 419]:

$$
U = R(\theta_{34})R(\theta_{24})R(\theta_{14})R(\theta_{23},\delta_3)R(\theta_{13},\delta_2)R(\theta_{12},\delta_1). \tag{6.50}
$$

Apart from $\delta_2$, which becomes the standard CP phase for $m_4 \to 0$, we have two potential new sources of CP violation, encoded in two phases $\delta_1$ and $\delta_3$. In the description of neutrino propagation in matter, we cannot disregard the role of the NC interactions because the sterile state does not feel at all the presence of matter; this results in the following evolution equations:

$$i\frac{d}{dt}\begin{pmatrix}\nu_e\\ \nu_\mu\\ \nu_\tau\\ \nu_s\end{pmatrix} = \tag{6.51}$$

$$= \left[\frac{1}{2E_\nu}U\begin{pmatrix}0&0&0&0\\0&\Delta m^2_{21}&0&0\\0&0&\Delta m^2_{31}&0\\0&0&0&\Delta m^2_{41}\end{pmatrix}U^\dagger + \begin{pmatrix}A_{CC}-A_{NC}&0&0&0\\0&-A_{NC}&0&0\\0&0&-A_{NC}&0\\0&0&0&0\end{pmatrix}\right]\begin{pmatrix}\nu_e\\ \nu_\mu\\ \nu_\tau\\ \nu_s\end{pmatrix},$$

where $\nu_s$ is the new sterile state, $A_{CC}$ is the usual matter charged current potential and $A_{NC}$ is the matter NC potential, $A_{NC} \equiv 1/\sqrt{2}G_F n_n$, with $n_n$ being the neutron density in the Earth crust.

The parameter space of the 3+1 model is therefore enlarged compared to the SM case by three new mixing angles $\theta_{i4}$, two more CP phases $\delta_{1,3}$ and the mass-squared difference $\Delta m^2_{41}$. Thus, in addition to the expansion parameters used in the previous sections $(r, s, a)$, we also expand in the small $s_{14}, s_{24}$ and $s_{34}$ (where $s_{i4} = \sin\theta_{i4}$) that we can still assume of $\mathcal{O}(0.1)$. To further simplify the analytic expressions of the asymmetries, we also introduce $V_{NC} = A_{NC}L/2\Delta_{31}$. It is useful to present the results in a form similar to eq.(6.44):

$$A_{\alpha\beta} = A^{SM}_{\alpha\beta} + A^{3+1}_{\alpha\beta} + \mathcal{O}(\lambda^n)\,, \tag{6.52}$$

where $A^{SM}_{\alpha\beta}$ are the SM asymmetries and the symbol $\lambda$ represents a common order of magnitude of all small quantities used in our perturbation theory, including $V_{CC}$ (but not $V_{NC}$, whose dependence in $A_{\alpha\beta}$ is exact). The exponent amount to $n = 3$ for $A_{\mu\tau}, A_{\mu\mu}$ and $n = 2$ for $A_{\mu e}$. Notice that, due to the parametrization adopted in this manuscript, the SM phase $\delta$ of eqs.(6.37)-(6.43) must be replaced by the combination $\delta_2 - \delta_1 - \delta_3$. Averaging out all the fast oscillations driven by $\Delta m^2_{41}$, the various $A^{3+1}_{\alpha\beta}$ have the following expressions:

$$\begin{aligned}
A^{3+1}_{\mu e} &\sim \frac{s_{14}s_{24}}{f_1}\{-6\,[2\alpha\Delta_{31}\sin\delta_1 + 3r\cos\Delta_{31}\sin(\delta_2-\delta_3)\sin\Delta_{31}]\} + \\
&\quad \frac{s_{14}s_{24}}{f_1^2}\{216r^2\alpha\Delta_{31}\cos(\delta_2-\ \delta_3)\sin(\delta_1-\delta_2+\delta_3)\ \sin^4\Delta_{31}\}\,,\\
A^{3+1}_{\mu\tau} &= 2s_{24}s_{34}\cot\Delta_{31}(\sin\delta_3 + 2V_{NC}\Delta_{31}\cos\delta_3)\,,\\
A^{3+1}_{\mu\mu} &= -4s_{24}s_{34}V_{NC}\Delta_{31}\cos\delta_3\tan\Delta_{31}\,.
\end{aligned} \tag{6.53}$$

To avoid large expressions, for $A_{\mu e}$ we only quote the corrections due to the new mixing angles.

First of all, we notice that the corrections to the $\mu e$ asymmetry are only linearly suppressed compared to the leading order results; thus, we expect such an asymmetry to be quite sensitive to new sources of CP violation. Then, both corrections to the $\mu\tau$ and the $\mu\mu$ asymmetries are linear in the combination $s_{24}s_{34}$. Since the angle $\theta_{34}$ has weak constraints (values of $20-30°$ are still allowed), these corrections can be relatively large. Notice also that, since $V_{NC}$ is roughly of the same order of magnitude as $V_{CC}$, $A^{3+1}_{\mu\tau}$ is expected to provide a large correction to the standard model asymmetries, making the $\nu_\tau$ appearance channel, at least in principle, very sensitive to NP effects. As for the PMNS phases, all leading order corrections depend only on the new phase $\delta_3$. This means that a long baseline experiment is mostly sensitive only to the combination $\delta_2 - \delta_1 - \delta_3$ and to the single phase $\delta_3$.

Beside the results of eq.(6.53), it is worth considering a new asymmetry corresponding to the $\nu_\mu \to \nu_s$ transition. Even though sterile neutrinos cannot be directly detected, the probability $P(\nu_\mu \to \nu_s)$ is a measure of the NC events in the detector. Indeed, being the NC interactions

| Asymmetry | SM | NSI | 3+1 |
|---|---|---|---|
| $A_{\mu e}$ | 1 | $\lambda$ | $\lambda$ |
| $A_{\mu\mu}$ | $\lambda^3$ | $\lambda^2$ | $\lambda^2$ |
| $A_{\mu\tau}$ | $\lambda^2$ | $\lambda^2$ | $\lambda^2$ |
| $A_{\mu s}$ | - | - | 1 |

Table 6.4: Order of magnitude estimates of the various contributions to the asymmetries discussed in this paper. $\lambda$ is a common order parameter such that: $r, s, a, \Delta_{21}, V_{CC}, \varepsilon_{\alpha\beta}, \theta_{i4} \sim \mathcal{O}(\lambda)$.

flavor independent, the number of events is proportional to the sum of the transition probabilities from the starting flavor ($\nu_\mu$) to the three active final flavors ($\nu_{e,\tau,\mu}$) because of the unitarity relation $P(\nu_\mu \to \nu_s) = 1 - P(\nu_\mu \to \nu_{e,\mu,\tau})$. The new asymmetry has vanishing matter corrections and, at the leading non-vanishing order, reads:

$$A_{\mu s}^{3+1} = -\frac{2 s_{24} s_{34} \sin\delta_3 \sin\Delta_{31} \cos\Delta_{31}}{2 s_{24}^2 + (s_{34}^2 - s_{24}^2)\sin^2\Delta_{31}} \,. \tag{6.54}$$

This is clearly an $\mathcal{O}(1)$ result since both numerator and denominator are of $\mathcal{O}(\lambda^2)$. In Tab.(6.4) we summarize the outcome of our analytic considerations on the magnitude of the NP corrections to the asymmetries discussed in this paper.

### 6.3.3 DUNE and the integrated asymmetries

As a case study to investigate the effects of the non-standard sources of CP violation, we choose the DUNE experiment. Our simulations have been performed considering all the CC channels and the NC channel [637], as in the previous discussions. For the running time we choose 3.5+3.5 years, while as neutrino flux we used both the standard one, peaked at 2.5 GeV, and the already mentioned high-energy one [652, 656].

The relevant question now is related to the experimental capability to measure the asymmetries we are considering: in fact, if the CP violating quantities will not be measured with a sufficient precision, then we cannot distinguish the deviation from the SM results due to NP. Instead of considering the asymmetries at the probability level, we deal with the experimentally relevant integrated asymmetries built from the number of expected events $N_\beta$ and $\bar{N}_\beta$:

$$A_{\alpha\beta} = \frac{N_\beta - \bar{N}_\beta}{N_\beta + \bar{N}_\beta} \,, \tag{6.55}$$

where the event rates for the $\nu_\alpha \to \nu_\beta$ and the CP conjugate $\bar{\nu}_\alpha \to \bar{\nu}_\beta$ transitions are computed from:

$$N_\beta = \int_{E_\nu} dE_\nu \, P_{\alpha\beta}(E_\nu)\, \sigma_\beta(E_\nu)\, \frac{d\phi_\alpha}{dE_\nu}(E_\nu)\, \varepsilon_\beta(E_\nu) \tag{6.56}$$

$$\bar{N}_\beta = \int_{E_\nu} dE_\nu \, P_{\bar{\alpha}\bar{\beta}}(E_\nu)\, \sigma_{\bar{\beta}}(E_\nu)\, \frac{d\phi_{\bar{\alpha}}}{dE_\nu}(E_\nu)\, \varepsilon_\beta(E_\nu) \,, \tag{6.57}$$

in which $\sigma_{\beta(\bar{\beta})}$ is the cross section[8] for producing the lepton $\beta(\bar{\beta})$, $\varepsilon_{\beta(\bar{\beta})}$ the detector efficiency to reveal that lepton and $\phi_{\alpha(\bar{\alpha})}$ the initial neutrino flux at the source. Since in the SM the only dependence on the CP phase is carried on by $\delta$, the correlations between the pair of asymmetries, for instance $(A_{\mu\tau}, A_{\mu e})$ and $(A_{\mu\tau}, A_{\mu\mu})$, is maximal and a close curve appears in the related physical planes. If, in addition, we also take into account the experimental errors on angles

[8]We used NC and CC inclusive cross sections from GENIE 2.8.4 included in the DUNE GLoBES files [562, 574], which are of the order of $\sigma/E = 10^{-39}$-$10^{-38}$ $cm^2/GeV$.

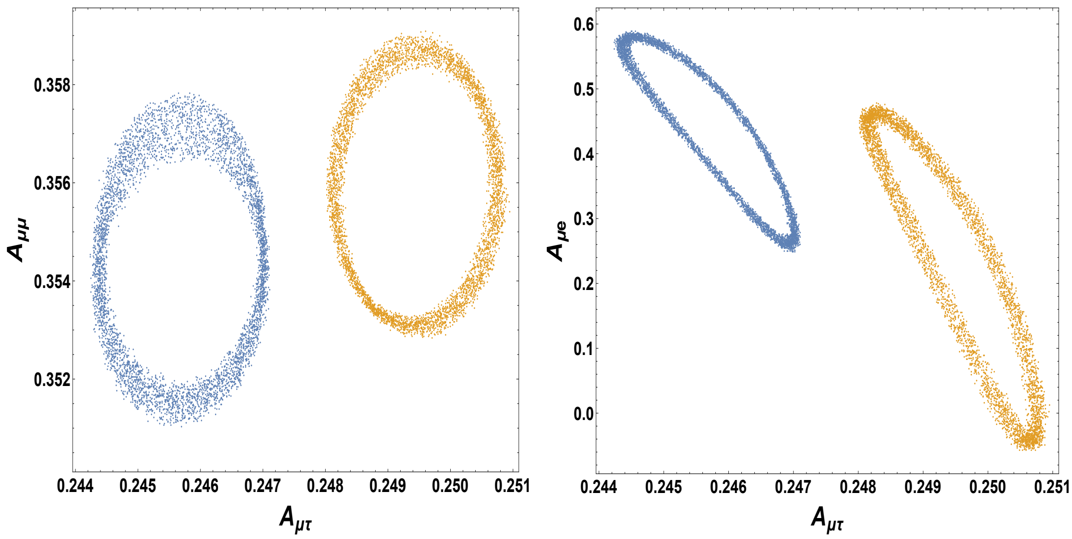


Figure 6.10: Numerical evaluation of the SM asymmetries of eq.(6.16) at DUNE, with standard flux. The SM parameters have been allowed to vary in their $1\sigma$ range, while all possible values for the CP phase have been taken into account. The blue dots represent asymmetries in the normal hierarchy hypothesis, while the orange ones represent asymmetries in the inverted hierarchy hypothesis.

and mass differences, the curves are scattered as reported in Fig.6.10, for the DUNE standard flux and in Fig.6.11 for the optimized flux. The blue dots are obtained using parameters in the normal hierarchy, while the orange ones are obtained using the inverse hierarchy hypothesis.

The first striking features of the integrated asymmetries is related to the fact that their sign is always positive; in fact, being integrated quantities, they are influences not only by the relative differences among $\nu$ and $\bar{\nu}$ probabilities, but also by the differences among $\nu$ and $\bar{\nu}$ fluxes and cross sections. The other important observation is that, as discussed above, $A_{\mu e}$ is the asymmetry that changes the most with a change of the CP phase. On the other hand, the other two asymmetries $A_{\mu\tau}$ and $A_{\mu\mu}$ change at a much slower rate.

Eventually, it is worth mentioning that, for each pair of asymmetries, the closed curves corresponding to NH and IH never overlap. This means that, at least in principle, one could be able to solve the neutrino hierarchy problem simply looking at the CP asymmetries. However, in DUNE as well as in other future experiments, the foreseen experimental errors on such asymmetries will probably be too large to allow for such a discrimination. Now we are ready to apply our strategy to check whether other sources of CP violation carried on by NP can be sufficiently distinguished from the SM phase. In order to do that, we first need to evaluate the experimental errors on the SM asymmetries and then recompute them as predicted by the NSI and the $3+1$ sterile models. From Fig.6.10 we see that the uncertainties on the standard angles and mass splittings are not playing an important role. A simple but accurate estimate from error propagation gives:

$$(\delta A_{\alpha\beta})^2 = \frac{4\bar{N}_\beta^2(\delta N_\beta)^2 + 4N_\beta^2(\delta\bar{N}_\beta)^2}{(N_\beta + \bar{N}_\beta)^4}\,, \tag{6.58}$$

where $\delta N$ is the uncertainty related to the number of expected events which receives contributions from the systematic error and the statistical error. For the $\nu_\mu$ disappearance channel, the first source of uncertainty is always dominating, since the number of events is very large and the statistical error is reduced. On the other hand, in the other two channels both terms are important. In particular, in the $\nu_\tau$ appearance, systematic errors are quite large (due to the poorly known cross section and to the systematics related to the complicated event reconstruction) and the number of events is small. Thus we expect $\delta A_{\mu\tau}$ to be particularly large.

In Fig.6.12 we show the values of the asymmetries where the effects of NSI are taken into account, computed by using the standard neutrino flux. The blue stars represent the asymme-

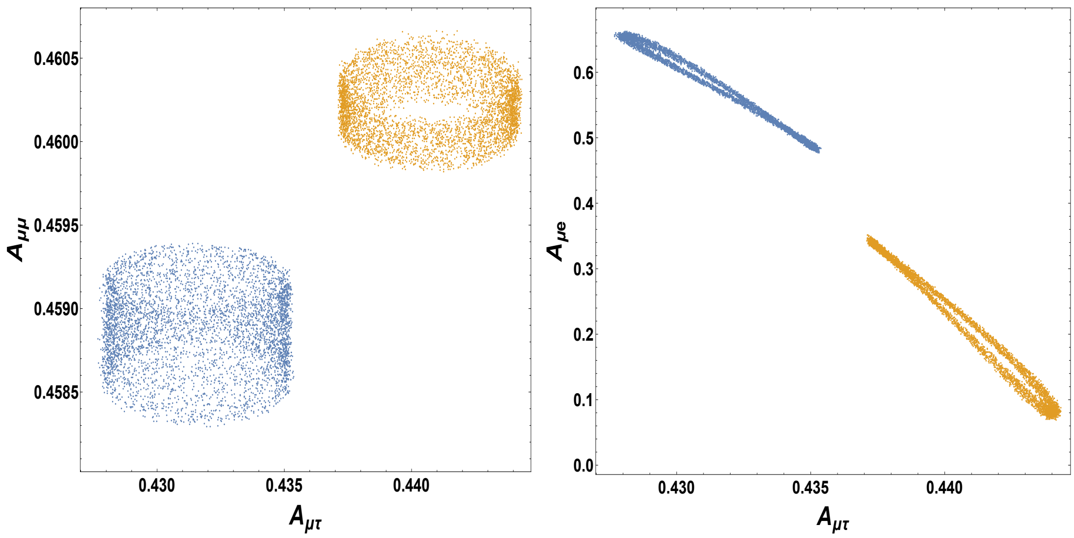


Figure 6.11: Same as Fig.6.10 but with the optimized flux. Notice the different vertical scales on the left and right panels.

| NSI parameters | $2\sigma$ bounds |
|---|---|
| $\varepsilon'_{ee}$ | (-0.2 , 0.45) |
| $\varepsilon'_{\tau\tau}$ | (-0.02 , 0.175) |
| $\lvert\varepsilon_{e\mu}\rvert$ | <0.1 |
| $\lvert\varepsilon_{e\tau}\rvert$ | <0.3 |
| $\lvert\varepsilon_{\mu\tau}\rvert$ | <0.03 |

Table 6.5: $2\sigma$ bounds on the moduli of the NSI parameters, from [475].

tries in the standard case (fixing all the standard parameters to their best fits[9] but varying the values of $\delta$), while the orange dots are the results obtained in presence of NSI, computed from the number of events corresponding to random flat extraction of the couplings in the ranges shown in Tab.6.5. The sides of the grey rectangles represent the maximum $1\sigma$ error bars on the standard asymmetries at different chosen values of $\delta$ as computed from eq.(6.58). For the sake of illustration, we do not show here the error bars associated to the NSI points because the number of events is not much different from the standard case, thus the error bars in the NSI framework are of the same order of magnitude as the displayed ones.

It is clear that $A_{\mu\tau}$ is very sensitive to New Physics. Indeed, the SM asymmetry has almost a fixed value $A_{\mu\tau} \sim 0.245$, as showed in Fig.6.10, while the NSI contributions can turn $A_{\mu\tau}$ into the range [0.21,0.27]. However, the error bars are much larger than the produced variation, making this asymmetry at the DUNE conditions not useful for discerning new CP phases. Even though the $A_{\mu e}$ asymmetry gets very different values in the standard case (in the range [0.28,0.55]), the inclusion of the NSI is able to even extend the foreseen asymmetry beyond such a range, enough to reach values outside the error bars of the standard asymmetries. The problem in this case is that, as discussed before, we should also take into account the error bars on the orange dots so that, when we include them, also $A_{\mu e}$ cannot give hints of NP at DUNE. Finally, for the $A_{\mu\mu}$ the very same analysis done for $A_{\mu\tau}$ applies.

With a higher energy flux, the results partially differ from what illustrated above (see Fig.6.13). Even though the larger number of events reduces the error bars, the $A_{\mu\tau}$ and $A_{\mu\mu}$ with NSI do not change enough in such a way to be clearly distinguished at an acceptable confidence

[9]We present here only results in Normal Hierarchy, for the Inverted Hierarchy case the conclusions are very similar.

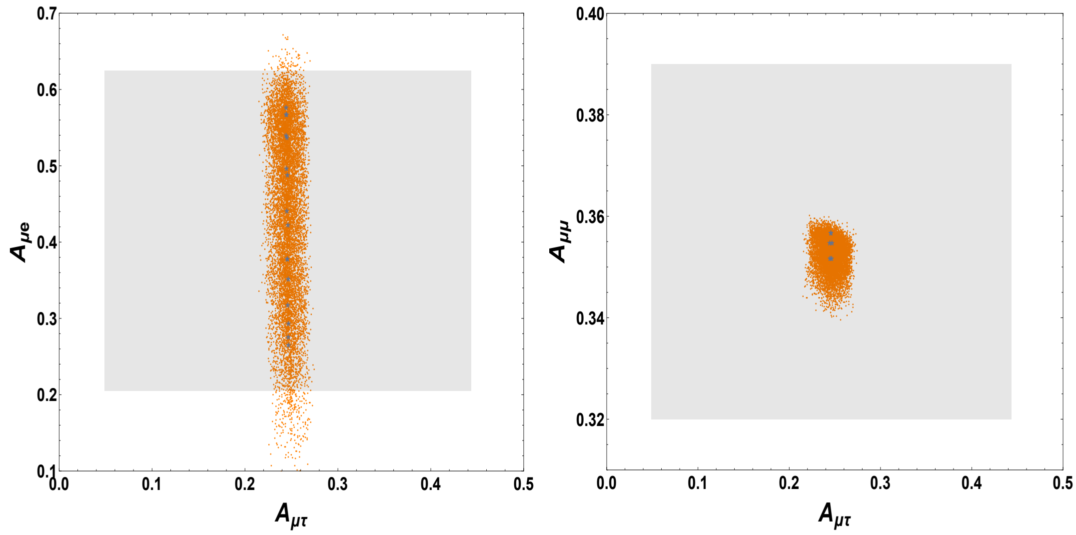


Figure 6.12: Integrated asymmetries in the $(A_{\mu\tau}, A_{\mu e})$ (left plot) and $(A_{\mu\tau}, A_{\mu\mu})$ planes (right plot). Blue stars represent the asymmetries in the SM case while the orange dots are the values obtained in presence of NSI. The grey rectangle shows the $1\sigma$ error range on the standard asymmetries. For sake of simplicity, we do not report here the error bars on the orange dots. Standard neutrino flux has been employed to compute the number of events.

level from the SM case. On the other hand, $A_{\mu e}$ can assume values very different from the SM ones, in particular, a sets of NSI parameters can push it toward negative values. Indeed, as it is clear from eqs.(6.45-6.47), NSI corrections to the asymmetries can be comparable to the SM case when $\varepsilon_{e\mu}$ and $\varepsilon_{e\tau}$ are of $\mathcal{O}(0.1)$. With higher energy fluxes, the appearance transition probabilities are mainly evaluated off peak, making the cosine of $\Delta_{31}$ in eqs.(6.46,6.47) no longer negligible. Thus NSI corrections become more and more important, causing an opposite sign of the asymmetry with respect to the SM case when $\cos(\delta - \delta_{e\mu,\tau})$ terms become negative.

In Fig.6.14, we report our numerical results for the 3+1 case, obtained for fixed $\Delta m^2_{41} = 1$ eV$^2$ and all mixing angles and phases extracted randomly flat in the ranges showed in Tab 6.5. Standard neutrino fluxes have been employed. As previously mentioned, we have four independent asymmetries. Three of them ($A_{\mu e}$, $A_{\mu\mu}$ and $A_{\mu\tau}$) are accessible through the corresponding oscillation channels. The other one, namely $A_{\mu s}$, can be measured looking at the NC events. Indeed, since the NC interactions are flavor independent, the number of events in this channel depends on the sum:

$$N_{NC} \propto P(\nu_\mu \to \nu_e) + P(\nu_\mu \to \nu_\mu) + P(\nu_\mu \to \nu_\tau)\,, \tag{6.59}$$

which, from the unitarity relation, corresponds to $1 - P(\nu_\mu \to \nu_s)$. Thus, the integrated asymmetry

$$A_{NC} = \frac{N_{NC} - \bar{N}_{NC}}{N_{NC} + \bar{N}_{NC}} \tag{6.60}$$

is closely related to the $\mu s$ asymmetry.
We present our results in the $(A_{\mu\tau}, A_{\mu e})$ and $(A_{\mu\mu}, A_{NC})$ planes, see Fig.6.14, for the standard flux. The situation is quite clear: even though the analytic corrections to $A_{\mu e} \sim \mathcal{O}(\lambda)$ and to $A_{\mu\mu,\mu\tau} \sim \mathcal{O}(\lambda^2)$, the relatively large uncertainties do no allow the 3+1 points to spread outside the error bars.

As before, the use of the higher energy flux reduces the error bands and increases the number of points outside the SM uncertainties, see Fig.6.15. Furthermore, as for the NSI case, the asymmetry which vary the most when NP enters into the game is $A_{\mu e}$ since, as shown in (6.53),

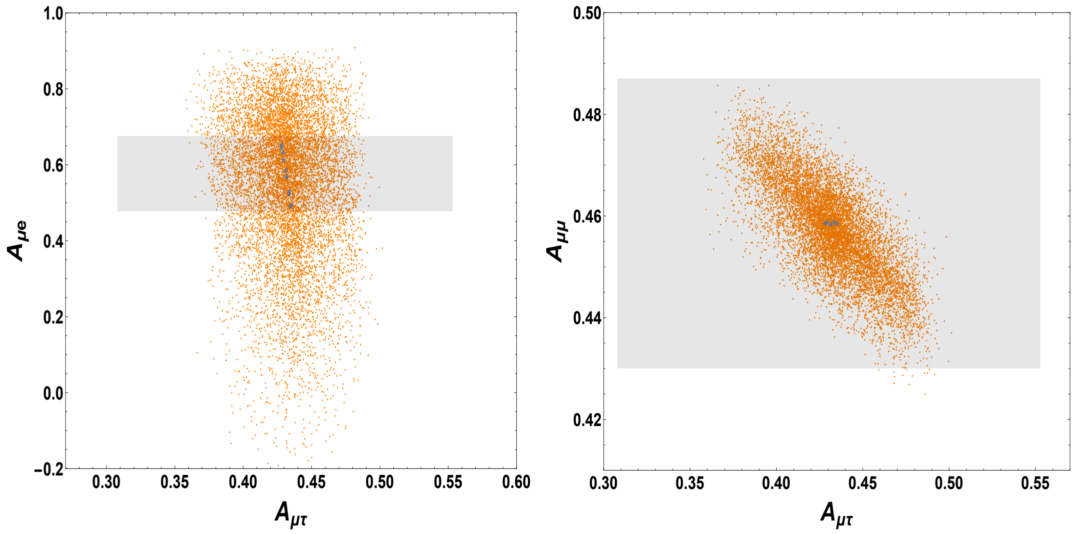


Figure 6.13: Same as Fig.6.12 but using the optimized flux.

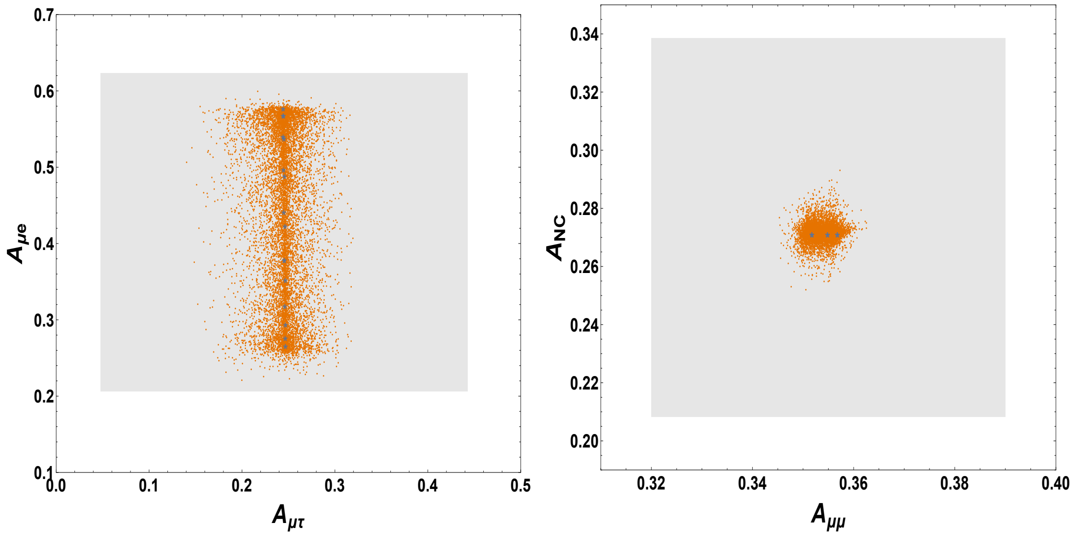


Figure 6.14: Integrated asymmetries in the $(A_{\mu\tau}, A_{\mu e})$ (left plot) and $(A_{\mu\mu}, A_{NC})$ planes (right plot) in the sterile neutrino model. The adopted legend for the symbols is the same as for the other plots. Standard neutrino flux has been employed to compute the number of events.

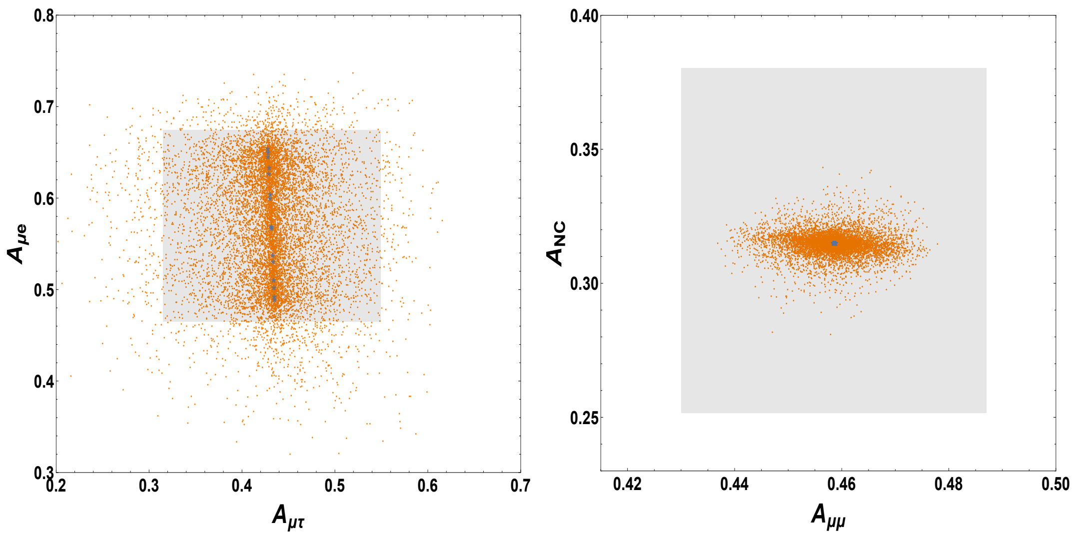


Figure 6.15: Same as Fig.6.14 but for the optimized flux.

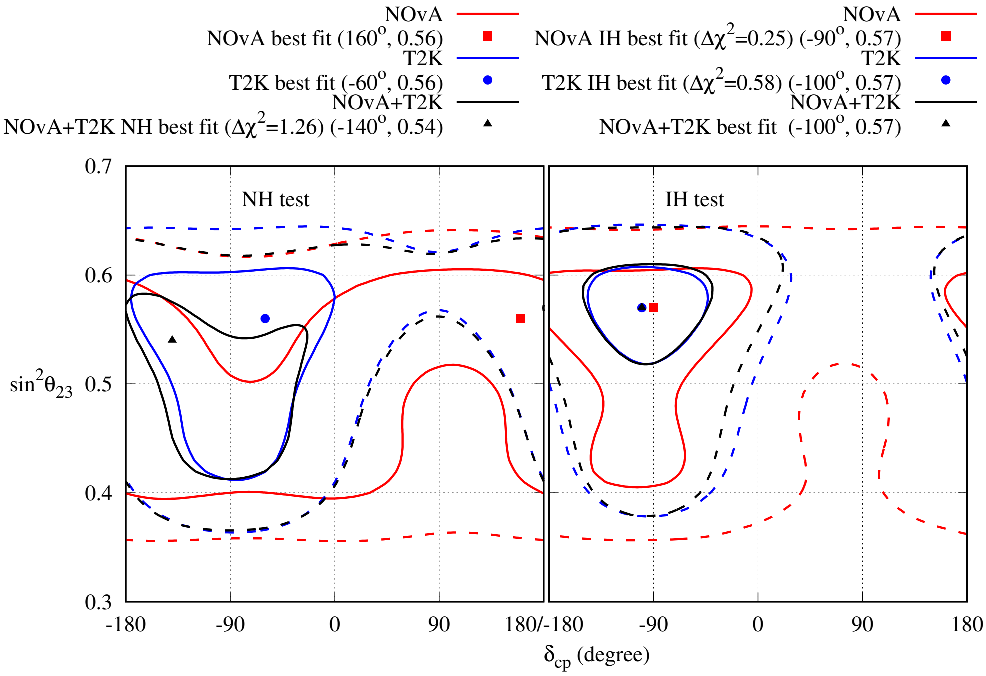


Figure 6.16: T2K (blue) and NO$\nu$A (red) appearance results in the $\delta_{CP}$-$\theta_{23}$ plane for NO (left panel) and IO (right panel). A combined analysis is also shown (black lines). Figure from [155].

the correction to SM asymmetry is at first order in our perturbative expansion. It is clear from the left panel of Fig.6.15 that there are some points at more than two sigmas away from the standard values but, differently from the previous case, $A_{\mu e}$ never becomes negative.
On the other hand, in the $(A_{\mu\mu}, A_{NC})$ plane, no orange point lies outside the grey rectangle.

In conclusion, for both New Physics scenarios, the $A_{\mu e}$ asymmetry can reach values well beyond the Standard Model expectation, including the foreseen statistics and systematic uncertainties, when an high energy flux is employed. A special mention should be devoted to $A_{\mu\tau}$: while analytic considerations indicates that New Physics sets large corrections compared to the Standard Model results, the uncertainties involved in the evaluation of the number of expected events obscure this important feature. An experimental effort should be carried out to reduce the uncertainties in $\tau$ detection. Moreover, further studies should try to find a way to distinguish the different new physics models at the asymmetry level; indeed, our approach can clearly suggest us the presence of BSM effects, but cannot tell us which is th source of such effects.

## 6.4 The T2K-NO$\nu$A tension BSM solutions: differentiating viable models at DUNE

Our last discussion will have as main topic how to distinguish the different models which can (partially) solve the T2K-NO$\nu$A tension. This $2\sigma$ tension [153–155], as already mentioned, is about the first measurement of the PMNS phase. Indeed, the appearance data from T2K seems to favour, in NO, $\delta_{CP}$ values around $3/2\pi$; on the other hand, NO$\nu$A, favours all the other values. We show this in left panel of Fig. 6.16. In IO, on the other hand the tension is much milder (see right panel of Fig. 6.16) and both experiments prefer $\delta_{CP} > \pi$. Different attempts to reduce the tension have been done in the literature [551, 657–662]. We discuss here three BSM scenarios which may reduce the tension: vector and scalar propagation NSI and 3+1 sterile neutrino models.

| | $\varepsilon_{ee}$ | $\varepsilon_{\tau\tau}$ | $\varepsilon_{e\mu}$ | $\varepsilon_{e\tau}$ | $\varepsilon_{\mu\tau}$ |
|---|---|---|---|---|---|
| LMA | [-0.31,0.40] | [-0.11,0.15] | [-0.11,0.02] | [-0.12,0.10] | [-0.004,0.011] |
| LMA-Dark | [-2.40,-1.70] | [-0.01,0.01] | [0.00,0.11] | [-0.13,0.13] | [-0.011,0.008] |

Table 6.6: The constraints at 90% for parameters taken one at a time for the Earth from [477]. The upper line is for the standard solution and the lower line is for $\Delta m^2_{21} < 0$ and the opposite sign on the atmospheric mass ordering.

### 6.4.1 Vector propagation NSI

Since the introduction of the matter effects in neutrino oscillations, the possibility that neutrinos can undergo NSIs with matter has been widely studied. As already mentioned in Sec. 3.2.2, we can describe them using an effective theory approach, including in the Lagrangian the following terms

$$\mathcal{L}^{eff}_{\rm NSI} = -2\sqrt{2}G_F \sum_{f,\alpha,\beta} \varepsilon^f_{\alpha\beta}(\bar{\nu}_\alpha\gamma_\rho\nu_\beta)(\bar{f}\gamma^\rho f)\,, \tag{6.61}$$

where $G_F$ is the Fermi constant, $\varepsilon^f_{\alpha\beta}$ is the parameter which describes the strength of the NSI, $f$ is a first generation SM fermion ($e$, $u$, or $d$) and $\alpha$ and $\beta$ denote the neutrino flavors $e$, $\mu$ or $\tau$. The $\varepsilon$ parameter can be related to the parameters in a simplified model or even a UV complete scenarios, since these details do not affect oscillations, we focus only on the $\varepsilon$ effective parameter. The presence of such interactions modifies the neutrino oscillation Hamiltonian to

$$H = \frac{1}{2E}\left[UM^2U^\dagger + a\begin{pmatrix} 1+\varepsilon_{ee} & \varepsilon_{e\mu} & \varepsilon_{e\tau} \\ \varepsilon^*_{e\mu} & \varepsilon_{\mu\mu} & \varepsilon_{\mu\tau} \\ \varepsilon^*_{e\tau} & \varepsilon^*_{\mu\tau} & \varepsilon_{\tau\tau}\end{pmatrix}\right], \tag{6.62}$$

where $U$ is the PMNS matrix [11, 663], $M^2 = \mathrm{diag}(0, \Delta m^2_{21}, \Delta m^2_{31})$, $a = 2\sqrt{2}G_F N_e E$, and $N_e$ is the electron number density. Due to the hermiticity of the Hamiltonian matrix, the diagonal NSI couplings $\varepsilon_{\alpha\alpha}$ must be real, while the non-diagonal ones are in general complex and can be written as $\varepsilon_{\alpha\beta} = |\varepsilon_{\alpha\beta}|e^{i\phi_{\alpha\beta}}$. Since we can subtract a matrix proportional to the identity without changing the oscillation probabilities, only two of the diagonal NSI parameters are independent. Without loss of generality we will focus on $\varepsilon_{ee}$ and $\varepsilon_{\tau\tau}$ for concreteness.

Various analyses of oscillation data[10] have been considered under different assumptions. A recent global analysis of oscillation data in the context of NSIs has estimated the constraints on the NSI parameters when translated to the Earth's crust [477] shown in table 6.6. Both LMA and LMA-Dark results are shown, with the difference mainly affecting $\varepsilon_{ee}$. The LMA-Dark solution [22, 468–470, 655, 672–675] is the solution with $\varepsilon_{ee} \simeq -2$ and the opposite sign[11] on $\Delta m^2_{31}$, $\Delta m^2_{21}$, and $\delta$. For a recent discussion of LMA-Dark in the context of the latest reactor constraints see [22].

Naively it would appear that charged lepton flavor violating constraints would be much stronger than those from oscillations, but numerous UV complete models with large $\varepsilon_{\alpha\beta} \gtrsim 0.1$ exist in the literature [236–239, 241, 444–447]. All of these models can be recast into the language of NSI which is exactly what makes NSI such an attractive BSM scenario to investigate.

Considering the same expansion in small parameters presented in the previous sections (see Sec. 6.3) and expanding also up to the second order in the NSI couplings, we obtain for the

[10] Scattering data are also sensitive to NSI [22, 470, 472, 473, 491, 664], although these data sets have a non-trivial dependence on the mediator mass, while oscillation data are essentially [240, 242, 665–671] independent on it.

[11] We take the definition of the three mass eigenstates as $|U_{e1}| > |U_{e2}| > |U_{e3}|$. Thus $\theta_{12} < 45°$ by definition and the sign of $\Delta m^2_{21}$ has been measured experimentally with solar neutrinos. Some define the mass eigenstates by $m_1 < m_2$, $|U_{e1}| > |U_{e3}|$, and $|U_{e2}| > |U_{e3}|$. In this case $\Delta m^2_{21} > 0$ by definition and the octant of $\theta_{12}$ is to be determined experimentally. See [675, 676].

electron appearance as corrections to the standard model probability,

$$
\begin{aligned}
P(\nu_\mu \to \nu_e)^{NSI} = & \frac{4}{3} V \alpha \Delta_{31} [\Delta_{31}(\varepsilon_{e\tau}\cos\phi_{e\tau} - \varepsilon_{e\mu}\cos\phi_{e\mu}) \\
& - \sin\Delta_{31}\varepsilon_{e\tau}(\cos\Delta_{31}\cos\phi_{e\tau} - \sin\Delta_{31}\sin\phi_{e\tau}) \\
& - \sin\Delta_{31}\varepsilon_{e\mu}(\cos\Delta_{31}\cos\phi_{e\mu} - \sin\Delta_{31}\sin\phi_{e\mu})] \\
& - 2Vr\sin\Delta_{31}[\Delta_{31}\cos\Delta_{31}(\varepsilon_{e\mu}\cos(\delta-\phi_{e\mu}) - \varepsilon_{e\tau}\cos(\delta-\phi_{e\tau})) \\
& + \Delta_{31}\sin\Delta_{31}(\varepsilon_{e\tau}\sin(\delta-\phi_{e\tau}) - \varepsilon_{e\mu}\sin(\delta-\phi_{e\mu})) \\
& + \sin\Delta_{31}(\varepsilon_{e\mu}\cos(\delta-\phi_{e\mu}) + \varepsilon_{e\tau}\cos(\delta-\phi_{e\tau}))] \,.
\end{aligned} \tag{6.63}
$$

We observe that, at the perturbative order taken into account, the probability depends on $\varepsilon_{e\mu}$ and $\varepsilon_{e\tau}$ only. In particular, if $\phi_{e\tau} = \phi_{e\mu}$, the only relevant combinations are $\varepsilon_{e\mu}+\varepsilon_{e\tau}$ and $\varepsilon_{e\mu}-\varepsilon_{e\tau}$. The same happens if $\phi_{e\mu} = \pi + \phi_{e\tau}$. For the muon disappearance channel, the NSI contribution is

$$
\begin{aligned}
P(\nu_\mu \to \nu_\mu)^{NSI} = V\Bigg\{ & -8\Delta_{31}\varepsilon_{\mu\tau}\cos\phi_{\mu\tau}\cos\Delta_{31}\sin\Delta_{31} + \frac{4}{3}\alpha\Delta_{31}^2[\varepsilon_{e\tau}\cos\phi_{e\tau}\cos^2\Delta_{31} \\
& - \varepsilon_{e\mu}\cos\phi_{e\mu}\cos^2\Delta_{31} + 4\varepsilon_{\mu\tau}\cos\phi_{\mu\tau}(1-2\sin^2\Delta_{31})] \\
& + 4t\Delta_{31}\varepsilon_{\tau\tau}\cos\Delta_{31}\sin\Delta_{31} \\
& + 4r\Delta_{31}\varepsilon_{e\mu}\cos(\delta-\phi_{e\mu})\cos\Delta_{31}\sin\Delta_{31} - 4a\varepsilon_{\tau\tau}\sin^2\Delta_{31} \\
& + \frac{4}{3}\alpha\Delta_{31}[\varepsilon_{e\tau}\cos\phi_{e\tau}\cos\Delta_{31}\sin\Delta_{31} - \varepsilon_{e\mu}\cos\phi_{e\mu}\cos\Delta_{31}\sin\Delta_{31}]\Bigg\} \,.
\end{aligned} \tag{6.64}
$$

Compared to the previous case, all NSI parameters but $\varepsilon_{ee}$ contribute. However, the term in $\varepsilon_{\mu\tau}$ is not suppressed by any of the small parameters $r$, $s$ and $t$. Thus, this probability is expected to be more sensitive to $\varepsilon_{\mu\tau}$ and its phase. The modification of the probabilities, in particular to the appearance one, may go in the same direction of the T2K-NO$\nu$A tension. This can happen, for instance, since at NO$\nu$A and T2K, the matter effects are very different. In the former case, we have a longer baseline, 810 km, with a matter density of 2.84 $g/cc$; in the latter case, the baseline is reduced almost by a factor of 3 (295 km) and the matter density is 2.6 $g/cc$. It has been shown in [657] that in presence of a non-vanishing $\varepsilon_{e\beta}$ with $\beta = \mu, \tau$, if the matter potential are different, two experiments can measure two separate values of the PMNS phase. In particular, it holds that

$$
|\varepsilon_{e\beta}| \sim \frac{s_{12}c_{12}c_{23}\pi\Delta m_{21}^2}{2s_{23}w_\beta}\left|\frac{\sin\delta_{T2K} - \sin\delta_{NO\nu A}}{a_{T2K} - a_{NO\nu A}}\right| \tag{6.65}
$$

where, $w_\beta = s_{23}\,(c_{23})$ for $\beta = \mu\,(\tau)$. Given the results of the two experiments, we expect that $|\varepsilon_{e\beta}| \sim 0.2$ may reduce the tension. Performing a fit on the appearance data of the two LBL experiment, authors of [657] found the results in Tab. 6.7 for different choices of the non-vanishing off-diagonal vector NSI parameters.

It is clear that in NO, when $\varepsilon_{e\mu}$ ($\varepsilon_{e\tau}$) is turned on, the fit is significantly better than the one performed with the SM, namely $\Delta\chi^2 = \chi^2_{SM} - \chi^2_{NSI} = 4.44\,(3.65)$. The best fit values for the magnitude of the NSI couplings is the one expected analitically. The other best fits can improve the fit, but not significantly. It is however interesting to notice that all possible scenarios improves the SM fit.

### 6.4.2 Scalar NSI

In addition to a vector mediator, one can consider different Lorentz structure for the underlying theory behind a new neutrino interaction (see Sec. 3.2.3). Scalar NSI has been investigated

| MO | NSI | $\lvert\epsilon_{\alpha\beta}\rvert$ | $\phi_{\alpha\beta}/\pi$ | $\delta/\pi$ | $\Delta\chi^2$ |
|---|---|---|---|---|---|
| NO | $\epsilon_{e\mu}$ | 0.19 | 1.50 | 1.46 | 4.44 |
| | $\epsilon_{e\tau}$ | 0.28 | 1.60 | 1.46 | 3.65 |
| | $\epsilon_{\mu\tau}$ | 0.35 | 0.60 | 1.83 | 0.90 |
| IO | $\epsilon_{e\mu}$ | 0.04 | 1.50 | 1.52 | 0.23 |
| | $\epsilon_{e\tau}$ | 0.15 | 1.46 | 1.59 | 0.69 |
| | $\epsilon_{\mu\tau}$ | 0.17 | 0.14 | 1.51 | 1.03 |

Table 6.7: Best fit values to NOvA and T2K data and $\Delta\chi^2 = \chi^2_{\rm SM} - \chi^2_{\rm NSI}$ for a fixed MO considering one complex vector NSI parameter at a time.

in the context of some neutrino oscillation experiments as well as early universe constraints [243, 499, 670, 677–679]. All previous studies, to our knowledge, focused on the diagonal scalar NSI parameters; we focus on the off-diagonal parameters. Early universe constraints and fifth-force probes may be stronger than terrestrial probes in many cases, although not necessarily all, depending primarily on the mediator mass [670]. That said, we do caution the reader to be aware of important non-oscillation constraints on scalar NSI.

The effective Lagrangian for scalar NSI is

$$\mathcal{L}^{eff}_{\text{scalar NSI}} = y_f Y_{\alpha\beta}(\bar{\nu}_\alpha \nu_\beta)(\bar{f} f)\,, \tag{6.66}$$

which is no longer a matter potential, but it can be seen as a Yukawa interaction term for Dirac neutrinos that induces a mass term that depends on the density of fermions sourcing the term. The Hamiltonian governing neutrino oscillations is modified from the the diagonal $M^2$ term to $(M + \delta M)(M + \delta M)^\dagger$. We then parameterize the correction term $\delta M$ as

$$\delta M = \sqrt{|\Delta m^2_{31}|}\begin{pmatrix} \eta_{ee} & \eta_{e\mu} & \eta_{e\tau} \\ \eta^*_{e\mu} & \eta_{\mu\mu} & \eta_{\mu\tau} \\ \eta^*_{e\tau} & \eta^*_{\mu\tau} & \eta_{\tau\tau} \end{pmatrix}\,, \tag{6.67}$$

where we have chosen to scale the size of $\delta M$ relative to $\sqrt{|\Delta m^2_{31}|}$ to make the parameters of the model, $\eta_{\alpha\beta}$, dimensionless. We have also chosen to make $\delta M$ Hermitian although it need not be (see e.g. [680]) depending on if the scalar mediator is real or complex; we encourage further research into the non-Hermitian case. Unlike in the vector case with the $\varepsilon_{\alpha\beta}$ parameters, $\eta_{\alpha\beta}$, are proportional to the matter density. As in the vector case, the diagonal parameters are real while the off-diagonal elements are complex, $\eta_{\alpha\beta} = |\eta_{\alpha\beta}|e^{i\phi_{\alpha\beta}}$. To be explicit, we can relate these $\eta_{\alpha\beta}$ parameters to the parameters of the underlying theory as

$$\eta_{\alpha\beta} = \frac{1}{m^2_\phi \sqrt{|\Delta m^2_{31}|}} \sum_f n_f y_f Y_{\alpha\beta}\,. \tag{6.68}$$

We will also later rescale all $\eta_{\alpha\beta} \to \eta_{\alpha\beta}(3)$ relative to a density at 3 g/cm$^3$ for the self-consistent comparison among different experiments at different densities. While the effect of this rescaling is minimal in long-baseline experiments as their densities are similar, it is essential in order to perform a correct comparison, and would have a larger effect when also considering atmospheric neutrinos and/or solar neutrinos. As discussed in Sec. 3.2.3, in this case, the oscillation probabilities depend also on the lightest of the neutrino masses.

Using the same expansion procedure described in the previous section and expanding up to the second order also in the parameter $\eta_{ij}$ it is possible to obtain approximate expressions also for the scalar NSI case see Ref. [499]. In order to avoid cumbersome expressions, we did not show here the effect of the solar mass splitting and of the lightest neutrino mass. In this context, neglecting the solar mass splitting which would complicate significantly the formulae, the correction to the the appearance probability in presence of scalar NSI is

$$
\begin{aligned}
P(\nu_\mu \to \nu_e)^{NSI} = & [\eta_{e\mu}^2 + \eta_{e\tau}^2 + 2r\eta_{e\mu}\cos(\delta+\phi_{12}) + 2r\eta_{e\tau}\cos(\delta+\phi_{13})]\sin^2\Delta_{13} + \\
& + 2\eta_{e\mu}\eta_{e\tau}\cos(\phi_{12}-\phi_{13})\sin^2\Delta_{13} + \\
& - 2V[\eta_{e\mu}^2 + \eta_{e\tau}^2 + 2r\eta_{e\mu}\cos(\delta+\phi_{12}) + 2r\eta_{e\tau}\cos(\delta+\phi_{13})]\times \\
& \times [\Delta_{13}\cos\Delta_{13}\sin\Delta_{13} - \sin^2\Delta_{13}] + \\
& - 2V\eta_{e\mu}\eta_{e\tau}\cos(\phi_{12}-\phi_{13})\sin^2\Delta_{13}[\Delta_{13}\cos\Delta_{13}\sin\Delta_{13} - \sin^2\Delta_{13}]\,.
\end{aligned}
\tag{6.69}
$$

It can be noticed that the probability depends only on $\eta_{e\mu}$ and $\eta_{e\tau}$. Both parameters appears in second order terms, proportional to $\eta^2$ or to $r\eta$.

The $\nu_\mu$ disappearance probability, on the other hand, can be written as

$$
\begin{aligned}
P(\nu_\mu \to \nu_\mu)^{NSI} = & -\Delta_{13}(\eta_{\mu\mu} + \eta_{\tau\tau} + 2\eta_{\mu\tau}\cos\phi_{\mu\tau})\sin 2\Delta_{13} + \\
& - \frac{1}{2}\Delta_{13}(\eta_{e\mu}^2 + \eta_{e\tau}^2 + 4\eta_{\mu\tau}^2\sin\phi_{\mu\tau}^2)\sin 2\Delta_{13} + \\
& - 4\Delta_{13}^2\eta_{\mu\tau}^2\cos\phi_{\mu\tau}^2\sin 2\Delta_{13} + \\
& + \frac{1}{2}(\eta_{\mu\mu}^2 + \eta_{\tau\tau}^2)[1 - (1-\Delta_{13}^2)\cos 2\Delta_{13} - \Delta_{13}\sin 2\Delta_{13}] + \\
& - 2\Delta_{13}[r\eta_{e\mu}\cos(\delta-\phi_{e\mu}) + r\eta_{e\tau}\cos(\delta+\phi_{e\tau})]\sin 2\Delta_{13} + \\
& + 2t(\eta_{\tau\tau} - \eta_{\mu\mu})[-1 + \cos 2\Delta_{13} + \Delta_{13}\sin 2\Delta_{13}] + \\
& - 3\Delta_{13}\eta_{e\mu}\eta_{e\tau}\cos(\phi_{e\mu} - \phi_{e\tau})\sin 2\Delta_{13} + \\
& - 2\Delta_{13}\eta_{\mu\mu}\eta_{\mu\tau}\cos\phi_{\mu\tau}(2\Delta_{13}\cos 2\Delta_{13} + \sin 2\Delta_{13}) + \\
& + \eta_{\mu\mu}\eta_{\tau\tau}[-1 + (1-2\Delta_{13}^2)\cos 2\Delta_{13} + \Delta_{13}\sin 2\Delta_{13}] + \\
& - 2\Delta_{13}\eta_{\mu\tau}\eta_{\tau\tau}\cos\phi_{\mu\tau}(2\Delta_{13}\cos 2\Delta_{13} + \sin 2\Delta_{13})
\end{aligned}
\tag{6.70}
$$

In this case, all the scalar NSI parameters but $\eta_{ee}$ appear. $\eta_{\mu\mu}$, $\eta_{\tau\tau}$ and $\eta_{\mu\tau}$ modify the probability at the first order in perturbation theory; we expect them to strongly affect the $\Delta m_{13}^2$ measurement, since they are strongly correlated to the quantity $\sin 2\Delta_{13}$. Apart from the atmospheric mass splitting, the scalar NSI parameters in this probability appear coupled also to $r$ and $t$. Notice that, in our analytical approach, the probabilities are symmetric under the $\eta_{e\tau}$-$\eta_{e\mu}$ exchange.

Also in this case, depending the scalar NSI parameters on the matter density, two different experiments like T2K and NO$\nu$A may perform two different $\delta_{CP}$ measurements in presence of this new kind of interactions. We redo the analysis described in [657] in the context of vector NSI, also for scalar NSI. We show our results in Fig. 6.17 and in Tab. 6.8, where we also consider different values of the lightest neutrino mass.

We make some comments on these results. We note that the IO is always preferred over the NO, but at even lower significance than for vector NSI. In addition, we also recall that SuperK's atmospheric data prefers the NO [111, 657, 681] and will be affected by scalar NSI in quite a different fashion to long-baseline data [243, 499]. Thus we find that scalar NSI is not a satisfactory improvement to the slight NOvA and T2K tension, but we can still regard the best fit points as valuable benchmarks moving forward.

Unlike in vector NSI, for scalar NSI the absolute neutrino mass scale plays a role. In general the effect of $m_{\text{lightest}}$, even to values quite a bit larger than allowed by cosmology [682] where the upper limit is $\sim$few$\times 10^{-2}$ eV, on the results is quite small. That said, in some cases we see that the best fit value changes by a fair amount as $m_{\text{lightest}}$ changes; this is due to the existence of multiple quasi-degenerate local minima that slightly change as $m_{\text{lightest}}$ changes.

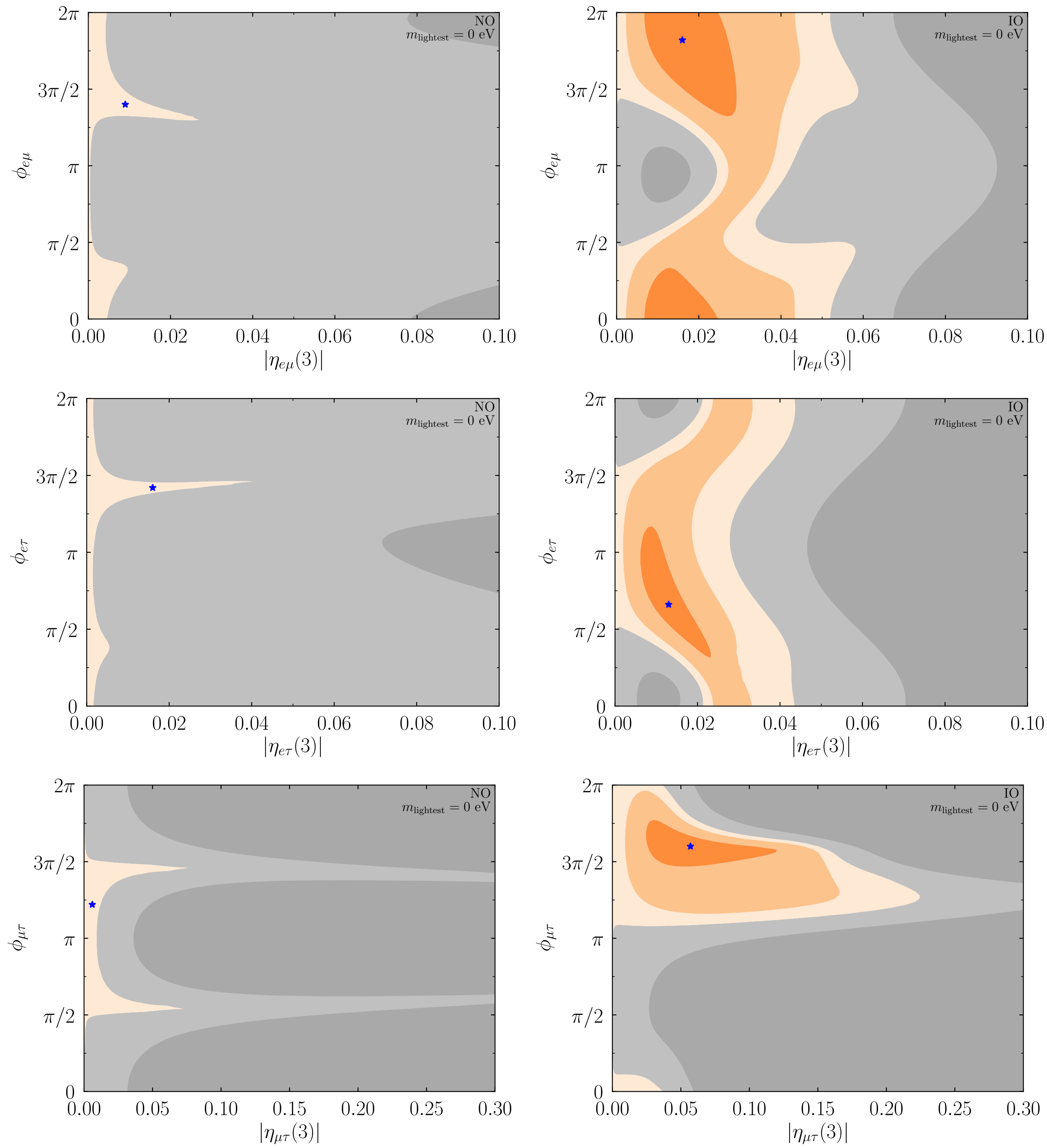


Figure 6.17: The preferred and disfavored regions of scalar NSI given by NOvA and T2K data with information from Daya Bay and KamLAND data as well. $\Delta m^2_{31}$, $\theta_{23}$, and $\delta$ are minimized over and $\theta_{13}$, $\theta_{12}$, and $\Delta m^2_{21}$ are fixed to the best fit values from Daya Bay and KamLAND. The top, middle, and bottom rows correspond to $\eta_{e\mu}(3)$, $\eta_{e\tau}(3)$, and $\eta_{\mu\tau}(3)$ respectively, and the left and right columns correspond to the NO and IO respectively. The mass of the lightest neutrino is taken to be zero here. The (3) refers to the fact that the scalar NSI parameters are plotted as rescaled to a density of 3 g/cm$^3$. The blue stars are the best fit points, the light gray regions are slightly disfavored and the dark gray regions are disfavored at 68% CL. The successive orange colors represent integer units of $\Delta\chi^2$.

$m_{\text{lightest}} = 0$ eV

| MO | NSI | $\lvert\eta_{\alpha\beta}(3)\rvert$ | $\phi_{\alpha\beta}/\pi$ | $\delta/\pi$ | $\Delta\chi^2$ |
|---|---|---|---|---|---|
| NO | $\eta_{e\mu}(3)$ | 0.009 | 1.40 | 1.17 | 0.04 |
| | $\eta_{e\tau}(3)$ | 0.016 | 1.42 | 1.10 | 0.02 |
| | $\eta_{\mu\tau}(3)$ | 0.006 | 1.22 | 1.11 | 0.08 |
| IO | $\eta_{e\mu}(3)$ | 0.016 | 1.82 | 1.86 | 2.33 |
| | $\eta_{e\tau}(3)$ | 0.013 | 0.66 | 1.89 | 2.20 |
| | $\eta_{\mu\tau}(3)$ | 0.057 | 1.60 | 1.85 | 2.33 |

$m_{\text{lightest}} = 0.05$ eV

| MO | NSI | $\lvert\eta_{\alpha\beta}(3)\rvert$ | $\phi_{\alpha\beta}/\pi$ | $\delta/\pi$ | $\Delta\chi^2$ |
|---|---|---|---|---|---|
| NO | $\eta_{e\mu}(3)$ | 0.002 | 1.66 | 1.18 | 0.10 |
| | $\eta_{e\tau}(3)$ | 0.003 | 0.62 | 1.13 | 0.08 |
| | $\eta_{\mu\tau}(3)$ | 0.009 | 0.56 | 1.17 | 0.06 |
| IO | $\eta_{e\mu}(3)$ | 0.010 | 1.72 | 1.88 | 2.21 |
| | $\eta_{e\tau}(3)$ | 0.010 | 0.58 | 1.90 | 2.18 |
| | $\eta_{\mu\tau}(3)$ | 0.033 | 1.58 | 1.79 | 2.36 |

$m_{\text{lightest}} = 0.10$ eV

| MO | NSI | $\lvert\eta_{\alpha\beta}(3)\rvert$ | $\phi_{\alpha\beta}/\pi$ | $\delta/\pi$ | $\Delta\chi^2$ |
|---|---|---|---|---|---|
| NO | $\eta_{e\mu}(3)$ | 0.001 | 1.74 | 1.17 | 0.12 |
| | $\eta_{e\tau}(3)$ | 0.002 | 0.64 | 1.14 | 0.11 |
| | $\eta_{\mu\tau}(3)$ | 0.006 | 0.56 | 1.19 | 0.06 |
| IO | $\eta_{e\mu}(3)$ | 0.006 | 1.72 | 1.86 | 2.20 |
| | $\eta_{e\tau}(3)$ | 0.006 | 0.60 | 1.88 | 2.19 |
| | $\eta_{\mu\tau}(3)$ | 0.024 | 1.56 | 1.83 | 2.36 |

Table 6.8: Best fit values to NOvA and T2K data and $\Delta\chi^2 = \chi^2_{\text{SM}} - \chi^2_{\text{NSI}}$ for a fixed MO considering one complex scalar NSI parameter at a time, rescaled to what it would be for a density of 3 g/cm$^3$ for various values of $m_{\text{lightest}}$. (For the SM, $\chi^2_{\text{NO}} - \chi^2_{\text{IO}} = 2.3$ .)

### 6.4.3 Sterile neutrinos

Sterile neutrinos are a simple, phenomenologically rich, and theoretically and experimentally motivated extension to the standard three-flavor neutrino scenario. Since neutrinos have mass, there are additional particles and sterile neutrinos are present in many of the explanations. In addition, there are numerous hints of various significances (see Sec. 3.1) and robustness that indicates that new light ($m_4 \lesssim 10$ eV) neutrinos may exist [228, 229, 231, 232, 683–685] although strong constraints also exist [414, 552, 686], see refs. [117, 409, 415, 420–423] for recent reviews. Sterile neutrinos also play a role in long-baseline accelerator neutrino experiments, although typically at somewhat lighter masses than the above hints $\sim 1$ eV [418, 419, 424–427, 637, 659, 687–703]. We focus on the scenario with a single light sterile neutrino which modifies the neutrino oscillation Hamiltonian to

$$H = \frac{1}{2E}\left[U_4 \begin{pmatrix} 0 & & & \\ & \Delta m^2_{21} & & \\ & & \Delta m^2_{31} & \\ & & & \Delta m^2_{41} \end{pmatrix} U_4^\dagger + \begin{pmatrix} V-V' & & & \\ & -V' & & \\ & & -V' & \\ & & & 0 \end{pmatrix}\right], \tag{6.71}$$

where

$$U_4 \equiv R_{34}(\theta_{34})R_{24}(\theta_{24})R_{14}(\theta_{14})U_{23}(\theta_{23},\delta_{23})U_{13}(\theta_{13},\delta_{13})U_{12}(\theta_{12},\delta_{12})\,, \tag{6.72}$$

the relevant $2\times 2$ submatrix of $U_{ij}$ is

$$U_{ij}(\theta_{ij},\delta_{ij}) = \begin{pmatrix} c_{ij} & s_{ij}e^{-i\delta_{ij}} \\ -s_{ij}e^{i\delta_{ij}} & c_{ij} \end{pmatrix}, \tag{6.73}$$

and $R_{ij}(\theta_{ij}) = U_{ij}(\theta_{ij},0)$. At the probability level, performing the same expansion discussed above and expanding up to the second order also in the small $s_{i4} = \sin\theta_{i4}$ angles, we obtain as correction to the standard oscillation probabilities

$$P^{3+1}_{\nu_\mu\to\nu_e} = 0 \tag{6.74}$$

and

$$P^{3+1}_{\nu_\mu\to\nu_\mu} = -\,2s_{24}^2\cos^2\Delta_{31} - 2V'\Delta_{31}s_{24}s_{34}\cos\delta_{23}\sin 2\Delta_{31}\,. \tag{6.75}$$

where $V'$ is the NC matter potential, which appears in the probabilities due to the presence of a fourth sterile state. Notice that given our PMNS parameterization, in the standard model probabilities we should substitute the usual 3×3 phase $\delta_{CP}$ with the combination $\delta_{12}+\delta_{13}-\delta_{23}$. It is clear that, at our expansion order, only $\theta_{24}$ modifies the disappearance probabilities, multiplied however to the small (at the atmospheric peak) $\cos^2\Delta_{31}$. For this reason, the NOvA and T2K data are not substantially improved by the addition of a light sterile neutrino; one can nonetheless perform the analysis. In Ref. [659] they considered a benchmark point of $\theta_{14} = \theta_{24} = 8^\circ$ and $\theta_{34} = 0$ with $\Delta m^2_{41} = 1$ eV$^2$. We note that long-baseline experiments are not particularly sensitive to the value of $\Delta m^2_{41}$ so long as it is well above $\Delta m^2_{31}$. Meanwhile, these values of the two non-zero sterile mixing angles, $\theta_{14}$ and $\theta_{24}$ are near the existing limits from solar data [704] and long-baseline disappearance data [552] respectively. We then consider two benchmark points for each mass ordering and complex phases from a fit to to NOvA and T2K data which is somewhat constraining for $\delta_{13}$, the usual CP phase, it is not constraining for $\delta_{14}$, a new CP phase that is physical due to the fourth neutrino. The benchmark points are then shown in table 6.9.

| MO | $\Delta m^2_{41}$ [eV$^2$] | $\theta_{14}$ | $\theta_{24}$ | $\delta_{13}/\pi$ | $\delta_{12}/\pi$ |
|---|---|---|---|---|---|
| NO | 1 | 8° | 8° | 1.9 | 0.7 |
| IO | 1 | 8° | 8° | 0 | 0.5 |

Table 6.9: Benchmark sterile neutrino parameters from NOvA and T2K data from Ref. [659].Sterile parameters not shown are zero and standard oscillation parameters not shown are taken to the standard values from [111].

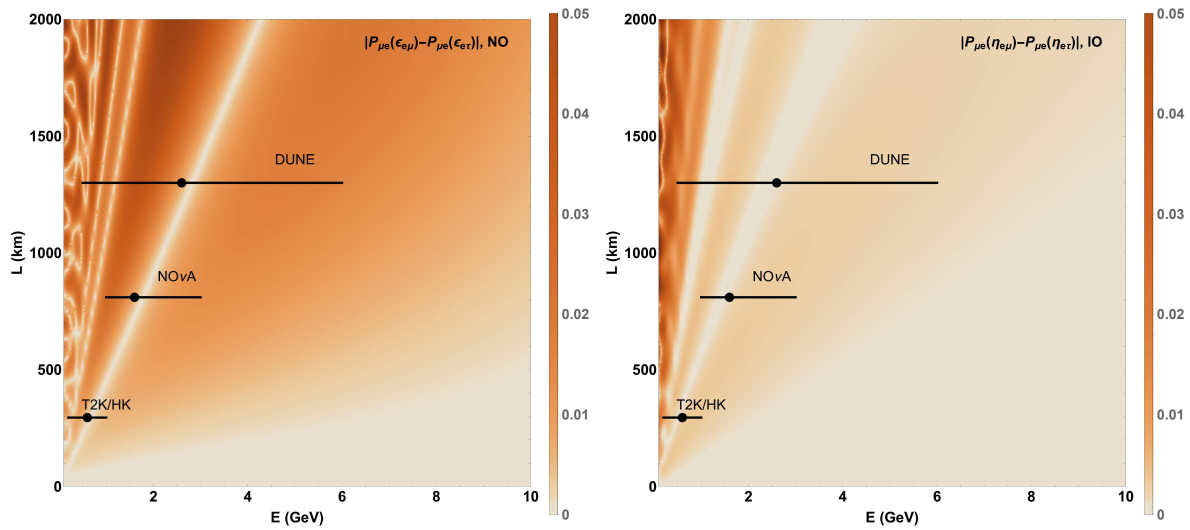


Figure 6.18: The difference in neutrino appearance probabilities for two benchmark cases (see table 6.7 as a function of baseline and neutrino energy. On the left the difference is between the probabilities with vector NSI and $\varepsilon_{e\mu}$ and $\varepsilon_{e\tau}$ in normal ordering and the right is between probabilities with scalar NSI and $\eta_{e\mu}$ and $\eta_{e\tau}$ in inverted ordering. The regions probed by the different long-baseline experiments are indicated. The density is taken to be that for DUNE, 2.848 g/cm$^3$, throughout.

### 6.4.4 DUNE sensitivity to T2K-NO$\nu$A analysis benchmark models

We have shown that different CP-violating models can be used to assess the T2K-NO$\nu$A tension. This basically means that these two long baseline experiments should not be able to distinguish at a considerable confidence level such models. Moreover, due to the relatively small $\Delta\chi^2$ values with respect to the SM, we can also say that the considered models cannot be discerned by the standard oscillation at a good confidence level. We can now ask ourselves if, on the other hand, the more performing DUNE experiment may have better performances in probing the benchmark values. We expect that this can happen, as we can see in Fig. 6.18, where we plot at the appearance probability level, which are the differences between two benchmark values in the vector and scalar NSI models. In particular, we plot $P_{\mu e}(\varepsilon_{e\mu}) - P_{\mu e}(\varepsilon_{e\tau})$ in NO and $P_{\mu e}(\eta_{e\mu}) - P_{\mu e}(\eta_{e\tau})$ in IO. It is clear that at the atmospheric peak, the differences between the probabilities are very small; however, the DUNE broad band beam is able to cover a wide range of L/E so that the differences become more important.

#### Vector NSI

We discuss here the performances of the DUNE Far Detector in constraining the NSI parameters in the benchmark scenarios discussed above. For the vector NSI case, we observe that the most interesting results are obtained when the mass ordering is normal, since the $\Delta\chi^2$-s with respect to the standard model, when the fits are performed considering $\varepsilon_{e\mu}$ and $\varepsilon_{e\tau}$, are respectively 4.44 and 3.65 (see table 6.7 taken from [657]); however, for sake of completeness, we show the results considering also the IO scenarios. Fig. 6.19 shows the DUNE allowed regions at 68, 90, and 99% CL in the $(\varepsilon_{\alpha\beta} - \phi_{\alpha\beta})$. The top (bottom) panels show the results using the NO (IO) hypothesis.

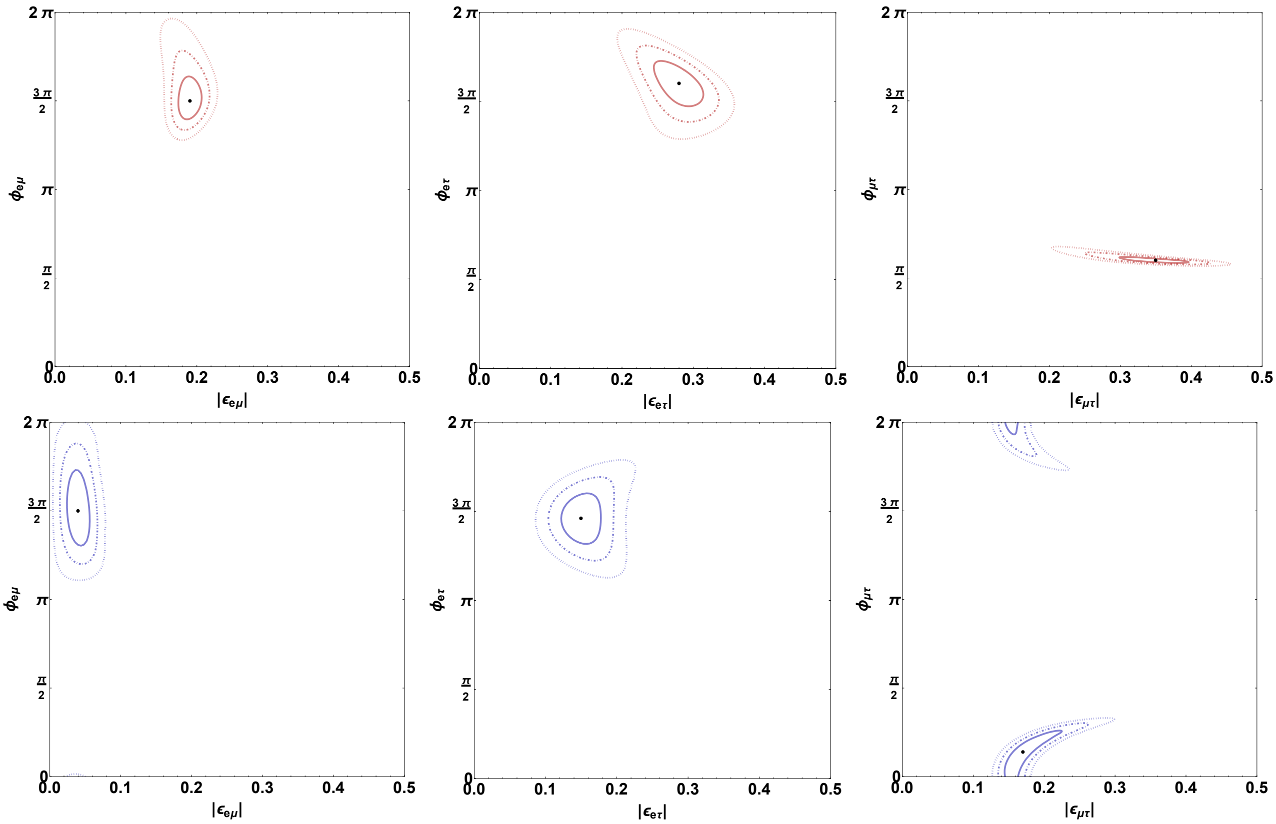


Figure 6.19: 68% (solid lines), 95% (dashed lines) and 99% (dotted lines) contours in DUNE in the vector NSI $(|\varepsilon_{ij}| - \phi_{ij})$-planes when data are generated using vector NSI best fits considering one parameter at a time. The top (bottom) panels with red (blue) contours have been obtained usign NO (IO) best fits.

In order to obtain the contours, we consider as true values for the two mass splittings and the mixing angles the ones from [111] and the values for $\varepsilon_{\alpha\beta}$, $\phi_{\alpha\beta}$ and $\delta$ from the T2K-NO$\nu$A fit. For the fit we marginalize over the oscillation parameters with pull terms. All the NSI parameters that do not appear in each plot are fixed to 0 both in the theory and in the fit.

It is clear that DUNE is expected to be able to measure all the above mentioned vector NSI parameter with a good precision. Indeed, when $\varepsilon_{e\mu}$ is considered in NO, in the 2-dimensional plane (2 degrees of freedom), the 68% CL allowed region includes the intervals [0.16,0.21] for $\varepsilon_{e\mu}$ and [1.3,1.8]$\pi$ for $\phi_{e\mu}$. This means that in the first benchmark scenario, DUNE would be able to determine both NSI parameters with a precision of roughly 10%. In the IO case, since the best fit value for $\varepsilon_{e\mu}$ is smaller (0.04), the allowed region is bigger, but still excludes at 99% CL the standard model.

In the middle panels, namely when the benchmark scenario presents non-zero values for $\varepsilon_{e\tau}$ and $\phi_{e\tau}$, it is possible to observe that the DUNE performances are similar to the previous case. In particular, the allowed regions includes the intervals [0.22,0.34] for $\varepsilon_{e\tau}$ and [1.4,1.8]$\pi$ for $\phi_{e\tau}$ which correspond to a precision of roughly 20% for the magnitude of the parameter and 10% for its phase for the NO case. When we consider the IO scenario, the precision on the parameters remains basically the same, even though the best fit value for the NSI coupling magnitude is reduced by almost a factor 2.

The results are very different when $\varepsilon_{\mu\tau}$ is switched on. In this case, the best fit value for $\phi_{\mu\tau}$ from T2K and NO$\nu$A is very close to $\pi/2$ in the NO case. Since the NSI correction to the $\nu_\mu$ disappearance probability depends at the leading order to the combination $\varepsilon_{\mu\tau}\cos\phi_{\mu\tau}$, see Eq. (6.64), DUNE is expected to be very sensitive to small variation of the phase around $3/2\pi$, but is not adequate to constrain the magnitude $|\varepsilon_{\mu\tau}|$ with the same precision reached for the

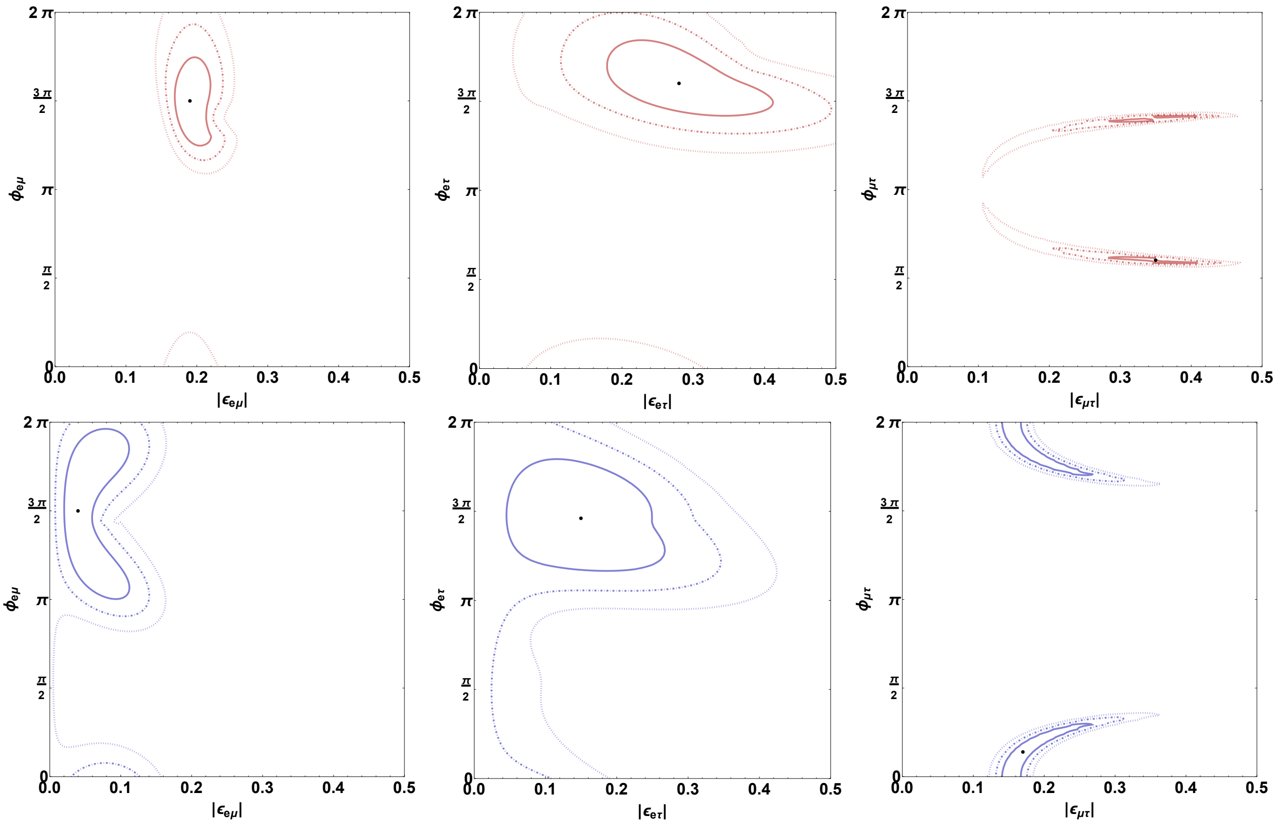


Figure 6.20: 68% (solid lines), 95% (dashed lines) and 99% (dotted lines) contours in DUNE in the vector NSI ($|\varepsilon_{ij}| - \phi_{ij}$)-planes when data are generated using NSI best fits marginalizing over all the NSI parameters. The three top (bottom) plots with red (blue) contours have been obtained using NO (IO) best fits.

other parameters. When we consider the IO hypothesis, the situation is the opposite, since the phase best fit is close to zero: the magnitude is tightly constrained while the phase can vary in a relatively large interval.

When a full marginalization over all the NSI parameters is performed in Fig. 6.20, the contours are obviously enlarged, however DUNE is still be able to exclude large portions of the parameters spaces in the studied benchmark scenarios. For the marginalization we use the following priors: $\varepsilon_{\mu\tau} < 0.02$ (when undisplayed) [705] and $\varepsilon_{ee} < 0.3$ [475]. The most interesting features that can be observed are the following

- In the NO case, when we consider $\varepsilon_{\mu\tau}$, a degenerate solution around $\phi_{\mu\tau} \sim 3/2\pi$ appears.
- In the IO case, now the SM is allowed at 99% (95%) CL in the $\varepsilon_{e\mu}$ ($\varepsilon_{e\tau}$) scenarios.

### Scalar NSI

For the sensitivities performed using the scalar NSI benchmark scenarios, we use the same approach described in the previous subsection. Differently from the previous case, the results with more statistical significance in the T2K-NO$\nu$A fit are the IO ones. In Fig. 6.21 we show our results in the ($\eta_{\alpha\beta} - \phi_{\alpha\beta}$) planes in the case in which the lightest neutrino mass is zero.

When the mass ordering is inverted, DUNE is expected to constrain scalar NSI at the following levels at 68% CL: $|\eta_{e\mu}| \in [0.012, 0.035]$ and $|\eta_{e\tau}| \in [0.008, 0.012]$. On the other hand, DUNE cannot set remarkable bounds on the phases, being able to exclude at 68% CL only one third of the possible values of $\phi_{e\mu}$ (from $0.44\pi$ to $1.1\pi$) and one sixth of the possible values of $\phi_{e\tau}$ (from $1.6\pi$ to $1.9\pi$). For the non-zero $\eta_{\mu\tau}$ scenario, in which the scalar NSI coupling best

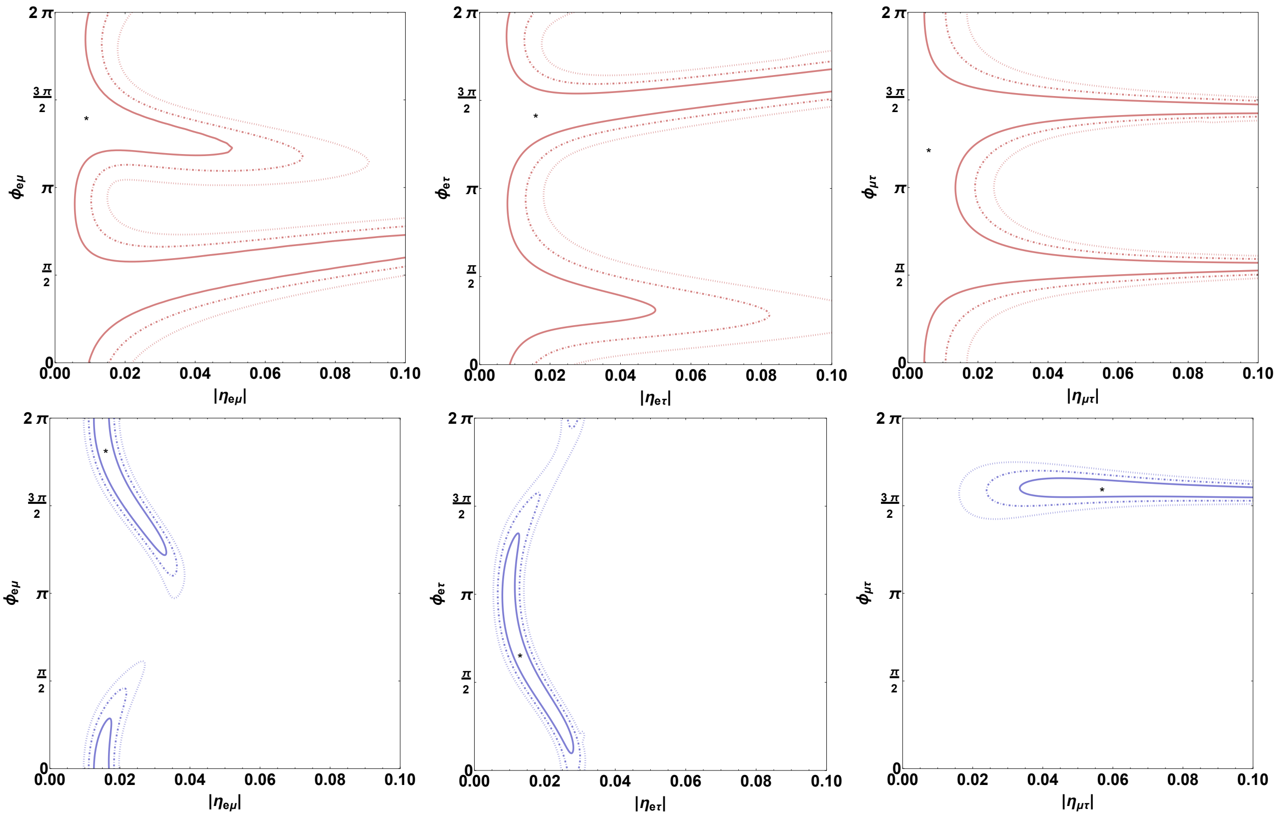


Figure 6.21: 68% (solid lines), 95% (dashed lines) and 99% (dotted lines) contours in DUNE in the scalar NSI ($|\eta_{ij}| - \phi_{ij}$)-planes when data are generated using scalar NSI best fits (with $m_{lightest} = 0$) considering one NSI parameter at a time.The three top (bottom) plots with red (blue) contours have been obtained using NO (IO) best fits.

fit is bigger, we have a different situation. Indeed, DUNE is expected in this case to bound with a good precision the phase, but can only set a lower limit ($|\eta_{\mu\tau}| < 0.02$ on the magnitude (the upper limit correspond to a big unrealistic value of the NSI coupling). set In the NO case, the T2K-NO$\nu$A results are characterized by very small best values and small $\Delta\chi^2$-s. When we perform sensitivity scans with DUNE, we can observe that this experiment is not able to distinguish the new physics scenarios from the Standard Model not even at 68% level. Moreover, the magnitudes of the three non diagonal scalar NSI parameters cannot be bounded from above and the phases are unconstrained by DUNE.

We checked that when a full marginalization is performed, DUNE is not able to exclude remarkable portions of the parameters space at a good confidence level. Indeed, the scalar NSI scenarios produce very similar phenomenology at DUNE (see Sec. 6.4.5); thus, when we allow all the parameters to vary in the fit, the effects of the $\eta$-s can be reduced by the presence of other non-zero parameters.

We have mentioned that one of the most interesting features of the scalar NSI model is that the oscillation probabilities in this case depend on the neutrino mass scale. A non-zero $m_{lightest}$ can slightly change the T2K-NO$\nu$A best fits. In particular, increasing the neutrino mass scale, the phase best fits are almost the same, while the magnitudes of the $\eta_{ij}$ parameters decrease. The most significant reduction of the best fits can be observed in the IO case, in which, as already pointed out, the phenomenology would allow us to distinguish the scalar NSI parameters from the SM oscillations. In Fig. 6.22 we show the 68% contours using the best fits for $m_{lightest} = 0, 0.05, 0.1$ eV. It is clear that the contours shapes are not drastically altered by the decrease of the scalar NSI parameters magnitudes. However, when the lightest neutrino is not massless, DUNE is expected to be able to set upper limits on $\eta_{\mu\tau}$: $|\eta_{\mu\tau}| < 0.08\,(0.06)$ at 68%

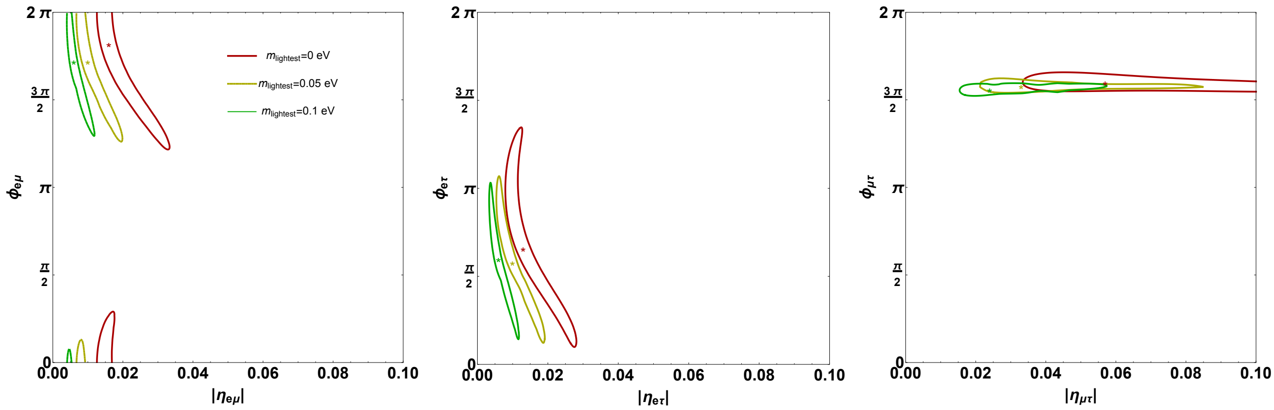


Figure 6.22: 68% contours in DUNE in the $(|\eta_{ij}| - \phi_{ij})$-planes when data are generated using scalar NSI best fits in the IO case considering one NSI parameter at a time. The red curve is obtained with $m_{lightest} = 0$, the blue one with $m_{lightest} = 0.05$ eV and the green one with $m_{lightest} = 0.1$ eV.

CL when $m_{lightest} = 0.05\,(0.1)$ eV.

**Sterile neutrinos**

In Fig. 6.23 we show the performances of the DUNE Far Detector in constraining the 3+1 parameters if the best fits are the ones reported in table 6.9 from NOvA and T2K data. In the analysis, we marginalize over the undisplayed parameters, giving the upper bound $\theta_{i4} < 25^\circ$ on the non-standard mixing angles. In both IO and NO, in the $(\theta_{24} - \theta_{14})$ planes, it is evident an anti-correlation between the two parameters. Moreover, DUNE is expected to have a similar sensitivity to both the mixing angles. Indeed, if the true values are 8°, the 68% allowed ranges are [5-12]° for $\theta_{14}$ and [4-10]° degrees for $\theta_{24}$. When we scrutinize the DUNE capabilities in measuring the 3+1 phases, we observe in Fig. 6.23 that, if $\delta_{12} \sim 0.5\pi$, then there exists two $\Delta\chi^2$ minima, one around the best fit and one around $\delta_{12} \sim 1.5\pi$ for both the IO and NO case. We checked that, on the other hand, given the best fits in table 6.9, the DUNE experiment should not be sensitive to $\delta_{13}$ and $\delta_{23}$.

### 6.4.5 Differentiating the models

We now discuss the ability for DUNE to differentiate among different benchmark scenarios. We take one benchmark new physics point and attempt to reconstruct with a different new physics parameter in either the same model or a different model. The minimum $\Delta\chi^2$'s are shown in tables 6.10 and 6.11. For the $\chi^2$ computations we marginalize over all the standard oscillation parameters and we consider only one NSI parameter at a time, varying its magnitude up to 0.5 and its phase over the entire $2\pi$ range. In the last column, we show also the $\chi^2$ that correspond to the case in which the data are fitted with the 3+1 sterile neutrino models, considering $\Delta m^2_{41}$ in the range $[10^{-5} - 10]$ eV$^2$, and the mixing angles in the range $[0 - 30]^\circ$[12].

In the case in which data are generated using the best fits related to the scalar NSI model, it is clear that, for NO, the minimum $\chi^2$ values are very small even in the standard model scenario (when all the new physics parameters are fixed to zero). This is because the fit at the T2K and NO$\nu$A data, if performed adding the scalar NSI in NO, gives very small best fit values for the $\eta$ couplings. For this reason, we expect that DUNE would not be able in this case to distinguish

[12]We do not consider here any limit on the new physics parameters obtained by other oscillation experiments, since our goal is to show at which confidence level DUNE would be able to distinguish various model without external inputs on the new physics when the fit is performed.

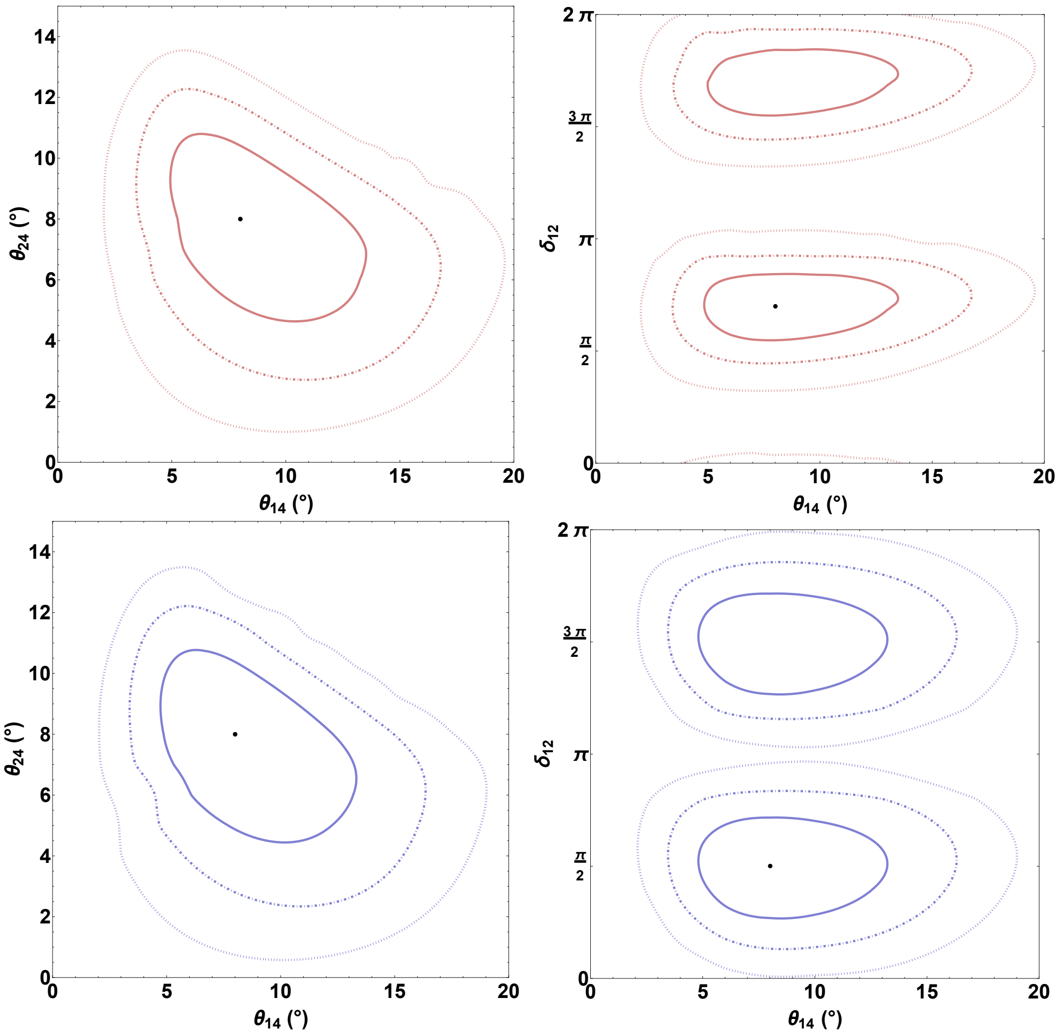


Figure 6.23: 68% (solid lines), 95% (dashed lines) and 99% (dotted lines) contours in DUNE in the $(\theta_{14} - \theta_{24})$ and $(\theta_{14} - \delta_{12})$ planes when data are generated using 3+1 model best fits. The three top (bottom) plots with red (blue) contours have been obtained using NO (IO) best fits.

at any confidence level these scenario with the standard three neutrino framework. If we fit data with models in which other $\eta$ parameters are used in the fit, we obtain even smaller minima for the $\chi^2$, as expected. The same happens in the case in which we fit the scalar NSI data with sterile neutrino models. On the other hand, when we try to fit them with vector NSI models, apart from the $\eta_{e\mu}$ case, the best fit point is always found when $\varepsilon_{ij} = 0$. The best fit for the scalar NSI parameters in the IO case give even more interesting results. In this case, the three neutrino framework is completely excluded ($\chi^2 > 30$ in all three cases). However, we can found minima of the $\chi^2$ much smaller the standard model ones when we fit data with other scalar NSI models. In particular, if data are generated using the best fits for $\eta_{e\tau}$, DUNE would have very limited discrimination capabilities when we switch on only $\eta_{e\mu}$ or $\eta_{\mu\tau}$ at more than $1.5\sigma$. On the other hand, when data are generated with $\eta_{e\mu}$ or $\eta_{\mu\tau}$ best fits, the $\chi^2$ related to the fits with the other $\eta$ models are in the range $4.6 - 6.3$. Thus, DUNE would also have some difficulty distinguishing different scalar NSI models in the IO if the true values for the $\eta$-s are the ones compatible with the NO$\nu$A-T2K tension. If we try to fit scalar NSI data with single parameter vector NSI models, DUNE would differentiate them at a good confidence level. Only in the $\eta_{\mu\tau}$ case, the vector NSI models could be rejected at less than $5\sigma$. Finally, the IO scalar NSI models generated with $\eta_{e\tau}$ and $\eta_{\mu\tau}$ best fits cannot be distinguished at more than $3.2\sigma$ from the sterile neutrino models. On the other hand, we reach almost $5\sigma$ in the case of the $\eta_{e\mu}$ model. Even though our analytical approach (eq. (6.69) and 6.70) the probabilities are symmetric under the $\eta_{e\tau}$-$\eta_{e\mu}$ exchange. However, from table 6.11, it is clear that this symmetry cannot be exact. Indeed, we checked that, when we consider include in the expansion also the solar mass splitting, the symmetry is broken. From table 6.11 we can also interestingly see that, even though the disappearance probability strongly depends on $\eta_{\mu\tau}$, since the best fit for $\phi_{\mu\tau}$ is similar to $\pi/2$, the leading term in the probability is suppressed. Thus, the fits to the data generated with $\eta_{\mu\tau}$ are better than the ones where data are generated using the other scalar NSI parameters.

Let us now focus on the case in which data are generated using the best fit points for vector NSI. In this case, both in the NO and IO case, the data could not be fitted appropriately with the three neutrino standard probabilities ($\chi^2 > 60$). Moreover, all the models obtained generating data with $\varepsilon$ best fits from the T2K and NO$\nu$A data can be distinguished at at least $7\sigma$ from the scalar NSI models. When we try to fit the vector NSI data with other vector NSI models or 3+1 models, the only interesting case (namely the only case in which DUNE would struggle in differentiating the models) is when data are generated using $\varepsilon_{e\mu}$ best fits in the IO case. In this framework, the minima of the $\chi^2$ are 10, 13 and 3 when we fit the data with the $\varepsilon_{e\tau}$, $\varepsilon_{\mu\tau}$ and 3+1 models respectively. In light of the analytic formulae shown in eq. (6.69) and (6.70), we can try to understand the results in table 6.10. It is clear that, due to the strong dependence of the disappearance probability to $\varepsilon_{\mu\tau}$, if we generate data with this parameter's true value different from zero, we expect very high $\chi^2$. Indeed, it is very difficult to find some values for the other parameters which fit well the disappearance data. Moreover, even if the appearance probability has the same dependence on $\varepsilon_{e\mu}$ and $\varepsilon_{e\tau}$, the disappearance probability contains one more term in $\varepsilon_{e\mu}$. For this reason, it is easy to fit data generated with $\varepsilon_{e\tau} \neq 0$ with a theory that contains $\varepsilon_{e\mu}$, but the opposite is more complicated. This is clear from table 6.10, since $\chi^2$ in the $\varepsilon_{e\mu}$ rows are bigger with respect to the $\varepsilon_{e\tau}$ ones.

All these results have been obtained considering only one parameter at-a-time for each model, namely switching on only one off-diagonal scalar or vector parameter for each fit model. We checked that, if we vary all the off diagonal parameters together, varying their phases in the entire allowed range, the results are not changing drastically. This means that, for instance, if we fit data generated with one of the $\eta$'s best fits using the vector NSI model in which we scan over the whole $(\varepsilon_{e\mu}, \varepsilon_{e\tau}, \varepsilon_{\mu\tau})$ parameter space, the minimum of the $\chi^2$ is very close to the smaller minima of the $\chi^2$-s obtained using only one parameter at-a-time. This suggest that there are no strong correlations between parameters that could mimic data generated with a different model.

| $\Delta\chi^2$ | SM | $\eta_{e\mu}$ | $\eta_{e\tau}$ | $\eta_{\mu\tau}$ | $\varepsilon_{e\mu}$ | $\varepsilon_{e\tau}$ | $\varepsilon_{\mu\tau}$ | 3+1 |
|---|---|---|---|---|---|---|---|---|
| $\varepsilon_{e\mu}$ NO | 200 | 140 | 140 | 170 | / | 180 | 160 | 80 |
| $\varepsilon_{e\tau}$ NO | 60 | 48 | 50 | 45 | 50 | / | 50 | 40 |
| $\varepsilon_{\mu\tau}$ NO | 200 | 180 | 170 | 180 | 160 | 180 | / | 80 |
| $\varepsilon_{e\mu}$ IO | 170 | 80 | 75 | 90 | / | 10 | 13 | 3 |
| $\varepsilon_{e\tau}$ IO | 70 | 50 | 50 | 45 | 45 | / | 60 | 20 |
| $\varepsilon_{\mu\tau}$ IO | 500 | 400 | 400 | 400 | 300 | 350 | / | 160 |

Table 6.10: $\Delta\chi^2$ obtained fitting to each case all the models taken into account using as true values the best fits of the vector NSI case.

| $\Delta\chi^2$ | SM | $\eta_{e\mu}$ | $\eta_{e\tau}$ | $\eta_{\mu\tau}$ | $\varepsilon_{e\mu}$ | $\varepsilon_{e\tau}$ | $\varepsilon_{\mu\tau}$ | 3+1 |
|---|---|---|---|---|---|---|---|---|
| $\eta_{e\mu}$ NO | 0.14 | / | 0.005 | 0.088 | 0.071 | 0.033 | 0.055 | 0.02 |
| $\eta_{e\tau}$ NO | 0.08 | 0.003 | / | 0.041 | SM | SM | SM | 0.01 |
| $\eta_{\mu\tau}$ NO | 0.60 | 0.48 | 0.48 | / | SM | SM | SM | 0.02 |
| $\eta_{e\mu}$ IO | 100 | / | 4.7 | 6.3 | 80 | 70 | 90 | 21 |
| $\eta_{e\tau}$ IO | 60 | 1.0 | / | 1.5 | 44 | 38 | 50 | 11 |
| $\eta_{\mu\tau}$ IO | 30 | 4.6 | 4.8 | / | 23 | 20 | 29 | 12 |

Table 6.11: Same as table 6.10 but with true values set to the best fits of scalar NSI.

Finally, when the data are obtained in the 3+1 framework (see table 6.12), with the best fits shown in table 6.9, we observe that the SM solution is excluded with $\Delta\chi^2 = 20$, namely at $4.5\sigma$. On the other hand, when the fit is performed with the NSI models, it is clear that in both NO and IO, the $\Delta\chi^2$ is reduced up to 5.2 in the vector case. The vector model which can be distinguished more easily from the 3+1 is the one where we turn on $\varepsilon_{\mu\tau}$ in NO ($\Delta\chi^2 = 10$). This is because $\varepsilon_{\mu\tau}$ in DUNE, as already mentioned, is the one that modifies the most the disappearance probability. In the scalar case, on the other hand, the $\Delta\chi^2$ are not drastically reduced with respect to the Standard Model case if the mass ordering is inverted. Indeed, if we perform the fit allowing $\eta_{e\mu}$ to vary we reach $\Delta\chi^2 = 13$, while in the opposite case, when we change the value of $\eta_{e\tau}$, the best fit is achieved when the scalar NSI parameter vanishes, namely in the Standard Model case. This suggests us that in inverted ordering, if the sterile neutrino mixing angles are as small as $8°$ and $\theta_{34}$ is fixed to zero, the phenomenology of 3+1 and scalar NSI models are moving in the opposite direction. On the contrary, in the scalar NSI NO case, the the $\Delta\chi^2$ are as low as the vector NSI ones. We checked also in this case that a full marginalization over the NSI parameter spaces do not alter significantly the $\Delta\chi^2$-s.

Looking at the probabilities in eqs. 6.74 and 6.75, we can understand why in table 6.12 the Standard Model is excluded only at $4.5\sigma$ even if the true values for $\theta_{14}$ and $\theta_{24}$ are relatively big ($8°$). Indeed, up to the second order only the disappearance probability is modified by the small quantity $s_{24}^2$. Moreover, it is clear that, since $\delta_{12} \sim 1.9\pi$ or 0 in two best fits, the DUNE sensitivity to the CP violating phase translates directly to the sensitivity to $\delta_{12}$, whose best fits are maximal. Another interesting feature of the disappearance probability is that it is always reduced if $\theta_{24} \neq 0$. This explains why, for instance, a scalar NSI model in NO fits better the 3+1 data than the same model in IO. We can indeed observe that, the third line in eq. (6.70) reduces the disappearance probability in NO, while it enhances the probability in IO.

| $\Delta\chi^2$ | SM | $\eta_{e\mu}$ | $\eta_{e\tau}$ | $\eta_{\mu\tau}$ | $\varepsilon_{e\mu}$ | $\varepsilon_{e\tau}$ | $\varepsilon_{\mu\tau}$ |
|---|---|---|---|---|---|---|---|
| 3+1 NO | 20 | 8.2 | 7.9 | 6.7 | 5.2 | 6.6 | 10 |
| 3+1 IO | 20 | 13 | SM | 18 | 7.4 | 6.2 | 9.5 |

Table 6.12: Same as table 6.10 but with true values set to the best fits of 3+1 sterile neutrino model.

# Conclusions and discussions

The discovery of neutrino oscillation is one of the most important particle physics result of the last decades and we are now entering in the precision measurements era in the neutrino sector. Indeed, a relatively large number of oscillation experiments have been able to determine the neutrino oscillation parameters with a good precision and the next generation generation of experiments is expected to improve all the measurements and to answer all the open questions in the oscillation sector. In the context of accelerator experiments, in which a muon neutrino beam is generated artificially, two experiments are expected to start their data taking at the end of 2020s: DUNE, in the USA and T2HK in Japan. These two experiments have very different features, even though their scopes are very similar. In particular, T2HK will employ a narrow-band off-axis beam with a short baseline ($\sim$ 300 km), while DUNE will use a broad-band on-axis beam with a longer baseline ($\sim$ 1300 km). Moreover, the Japanese experiments may also be extended with a second detector in Korea, at a longer baseline. Both experiments are expected to be very performing in measuring the oscillation parameters; moreover, due to their precision, they may also be able to put stringent bounds on new physics models. Indeed, there exist a large number of BSM (Beyond Standard Model) models in which the neutrino oscillation probabilities are modified; thus, in principle, precise experiments should be able to catch the tiny new physics effects. In this thesis, we discussed the performances of DUNE and T2HK in various contexts. Our main results are the following.

- The most unknown standard oscillation parameter is the PMNS phase $\delta_{CP}$ and one of the main goal of the future long baseline experiments will be to measure it. We checked that, if we set as primary physics goal the reaching of a $3\sigma$ sensitivity for at least 75% of the possible $\delta_{CP}$ values (75% CP coverage), both DUNE and T2HK may not reach it after 10 years of data taking. In particular, we studied how the CP coverage is affected by the true value of $\theta_{23}$, which is currently the mixing angle with the largest uncertainty. Our main results are that large values of the atmospheric mixing angle worsen the sensitivity to $\delta_{CP}$ (as it is well known in the literature [96, 165, 609–611]). Moreover, due to its smaller systematic uncertainties, DUNE capabilities overcome the T2HK ones for every reasonable value of $\theta_{23}$ except for an interval around maximal mixing ($\theta_{23} = 45°$), where the relatively large matter effects in DUNE enhance the $\delta_{CP} - \theta_{23}$ degeneracy. Even though the single experiments may fail in reaching the 75% CP coverage goal in 10 years of data taking, we showed in Sec. 5.2 that the combination of DUNE and T2HK data may be enough to reach the goal for all possible choices of the atmospheric angle $\theta_{23}$ in its current $3\sigma$ allowed range. In addition, we demonstrated that the complementarity of the two experiments may allow to reach more than 75% coverage also with half of their nominal exposure or with larger systematic uncertainties. It is worth to mention, that if a second T2HK detector will be built in Korea at the second oscillation maximum, the combination of all data from future long-baseline experiments may improve the $3\sigma$ CP coverage up to 85%.
- In Sec. 5.3 we showed that not only the standard PMNS parameters measurements but also the bounds on BSM models may benefit of the combination of the two LBL experiments data. In particular, we considered a model in which the PMNS matrix is no longer unitary,

having in mind that the loss of the unitarity of the mixing matrix is one of the main phenomenological consequences of most of the SM extensions in which new heavy neutral leptons are added *refs*. In such a model, six new parameters $\alpha_{ij}$, where $i, j = 1, 2, 3$ and $i \geq j$, can be used to encode all the new physics effects. The possibility to measure some of these parameters using neutrino oscillation data has been extensively studied in literature [249–254]. In our analysis, we showed that DUNE and T2HK alone have different performances: while T2HK is able to set tight bounds on $\alpha_{21}$, $\alpha_{22}$ and $\alpha_{11}$ due to its larger statistics and lower disappearance systematics, DUNE have access also to the other three Non-Unitarity parameters due to the presence of larger matter effects. However, none of the two experiments may be able to bound in a satisfactory way all the parameters at the same time. We demonstrated that the combination of the data from the two experiments should allow to set bounds on all six Non-Unitarity parameters competitive to the bounds obtained by current global neutrino oscillation analysis [551]. We also discussed how our results can be improved considering data from Near Detectors, from the DUNE $\nu_\tau$ appearance sample or from the possible T2HK second Korean detector.

- The DUNE experiment is expected to be able to collect events from different charged current oscillation channels: $\nu_e$ and $\nu_\tau$ appearances and $\nu_\mu$ disappearance. However, there are some BSM models in which, after neutrino propagation, the total number of neutrinos is not conserved. In this case, the Neutral Current (NC) events sample, which usually is insensitive to the oscillation parameters, may be sensitive to new physics. In Sec. 6.1 we took into account one of these models: the neutrino invisible decay model. We consider the third neutrino mass eigenstate to be unstable and to decay into invisible particles, in particular a massless scalar and a lighter sterile neutrino. We performed a full analysis of the DUNE data sample, including all the charged current and the neutral current channels. Our main result is that the inclusion of the NC sample improves the DUNE bound on the third neutrino state lifetime by about 15%. In particular, we found $\beta_3 = \tau_3/m_3 > 5.1 \times 10^{-11}\ s/eV$, where $\tau_3$ is the lifetime and $m_3$ is the third neutrino mass. This upper bound is expected to be the best among the ones obtained from the analysis of current and past long-baseline experiments [524, 630–635].

- The DUNE Near Detector will have many purposes. Apart from being a beam monitor, it should be able to collect a large number of events. If new physics introduce probability terms which are different from zero also at zero baseline, the Near Detector may be able to bound them. In Sec. 6.2 we showed how this can be possible considering as BSM model the source and detector Non Standard Interaction (NSI). In this model, during their production or detection, neutrinos can undergo new interactions whose strength are proportional to the parameters $\varepsilon^{s/d}_{\alpha\beta}$, where $\alpha, \beta = e, \mu, \tau$. Since these new physics effects do not need propagation in order to occur, the DUNE Near Detector provides a very clear environment where to probe them. Performing a simple Gaussian $\chi^2$ analysis using only the total ND number of observed events in all the charged current channels we showed that it is possible to exclude large portions of the NSI parameters space. Our results are complementary to the ones which have been obtained in literature using the DUNE Far Detector [642]. We also discussed the effect of the systematic uncertainties on our results, being crucial when a Near Detector analysis is performed. It is interesting to notice how all the numerical results showed in this context are corroborated by our strong analytical prediction.

- The unprecedent capabilities of the DUNE experiment to determine the CP-violating phase $\delta_{CP}$ suggest that the CP-odd probability asymmetries may be also useful to search for hints of the presence of new physics if the non standard effects involve new sources of CP violation. In Sec. 6.3 we studied the effects of new physics on the DUNE integrated asymmetries, defined as $A_{\alpha\beta} = \frac{N_\beta - \bar{N}_\beta}{N_\beta + \bar{N}_\beta}$ where $N$ is the number of events in neutrino mode and $\bar{N}$ is the number of events in antineutrino mode in each oscillation channel $\nu_\alpha \to \nu_\beta$. This really simple and relatively easy to evaluate observable is closely related to the CP-odd probability asymmetries and for this reason may unveil the presence of CP-violating new physics effects. We computed the possible values of such integrated asymmetries in DUNE given the standard neutrino oscillation probabilities and we compared them with the asymmetries one would obtain in presence of a light sterile neutrino (3+1 model) or in presence of propagation Non-Standard Interactions. We showed that the effects of new physics are in principle too tiny to be observed using only the integrated asymmetries. However, if DUNE will employ an high energy neutrino flux, which has been proposed to optimize $\nu_\tau$ appearance searches, the measurement of the integrated asymmetries related to the $\nu_e$ appearance channel may be enough to at least reveal the presence of new physics.

- The T2K and NO$\nu$A experiments were able to perform the first measurements of the PMNS phase. However, their results show a $2\sigma$ tension [155]. In the last two years, it has been studied how in presence of CP-violating propagation NSI or in presence of sterile neutrinos, the tension can be reduced. In Sec. 6.4 we showed for the first time that this happens also in presence of scalar NSI. In such a model, we consider the Non-Standard neutrino interactions with matter to be mediated by a scalar particle. This introduces a completely new phenomenology in which the neutrino mass matrix is modified. In our analysis, after providing a list of all the BSM models which in principle may alleviate the T2K-NO$\nu$A tension, we studied the capability of the future DUNE experiment to differentiate among them. Even though several DUNE analyses have been already performed for the NSI and sterile neutrino cases (see [706] for a recent review), our study is particularly interesting since we investigated the DUNE phenomenological implications of specific models selected to reduce the current small but significant long-baseline tension on the $\delta_{CP}$ measurement. We found out that DUNE is expected to be very performing in the identification of the various models; moreover, if the source of the T2K-NO$\nu$A discrepancy is vector NSI in Normal Ordering or scalar NSI in Inverted Ordering, DUNE should be able to distinguish them from the other models presented in our work at a very high confidence level.

With our results, briefly described here, we want to stress that phenomenological studies in the neutrino oscillation context have an important and primary role in suggesting how to get the most from an experiment. This is particularly useful if we consider BSM models: indeed, other than observing tensions between data and theories, an experiment should be able to develop a strategy to determine which is the most probable source of new physics. For this reason, the parallel development of phenomenology and experimental physics will be crucial in the next years.

# Bibliography


[1] E. Fermi, *An attempt of a theory of beta radiation. 1.*, *Z. Phys.* **88** (1934) 161.

[2] C.L. Cowan, F. Reines, F.B. Harrison, H.W. Kruse and A.D. McGuire, *Detection of the free neutrino: A Confirmation*, *Science* **124** (1956) 103.

[3] S.H. Neddermeyer and C.D. Anderson, *Note on the Nature of Cosmic Ray Particles*, *Phys. Rev.* **51** (1937) 884.

[4] G. Danby, J.M. Gaillard, K.A. Goulianos, L.M. Lederman, N.B. Mistry, M. Schwartz et al., *Observation of High-Energy Neutrino Reactions and the Existence of Two Kinds of Neutrinos*, *Phys. Rev. Lett.* **9** (1962) 36.

[5] M.L. Perl et al., *Evidence for Anomalous Lepton Production in e+ - e- Annihilation*, *Phys. Rev. Lett.* **35** (1975) 1489.

[6] M.L. Perl, *The Discovery of The Tau Lepton*, *NATO Sci. Ser. B* **352** (1996) 277.

[7] DONUT collaboration, *Observation of tau neutrino interactions*, *Phys. Lett. B* **504** (2001) 218 [hep-ex/0012035].

[8] R. Davis, Jr., D.S. Harmer and K.C. Hoffman, *Search for neutrinos from the sun*, *Phys. Rev. Lett.* **20** (1968) 1205.

[9] R. Davis, *A review of the Homestake solar neutrino experiment*, *Prog. Part. Nucl. Phys.* **32** (1994) 13.

[10] Super-Kamiokande collaboration, *Evidence for oscillation of atmospheric neutrinos*, *Phys. Rev. Lett.* **81** (1998) 1562 [hep-ex/9807003].

[11] B. Pontecorvo, *Mesonium and anti-mesonium*, *Sov. Phys. JETP* **6** (1957) 429.

[12] Z. Maki, M. Nakagawa and S. Sakata, *Remarks on the unified model of elementary particles*, in *11th International Conference on High-energy Physics*, pp. 663–666, 1962.

[13] Particle Data Group collaboration, *Review of Particle Physics*, *PTEP* **2022** (2022) 083C01.

[14] DUNE collaboration, *Long-Baseline Neutrino Facility (LBNF) and Deep Underground Neutrino Experiment (DUNE): Conceptual Design Report, Volume 2: The Physics Program for DUNE at LBNF*, 1512.06148.

[15] Hyper-Kamiokande collaboration, *Physics potentials with the second Hyper-Kamiokande detector in Korea*, *PTEP* **2018** (2018) 063C01 [1611.06118].

[16] A. Ghoshal, A. Giarnetti and D. Meloni, *On the role of the $\nu_\tau$ appearance in DUNE in constraining standard neutrino physics and beyond*, *JHEP* **12** (2019) 126 [1906.06212].

[17] S.K. Agarwalla, S. Das, A. Giarnetti, M. Singh and D. Meloni, *Enhancing sensitivity to leptonic cpv using complementarity among dune, t2hk, and t2hkk*, *Draft in preparation* (2022) .

[18] S.K. Agarwalla, S. Das, A. Giarnetti and D. Meloni, *Model-Independent Constraints on Non-Unitary Neutrino Mixing from High-Precision Long-Baseline Experiments*, 2111.00329.

[19] A. Ghoshal, A. Giarnetti and D. Meloni, *Neutrino Invisible Decay at DUNE: a multi-channel analysis*, *J. Phys. G* **48** (2021) 055004 [2003.09012].

[20] A. Giarnetti and D. Meloni, *Probing source and detector nonstandard interaction parameters at the DUNE near detector*, *Phys. Rev. D* **104** (2021) 015027 [2005.10272].

[21] A. Giarnetti and D. Meloni, *New Sources of Leptonic CP Violation at the DUNE Neutrino Experiment*, *Universe* **7** (2021) 240 [2106.00030].

[22] P.B. Denton and J. Gehrlein, *New reactor data improves robustness of neutrino mass ordering determination*, *Phys. Rev. D* **106** (2022) 015022 [2204.09060].

[23] S.L. Glashow, *Partial Symmetries of Weak Interactions*, *Nucl. Phys.* **22** (1961) 579.

[24] A. Salam, *Weak and electromagnetic interactions*, in *Elementary particle theory*, N. Svartholm, ed., pp. 367–377, Almquist & Wiksell.

[25] S. Weinberg, *A Model of Leptons*, *Phys. Rev. Lett.* **19** (1967) 1264.

[26] P.W. Higgs, *Broken symmetries, massless particles and gauge fields*, *Phys. Lett.* **12** (1964) 132.

[27] P.W. Higgs, *Broken Symmetries and the Masses of Gauge Bosons*, *Phys. Rev. Lett.* **13** (1964) 508.

[28] G.S. Guralnik, C.R. Hagen and T.W.B. Kibble, *Global Conservation Laws and Massless Particles*, *Phys. Rev. Lett.* **13** (1964) 585.

[29] F. Englert and R. Brout, *Broken Symmetry and the Mass of Gauge Vector Mesons*, *Phys. Rev. Lett.* **13** (1964) 321.

[30] ATLAS collaboration, *Observation of a new particle in the search for the Standard Model Higgs boson with the ATLAS detector at the LHC*, *Phys. Lett. B* **716** (2012) 1 [1207.7214].

[31] CMS collaboration, *Observation of a New Boson at a Mass of 125 GeV with the CMS Experiment at the LHC*, *Phys. Lett. B* **716** (2012) 30 [1207.7235].

[32] P.M. Watkins, *DISCOVERY OF THE W AND Z BOSONS*, *Contemp. Phys.* **27** (1986) 291.

[33] G.S. Abrams et al., *Measurement of Z Decays Into Lepton Pairs*, *Phys. Rev. Lett.* **63** (1989) 2780.

[34] A. Djouadi, G. Girardi, C. Verzegnassi, W. Hollik and F.M. Renard, *$b\bar{b}$ Production on the Z Resonance: A Challenge to the Standard Model*, *Nucl. Phys. B* **349** (1991) 48.

[35] B.W. Lynn and C. Verzegnassi, *Longitudinal $e^-$ Beam Polarization Asymmetry in $e^+e^- \to$ Hadrons*, *Phys. Rev. D* **35** (1987) 3326.

[36] J. Erler and M. Schott, *Electroweak Precision Tests of the Standard Model after the Discovery of the Higgs Boson*, *Prog. Part. Nucl. Phys.* **106** (2019) 68 [1902.05142].

[37] R.D. Peccei and H.R. Quinn, *CP Conservation in the Presence of Instantons*, *Phys. Rev. Lett.* **38** (1977) 1440.

[38] R.D. Peccei, *The Strong CP problem and axions*, *Lect. Notes Phys.* **741** (2008) 3 [hep-ph/0607268].

[39] H.M. Lee, *Lectures on physics beyond the Standard Model*, *J. Korean Phys. Soc.* **78** (2021) 985 [1907.12409].

[40] G. 't Hooft, *Naturalness, chiral symmetry, and spontaneous chiral symmetry breaking*, *NATO Sci. Ser. B* **59** (1980) 135.

[41] F. Jegerlehner, *The hierarchy problem of the electroweak Standard Model revisited*, 1305.6652.

[42] M.C. Gonzalez-Garcia and Y. Nir, *Neutrino Masses and Mixing: Evidence and Implications*, *Rev. Mod. Phys.* **75** (2003) 345 [hep-ph/0202058].

[43] M. Dine, *TASI lectures on the strong CP problem*, in *Theoretical Advanced Study Institute in Elementary Particle Physics (TASI 2000): Flavor Physics for the Millennium*, pp. 349–369, 6, 2000 [hep-ph/0011376].

[44] C.-N. Yang and R.L. Mills, *Conservation of Isotopic Spin and Isotopic Gauge Invariance*, *Phys. Rev.* **96** (1954) 191.

[45] K. Nishijima, *Charge Independence Theory of V Particles*, *Prog. Theor. Phys.* **13** (1955) 285.

[46] M. Gell-Mann, *The interpretation of the new particles as displaced charge multiplets*, *Nuovo Cim.* **4** (1956) 848.

[47] A. Gullstrand, *Presentation of the nobel prize to robert a. millikan*, *Science* **59** (1924) 325 [https://www.science.org/doi/pdf/10.1126/science.59.1528.325].

[48] CDF collaboration, *High-precision measurement of the W boson mass with the CDF II detector*, *Science* **376** (2022) 170.

[49] ATLAS collaboration, *Measurement of the $W$-boson mass in pp collisions at $\sqrt{s} = 7$ TeV with the ATLAS detector*, *Eur. Phys. J. C* **78** (2018) 110 [1701.07240].

[50] CMS collaboration, *Towards the $W$-boson mass measurement with the CMS experiment*, *Nuovo Cim. C* **42** (2019) 160.

[51] Working Group on LEP Energy, ALEPH, DELPHI, L3, OPAL collaboration, *Measurement of the mass of the Z boson and the energy calibration of LEP*, *Phys. Lett. B* **307** (1993) 187.

[52] CMS collaboration, *Precision measurement of the Z boson invisible width in pp collisions at $\sqrt{s}$ = 13 TeV*, 2206.07110.

[53] C.D. Froggatt and H.B. Nielsen, *Hierarchy of Quark Masses, Cabibbo Angles and CP Violation*, *Nucl. Phys. B* **147** (1979) 277.

[54] F. Feruglio and A. Romanino, *Lepton flavor symmetries*, *Rev. Mod. Phys.* **93** (2021) 015007 [1912.06028].

[55] N. Cabibbo, *Unitary Symmetry and Leptonic Decays*, *Phys. Rev. Lett.* **10** (1963) 531.

[56] M. Kobayashi and T. Maskawa, *CP Violation in the Renormalizable Theory of Weak Interaction*, *Prog. Theor. Phys.* **49** (1973) 652.

[57] G.W. Gibbons, S. Gielen, C.N. Pope and N. Turok, *Measures on Mixing Angles*, *Phys. Rev. D* **79** (2009) 013009 [0810.4813].

[58] A. de Gouvea and P. Vogel, *Lepton Flavor and Number Conservation, and Physics Beyond the Standard Model*, *Prog. Part. Nucl. Phys.* **71** (2013) 75 [1303.4097].

[59] Z. Maki, M. Nakagawa and S. Sakata, *Remarks on the Unified Model of Elementary Particles*, *Progress of Theoretical Physics* **28** (1962) 870 [https://academic.oup.com/ptp/article-pdf/28/5/870/5258750/28-5-870.pdf].

[60] B.T. Cleveland, T. Daily, R. Davis, Jr., J.R. Distel, K. Lande, C.K. Lee et al., *Measurement of the solar electron neutrino flux with the Homestake chlorine detector*, *Astrophys. J.* **496** (1998) 505.

[61] GALLEX collaboration, *GALLEX results from the first 30 solar neutrino runs*, *Phys. Lett. B* **327** (1994) 377.

[62] GALLEX collaboration, *GALLEX solar neutrino observations: Results for GALLEX IV*, *Phys. Lett. B* **447** (1999) 127.

[63] SAGE collaboration, *Solar neutrino flux measurements by the Soviet-American Gallium Experiment (SAGE) for half the 22 year solar cycle*, *J. Exp. Theor. Phys.* **95** (2002) 181 [astro-ph/0204245].

[64] SAGE collaboration, *Measurement of the solar neutrino capture rate with gallium metal. III: Results for the 2002–2007 data-taking period*, *Phys. Rev. C* **80** (2009) 015807 [0901.2200].

[65] S.M. Bilenky and B. Pontecorvo, *Lepton Mixing and Neutrino Oscillations*, *Phys. Rept.* **41** (1978) 225.

[66] Troitsk collaboration, *An upper limit on electron antineutrino mass from Troitsk experiment*, *Phys. Rev. D* **84** (2011) 112003 [1108.5034].

[67] C. Kraus et al., *Final results from phase II of the Mainz neutrino mass search in tritium beta decay*, *Eur. Phys. J. C* **40** (2005) 447 [hep-ex/0412056].

[68] K. Assamagan et al., *Upper limit of the muon-neutrino mass and charged pion mass from momentum analysis of a surface muon beam*, *Phys. Rev. D* **53** (1996) 6065.

[69] F. Cerutti, *Determination of the upper limit on m(neutrino tau) from LEP*, in *American Physical Society (APS) Meeting of the Division of Particles and Fields (DPF 99)*, p. 2.01, 1, 1999 [hep-ex/9903062].

[70] KATRIN collaboration, *First operation of the KATRIN experiment with tritium*, *Eur. Phys. J. C* **80** (2020) 264 [1909.06069].

[71] KATRIN collaboration, *KATRIN: status and prospects for the neutrino mass and beyond*, *J. Phys. G* **49** (2022) 100501 [2203.08059].

[72] C. Dvorkin et al., *Neutrino Mass from Cosmology: Probing Physics Beyond the Standard Model*, 1903.03689.

[73] Planck collaboration, *Planck 2018 results. VI. Cosmological parameters*, *Astron. Astrophys.* **641** (2020) A6 [1807.06209].

[74] M.M. Ivanov, M. Simonović and M. Zaldarriaga, *Cosmological Parameters and Neutrino Masses from the Final Planck and Full-Shape BOSS Data*, *Phys. Rev. D* **101** (2020) 083504 [1912.08208].

[75] S.P. Mikheyev and A.Y. Smirnov, *Resonance Amplification of Oscillations in Matter and Spectroscopy of Solar Neutrinos*, *Sov. J. Nucl. Phys.* **42** (1985) 913.

[76] S.P. Mikheyev and A.Y. Smirnov, *Resonant amplification of $\nu$ oscillations in matter and solar-neutrino spectroscopy*, *Il Nuovo Cimento C* **9** (1986) 17.

[77] L. Wolfenstein, *Neutrino Oscillations in Matter*, *Phys. Rev. D* **17** (1978) 2369.

[78] M. Blennow, *Theoretical and phenomenological studies of neutrino physics*, *PhD thesis* .

[79] E.K. Akhmedov, *Three-flavor effects and CP- and T-violation in neutrino oscillations*, *Phys. Scripta T* **121** (2005) 65 [hep-ph/0412029].

[80] T.-K. Kuo and J.T. Pantaleone, *The Solar Neutrino Problem and Three Neutrino Oscillations*, *Phys. Rev. Lett.* **57** (1986) 1805.

[81] S.S. Aleshin, O.G. Kharlanov and A.E. Lobanov, *Analytical treatment of long-term observations of the day-night asymmetry for solar neutrinos*, *Phys. Rev. D* **87** (2013) 045025 [1302.7201].

[82] M. Bustamante, *NuOscProbExact: a general-purpose code to compute exact two-flavor and three-flavor neutrino oscillation probabilities*, 1904.12391.

[83] M. Blennow and T. Ohlsson, *Exact series solution to the two flavor neutrino oscillation problem in matter*, *J. Math. Phys.* **45** (2004) 4053 [hep-ph/0405033].

[84] P.M. Fishbane and S.G. Gasiorowicz, *On equations for neutrino propagation in matter*, *Phys. Rev. D* **64** (2001) 113017 [hep-ph/0012230].

[85] P. Osland and T.T. Wu, *Solar Mikheev-Smirnov-Wolfenstein effect with three generations of neutrinos*, *Phys. Rev. D* **62** (2000) 013008 [hep-ph/9912540].

[86] S. Petcov, *On the oscillations of solar neutrinos in the sun*, *Physics Letters B* **214** (1988) 139.

[87] E. Torrente Lujan, *An Exact analytic description of neutrino oscillations in matter with exponentially varying density for arbitrary number of neutrino species*, *Phys. Rev. D* **53** (1996) 4030 [hep-ph/9505209].

[88] H. Lehmann, P. Osland and T.T. Wu, *Mikheyev-Smirnov-Wolfenstein effect for linear electron density*, *Commun. Math. Phys.* **219** (2001) 77 [hep-ph/0006213].

[89] V.D. Barger, K. Whisnant and R.J.N. Phillips, *CP Nonconservation in Three-Neutrino Oscillations*, *Phys. Rev. Lett.* **45** (1980) 2084.

[90] C. Jarlskog, *Commutator of the Quark Mass Matrices in the Standard Electroweak Model and a Measure of Maximal CP Violation*, *Phys. Rev. Lett.* **55** (1985) 1039.

[91] M. Freund, *Analytic approximations for three neutrino oscillation parameters and probabilities in matter*, *Phys. Rev. D* **64** (2001) 053003 [hep-ph/0103300].

[92] A. Cervera, A. Donini, M.B. Gavela, J.J. Gomez Cadenas, P. Hernandez, O. Mena et al., *Golden measurements at a neutrino factory*, *Nucl. Phys. B* **579** (2000) 17 [hep-ph/0002108].

[93] M. Freund, P. Huber and M. Lindner, *Systematic exploration of the neutrino factory parameter space including errors and correlations*, *Nucl. Phys. B* **615** (2001) 331 [hep-ph/0105071].

[94] E.K. Akhmedov, R. Johansson, M. Lindner, T. Ohlsson and T. Schwetz, *Series expansions for three flavor neutrino oscillation probabilities in matter*, *JHEP* **04** (2004) 078 [hep-ph/0402175].

[95] T. Ohlsson and H. Snellman, *Three flavor neutrino oscillations in matter*, *J. Math. Phys.* **41** (2000) 2768 [hep-ph/9910546].

[96] V. Barger, D. Marfatia and K. Whisnant, *Breaking eight fold degeneracies in neutrino CP violation, mixing, and mass hierarchy*, *Phys. Rev. D* **65** (2002) 073023 [hep-ph/0112119].

[97] J.N. Bahcall, M.H. Pinsonneault and S. Basu, *Solar models: Current epoch and time dependences, neutrinos, and helioseismological properties*, *Astrophys. J.* **555** (2001) 990 [astro-ph/0010346].

[98] J.N. Bahcall and M.H. Pinsonneault, *What do we (not) know theoretically about solar neutrino fluxes?*, *Phys. Rev. Lett.* **92** (2004) 121301 [astro-ph/0402114].

[99] J. Bergstrom, M.C. Gonzalez-Garcia, M. Maltoni, C. Pena-Garay, A.M. Serenelli and N. Song, *Updated determination of the solar neutrino fluxes from solar neutrino data*, *JHEP* **03** (2016) 132 [1601.00972].

[100] K.S. Hirata, T. Kajita, T. Kifune, K. Kihara, M. Nakahata, K. Nakamura et al., *Observation of* $^8$B *solar neutrinos in the kamiokande-ii detector*, *Phys. Rev. Lett.* **63** (1989) 16.

[101] M. Nakahata, *History of Solar Neutrino Observations*, 2202.12421.

[102] F. Kaether, W. Hampel, G. Heusser, J. Kiko and T. Kirsten, *Reanalysis of the gallex solar neutrino flux and source experiments*, *Physics Letters B* **685** (2010) 47.

[103] G. Bellini et al., *Precision measurement of the 7Be solar neutrino interaction rate in Borexino*, *Phys. Rev. Lett.* **107** (2011) 141302 [1104.1816].

[104] Borexino collaboration, *Final results of Borexino Phase-I on low energy solar neutrino spectroscopy*, *Phys. Rev. D* **89** (2014) 112007 [1308.0443].

[105] Super-Kamiokande collaboration, *Solar neutrino measurements in super-Kamiokande-I*, *Phys. Rev. D* **73** (2006) 112001 [hep-ex/0508053].

[106] Super-Kamiokande collaboration, *Solar neutrino measurements in Super-Kamiokande-II*, *Phys. Rev. D* **78** (2008) 032002 [0803.4312].

[107] Super-Kamiokande collaboration, *Solar neutrino results in Super-Kamiokande-III*, *Phys. Rev. D* **83** (2011) 052010 [1010.0118].

[108] G. Ranucci, *First detection of solar neutrinos from CNO cycle with Borexino*, June, 2020. 10.5281/zenodo.4134014.

[109] Y. Nakajima, *Recent results and future prospects from Super- Kamiokande*, June, 2020. 10.5281/zenodo.3959640.

[110] SNO collaboration, *Combined Analysis of all Three Phases of Solar Neutrino Data from the Sudbury Neutrino Observatory*, *Phys. Rev. C* **88** (2013) 025501 [1109.0763].

[111] I. Esteban, M.C. Gonzalez-Garcia, M. Maltoni, T. Schwetz and A. Zhou, *The fate of hints: updated global analysis of three-flavor neutrino oscillations*, *JHEP* **09** (2020) 178 [2007.14792].

[112] P.F. de Salas, D.V. Forero, S. Gariazzo, P. Martínez-Miravé, O. Mena, C.A. Ternes et al., *2020 global reassessment of the neutrino oscillation picture*, *JHEP* **02** (2021) 071 [2006.11237].

[113] F. Capozzi, E. Di Valentino, E. Lisi, A. Marrone, A. Melchiorri and A. Palazzo, *Unfinished fabric of the three neutrino paradigm*, *Phys. Rev. D* **104** (2021) 083031 [2107.00532].

[114] C. Mariani, *Review of Reactor Neutrino Oscillation Experiments*, *Mod. Phys. Lett. A* **27** (2012) 1230010 [1201.6665].

[115] L.J.W.J. Cao and Y.F. Wang, *Reactor Neutrino Experiments: Present and Future*, *Ann. Rev. Nucl. Part. Sci.* **67** (2017) 183 [1803.10162].

[116] M. Danilov, *Review of sterile neutrino searches at very short-baseline reactor experiments*, *Phys. Scripta* **97** (2022) 094001 [2203.03042].

[117] J.M. Berryman and P. Huber, *Sterile Neutrinos and the Global Reactor Antineutrino Dataset*, *JHEP* **01** (2021) 167 [2005.01756].

[118] A. Cabrera Serra, *Double Chooz Improved Multi-Detector Measurements. Double Chooz Improved Multi-Detector Measurements*, .

[119] RENO collaboration, *Measurement of Reactor Antineutrino Oscillation Amplitude and Frequency at RENO*, *Phys. Rev. Lett.* **121** (2018) 201801 [1806.00248].

[120] Daya Bay collaboration, *Measurement of the Electron Antineutrino Oscillation with 1958 Days of Operation at Daya Bay*, *Phys. Rev. Lett.* **121** (2018) 241805 [1809.02261].

[121] KamLAND collaboration, *Precision Measurement of Neutrino Oscillation Parameters with KamLAND*, *Phys. Rev. Lett.* **100** (2008) 221803 [0801.4589].

[122] KamLAND collaboration, *Constraints on $\theta_{13}$ from A Three-Flavor Oscillation Analysis of Reactor Antineutrinos at KamLAND*, *Phys. Rev. D* **83** (2011) 052002 [1009.4771].

[123] KamLAND collaboration, *Reactor On-Off Antineutrino Measurement with KamLAND*, *Phys. Rev. D* **88** (2013) 033001 [1303.4667].

[124] T.K. Gaisser and M. Honda, *Flux of atmospheric neutrinos*, *Ann. Rev. Nucl. Part. Sci.* **52** (2002) 153 [hep-ph/0203272].

[125] M. Honda, T. Kajita, K. Kasahara and S. Midorikawa, *Improvement of low energy atmospheric neutrino flux calculation using the JAM nuclear interaction model*, *Phys. Rev. D* **83** (2011) 123001 [1102.2688].

[126] G. Battistoni, A. Ferrari, T. Montaruli and P.R. Sala, *The FLUKA atmospheric neutrino flux calculation*, *Astropart. Phys.* **19** (2003) 269 [hep-ph/0207035].

[127] Super-Kamiokande collaboration, *A Measurement of atmospheric neutrino oscillation parameters by SUPER-KAMIOKANDE I*, *Phys. Rev. D* **71** (2005) 112005 [hep-ex/0501064].

[128] IceCube collaboration, *Neutrinos below 100 TeV from the southern sky employing refined veto techniques to IceCube data*, *Astropart. Phys.* **116** (2020) 102392 [1902.05792].

[129] Super-Kamiokande collaboration, *Atmospheric neutrino oscillation analysis with external constraints in Super-Kamiokande I-IV*, *Phys. Rev. D* **97** (2018) 072001 [1710.09126].

[130] IceCube collaboration, *Measurement of Atmospheric Neutrino Oscillations at 6–56 GeV with IceCube DeepCore*, *Phys. Rev. Lett.* **120** (2018) 071801 [1707.07081].

[131] IceCube collaboration, *Measurement of Atmospheric Tau Neutrino Appearance with IceCube DeepCore*, *Phys. Rev. D* **99** (2019) 032007 [1901.05366].

[132] M. Schwartz, *Feasibility of using high-energy neutrinos to study the weak interactions*, *Phys. Rev. Lett.* **4** (1960) 306.

[133] U. Dore, P. Loverre and L. Ludovici, *History of accelerator neutrino beams*, *Eur. Phys. J. H* **44** (2019) 271 [1805.01373].

[134] NOMAD collaboration, *The NOMAD experiment at the CERN SPS*, *Nucl. Instrum. Meth. A* **404** (1998) 96.

[135] CHORUS collaboration, *The CHORUS experiment to search for muon-neutrino –> tau-neutrino oscillation*, *Nucl. Instrum. Meth. A* **401** (1997) 7.

[136] LSND collaboration, *The LSND experiment*, in *8th International Nuclear Physics Conference (INPC 95)*, pp. 679–689, 8, 1995.

[137] MicroBooNE collaboration, *Proposal for a New Experiment Using the Booster and NuMI Neutrino Beamlines: MicroBooNE*, .

[138] MiniBooNE collaboration, *MiniBooNE: Status and prospects*, in *3rd International Workshop on the Identification of Dark Matter*, pp. 532–537, 9, 2000.

[139] K2K collaboration, *Measurement of Neutrino Oscillation by the K2K Experiment*, *Phys. Rev. D* **74** (2006) 072003 [hep-ex/0606032].

[140] T2K collaboration, *The T2K Experiment*, *Nucl. Instrum. Meth. A* **659** (2011) 106 [1106.1238].

[141] R. Acquafredda et al., *The OPERA experiment in the CERN to Gran Sasso neutrino beam*, *JINST* **4** (2009) P04018.

[142] ICARUS collaboration, *The ICARUS experiment: A Second generation proton decay experiment and neutrino observatory at the Gran Sasso Laboratory*, hep-ex/0103008.

[143] MINOS collaboration, *The MINOS Detectors Technical Design Report*, .

[144] MINOS+ collaboration, *MINOS+: a Proposal to FNAL to run MINOS with the medium energy NuMI beam*, .

[145] NOvA collaboration, *The NOvA Technical Design Report*, .

[146] MicroBooNE collaboration, *Differential cross section measurement of charged current electron neutrino interactions without final-state pions in MicroBooNE*, *Phys. Rev. D* **106** (2022) L051102 [2208.02348].

[147] J. Grange and T. Katori, *Charged Current Quasi-Elastic Cross Section Measurements in MiniBooNE*, *Mod. Phys. Lett. A* **29** (2014) 1430011 [1404.6484].

[148] NOMAD collaboration, *Cross-section measurements in the NOMAD experiment*, *Nucl. Phys. B Proc. Suppl.* **159** (2006) 56 [hep-ex/0602022].

[149] OPERA collaboration, *Latest results of the OPERA experiment on nu-tau appearance in the CNGS neutrino beam*, *SciPost Phys. Proc.* **1** (2019) 028 [1811.00095].

[150] T2K collaboration, *Recent Results from T2K*, in *55th Rencontres de Moriond on Electroweak Interactions and Unified Theories*, 5, 2021 [2105.06732].

[151] NOvA collaboration, *Recent results from NOvA*, in *56th Rencontres de Moriond on Electroweak Interactions and Unified Theories*, 6, 2022 [2206.03542].

[152] *NuFIT 5.1 (2021), www.nu-fit.org*, .

[153] A. Himmel, *New Oscillation Results from the NOvA Experiment*, .

[154] T2K collaboration, *The Latest T2K Neutrino Oscillation Results and the Future of the T2K and Hyper-Kamiokande Experiments*, *Acta Phys. Polon. Supp.* **15** (2022) 23.

[155] U. Rahaman and S. Raut, *On the tension between the latest \nova and T2K data*, 2112.13186.

[156] Hyper-Kamiokande collaboration, *Hyper-Kamiokande Design Report*, 1805.04163.

[157] DUNE collaboration, *Deep Underground Neutrino Experiment (DUNE) Near Detector Conceptual Design Report*, 2103.13910.

[158] JUNO collaboration, *Neutrino Physics with JUNO*, *J. Phys. G* **43** (2016) 030401 [1507.05613].

[159] Hyper-Kamiokande Proto- collaboration, *Physics potential of a long-baseline neutrino oscillation experiment using a J-PARC neutrino beam and Hyper-Kamiokande*, *PTEP* **2015** (2015) 053C02 [1502.05199].

[160] M. Blennow, E. Fernandez-Martinez, T. Ota and S. Rosauro-Alcaraz, *Physics potential of the ESS$\nu$SB*, *Eur. Phys. J. C* **80** (2020) 190 [1912.04309].

[161] S.K. Agarwalla, R. Kundu, S. Prakash and M. Singh, *A close look on 2-3 mixing angle with DUNE in light of current neutrino oscillation data*, *JHEP* **03** (2022) 206 [2111.11748].

[162] Super-Kamiokande collaboration, *Atmospheric Neutrino Oscillation Analysis with Improved Event Reconstruction in Super-Kamiokande IV*, *PTEP* **2019** (2019) 053F01 [1901.03230].

[163] S.K. Agarwalla, S. Prakash and S.U. Sankar, *Resolving the octant of $\theta_{23}$ with T2K and NOvA*, *JHEP* **07** (2013) 131 [1301.2574].

[164] G.L. Fogli and E. Lisi, *Tests of three-flavor mixing in long-baseline neutrino oscillation experiments*, *Phys. Rev.* **D54** (1996) 3667 [hep-ph/9604415].

[165] H. Minakata, H. Nunokawa and S.J. Parke, *Parameter Degeneracies in Neutrino Oscillation Measurement of Leptonic CP and T Violation*, *Phys. Rev. D* **66** (2002) 093012 [hep-ph/0208163].

[166] J. Burguet-Castell, M.B. Gavela, J.J. Gomez-Cadenas, P. Hernandez and O. Mena, *On the Measurement of leptonic CP violation*, *Nucl. Phys. B* **608** (2001) 301 [hep-ph/0103258].

[167] H. Minakata and H. Nunokawa, *Exploring neutrino mixing with low energy superbeams*, *Journal of High Energy Physics* **2001** (2001) 001.

[168] A. Donini, D. Meloni and S. Rigolin, *Clone flow analysis for a theory inspired neutrino experiment planning*, *JHEP* **06** (2004) 011 [hep-ph/0312072].

[169] A. Bogacz et al., *The Physics Case for a Neutrino Factory*, in *2022 Snowmass Summer Study*, 3, 2022 [2203.08094].

[170] S. Geer, *Neutrino beams from muon storage rings: Characteristics and physics potential*, *Phys. Rev. D* **57** (1998) 6989 [hep-ph/9712290].

[171] IDS-NF collaboration, *International Design Study for the Neutrino Factory, Interim Design Report*, 1112.2853.

[172] J.-P. Delahaye et al., *Enabling Intensity and Energy Frontier Science with a Muon Accelerator Facility in the U.S.: A White Paper Submitted to the 2013 U.S. Community Summer Study of the Division of Particles and Fields of the American Physical Society*, in *Community Summer Study 2013: Snowmass on the Mississippi*, 8, 2013 [1308.0494].

[173] S. Adrián-Martínez, M. Ageron, F. Aharonian, S. Aiello, A. Albert, F. Ameli et al., *Letter of intent for km3net 2.0*, *Journal of Physics G: Nuclear and Particle Physics* **43** (2016) .

[174] A. Zee, *A Theory of Lepton Number Violation, Neutrino Majorana Mass, and Oscillation*, *Phys. Lett. B* **93** (1980) 389.

[175] A. Zee, *Quantum Numbers of Majorana Neutrino Masses*, *Nucl. Phys. B* **264** (1986) 99.

[176] L. Wolfenstein, *A Theoretical Pattern for Neutrino Oscillations*, *Nucl. Phys. B* **175** (1980) 93.

[177] K.S. Babu, *Model of 'Calculable' Majorana Neutrino Masses*, *Phys. Lett. B* **203** (1988) 132.

[178] K.S. Babu and C.N. Leung, *Classification of effective neutrino mass operators*, *Nucl. Phys. B* **619** (2001) 667 [hep-ph/0106054].

[179] E. Ma, *Verifiable radiative seesaw mechanism of neutrino mass and dark matter*, *Phys. Rev. D* **73** (2006) 077301 [hep-ph/0601225].

[180] A. de Gouvea and J. Jenkins, *A Survey of Lepton Number Violation Via Effective Operators*, *Phys. Rev. D* **77** (2008) 013008 [0708.1344].

[181] P.W. Angel, N.L. Rodd and R.R. Volkas, *Origin of neutrino masses at the LHC: $\Delta L = 2$ effective operators and their ultraviolet completions*, *Phys. Rev. D* **87** (2013) 073007 [1212.6111].

[182] M. Doi, T. Kotani and E. Takasugi, *Double beta Decay and Majorana Neutrino*, *Prog. Theor. Phys. Suppl.* **83** (1985) 1.

[183] S.M. Bilenky, J. Hosek and S.T. Petcov, *On Oscillations of Neutrinos with Dirac and Majorana Masses*, *Phys. Lett. B* **94** (1980) 495.

[184] A. Atre, T. Han, S. Pascoli and B. Zhang, *The Search for Heavy Majorana Neutrinos*, *JHEP* **05** (2009) 030 [0901.3589].

[185] H.V. Klapdor-Kleingrothaus, A. Dietz, H.L. Harney and I.V. Krivosheina, *Evidence for neutrinoless double beta decay*, *Mod. Phys. Lett. A* **16** (2001) 2409 [hep-ph/0201231].

[186] J. Suhonen and O. Civitarese, *Weak-interaction and nuclear-structure aspects of nuclear double beta decay*, *Phys. Rept.* **300** (1998) 123.

[187] S.R. Elliott and P. Vogel, *Double beta decay*, *Ann. Rev. Nucl. Part. Sci.* **52** (2002) 115 [hep-ph/0202264].

[188] W. Rodejohann, *Neutrino-less Double Beta Decay and Particle Physics*, *Int. J. Mod. Phys. E* **20** (2011) 1833 [1106.1334].

[189] GERDA collaboration, *Final Results of GERDA on the Search for Neutrinoless Double-$\beta$ Decay*, *Phys. Rev. Lett.* **125** (2020) 252502 [2009.06079].

[190] D. Tosi, *Latest results from EXO-200*, *Nuovo Cim. C* **037** (2014) 197.

[191] CUORE collaboration, *Search for Majorana neutrinos exploiting millikelvin cryogenics with CUORE*, *Nature* **604** (2022) 53 [2104.06906].

[192] KamLAND-Zen collaboration, *Results from KamLAND-Zen*, *AIP Conf. Proc.* **1666** (2015) 170003 [1409.0077].

[193] KamLAND-Zen collaboration, *First Search for the Majorana Nature of Neutrinos in the Inverted Mass Ordering Region with KamLAND-Zen*, 2203.02139.

[194] CUPID collaboration, *Final Result on the Neutrinoless Double Beta Decay of $^{82}$Se with CUPID-0*, *Phys. Rev. Lett.* **129** (2022) 111801 [2206.05130].

[195] H. Fritzsch and P. Minkowski, *Vector-Like Weak Currents, Massive Neutrinos, and Neutrino Beam Oscillations*, *Phys. Lett. B* **62** (1976) 72.

[196] H. Fritzsch, M. Gell-Mann and P. Minkowski, *Vectorlike weak currents and new elementary fermions*, *Physics Letters B* **59** (1975) 256.

[197] P. Minkowski, *$\mu \to e\gamma$ at a Rate of One Out of $10^9$ Muon Decays?*, *Phys. Lett. B* **67** (1977) 421.

[198] M. Gell-Mann, P. Ramond and R. Slansky, *Complex Spinors and Unified Theories*, *Conf. Proc. C* **790927** (1979) 315 [1306.4669].

[199] T. Yanagida, *Horizontal Symmetry and Masses of Neutrinos*, *Prog. Theor. Phys.* **64** (1980) 1103.

[200] S.L. Glashow, *The Future of Elementary Particle Physics*, *NATO Sci. Ser. B* **61** (1980) 687.

[201] R.N. Mohapatra and G. Senjanovic, *Neutrino Mass and Spontaneous Parity Nonconservation*, *Phys. Rev. Lett.* **44** (1980) 912.

[202] M. Magg and C. Wetterich, *Neutrino Mass Problem and Gauge Hierarchy*, *Phys. Lett. B* **94** (1980) 61.

[203] J. Schechter and J.W.F. Valle, *Neutrino Masses in SU(2) x U(1) Theories*, *Phys. Rev. D* **22** (1980) 2227.

[204] R.N. Mohapatra and G. Senjanovic, *Neutrino Masses and Mixings in Gauge Models with Spontaneous Parity Violation*, *Phys. Rev. D* **23** (1981) 165.

[205] G. Senjanovic and R.N. Mohapatra, *Exact Left-Right Symmetry and Spontaneous Violation of Parity*, *Phys. Rev. D* **12** (1975) 1502.

[206] R.N. Mohapatra, F.E. Paige and D.P. Sidhu, *Symmetry Breaking and Naturalness of Parity Conservation in Weak Neutral Currents in Left-Right Symmetric Gauge Theories*, *Phys. Rev. D* **17** (1978) 2462.

[207] R. Foot, H. Lew, X.G. He and G.C. Joshi, *Seesaw Neutrino Masses Induced by a Triplet of Leptons*, *Z. Phys. C* **44** (1989) 441.

[208] A. Arbey and F. Mahmoudi, *Dark matter and the early Universe: a review*, *Prog. Part. Nucl. Phys.* **119** (2021) 103865 [2104.11488].

[209] M. McCullough, *Lectures on Physics Beyond the Standard Model.*, in *6th Tri-Institute Summer School on Elementary Particles*, 2018.

[210] R.D. Peccei and H.R. Quinn, CP *conservation in the presence of pseudoparticles*, *Phys. Rev. Lett.* **38** (1977) 1440.

[211] A. D'Alise et al., *Standard model anomalies: lepton flavour non-universality, $g-2$ and W-mass*, *JHEP* **08** (2022) 125 [2204.03686].

[212] LHCb collaboration, *Differential branching fractions and isospin asymmetries of $B \to K^{(*)}\mu^+\mu^-$ decays*, *JHEP* **06** (2014) 133 [1403.8044].

[213] LHCb collaboration, *Measurements of the S-wave fraction in $B^0 \to K^+\pi^-\mu^+\mu^-$ decays and the $B^0 \to K^*(892)^0\mu^+\mu^-$ differential branching fraction*, *JHEP* **11** (2016) 047 [1606.04731].

[214] LHCb collaboration, *Test of lepton universality with $B^0 \to K^{*0}\ell^+\ell^-$ decays*, *JHEP* **08** (2017) 055 [1705.05802].

[215] LHCb collaboration, *Angular Analysis of the $B^+ \to K^{*+}\mu^+\mu^-$ Decay*, *Phys. Rev. Lett.* **126** (2021) 161802 [2012.13241].

[216] LHCb collaboration, *Measurement of the $B_s^0 \to \mu^+\mu^-$ decay properties and search for the $B^0 \to \mu^+\mu^-$ and $B_s^0 \to \mu^+\mu^-\gamma$ decays*, *Phys. Rev. D* **105** (2022) 012010 [2108.09283].

[217] LHCb collaboration, *Test of lepton universality in beauty-quark decays*, *Nature Phys.* **18** (2022) 277 [2103.11769].

[218] LHCb collaboration, *Branching Fraction Measurements of the Rare $B_s^0 \to \phi\mu^+\mu^-$ and $B_s^0 \to f_2'(1525)\mu^+\mu^-$- Decays*, *Phys. Rev. Lett.* **127** (2021) 151801 [2105.14007].

[219] BELLE collaboration, *Test of lepton flavor universality and search for lepton flavor violation in $B \to K\ell\ell$ decays*, *JHEP* **03** (2021) 105 [1908.01848].

[220] Belle collaboration, *Test of Lepton-Flavor Universality in $B \to K^*\ell^+\ell^-$ Decays at Belle*, *Phys. Rev. Lett.* **126** (2021) 161801 [1904.02440].

[221] ATLAS collaboration, *Study of the rare decays of $B_s^0$ and $B^0$ mesons into muon pairs using data collected during 2015 and 2016 with the ATLAS detector*, *JHEP* **04** (2019) 098 [1812.03017].

[222] BaBar collaboration, *Measurement of the $B \to X_s l^+l^-$ branching fraction and search for direct CP violation from a sum of exclusive final states*, *Phys. Rev. Lett.* **112** (2014) 211802 [1312.5364].

[223] Muon g-2 collaboration, *Final Report of the Muon E821 Anomalous Magnetic Moment Measurement at BNL*, *Phys. Rev. D* **73** (2006) 072003 [hep-ex/0602035].

[224] Muon g-2 collaboration, *Measurement of the Positive Muon Anomalous Magnetic Moment to 0.46 ppm*, *Phys. Rev. Lett.* **126** (2021) 141801 [2104.03281].

[225] ATLAS Collaboration collaboration, *Angular analysis of $B_d^0 \to K^*\mu^+\mu^-$ decays in pp collisions at $\sqrt{s} = 8$ TeV with the ATLAS detector*, Tech. Rep. ATLAS-CONF-2017-023, CERN, Geneva (2017).

[226] C.A. Argüelles et al., *New opportunities at the next-generation neutrino experiments I: BSM neutrino physics and dark matter*, *Rept. Prog. Phys.* **83** (2020) 124201 [1907.08311].

[227] C.A. Argüelles et al., *Snowmass White Paper: Beyond the Standard Model effects on Neutrino Flavor*, in *2022 Snowmass Summer Study*, 3, 2022 [2203.10811].

[228] G. Mention, M. Fechner, T. Lasserre, T.A. Mueller, D. Lhuillier, M. Cribier et al., *The Reactor Antineutrino Anomaly*, *Phys. Rev. D* **83** (2011) 073006 [1101.2755].

[229] LSND collaboration, *Evidence for neutrino oscillations from the observation of $\bar{\nu}_e$ appearance in a $\bar{\nu}_\mu$ beam*, *Phys. Rev. D* **64** (2001) 112007 [hep-ex/0104049].

[230] MiniBooNE collaboration, *Significant Excess of ElectronLike Events in the MiniBooNE Short-Baseline Neutrino Experiment*, *Phys. Rev. Lett.* **121** (2018) 221801 [1805.12028].

[231] MiniBooNE collaboration, *Updated MiniBooNE neutrino oscillation results with increased data and new background studies*, *Phys. Rev. D* **103** (2021) 052002 [2006.16883].

[232] C. Giunti and M. Laveder, *Statistical Significance of the Gallium Anomaly*, *Phys. Rev. C* **83** (2011) 065504 [1006.3244].

[233] A.P. Serebrov.

[234] M. Guzzo, A. Masiero and S. Petcov, *On the MSW effect with massless neutrinos and no mixing in the vacuum*, *Phys. Lett. B* **260** (1991) 154.

[235] Y. Grossman, *Nonstandard neutrino interactions and neutrino oscillation experiments*, *Phys. Lett. B* **359** (1995) 141 [hep-ph/9507344].

[236] *Neutrino Non-Standard Interactions: A Status Report*, vol. 2, 2019. 10.21468/SciPostPhysProc.2.001.

[237] Y. Farzan and I.M. Shoemaker, *Lepton Flavor Violating Non-Standard Interactions via Light Mediators*, *JHEP* **07** (2016) 033 [1512.09147].

[238] K. Babu, A. Friedland, P. Machado and I. Mocioiu, *Flavor Gauge Models Below the Fermi Scale*, *JHEP* **12** (2017) 096 [1705.01822].

[239] P.B. Denton, Y. Farzan and I.M. Shoemaker, *Activating the fourth neutrino of the 3+1 scheme*, *Phys. Rev. D* **99** (2019) 035003 [1811.01310].

[240] H. Davoudiasl, H.-S. Lee and W.J. Marciano, *Long-Range Lepton Flavor Interactions and Neutrino Oscillations*, *Phys. Rev. D* **84** (2011) 013009 [1102.5352].

[241] Y. Farzan and J. Heeck, *Neutrinophilic nonstandard interactions*, *Phys. Rev. D* **94** (2016) 053010 [1607.07616].

[242] M.B. Wise and Y. Zhang, *Lepton Flavorful Fifth Force and Depth-dependent Neutrino Matter Interactions*, *JHEP* **06** (2018) 053 [1803.00591].

[243] S.-F. Ge and S.J. Parke, *Scalar Nonstandard Interactions in Neutrino Oscillation*, *Phys. Rev. Lett.* **122** (2019) 211801 [1812.08376].

[244] D. Aristizabal Sierra, V. De Romeri and N. Rojas, *COHERENT analysis of neutrino generalized interactions*, *Phys. Rev. D* **98** (2018) 075018 [1806.07424].

[245] R.N. Mohapatra and J.W.F. Valle, *Neutrino Mass and Baryon Number Nonconservation in Superstring Models*, *Phys. Rev. D* **34** (1986) 1642.

[246] E.K. Akhmedov, M. Lindner, E. Schnapka and J.W.F. Valle, *Left-right symmetry breaking in NJL approach*, *Phys. Lett. B* **368** (1996) 270 [hep-ph/9507275].

[247] M. Malinsky, J.C. Romao and J.W.F. Valle, *Novel supersymmetric SO(10) seesaw mechanism*, *Phys. Rev. Lett.* **95** (2005) 161801 [hep-ph/0506296].

[248] D.V. Forero, S. Morisi, M. Tortola and J.W.F. Valle, *Lepton flavor violation and non-unitary lepton mixing in low-scale type-I seesaw*, *JHEP* **09** (2011) 142 [1107.6009].

[249] F.J. Escrihuela, D.V. Forero, O.G. Miranda, M. Tortola and J.W.F. Valle, *On the description of nonunitary neutrino mixing*, *Phys. Rev. D* **92** (2015) 053009 [1503.08879].

[250] Y.-F. Li and S. Luo, *Neutrino Oscillation Probabilities in Matter with Direct and Indirect Unitarity Violation in the Lepton Mixing Matrix*, *Phys. Rev. D* **93** (2016) 033008 [1508.00052].

[251] C.S. Fong, H. Minakata and H. Nunokawa, *A framework for testing leptonic unitarity by neutrino oscillation experiments*, *JHEP* **02** (2017) 114 [1609.08623].

[252] H. Päs and P. Sicking, *Discriminating sterile neutrinos and unitarity violation with CP invariants*, *Phys. Rev. D* **95** (2017) 075004 [1611.08450].

[253] F.J. Escrihuela, D.V. Forero, O.G. Miranda, M. Tórtola and J.W.F. Valle, *Probing CP violation with non-unitary mixing in long-baseline neutrino oscillation experiments: DUNE as a case study*, *New J. Phys.* **19** (2017) 093005 [1612.07377].

[254] M. Blennow, P. Coloma, E. Fernandez-Martinez, J. Hernandez-Garcia and J. Lopez-Pavon, *Non-Unitarity, sterile neutrinos, and Non-Standard neutrino Interactions*, *JHEP* **04** (2017) 153 [1609.08637].

[255] G.B. Gelmini and M. Roncadelli, *Left-Handed Neutrino Mass Scale and Spontaneously Broken Lepton Number*, *Phys. Lett. B* **99** (1981) 411.

[256] C.S. Aulakh and R.N. Mohapatra, *Neutrino as the Supersymmetric Partner of the Majoron*, *Phys. Lett. B* **119** (1982) 136.

[257] M.C. Gonzalez-Garcia and J.W.F. Valle, *Fast Decaying Neutrinos and Observable Flavor Violation in a New Class of Majoron Models*, *Phys. Lett. B* **216** (1989) 360.

[258] M. Lindner, T. Ohlsson and W. Winter, *A Combined treatment of neutrino decay and neutrino oscillations*, *Nucl. Phys. B* **607** (2001) 326 [hep-ph/0103170].

[259] A.M. Gago, R.A. Gomes, A.L.G. Gomes, J. Jones-Perez and O.L.G. Peres, *Visible neutrino decay in the light of appearance and disappearance long baseline experiments*, *JHEP* **11** (2017) 022 [1705.03074].

[260] P. Coloma and O.L.G. Peres, *Visible neutrino decay at DUNE*, 1705.03599.

[261] M.V. Ascencio-Sosa, A.M. Calatayud-Cadenillas, A.M. Gago and J. Jones-Pérez, *Matter effects in neutrino visible decay at future long-baseline experiments*, *Eur. Phys. J. C* **78** (2018) 809 [1805.03279].

[262] S. Hannestad and G. Raffelt, *Constraining invisible neutrino decays with the cosmic microwave background*, *Phys. Rev. D* **72** (2005) 103514 [hep-ph/0509278].

[263] V.A. Kostelecky and S. Samuel, *Spontaneous Breaking of Lorentz Symmetry in String Theory*, *Phys. Rev. D* **39** (1989) 683.

[264] V.A. Kostelecky and M. Mewes, *Lorentz and CPT violation in neutrinos*, *Phys. Rev. D* **69** (2004) 016005 [hep-ph/0309025].

[265] V.A. Kostelecky and M. Mewes, *Lorentz violation and short-baseline neutrino experiments*, *Phys. Rev. D* **70** (2004) 076002 [hep-ph/0406255].

[266] T. Katori, V.A. Kostelecky and R. Tayloe, *Global three-parameter model for neutrino oscillations using Lorentz violation*, *Phys. Rev. D* **74** (2006) 105009 [hep-ph/0606154].

[267] J.S. Diaz and A. Kostelecky, *Lorentz- and CPT-violating models for neutrino oscillations*, *Phys. Rev. D* **85** (2012) 016013 [1108.1799].

[268] A. Kostelecky and M. Mewes, *Neutrinos with Lorentz-violating operators of arbitrary dimension*, *Phys. Rev. D* **85** (2012) 096005 [1112.6395].

[269] J.S. Diaz, *Correspondence between nonstandard interactions and CPT violation in neutrino oscillations*, 1506.01936.

[270] G. Barenboim, C.A. Ternes and M. Tórtola, *New physics vs new paradigms: distinguishing CPT violation from NSI*, *Eur. Phys. J. C* **79** (2019) 390 [1804.05842].

[271] G. Barenboim, C.A. Ternes and M. Tórtola, *Neutrinos, DUNE and the world best bound on CPT invariance*, *Phys. Lett. B* **780** (2018) 631 [1712.01714].

[272] IceCube collaboration, *Neutrino Interferometry for High-Precision Tests of Lorentz Symmetry with IceCube*, *Nature Phys.* **14** (2018) 961 [1709.03434].

[273] C.A. Argüelles, T. Katori and J. Salvado, *New Physics in Astrophysical Neutrino Flavor*, *Phys. Rev. Lett.* **115** (2015) 161303 [1506.02043].

[274] IceCube collaboration, *Search for a Lorentz-violating sidereal signal with atmospheric neutrinos in IceCube*, *Phys. Rev. D* **82** (2010) 112003 [1010.4096].

[275] MINOS collaboration, *Testing Lorentz Invariance and CPT Conservation with NuMI Neutrinos in the MINOS Near Detector*, *Phys. Rev. Lett.* **101** (2008) 151601 [0806.4945].

[276] MINOS collaboration, *A Search for Lorentz Invariance and CPT Violation with the MINOS Far Detector*, *Phys. Rev. Lett.* **105** (2010) 151601 [1007.2791].

[277] Super-Kamiokande collaboration, *Study of Non-Standard Neutrino Interactions with Atmospheric Neutrino Data in Super-Kamiokande I and II*, *Phys. Rev. D* **84** (2011) 113008 [1109.1889].

[278] MiniBooNE collaboration, *Test of Lorentz and CPT violation with Short Baseline Neutrino Oscillation Excesses*, *Phys. Lett. B* **718** (2013) 1303 [1109.3480].

[279] Double Chooz collaboration, *First Test of Lorentz Violation with a Reactor-based Antineutrino Experiment*, *Phys. Rev. D* **86** (2012) 112009 [1209.5810].

[280] EXO-200 collaboration, *First Search for Lorentz and CPT Violation in Double Beta Decay with EXO-200*, *Phys. Rev. D* **93** (2016) 072001 [1601.07266].

[281] T2K collaboration, *Search for Lorentz and CPT violation using sidereal time dependence of neutrino flavor transitions over a short baseline*, *Phys. Rev. D* **95** (2017) 111101 [1703.01361].

[282] ICAL collaboration, *Physics Potential of the ICAL detector at the India-based Neutrino Observatory (INO)*, *Pramana* **88** (2017) 79 [1505.07380].

[283] Daya Bay collaboration, *Search for a time-varying electron antineutrino signal at Daya Bay*, *Phys. Rev. D* **98** (2018) 092013 [1809.04660].

[284] G. Barenboim, M. Masud, C.A. Ternes and M. Tórtola, *Exploring the intrinsic Lorentz-violating parameters at DUNE*, *Phys. Lett. B* **788** (2019) 308 [1805.11094].

[285] M.J. Longo, *Tests of Relativity From Sn1987a*, *Phys. Rev. D* **36** (1987) 3276.

[286] MINOS collaboration, *Precision Measurement of the Speed of Propagation of Neutrinos using the MINOS Detectors*, *Phys. Rev. D* **92** (2015) 052005 [1507.04328].

[287] ICARUS collaboration, *A Search for the analogue to Cherenkov radiation by high energy neutrinos at superluminal speeds in ICARUS*, *Phys. Lett. B* **711** (2012) 270 [1110.3763].

[288] A.G. Cohen and S.L. Glashow, *Pair Creation Constrains Superluminal Neutrino Propagation*, *Phys. Rev. Lett.* **107** (2011) 181803 [1109.6562].

[289] N. Fiza, N.R. Khan Chowdhury and M. Masud, *Investigating Lorentz Violation with the long baseline experiment P2O*, 2206.14018.

[290] A. Roberts, *Astrophysical Neutrinos in Testing Lorentz Symmetry*, *Galaxies* **9** (2021) 47.

[291] S. Sahoo, A. Kumar, S.K. Agarwalla and A. Dighe, *Core-passing atmospheric neutrinos: a unique probe to discriminate between Lorentz violation and non-standard interactions*, 2205.05134.

[292] F.N. Díaz, J. Hoefken and A.M. Gago, *Effects of the Violation of the Equivalence Principle at DUNE*, *Phys. Rev. D* **102** (2020) 055020 [2003.13712].

[293] R. Majhi, S. Chembra and R. Mohanta, *Exploring the effect of Lorentz invariance violation with the currently running long-baseline experiments*, *Eur. Phys. J. C* **80** (2020) 364 [1907.09145].

[294] H. Davoudiasl, P. Langacker and M. Perelstein, *Constraints on large extra dimensions from neutrino oscillation experiments*, *Phys. Rev. D* **65** (2002) 105015 [hep-ph/0201128].

[295] P.A.N. Machado, H. Nunokawa and R. Zukanovich Funchal, *Testing for Large Extra Dimensions with Neutrino Oscillations*, *Phys. Rev. D* **84** (2011) 013003 [1101.0003].

[296] P.A.N. Machado, H. Nunokawa, F.A.P. dos Santos and R.Z. Funchal, *Bulk Neutrinos as an Alternative Cause of the Gallium and Reactor Anti-neutrino Anomalies*, *Phys. Rev. D* **85** (2012) 073012 [1107.2400].

[297] A. Di Iura, I. Girardi and D. Meloni, *Probing new physics scenarios in accelerator and reactor neutrino experiments*, *J. Phys. G* **42** (2015) 065003 [1411.5330].

[298] A. Esmaili, O.L.G. Peres and Z. Tabrizi, *Probing Large Extra Dimensions With IceCube*, *JCAP* **12** (2014) 002 [1409.3502].

[299] J.M. Berryman, A. de Gouvêa, K.J. Kelly, O.L.G. Peres and Z. Tabrizi, *Large, Extra Dimensions at the Deep Underground Neutrino Experiment*, *Phys. Rev. D* **94** (2016) 033006 [1603.00018].

[300] G.V. Stenico, D.V. Forero and O.L.G. Peres, *A Short Travel for Neutrinos in Large Extra Dimensions*, *JHEP* **11** (2018) 155 [1808.05450].

[301] MINOS collaboration, *Constraints on Large Extra Dimensions from the MINOS Experiment*, *Phys. Rev. D* **94** (2016) 111101 [1608.06964].

[302] A.N. Khan, *Extra dimensions with light and heavy neutral leptons: An application to CE$\nu$NS*, 2208.09584.

[303] D.V. Forero, C. Giunti, C.A. Ternes and O. Tyagi, *Large extra dimensions and neutrino experiments*, *Phys. Rev. D* **106** (2022) 035027 [2207.02790].

[304] M. Ettengruber, *Neutrino physics in TeV scale gravity theories*, *Phys. Rev. D* **106** (2022) 055028 [2206.00034].

[305] W. Czyz, G.C. Sheppey and J.D. Walecka, *Neutrino production of lepton pairs through the point four-fermion interaction*, *Nuovo Cim.* **34** (1964) 404.

[306] J. Lovseth and M. Radomiski, *Kinematical distributions of neutrino-produced lepton triplets*, *Phys. Rev. D* **3** (1971) 2686.

[307] K. Fujikawa, *The self-coupling of weak lepton currents in high-energy neutrino and muon reactions*, *Annals Phys.* **68** (1971) 102.

[308] K. Koike, M. Konuma, K. Kurata and K. Sugano, *Neutrino production of lepton pairs. 1. -*, *Prog. Theor. Phys.* **46** (1971) 1150.

[309] K. Koike, M. Konuma, K. Kurata and K. Sugano, *Neutrino production of lepton pairs. 2.*, *Prog. Theor. Phys.* **46** (1971) 1799.

[310] R. Belusevic and J. Smith, *W - Z Interference in Neutrino - Nucleus Scattering*, *Phys. Rev. D* **37** (1988) 2419.

[311] R.W. Brown, R.H. Hobbs, J. Smith and N. Stanko, *Intermediate boson. iii. virtual-boson effects in neutrino trident production*, *Phys. Rev. D* **6** (1972) 3273.

[312] B. Zhou and J.F. Beacom, *Neutrino-nucleus cross sections for W-boson and trident production*, *Phys. Rev. D* **101** (2020) 036011 [1910.08090].

[313] CHARM-II collaboration, *First observation of neutrino trident production*, *Phys. Lett. B* **245** (1990) 271.

[314] NuTeV collaboration, *Evidence for diffractive charm production in muon-neutrino Fe and anti-muon-neutrino Fe scattering at the Tevatron*, *Phys. Rev. D* **61** (2000) 092001 [hep-ex/9909041].

[315] CCFR collaboration, *Neutrino tridents and W Z interference*, *Phys. Rev. Lett.* **66** (1991) 3117.

[316] X.G. He, G.C. Joshi, H. Lew and R.R. Volkas, *NEW Z-prime PHENOMENOLOGY*, *Phys. Rev. D* **43** (1991) 22.

[317] X.-G. He, G.C. Joshi, H. Lew and R.R. Volkas, *Simplest Z-prime model*, *Phys. Rev. D* **44** (1991) 2118.

[318] P. Ballett, M. Hostert, S. Pascoli, Y.F. Perez-Gonzalez, Z. Tabrizi and R. Zukanovich Funchal, *Neutrino Trident Scattering at Near Detectors*, *JHEP* **01** (2019) 119 [1807.10973].

[319] P. Ballett, M. Hostert, S. Pascoli, Y.F. Perez-Gonzalez, Z. Tabrizi and R. Zukanovich Funchal, *$Z'$s in neutrino scattering at DUNE*, *Phys. Rev. D* **100** (2019) 055012 [1902.08579].

[320] E.K. Akhmedov, V.A. Rubakov and A.Y. Smirnov, *Baryogenesis via neutrino oscillations*, *Phys. Rev. Lett.* **81** (1998) 1359 [hep-ph/9803255].

[321] T. Asaka and M. Shaposhnikov, *The $\nu$MSM, dark matter and baryon asymmetry of the universe*, *Phys. Lett. B* **620** (2005) 17 [hep-ph/0505013].

[322] P. Ballett, M. Hostert and S. Pascoli, *Neutrino Masses from a Dark Neutrino Sector below the Electroweak Scale*, *Phys. Rev. D* **99** (2019) 091701 [1903.07590].

[323] M. Drewes, *The Phenomenology of Right Handed Neutrinos*, *Int. J. Mod. Phys. E* **22** (2013) 1330019 [1303.6912].

[324] N. Sabti, A. Magalich and A. Filimonova, *An Extended Analysis of Heavy Neutral Leptons during Big Bang Nucleosynthesis*, *JCAP* **11** (2020) 056 [2006.07387].

[325] A.M. Abdullahi et al., *The Present and Future Status of Heavy Neutral Leptons*, in *2022 Snowmass Summer Study*, 3, 2022 [2203.08039].

[326] T2K collaboration, *Search for heavy neutrinos with the T2K near detector ND280*, *Phys. Rev. D* **100** (2019) 052006 [1902.07598].

[327] P. Ballett, S. Pascoli and M. Ross-Lonergan, *MeV-scale sterile neutrino decays at the Fermilab Short-Baseline Neutrino program*, *JHEP* **04** (2017) 102 [1610.08512].

[328] P. Ballett, T. Boschi and S. Pascoli, *Heavy Neutral Leptons from low-scale seesaws at the DUNE Near Detector*, *JHEP* **03** (2020) 111 [1905.00284].

[329] A. Berlin, *Neutrino Oscillations as a Probe of Light Scalar Dark Matter*, *Phys. Rev. Lett.* **117** (2016) 231801 [1608.01307].

[330] G. Krnjaic, P.A.N. Machado and L. Necib, *Distorted neutrino oscillations from time varying cosmic fields*, *Phys. Rev. D* **97** (2018) 075017 [1705.06740].

[331] V. Brdar, J. Kopp, J. Liu, P. Prass and X.-P. Wang, *Fuzzy dark matter and nonstandard neutrino interactions*, *Phys. Rev. D* **97** (2018) 043001 [1705.09455].

[332] F. Capozzi, I.M. Shoemaker and L. Vecchi, *Solar Neutrinos as a Probe of Dark Matter-Neutrino Interactions*, *JCAP* **07** (2017) 021 [1702.08464].

[333] J. Liao, D. Marfatia and K. Whisnant, *Light scalar dark matter at neutrino oscillation experiments*, *JHEP* **04** (2018) 136 [1803.01773].

[334] F. Capozzi, I.M. Shoemaker and L. Vecchi, *Neutrino Oscillations in Dark Backgrounds*, *JCAP* **07** (2018) 004 [1804.05117].

[335] Y. Tsai, L.-T. Wang and Y. Zhao, *Faking ordinary photons by displaced dark photon decays*, *Phys. Rev. D* **95** (2017) 015027 [1603.00024].

[336] C. Boehm, Y. Farzan, T. Hambye, S. Palomares-Ruiz and S. Pascoli, *Is it possible to explain neutrino masses with scalar dark matter?*, *Phys. Rev. D* **77** (2008) 043516 [hep-ph/0612228].

[337] J. Asaadi, E. Church, R. Guenette, B.J.P. Jones and A.M. Szelc, *New light Higgs boson and short-baseline neutrino anomalies*, *Phys. Rev. D* **97** (2018) 075021 [1712.08019].

[338] E. Bertuzzo, S. Jana, P.A.N. Machado and R. Zukanovich Funchal, *Dark Neutrino Portal to Explain MiniBooNE excess*, *Phys. Rev. Lett.* **121** (2018) 241801 [1807.09877].

[339] S.W. Hawking, *Particle Creation by Black Holes*, *Commun. Math. Phys.* **43** (1975) 199.

[340] J.R. Ellis, N.E. Mavromatos and D.V. Nanopoulos, *String theory modifies quantum mechanics*, *Phys. Lett. B* **293** (1992) 37 [hep-th/9207103].

[341] J.R. Ellis, N.E. Mavromatos, D.V. Nanopoulos and E. Winstanley, *Quantum decoherence in a four-dimensional black hole background*, *Mod. Phys. Lett. A* **12** (1997) 243 [gr-qc/9602011].

[342] J.R. Ellis, N.E. Mavromatos and D.V. Nanopoulos, *Quantum decoherence in a D foam background*, *Mod. Phys. Lett. A* **12** (1997) 1759 [hep-th/9704169].

[343] F. Benatti and R. Floreanini, *Non-standard Neutral Kaon Dynamics from Infinite Statistics*, *Annals Phys.* **273** (1999) 58 [hep-th/9811196].

[344] P. Coloma, J. Lopez-Pavon, I. Martinez-Soler and H. Nunokawa, *Decoherence in Neutrino Propagation Through Matter, and Bounds from IceCube/DeepCore*, *Eur. Phys. J. C* **78** (2018) 614 [1803.04438].

[345] G. Balieiro Gomes, M.M. Guzzo, P.C. de Holanda and R.L.N. Oliveira, *Parameter Limits for Neutrino Oscillation with Decoherence in KamLAND*, *Phys. Rev. D* **95** (2017) 113005 [1603.04126].

[346] M. Masud, M. Bishai and P. Mehta, *Extricating New Physics Scenarios at DUNE with Higher Energy Beams*, *Sci. Rep.* **9** (2019) 352 [1704.08650].

[347] G. Balieiro Gomes, D.V. Forero, M.M. Guzzo, P.C. De Holanda and R.L.N. Oliveira, *Quantum Decoherence Effects in Neutrino Oscillations at DUNE*, *Phys. Rev. D* **100** (2019) 055023 [1805.09818].

[348] J.A. Carpio, E. Massoni and A.M. Gago, *Testing quantum decoherence at DUNE*, *Phys. Rev. D* **100** (2019) 015035 [1811.07923].

[349] T. Stuttard and M. Jensen, *Neutrino decoherence from quantum gravitational stochastic perturbations*, *Phys. Rev. D* **102** (2020) 115003 [2007.00068].

[350] D. Hellmann, H. Päs and E. Rani, *Searching new particles at neutrino telescopes with quantum-gravitational decoherence*, *Phys. Rev. D* **105** (2022) 055007 [2103.11984].

[351] T. Stuttard, *Neutrino signals of lightcone fluctuations resulting from fluctuating spacetime*, *Phys. Rev. D* **104** (2021) 056007 [2103.15313].

[352] D.V. Ahluwalia, *Ambiguity in source flux of high-energy cosmic / astrophysical neutrinos: Effects of bimaximal mixing and quantum gravity induced decoherence*, *Mod. Phys. Lett. A* **16** (2001) 917 [hep-ph/0104316].

[353] D. Hooper, D. Morgan and E. Winstanley, *Probing quantum decoherence with high-energy neutrinos*, *Phys. Lett. B* **609** (2005) 206 [hep-ph/0410094].

[354] L.A. Anchordoqui, H. Goldberg, M.C. Gonzalez-Garcia, F. Halzen, D. Hooper, S. Sarkar et al., *Probing Planck scale physics with IceCube*, *Phys. Rev. D* **72** (2005) 065019 [hep-ph/0506168].

[355] ALEPH collaboration, *Determination of the Number of Light Neutrino Species*, *Phys. Lett. B* **231** (1989) 519.

[356] ALEPH collaboration, *A Precise Determination of the Number of Families With Light Neutrinos and of the Z Boson Partial Widths*, *Phys. Lett. B* **235** (1990) 399.

[357] DELPHI collaboration, *Measurement of the Mass and Width of the $Z^0$ Particle from Multi - Hadronic Final States Produced in $e^+e^-$ Annihilations*, *Phys. Lett. B* **231** (1989) 539.

[358] L3 collaboration, *A Determination of the Properties of the Neutral Intermediate Vector Boson $Z^0$*, *Phys. Lett. B* **231** (1989) 509.

[359] A. Strumia, *Interpreting the LSND anomaly: Sterile neutrinos or CPT violation or...?*, *Phys. Lett. B* **539** (2002) 91 [hep-ph/0201134].

[360] W. Abdallah, R. Gandhi and S. Roy, *Two-Higgs doublet solution to the LSND, MiniBooNE and muon g-2 anomalies*, *Phys. Rev. D* **104** (2021) 055028 [2010.06159].

[361] A. de Gouvea and Y. Grossman, *A Three-flavor, Lorentz-violating solution to the LSND anomaly*, *Phys. Rev. D* **74** (2006) 093008 [hep-ph/0602237].

[362] Y. Farzan, T. Schwetz and A.Y. Smirnov, *Reconciling results of LSND, MiniBooNE and other experiments with soft decoherence*, *JHEP* **07** (2008) 067 [0805.2098].

[363] S. Hollenberg, O. Micu and H. Pas, *Neutrino-antineutrino oscillations as a possible solution for the LSND and MiniBooNE anomalies?*, *Phys. Rev. D* **80** (2009) 053010 [0906.5072].

[364] E. Akhmedov and T. Schwetz, *MiniBooNE and LSND data: Non-standard neutrino interactions in a (3+1) scheme versus (3+2) oscillations*, *JHEP* **10** (2010) 115 [1007.4171].

[365] B. Dutta, D. Kim, A. Thompson, R.T. Thornton and R.G. Van de Water, *Solutions to the MiniBooNE Anomaly from New Physics in Charged Meson Decays*, *Phys. Rev. Lett.* **129** (2022) 111803 [2110.11944].

[366] A. Abdullahi, M. Hostert and S. Pascoli, *A dark seesaw solution to low energy anomalies: MiniBooNE, the muon g-2, and BaBar*, *Phys. Lett. B* **820** (2021) 136531 [2007.11813].

[367] L. Alvarez-Ruso, J. Nieves, E. Saúl Sala and E. Wang, *Neutrino Interactions in the few-GeV region and the MiniBooNE anomaly*, *J. Phys. Conf. Ser.* **1056** (2018) 012001.

[368] RENO collaboration, *Observation of Reactor Electron Antineutrino Disappearance in the RENO Experiment*, *Phys. Rev. Lett.* **108** (2012) 191802 [1204.0626].

[369] Daya Bay collaboration, *Observation of electron-antineutrino disappearance at Daya Bay*, *Phys. Rev. Lett.* **108** (2012) 171803 [1203.1669].

[370] Y. Declais et al., *Study of reactor anti-neutrino interaction with proton at Bugey nuclear power plant*, *Phys. Lett. B* **338** (1994) 383.

[371] Y. Declais et al., *Search for neutrino oscillations at 15-meters, 40-meters, and 95-meters from a nuclear power reactor at Bugey*, *Nucl. Phys. B* **434** (1995) 503.

[372] A. Kuvshinnikov, L. Mikaelyan, S. Nikolaev, M. Skorokhvatov and A. Etenko, *Measuring the anti-electron-neutrino + p - ¿ n + e+ cross-section and beta decay axial constant in a new experiment at rovno npp reactor*, *JETP Lett.* **54** (1991) 253.

[373] CALTECH-SIN-TUM collaboration, *Neutrino Oscillation Experiments at the Gosgen Nuclear Power Reactor*, *Phys. Rev. D* **34** (1986) 2621.

[374] H. Kwon, F. Boehm, A.A. Hahn, H.E. Henrikson, J.L. Vuilleumier, J.F. Cavaignac et al., *Search for Neutrino Oscillations at a Fission Reactor*, *Phys. Rev. D* **24** (1981) 1097.

[375] G.S. Vidyakin, V.N. Vyrodov, I.I. Gurevich, Y.V. Kozlov, V.P. Martemyanov, S.V. Sukhotin et al., *Detection of Anti-neutrinos in the Flux From Two Reactors*, *Sov. Phys. JETP* **66** (1987) 243.

[376] G.S. Vidyakin et al., *Limitations on the characteristics of neutrino oscillations*, *JETP Lett.* **59** (1994) 390.

[377] Y.V. Kozlov, S.V. Khalturtsev, I.N. Machulin, A.V. Martemyanov, V.P. Martemyanov, S.V. Sukhotin et al., *Anti-neutrino deuteron experiment at Krasnoyarsk*, *Phys. Atom. Nucl.* **63** (2000) 1016 [hep-ex/9912047].

[378] Z.D. Greenwood et al., *Results of a two position reactor neutrino oscillation experiment*, *Phys. Rev. D* **53** (1996) 6054.

[379] A.I. Afonin, S.N. Ketov, V.I. Kopeikin, L.A. Mikaelian and M.D. Skorokhvatov, *A study of the reaction nu(-)e + p yields e(+) + n in a nuclear reactor*, *Zhurnal Eksperimentalnoi i Teoreticheskoi Fiziki* **94** (1988) 1.

[380] NUCIFER collaboration, *Online Monitoring of the Osiris Reactor with the Nucifer Neutrino Detector*, *Phys. Rev. D* **93** (2016) 112006 [1509.05610].

[381] F. Boehm et al., *Final results from the Palo Verde neutrino oscillation experiment*, *Phys. Rev. D* **64** (2001) 112001 [hep-ex/0107009].

[382] Double Chooz collaboration, *Improved measurements of the neutrino mixing angle $\theta_{13}$ with the Double Chooz detector*, *JHEP* **10** (2014) 086 [1406.7763].

[383] CHOOZ collaboration, *Search for neutrino oscillations on a long baseline at the CHOOZ nuclear power station*, *Eur. Phys. J. C* **27** (2003) 331 [hep-ex/0301017].

[384] DANSS collaboration, *Search for sterile neutrinos at the DANSS experiment*, *Phys. Lett. B* **787** (2018) 56 [1804.04046].

[385] NEOS collaboration, *Sterile Neutrino Search at the NEOS Experiment*, *Phys. Rev. Lett.* **118** (2017) 121802 [1610.05134].

[386] STEREO collaboration, *Improved sterile neutrino constraints from the STEREO experiment with 179 days of reactor-on data*, *Phys. Rev. D* **102** (2020) 052002 [1912.06582].

[387] L. Hayen, J. Kostensalo, N. Severijns and J. Suhonen, *First-forbidden transitions in the reactor anomaly*, *Phys. Rev. C* **100** (2019) 054323 [1908.08302].

[388] P. Huber, *On the determination of anti-neutrino spectra from nuclear reactors*, *Phys. Rev. C* **84** (2011) 024617 [1106.0687].

[389] T.A. Mueller et al., *Improved Predictions of Reactor Antineutrino Spectra*, *Phys. Rev. C* **83** (2011) 054615 [1101.2663].

[390] M. Estienne et al., *Updated Summation Model: An Improved Agreement with the Daya Bay Antineutrino Fluxes*, *Phys. Rev. Lett.* **123** (2019) 022502 [1904.09358].

[391] C. Giunti, Y.F. Li, C.A. Ternes and Z. Xin, *Reactor antineutrino anomaly in light of recent flux model refinements*, *Phys. Lett. B* **829** (2022) 137054 [2110.06820].

[392] P. Huber, *NEOS Data and the Origin of the 5 MeV Bump in the Reactor Antineutrino Spectrum*, *Phys. Rev. Lett.* **118** (2017) 042502 [1609.03910].

[393] J.M. Berryman, V. Brdar and P. Huber, *Particle physics origin of the 5 MeV bump in the reactor antineutrino spectrum?*, *Phys. Rev. D* **99** (2019) 055045 [1803.08506].

[394] V. Zacek, G. Zacek, P. Vogel and J.L. Vuilleumier, *Evidence for a 5 MeV Spectral Deviation in the Goesgen Reactor Neutrino Oscillation Experiment*, 1807.01810.

[395] Stereo, Prospect collaboration, *Joint Measurement of the $^{235}U$ Antineutrino Spectrum by Prospect and Stereo*, *Phys. Rev. Lett.* **128** (2022) 081802 [2107.03371].

[396] Daya Bay collaboration, *Extraction of the $^{235}U$ and $^{239}Pu$ Antineutrino Spectra at Daya Bay*, *Phys. Rev. Lett.* **123** (2019) 111801 [1904.07812].

[397] Daya Bay collaboration, *Evolution of the Reactor Antineutrino Flux and Spectrum at Daya Bay*, *Phys. Rev. Lett.* **118** (2017) 251801 [1704.01082].

[398] C. Giunti, Y.F. Li, B.R. Littlejohn and P.T. Surukuchi, *Diagnosing the Reactor Antineutrino Anomaly with Global Antineutrino Flux Data*, *Phys. Rev. D* **99** (2019) 073005 [1901.01807].

[399] RENO collaboration, *Fuel-composition dependent reactor antineutrino yield at RENO*, *Phys. Rev. Lett.* **122** (2019) 232501 [1806.00574].

[400] C. Giunti, X.P. Ji, M. Laveder, Y.F. Li and B.R. Littlejohn, *Reactor Fuel Fraction Information on the Antineutrino Anomaly*, *JHEP* **10** (2017) 143 [1708.01133].

[401] Y. Gebre, B.R. Littlejohn and P.T. Surukuchi, *Prospects for Improved Understanding of Isotopic Reactor Antineutrino Fluxes*, *Phys. Rev. D* **97** (2018) 013003 [1709.10051].

[402] S. Gariazzo, C. Giunti, M. Laveder and Y.F. Li, *Model-independent $\bar{\nu}_e$ short-baseline oscillations from reactor spectral ratios*, *Phys. Lett. B* **782** (2018) 13 [1801.06467].

[403] C. Giunti, Y.F. Li, C.A. Ternes and Y.Y. Zhang, *Neutrino-4 anomaly: oscillations or fluctuations?*, *Phys. Lett. B* **816** (2021) 136214 [2101.06785].

[404] C. Giunti, Y.F. Li, C.A. Ternes, O. Tyagi and Z. Xin, *Gallium Anomaly: Critical View from the Global Picture of $\nu_e$ and $\bar{\nu}_e$ Disappearance*, 2209.00916.

[405] J. Kostensalo, J. Suhonen, C. Giunti and P.C. Srivastava, *The gallium anomaly revisited*, *Phys. Lett. B* **795** (2019) 542 [1906.10980].

[406] M. Maltoni and T. Schwetz, *Sterile neutrino oscillations after first MiniBooNE results*, *Phys. Rev. D* **76** (2007) 093005 [0705.0107].

[407] V. Brdar and J. Kopp, *Can standard model and experimental uncertainties resolve the MiniBooNE anomaly?*, *Phys. Rev. D* **105** (2022) 115024 [2109.08157].

[408] IceCube collaboration, *Determining neutrino oscillation parameters from atmospheric muon neutrino disappearance with three years of IceCube DeepCore data*, *Phys. Rev. D* **91** (2015) 072004 [1410.7227].

[409] M. Dentler, A. Hernández-Cabezudo, J. Kopp, P.A.N. Machado, M. Maltoni, I. Martinez-Soler et al., *Updated Global Analysis of Neutrino Oscillations in the Presence of eV-Scale Sterile Neutrinos*, *JHEP* **08** (2018) 010 [1803.10661].

[410] KARMEN collaboration, *Upper limits for neutrino oscillations muon-anti-neutrino —> electron-anti-neutrino from muon decay at rest*, *Phys. Rev. D* **65** (2002) 112001 [hep-ex/0203021].

[411] NOMAD collaboration, *Search for nu(mu) —> nu(e) oscillations in the NOMAD experiment*, *Phys. Lett. B* **570** (2003) 19 [hep-ex/0306037].

[412] M. Antonello et al., *Experimental search for the "LSND anomaly" with the ICARUS detector in the CNGS neutrino beam*, *Eur. Phys. J. C* **73** (2013) 2345 [1209.0122].

[413] L. Borodovsky et al., *Search for muon-neutrino oscillations muon-neutrino —> electron-neutrino (anti-muon-neutrino —> anti-electron-neutrino in a wide band neutrino beam*, *Phys. Rev. Lett.* **68** (1992) 274.

[414] IceCube collaboration, *eV-Scale Sterile Neutrino Search Using Eight Years of Atmospheric Muon Neutrino Data from the IceCube Neutrino Observatory*, *Phys. Rev. Lett.* **125** (2020) 141801 [2005.12942].

[415] P.A. Machado, O. Palamara and D.W. Schmitz, *The Short-Baseline Neutrino Program at Fermilab*, *Ann. Rev. Nucl. Part. Sci.* **69** (2019) 363 [1903.04608].

[416] SBND, MicroBooNe, Icarus collaboration, *The Short Baseline Neutrino Program at Fermilab*, *PoS* **NuFact2021** (2022) 009 [2203.05814].

[417] MicroBooNE collaboration, *Search for an Excess of Electron Neutrino Interactions in MicroBooNE Using Multiple Final-State Topologies*, *Phys. Rev. Lett.* **128** (2022) 241801 [2110.14054].

[418] A. Donini, M. Maltoni, D. Meloni, P. Migliozzi and F. Terranova, *3+1 sterile neutrinos at the CNGS*, *JHEP* **12** (2007) 013 [0704.0388].

[419] D. Meloni, J. Tang and W. Winter, *Sterile neutrinos beyond LSND at the Neutrino Factory*, *Phys. Rev. D* **82** (2010) 093008 [1007.2419].

[420] M.A. Acero et al., *White Paper on Light Sterile Neutrino Searches and Related Phenomenology*, 2203.07323.

[421] A. Diaz, C.A. Argüelles, G.H. Collin, J.M. Conrad and M.H. Shaevitz, *Where Are We With Light Sterile Neutrinos?*, *Phys. Rept.* **884** (2020) 1 [1906.00045].

[422] S. Böser, C. Buck, C. Giunti, J. Lesgourgues, L. Ludhova, S. Mertens et al., *Status of Light Sterile Neutrino Searches*, *Prog. Part. Nucl. Phys.* **111** (2020) 103736 [1906.01739].

[423] B. Dasgupta and J. Kopp, *Sterile Neutrinos*, *Phys. Rept.* **928** (2021) 1 [2106.05913].

[424] S. Choubey, D. Dutta and D. Pramanik, *Measuring the Sterile Neutrino CP Phase at DUNE and T2HK*, *Eur. Phys. J. C* **78** (2018) 339 [1711.07464].

[425] S.K. Agarwalla, S.S. Chatterjee and A. Palazzo, *Physics Reach of DUNE with a Light Sterile Neutrino*, *JHEP* **09** (2016) 016 [1603.03759].

[426] S.K. Agarwalla, S.S. Chatterjee, A. Dasgupta and A. Palazzo, *Discovery Potential of T2K and NOvA in the Presence of a Light Sterile Neutrino*, *JHEP* **02** (2016) 111 [1601.05995].

[427] N. Klop and A. Palazzo, *Imprints of CP violation induced by sterile neutrinos in T2K data*, *Phys. Rev. D* **91** (2015) 073017 [1412.7524].

[428] N. Fiza, M. Masud and M. Mitra, *Exploring the new physics phases in 3+1 scenario in neutrino oscillation experiments*, *JHEP* **09** (2021) 162 [2102.05063].

[429] A.D. Dolgov, *Neutrinos in cosmology*, *Phys. Rept.* **370** (2002) 333 [hep-ph/0202122].

[430] J. Lesgourgues and S. Pastor, *Massive neutrinos and cosmology*, *Phys. Rept.* **429** (2006) 307 [astro-ph/0603494].

[431] J. Lesgourgues, G. Mangano, G. Miele and S. Pastor, *Neutrino Cosmology*, Cambridge University Press (2013), 10.1017/CBO9781139012874.

[432] M. Shaposhnikov, *A Possible symmetry of the nuMSM*, *Nucl. Phys. B* **763** (2007) 49 [hep-ph/0605047].

[433] M. Lindner, A. Merle and V. Niro, *Soft $L_e - L_\mu - L_\tau$ flavour symmetry breaking and sterile neutrino keV Dark Matter*, *JCAP* **01** (2011) 034 [1011.4950].

[434] T. Asaka, S. Blanchet and M. Shaposhnikov, *The nuMSM, dark matter and neutrino masses*, *Phys. Lett. B* **631** (2005) 151 [hep-ph/0503065].

[435] R.N. Mohapatra, *Mechanism for Understanding Small Neutrino Mass in Superstring Theories*, *Phys. Rev. Lett.* **56** (1986) 561.

[436] J.W.F. Valle, *Resonant Oscillations of Massless Neutrinos in Matter*, *Phys. Lett. B* **199** (1987) 432.

[437] E. Roulet, *Mikheyev-smirnov-wolfenstein effect with flavor-changing neutrino interactions*, *Phys. Rev. D* **44** (1991) R935.

[438] S. Bergmann, Y. Grossman and E. Nardi, *Neutrino propagation in matter with general interactions*, *Phys. Rev. D* **60** (1999) 093008 [hep-ph/9903517].

[439] T. Hattori, T. Hasuike and S. Wakaizumi, *Flavor changing neutrino interactions and CP violation in neutrino oscillations*, *Prog. Theor. Phys.* **114** (2005) 439 [hep-ph/0210138].

[440] M. Garbutt and B.H.J. McKellar, *Neutrino production, oscillation and detection in the presence of general four fermion interactions*, hep-ph/0308111.

[441] M. Blennow, T. Ohlsson and W. Winter, *Non-standard Hamiltonian effects on neutrino oscillations*, *Eur. Phys. J. C* **49** (2007) 1023 [hep-ph/0508175].

[442] A. De Gouvea, G.F. Giudice, A. Strumia and K. Tobe, *Phenomenological implications of neutrinos in extra dimensions*, *Nucl. Phys. B* **623** (2002) 395 [hep-ph/0107156].

[443] J. Kopp, M. Lindner, T. Ota and J. Sato, *Non-standard neutrino interactions in reactor and superbeam experiments*, *Phys. Rev. D* **77** (2008) 013007 [0708.0152].

[444] D.V. Forero and W.-C. Huang, *Sizable NSI from the $SU(2)_L$ scalar doublet-singlet mixing and the implications in DUNE*, *JHEP* **03** (2017) 018 [1608.04719].

[445] U.K. Dey, N. Nath and S. Sadhukhan, *Non-Standard Neutrino Interactions in a Modified $\nu$2HDM*, *Phys. Rev. D* **98** (2018) 055004 [1804.05808].

[446] Y. Farzan, *A model for large non-standard interactions of neutrinos leading to the LMA-Dark solution*, *Phys. Lett. B* **748** (2015) 311 [1505.06906].

[447] K. Babu, P.B. Dev, S. Jana and A. Thapa, *Non-Standard Interactions in Radiative Neutrino Mass Models*, *JHEP* **03** (2020) 006 [1907.09498].

[448] C. Biggio, M. Blennow and E. Fernandez-Martinez, *General bounds on non-standard neutrino interactions*, *JHEP* **08** (2009) 090 [0907.0097].

[449] S.K. Agarwalla, P. Bagchi, D.V. Forero and M. Tórtola, *Probing Non-Standard Interactions at Daya Bay*, *JHEP* **07** (2015) 060 [1412.1064].

[450] R. Adhikari, S. Chakraborty, A. Dasgupta and S. Roy, *Non-standard interaction in neutrino oscillations and recent Daya Bay, T2K experiments*, *Phys. Rev. D* **86** (2012) 073010 [1201.3047].

[451] O.G. Miranda and H. Nunokawa, *Non standard neutrino interactions: current status and future prospects*, *New J. Phys.* **17** (2015) 095002 [1505.06254].

[452] M. Blennow, S. Choubey, T. Ohlsson and S.K. Raut, *Exploring Source and Detector Non-Standard Neutrino Interactions at ESSνSB*, *JHEP* **09** (2015) 096 [1507.02868].

[453] A. Bolanos, O.G. Miranda, A. Palazzo, M.A. Tortola and J.W.F. Valle, *Probing non-standard neutrino-electron interactions with solar and reactor neutrinos*, *Phys. Rev. D* **79** (2009) 113012 [0812.4417].

[454] S.K. Agarwalla, F. Lombardi and T. Takeuchi, *Constraining Non-Standard Interactions of the Neutrino with Borexino*, *JHEP* **12** (2012) 079 [1207.3492].

[455] T. Ohlsson, *Status of non-standard neutrino interactions*, *Rept. Prog. Phys.* **76** (2013) 044201 [1209.2710].

[456] C. Giunti, *General COHERENT constraints on neutrino nonstandard interactions*, *Phys. Rev. D* **101** (2020) 035039 [1909.00466].

[457] A.N. Khan, *Global analysis of the source and detector nonstandard interactions using the short baseline ν-e and ν ¯-e scattering data*, *Phys. Rev. D* **93** (2016) 093019 [1605.09284].

[458] P. Coloma, I. Esteban, M. Gonzalez-Garcia and M. Maltoni, *Improved global fit to Non-Standard neutrino Interactions using COHERENT energy and timing data*, *JHEP* **02** (2020) 023 [1911.09109].

[459] B. Dutta, R.F. Lang, S. Liao, S. Sinha, L. Strigari and A. Thompson, *A global analysis strategy to resolve neutrino NSI degeneracies with scattering and oscillation data*, *JHEP* **20** (2020) 106 [2002.03066].

[460] J.A.B. Coelho, T. Kafka, W.A. Mann, J. Schneps and O. Altinok, *Constraints for non-standard interaction $\epsilon_{e\tau}V_e$ from $\nu_e$ appearance in MINOS and T2K*, *Phys. Rev. D* **86** (2012) 113015 [1209.3757].

[461] K. Huitu, T.J. Kärkkäinen, J. Maalampi and S. Vihonen, *Constraining the nonstandard interaction parameters in long baseline neutrino experiments*, *Phys. Rev. D* **93** (2016) 053016 [1601.07730].

[462] M. Masud and P. Mehta, *Nonstandard interactions and resolving the ordering of neutrino masses at DUNE and other long baseline experiments*, *Phys. Rev. D* **94** (2016) 053007 [1606.05662].

[463] S. Fukasawa and O. Yasuda, *The possibility to observe the non-standard interaction by the Hyperkamiokande atmospheric neutrino experiment*, *Nucl. Phys. B* **914** (2017) 99 [1608.05897].

[464] T. Han, J. Liao, H. Liu and D. Marfatia, *Nonstandard neutrino interactions at COHERENT, DUNE, T2HK and LHC*, *JHEP* **11** (2019) 028 [1910.03272].

[465] S. Verma and S. Bhardwaj, *Nonstandard Interactions and Prospects for Studying Standard Parameter Degeneracies in DUNE and T2HKK*, *Adv. High Energy Phys.* **2019** (2019) 8464535 [1808.04263].

[466] M.C. Gonzalez-Garcia, Y. Grossman, A. Gusso and Y. Nir, *New CP violation in neutrino oscillations*, *Phys. Rev. D* **64** (2001) 096006 [hep-ph/0105159].

[467] A. de Gouvea, A. Friedland and H. Murayama, *The Dark side of the solar neutrino parameter space*, *Phys. Lett. B* **490** (2000) 125 [hep-ph/0002064].

[468] P. Bakhti and Y. Farzan, *Shedding light on LMA-Dark solar neutrino solution by medium baseline reactor experiments: JUNO and RENO-50*, *JHEP* **07** (2014) 064 [1403.0744].

[469] P. Coloma and T. Schwetz, *Generalized mass ordering degeneracy in neutrino oscillation experiments*, *Phys. Rev. D* **94** (2016) 055005 [1604.05772].

[470] P. Coloma, P.B. Denton, M. Gonzalez-Garcia, M. Maltoni and T. Schwetz, *Curtailing the Dark Side in Non-Standard Neutrino Interactions*, *JHEP* **04** (2017) 116 [1701.04828].

[471] P. Coloma, M. Gonzalez-Garcia, M. Maltoni and T. Schwetz, *COHERENT Enlightenment of the Neutrino Dark Side*, *Phys. Rev. D* **96** (2017) 115007 [1708.02899].

[472] J. Liao and D. Marfatia, *COHERENT constraints on nonstandard neutrino interactions*, *Phys. Lett. B* **775** (2017) 54 [1708.04255].

[473] P.B. Denton, Y. Farzan and I.M. Shoemaker, *Testing large non-standard neutrino interactions with arbitrary mediator mass after COHERENT data*, *JHEP* **07** (2018) 037 [1804.03660].

[474] S.K. Agarwalla, S.S. Chatterjee and A. Palazzo, *Degeneracy between $\theta_{23}$ octant and neutrino non-standard interactions at DUNE*, *Phys. Lett. B* **762** (2016) 64 [1607.01745].

[475] I. Esteban, M.C. Gonzalez-Garcia and M. Maltoni, *On the Determination of Leptonic CP Violation and Neutrino Mass Ordering in Presence of Non-Standard Interactions: Present Status*, *JHEP* **06** (2019) 055 [1905.05203].

[476] M. Maltoni, *Global fit to non-standard neutrino interactions*, .

[477] I. Esteban, M.C. Gonzalez-Garcia, M. Maltoni, I. Martinez-Soler and J. Salvado, *Updated constraints on non-standard interactions from global analysis of oscillation data*, *JHEP* **08** (2018) 180 [1805.04530].

[478] W. Chao and H. Zhang, *One-loop renormalization group equations of the neutrino mass matrix in the triplet seesaw model*, *Phys. Rev. D* **75** (2007) 033003 [hep-ph/0611323].

[479] A. Abada, C. Biggio, F. Bonnet, M.B. Gavela and T. Hambye, *Low energy effects of neutrino masses*, *JHEP* **12** (2007) 061 [0707.4058].

[480] M.B. Gavela, D. Hernandez, T. Ota and W. Winter, *Large gauge invariant non-standard neutrino interactions*, *Phys. Rev. D* **79** (2009) 013007 [0809.3451].

[481] M. Malinsky, T. Ohlsson and H. Zhang, *Non-Standard Neutrino Interactions from a Triplet Seesaw Model*, *Phys. Rev. D* **79** (2009) 011301 [0811.3346].

[482] P.Q. Hung, *Sterile neutrino and accelerating universe*, hep-ph/0010126.

[483] R. Fardon, A.E. Nelson and N. Weiner, *Dark energy from mass varying neutrinos*, *JCAP* **10** (2004) 005 [astro-ph/0309800].

[484] D.B. Kaplan, A.E. Nelson and N. Weiner, *Neutrino oscillations as a probe of dark energy*, *Phys. Rev. Lett.* **93** (2004) 091801 [hep-ph/0401099].

[485] G.-Y. Huang and N. Nath, *Neutrinophilic Axion-Like Dark Matter*, *Eur. Phys. J. C* **78** (2018) 922 [1809.01111].

[486] G.J. Stephenson, Jr., J.T. Goldman and B.H.J. McKellar, *MSW - like enhancements without matter*, *Mod. Phys. Lett. A* **12** (1997) 2391 [hep-ph/9610317].

[487] J.F. Nieves and P.B. Pal, *Generalized Fierz identities*, *Am. J. Phys.* **72** (2004) 1100 [hep-ph/0306087].

[488] C.C. Nishi, *Simple derivation of general Fierz-like identities*, *Am. J. Phys.* **73** (2005) 1160 [hep-ph/0412245].

[489] B. Batell, N. Lange, D. McKeen, M. Pospelov and A. Ritz, *Muon anomalous magnetic moment through the leptonic Higgs portal*, *Phys. Rev. D* **95** (2017) 075003 [1606.04943].

[490] C. Gross, O. Lebedev and T. Toma, *Cancellation Mechanism for Dark-Matter–Nucleon Interaction*, *Phys. Rev. Lett.* **119** (2017) 191801 [1708.02253].

[491] Y. Farzan, M. Lindner, W. Rodejohann and X.-J. Xu, *Probing neutrino coupling to a light scalar with coherent neutrino scattering*, *JHEP* **05** (2018) 066 [1802.05171].

[492] G.-y. Huang, T. Ohlsson and S. Zhou, *Observational Constraints on Secret Neutrino Interactions from Big Bang Nucleosynthesis*, *Phys. Rev. D* **97** (2018) 075009 [1712.04792].

[493] B. Sevda, M. Deniz, S. Kerman, L. Singh, H.T. Wong and M. Zeyrek, *Constraints on Scalar-Pseudoscalar and Tensorial Non-Standard Interaction and Tensorial Unparticle Couplings from Neutrino-Electron Scattering*, *Phys. Rev. D* **95** (2017) 033008 [1611.07259].

[494] P.S. Pasquini and O.L.G. Peres, *Bounds on Neutrino-Scalar Yukawa Coupling*, *Phys. Rev. D* **93** (2016) 053007 [1511.01811].

[495] L. Heurtier and Y. Zhang, *Supernova Constraints on Massive (Pseudo)Scalar Coupling to Neutrinos*, *JCAP* **02** (2017) 042 [1609.05882].

[496] J. Liao, D. Marfatia and K. Whisnant, *Generalized perturbations in neutrino mixing*, *Phys. Rev. D* **92** (2015) 073004 [1506.03013].

[497] SNO collaboration, *Constraints on Neutrino Lifetime from the Sudbury Neutrino Observatory*, *Phys. Rev. D* **99** (2019) 032013 [1812.01088].

[498] Borexino collaboration, *First Simultaneous Precision Spectroscopy of pp, $^7$Be, and pep Solar Neutrinos with Borexino Phase-II*, *Phys. Rev. D* **100** (2019) 082004 [1707.09279].

[499] A. Medhi, D. Dutta and M.M. Devi, *Exploring the effects of scalar non standard interactions on the CP violation sensitivity at DUNE*, *JHEP* **06** (2022) 129 [2111.12943].

[500] Y. Chikashige, R.N. Mohapatra and R.D. Peccei, *Are There Real Goldstone Bosons Associated with Broken Lepton Number?*, *Phys. Lett. B* **98** (1981) 265.

[501] H. Kikuchi and E. Ma, *Neutrino decay in the doublet Majoron model*, *Phys. Lett. B* **335** (1994) 444 [hep-ph/9405405].

[502] S. Bertolini and A. Santamaria, *The doublet majoron model and solar neutrino oscillations*, *Nuclear Physics B* **310** (1988) 714.

[503] A. Santamaria and J. Valle, *Spontaneous r parity violation in supersymmetry: A model for solar neutrino oscillations*, *Physics Letters B* **195** (1987) 423.

[504] A.G. Dias, A. Doff, C.A. de S. Pires and P.S. Rodrigues da Silva, *Neutrino decay and neutrinoless double beta decay in a 3-3-1 model*, *Phys. Rev. D* **72** (2005) 035006 [hep-ph/0503014].

[505] Z.G. Berezhiani, G. Fiorentini, M. Moretti and A. Rossi, *Fast neutrino decay and solar neutrino detectors*, *Z. Phys. C* **54** (1992) 581.

[506] A. Acker, A. Joshipura and S. Pakvasa, *A Neutrino decay model, solar anti-neutrinos and atmospheric neutrinos*, *Phys. Lett. B* **285** (1992) 371.

[507] Z.G. Berezhiani, G. Fiorentini, A. Rossi and M. Moretti, *Neutrino decay solution of the solar neutrino problem revisited*, *JETP Lett.* **55** (1992) 151.

[508] S. Choubey, S. Goswami and D. Majumdar, *Status of the neutrino decay solution to the solar neutrino problem*, *Phys. Lett. B* **484** (2000) 73 [hep-ph/0004193].

[509] J.F. Beacom and N.F. Bell, *Do Solar Neutrinos Decay?*, *Phys. Rev. D* **65** (2002) 113009 [hep-ph/0204111].

[510] A. Bandyopadhyay, S. Choubey and S. Goswami, *Neutrino decay confronts the SNO data*, *Phys. Lett. B* **555** (2003) 33 [hep-ph/0204173].

[511] J.M. Berryman, A. de Gouvea and D. Hernandez, *Solar Neutrinos and the Decaying Neutrino Hypothesis*, *Phys. Rev. D* **92** (2015) 073003 [1411.0308].

[512] R. Picoreti, M.M. Guzzo, P.C. de Holanda and O.L.G. Peres, *Neutrino Decay and Solar Neutrino Seasonal Effect*, *Phys. Lett. B* **761** (2016) 70 [1506.08158].

[513] Kamiokande-II collaboration, *Observation of a Neutrino Burst from the Supernova SN 1987a*, *Phys. Rev. Lett.* **58** (1987) 1490.

[514] R.M. Bionta, G. Blewitt, C.B. Bratton, D. Casper, A. Ciocio, R. Claus et al., *Observation of a neutrino burst in coincidence with supernova 1987a in the large magellanic cloud*, *Phys. Rev. Lett.* **58** (1987) 1494.

[515] J.A. Frieman, H.E. Haber and K. Freese, *Neutrino Mixing, Decays and Supernova Sn1987a*, *Phys. Lett. B* **200** (1988) 115.

[516] M. Bustamante, J.F. Beacom and K. Murase, *Testing decay of astrophysical neutrinos with incomplete information*, *Phys. Rev. D* **95** (2017) 063013 [1610.02096].

[517] M.C. Gonzalez-Garcia and M. Maltoni, *Status of Oscillation plus Decay of Atmospheric and Long-Baseline Neutrinos*, *Phys. Lett. B* **663** (2008) 405 [0802.3699].

[518] M. Maltoni and W. Winter, *Testing neutrino oscillations plus decay with neutrino telescopes*, *JHEP* **07** (2008) 064 [0803.2050].

[519] P. Baerwald, M. Bustamante and W. Winter, *Neutrino Decays over Cosmological Distances and the Implications for Neutrino Telescopes*, *JCAP* **10** (2012) 020 [1208.4600].

[520] L. Dorame, O.G. Miranda and J.W.F. Valle, *Invisible decays of ultra-high energy neutrinos*, *Front. in Phys.* **1** (2013) 25 [1303.4891].

[521] G. Pagliaroli, A. Palladino, F.L. Villante and F. Vissani, *Testing nonradiative neutrino decay scenarios with IceCube data*, *Phys. Rev. D* **92** (2015) 113008 [1506.02624].

[522] P.B. Denton and I. Tamborra, *Invisible Neutrino Decay Could Resolve IceCube's Track and Cascade Tension*, *Phys. Rev. Lett.* **121** (2018) 121802 [1805.05950].

[523] A. Abdullahi and P.B. Denton, *Visible Decay of Astrophysical Neutrinos at IceCube*, *Phys. Rev. D* **102** (2020) 023018 [2005.07200].

[524] R.A. Gomes, A.L.G. Gomes and O.L.G. Peres, *Constraints on neutrino decay lifetime using long-baseline charged and neutral current data*, *Phys. Lett. B* **740** (2015) 345 [1407.5640].

[525] N.F. Bell, E. Pierpaoli and K. Sigurdson, *Cosmological signatures of interacting neutrinos*, *Phys. Rev. D* **73** (2006) 063523 [astro-ph/0511410].

[526] M. Cirelli and A. Strumia, *Cosmology of neutrinos and extra light particles after WMAP3*, *JCAP* **12** (2006) 013 [astro-ph/0607086].

[527] A. Friedland, K.M. Zurek and S. Bashinsky, *Constraining Models of Neutrino Mass and Neutrino Interactions with the Planck Satellite*, 0704.3271.

[528] A. Basboll, O.E. Bjaelde, S. Hannestad and G.G. Raffelt, *Are cosmological neutrinos free-streaming?*, *Phys. Rev. D* **79** (2009) 043512 [0806.1735].

[529] M. Archidiacono and S. Hannestad, *Updated constraints on non-standard neutrino interactions from Planck*, *JCAP* **07** (2014) 046 [1311.3873].

[530] Y. Farzan and S. Hannestad, *Neutrinos secretly converting to lighter particles to please both KATRIN and the cosmos*, *JCAP* **02** (2016) 058 [1510.02201].

[531] F. Forastieri, M. Lattanzi and P. Natoli, *Constraints on secret neutrino interactions after Planck*, *JCAP* **07** (2015) 014 [1504.04999].

[532] J. Lesgourgues, G. Marques-Tavares and M. Schmaltz, *Evidence for dark matter interactions in cosmological precision data?*, *JCAP* **02** (2016) 037 [1507.04351].

[533] C. Brust, Y. Cui and K. Sigurdson, *Cosmological Constraints on Interacting Light Particles*, *JCAP* **08** (2017) 020 [1703.10732].

[534] G. Franco Abellán, Z. Chacko, A. Dev, P. Du, V. Poulin and Y. Tsai, *Improved cosmological constraints on the neutrino mass and lifetime*, *JHEP* **08** (2022) 076 [2112.13862].

[535] S. Palomares-Ruiz, S. Pascoli and T. Schwetz, *Explaining LSND by a decaying sterile neutrino*, *JHEP* **09** (2005) 048 [hep-ph/0505216].

[536] H. Hettmansperger, M. Lindner and W. Rodejohann, *Phenomenological Consequences of sub-leading Terms in See-Saw Formulas*, *JHEP* **04** (2011) 123 [1102.3432].

[537] S. Antusch, C. Biggio, E. Fernandez-Martinez, M.B. Gavela and J. Lopez-Pavon, *Unitarity of the Leptonic Mixing Matrix*, *JHEP* **10** (2006) 084 [hep-ph/0607020].

[538] Z.-z. Xing, *Towards testing the unitarity of the 3X3 lepton flavor mixing matrix in a precision reactor antineutrino oscillation experiment*, *Phys. Lett. B* **718** (2013) 1447 [1210.1523].

[539] E. Nardi, E. Roulet and D. Tommasini, *Limits on neutrino mixing with new heavy particles*, *Phys. Lett. B* **327** (1994) 319 [hep-ph/9402224].

[540] M. Gronau, C.N. Leung and J.L. Rosner, *Extending Limits on Neutral Heavy Leptons*, *Phys. Rev. D* **29** (1984) 2539.

[541] P. Langacker and D. London, *Mixing Between Ordinary and Exotic Fermions*, *Phys. Rev. D* **38** (1988) 886.

[542] M.C. Gonzalez-Garcia, A. Santamaria and J.W.F. Valle, *Isosinglet Neutral Heavy Lepton Production in Z Decays and Neutrino Mass*, *Nucl. Phys. B* **342** (1990) 108.

[543] A. Abada, A.M. Teixeira, A. Vicente and C. Weiland, *Sterile neutrinos in leptonic and semileptonic decays*, *JHEP* **02** (2014) 091 [1311.2830].

[544] A. Abada, V. De Romeri and A.M. Teixeira, *Effect of steriles states on lepton magnetic moments and neutrinoless double beta decay*, *JHEP* **09** (2014) 074 [1406.6978].

[545] A. Abada, D. Das, A.M. Teixeira, A. Vicente and C. Weiland, *Tree-level lepton universality violation in the presence of sterile neutrinos: impact for $R_K$ and $R_\pi$*, *JHEP* **02** (2013) 048 [1211.3052].

[546] S. Antusch and O. Fischer, *Non-unitarity of the leptonic mixing matrix: Present bounds and future sensitivities*, *JHEP* **10** (2014) 094 [1407.6607].

[547] G. Czapek et al., *Branching ratio for the rare pion decay into positron and neutrino*, *Phys. Rev. Lett.* **70** (1993) 17.

[548] BaBar collaboration, *Measurements of Charged Current Lepton Universality and $|V_{us}|$ using Tau Lepton Decays to $e^-\bar{\nu}_e\nu_\tau$, $\mu^-\bar{\nu}_\mu\nu_\tau$, $\pi^-\nu_\tau$, and $K^-\nu_\tau$*, *Phys. Rev. Lett.* **105** (2010) 051602 [0912.0242].

[549] F.F. Deppisch, M. Hirsch and H. Pas, *Neutrinoless Double Beta Decay and Physics Beyond the Standard Model*, *J. Phys. G* **39** (2012) 124007 [1208.0727].

[550] C. Giunti, M. Laveder, Y.F. Li and H.W. Long, *Pragmatic View of Short-Baseline Neutrino Oscillations*, *Phys. Rev. D* **88** (2013) 073008 [1308.5288].

[551] D.V. Forero, C. Giunti, C.A. Ternes and M. Tortola, *Nonunitary neutrino mixing in short and long-baseline experiments*, *Phys. Rev. D* **104** (2021) 075030 [2103.01998].

[552] MINOS+ collaboration, *Search for sterile neutrinos in MINOS and MINOS+ using a two-detector fit*, *Phys. Rev. Lett.* **122** (2019) 091803 [1710.06488].

[553] S.R. Juárez Wysozka, P. Kielanowski and L.V. Mercado, *Quark unitarity triangles*, 2205.12455.

[554] C. Jarlskog and R. Stora, *Unitarity Polygons and CP Violation Areas and Phases in the Standard Electroweak Model*, *Phys. Lett. B* **208** (1988) 268.

[555] S.A.R. Ellis, K.J. Kelly and S.W. Li, *Current and Future Neutrino Oscillation Constraints on Leptonic Unitarity*, *JHEP* **12** (2020) 068 [2008.01088].

[556] S.A.R. Ellis, K.J. Kelly and S.W. Li, *Leptonic Unitarity Triangles*, *Phys. Rev. D* **102** (2020) 115027 [2004.13719].

[557] JUNO collaboration, *Talk given at EPS-HEP 2021*, .

[558] D.V. Forero, S.J. Parke, C.A. Ternes and R.Z. Funchal, *JUNO's prospects for determining the neutrino mass ordering*, *Phys. Rev. D* **104** (2021) 113004 [2107.12410].

[559] JUNO collaboration, *JUNO Oscillation Physics*, *J. Phys. Conf. Ser.* **2156** (2021) 012110 [2111.10112].

[560] DUNE collaboration, *Deep Underground Neutrino Experiment (DUNE), Far Detector Technical Design Report, Volume I Introduction to DUNE*, *JINST* **15** (2020) T08008 [2002.02967].

[561] DUNE collaboration, *Deep Underground Neutrino Experiment (DUNE), Far Detector Technical Design Report, Volume II: DUNE Physics*, 2002.03005.

[562] DUNE collaboration, *Experiment Simulation Configurations Used in DUNE CDR*, 1606.09550.

[563] A. Ereditato and A. Rubbia, *The Liquid argon TPC: A Powerful detector for future neutrino experiments and proton decay searches*, *Nucl. Phys. B Proc. Suppl.* **154** (2006) 163 [hep-ph/0509022].

[564] DUNE collaboration, *Design, construction and operation of the ProtoDUNE-SP Liquid Argon TPC*, *JINST* **17** (2022) P01005 [2108.01902].

[565] P.-J. Chiu, *ProtoDUNE-DP PROTOtype for the Deep Underground Neutrino Experiment - Dual Phase detector: Electrostatic Simulations and Performance Studies*, Master's thesis, Zurich, ETH, 2017, 10.3929/ethz-b-000185858.

[566] DUNE collaboration, *Deep Underground Neutrino Experiment (DUNE), Far Detector Technical Design Report, Volume IV: Far Detector Single-phase Technology*, *JINST* **15** (2020) T08010 [2002.03010].

[567] F. Pietropaolo, *Vertical Drift LAr-TPC for the DUNE Experiment. Vertical Drift LAr-TPC for the DUNE Experiment*, .

[568] DUNE collaboration, *The DUNE vertical drift photon detection system*, *JINST* **17** (2022) C01067 [2112.09520].

[569] O. Lantwin, *The DUNE vertical drift TPC*, *PoS* **ICHEP2022** (2022) 332 [2211.11339].

[570] DUNE collaboration, *A LArTPC with Vertical Drift for the DUNE Far Detector*, *PoS* **NuFact2021** (2022) 173.

[571] LBNE collaboration, *The Long-Baseline Neutrino Experiment: Exploring Fundamental Symmetries of the Universe*, in *Snowmass 2013: Workshop on Energy Frontier*, 7, 2013 [1307.7335].

[572] LAGUNA-LBNO collaboration, *Optimised sensitivity to leptonic CP violation from spectral information: the LBNO case at 2300 km baseline*, 1412.0593.

[573] OPERA collaboration, *Final Results of the OPERA Experiment on $\nu_\tau$ Appearance in the CNGS Neutrino Beam*, *Phys. Rev. Lett.* **120** (2018) 211801 [1804.04912].

[574] DUNE collaboration, *Experiment Simulation Configurations Approximating DUNE TDR*, 2103.04797.

[575] S.S. Wilks, *The Large-Sample Distribution of the Likelihood Ratio for Testing Composite Hypotheses*, *Annals Math. Statist.* **9** (1938) 60.

[576] S. Algeri, J. Aalbers, K. Dundas Morå and J. Conrad, *Searching for new phenomena with profile likelihood ratio tests*, *Nature Rev. Phys.* **2** (2020) 245 [1911.10237].

[577] IceCube collaboration, *Measurement of Astrophysical Tau Neutrinos in IceCube's High-Energy Starting Events*, 2011.03561.

[578] I. Esteban, M.C. Gonzalez-Garcia, A. Hernandez-Cabezudo, M. Maltoni and T. Schwetz, *Global analysis of three-flavour neutrino oscillations: synergies and tensions in the determination of $\theta_{23}$, $\delta_{CP}$, and the mass ordering*, *JHEP* **01** (2019) 106 [1811.05487].

[579] A. De Gouvêa, K.J. Kelly, G.V. Stenico and P. Pasquini, *Physics with Beam Tau-Neutrino Appearance at DUNE*, *Phys. Rev. D* **100** (2019) 016004 [1904.07265].

[580] ICARUS collaboration, *A second-generation proton decay experiment and neutrino observatory at the gran sasso laboratory*, *CERN-SPSC-2002-027, CERN-SPSC-P-323* .

[581] V.D. Barger, A.M. Gago, D. Marfatia, W.J.C. Teves, B.P. Wood and R. Zukanovich Funchal, *Neutrino oscillation parameters from MINOS, ICARUS and OPERA combined*, *Phys. Rev. D* **65** (2002) 053016 [hep-ph/0110393].

[582] P. Machado, H. Schulz and J. Turner, *Tau neutrinos at DUNE: New strategies, new opportunities*, *Phys. Rev. D* **102** (2020) 053010 [2007.00015].

[583] P.B. Denton and J. Gehrlein, *New tau neutrino oscillation and scattering constraints on unitarity violation*, 2109.14575.

[584] I. Martinez-Soler and H. Minakata, *Measuring tau neutrino appearance probability via unitarity*, 2109.06933.

[585] M. Masud, P. Mehta, C.A. Ternes and M. Tortola, *Non-standard neutrino oscillations: perspective from unitarity triangles*, *JHEP* **05** (2021) 171 [2103.11143].

[586] R.M. Abraham et al., *Tau Neutrinos in the Next Decade: from GeV to EeV*, 2203.05591.

[587] T2K collaboration, *Observation of Electron Neutrino Appearance in a Muon Neutrino Beam*, *Phys. Rev. Lett.* **112** (2014) 061802 [1311.4750].

[588] Super-Kamiokande collaboration, *First Study of Neutron Tagging with a Water Cherenkov Detector*, *Astropart. Phys.* **31** (2009) 320 [0811.0735].

[589] J.R. Alonso et al., *Advanced Scintillator Detector Concept (ASDC): A Concept Paper on the Physics Potential of Water-Based Liquid Scintillator*, 1409.5864.

[590] ArgoNeuT collaboration, *Detection of Back-to-Back Proton Pairs in Charged-Current Neutrino Interactions with the ArgoNeuT Detector in the NuMI Low Energy Beam Line*, *Phys. Rev. D* **90** (2014) 012008 [1405.4261].

[591] U. Mosel, O. Lalakulich and K. Gallmeister, *Energy reconstruction in the Long-Baseline Neutrino Experiment*, *Phys. Rev. Lett.* **112** (2014) 151802 [1311.7288].

[592] Hyper-Kamiokande Working Group collaboration, *A Long Baseline Neutrino Oscillation Experiment Using J-PARC Neutrino Beam and Hyper-Kamiokande*, 12, 2014 [1412.4673].

[593] A. Ferrero, *The nd280 near detector of the t2k experiment*, *AIP Conference Proceedings* **1189** (2009) 77 [https://aip.scitation.org/doi/pdf/10.1063/1.3274192].

[594] T2K Collaboration collaboration, *Combined analysis of neutrino and antineutrino oscillations at t2k*, *Phys. Rev. Lett.* **118** (2017) 151801.

[595] T2K collaboration, *Updated T2K measurements of muon neutrino and antineutrino disappearance using $1.5\times10^{21}$ protons on target*, *Phys. Rev. D* **96** (2017) 011102 [1704.06409].

[596] M. Day and K.S. McFarland, *Differences in Quasi-Elastic Cross-Sections of Muon and Electron Neutrinos*, *Phys. Rev. D* **86** (2012) 053003 [1206.6745].

[597] L.-I. Munteanu, *Long-baseline neutrino oscillation sensitivities with Hyper-Kamiokande*, *PoS* **NuFact2021** (2022) 056.

[598] M. Tanimoto, *Indirect search for CP violation in neutrino oscillations*, *Phys. Lett. B* **435** (1998) 373 [hep-ph/9806375].

[599] V.D. Barger, K. Whisnant, S. Pakvasa and R.J.N. Phillips, *Matter Effects on Three-Neutrino Oscillations*, *Phys. Rev. D* **22** (1980) 2718.

[600] J. Arafune, M. Koike and J. Sato, *CP violation and matter effect in long baseline neutrino oscillation experiments*, *Phys. Rev. D* **56** (1997) 3093 [hep-ph/9703351].

[601] J. Rout, S. Shafaq, M. Bishai and P. Mehta, *Physics prospects with the second oscillation maximum at the Deep Underground Neutrino Experiment*, *Phys. Rev. D* **103** (2021) 116003 [2012.08269].

[602] J. Tang, S. Vihonen and T.-C. Wang, *Precision measurements on $\delta_{CP}$ in MOMENT*, *JHEP* **12** (2019) 130 [1909.01548].

[603] P. Huber, M. Lindner and W. Winter, *Simulation of long-baseline neutrino oscillation experiments with GLoBES (General Long Baseline Experiment Simulator)*, *Comput. Phys. Commun.* **167** (2005) 195 [hep-ph/0407333].

[604] P. Huber, J. Kopp, M. Lindner, M. Rolinec and W. Winter, *New features in the simulation of neutrino oscillation experiments with GLoBES 3.0: General Long Baseline Experiment Simulator*, *Comput. Phys. Commun.* **177** (2007) 432 [hep-ph/0701187].

[605] T. Ohlsson and H. Snellman, *Neutrino oscillations with three flavors in matter: Applications to neutrinos traversing the Earth*, *Phys. Lett. B* **474** (2000) 153 [hep-ph/9912295].

[606] P. Huber, M. Lindner and W. Winter, *Superbeams versus neutrino factories*, *Nucl. Phys. B* **645** (2002) 3 [hep-ph/0204352].

[607] G.L. Fogli, E. Lisi, A. Marrone, D. Montanino and A. Palazzo, *Getting the most from the statistical analysis of solar neutrino oscillations*, *Phys. Rev. D* **66** (2002) 053010 [hep-ph/0206162].

[608] A.M. Ankowski and C. Mariani, *Systematic uncertainties in long-baseline neutrino-oscillation experiments*, *J. Phys. G* **44** (2017) 054001 [1609.00258].

[609] H. Minakata, M. Sonoyama and H. Sugiyama, *Determination of $\theta_{23}$ in long-baseline neutrino oscillation experiments with three-flavor mixing effects*, *Phys. Rev. D* **70** (2004) 113012 [hep-ph/0406073].

[610] K. Hiraide, H. Minakata, T. Nakaya, H. Nunokawa, H. Sugiyama, W.J.C. Teves et al., *Resolving $\theta_{23}$ degeneracy by accelerator and reactor neutrino oscillation experiments*, *Phys. Rev. D* **73** (2006) 093008 [hep-ph/0601258].

[611] C.R. Das, J.a. Pulido, J. Maalampi and S. Vihonen, *Determination of the $\theta_{23}$ octant in long baseline neutrino experiments within and beyond the standard model*, *Phys. Rev. D* **97** (2018) 035023 [1708.05182].

[612] J. Bernabéu and A. Segarra, *Do T asymmetries for neutrino oscillations in uniform matter have a CP-even component?*, *JHEP* **03** (2019) 103 [1901.02761].

[613] J. Bernabéu and A. Segarra, *Signatures of the genuine and matter-induced components of the CP violation asymmetry in neutrino oscillations*, *JHEP* **11** (2018) 063 [1807.11879].

[614] T. Ohlsson and S. Zhou, *Extrinsic and Intrinsic CPT Asymmetries in Neutrino Oscillations*, *Nucl. Phys. B* **893** (2015) 482 [1408.4722].

[615] H. Nunokawa, S.J. Parke and J.W.F. Valle, *CP Violation and Neutrino Oscillations*, *Prog. Part. Nucl. Phys.* **60** (2008) 338 [0710.0554].

[616] S.J. Parke, *CP Violation in the Neutrino Sector*, in *6th Conference on Flavor Physics and CP Violation*, 7, 2008 [0807.3311].

[617] T2K collaboration, *Constraint on the matter–antimatter symmetry-violating phase in neutrino oscillations*, *Nature* **580** (2020) 339 [1910.03887].

[618] S.F. King, *Parametrizing the lepton mixing matrix in terms of deviations from tri-bimaximal mixing*, *Phys. Lett. B* **659** (2008) 244 [0710.0530].

[619] S. Pakvasa, W. Rodejohann and T.J. Weiler, *Unitary parametrization of perturbations to tribimaximal neutrino mixing*, *Phys. Rev. Lett.* **100** (2008) 111801 [0711.0052].

[620] "NuFit 5.0 (2020),http://www.nu-fit.org/ ."

[621] M. Blennow, P. Coloma, P. Huber and T. Schwetz, *Quantifying the sensitivity of oscillation experiments to the neutrino mass ordering*, *JHEP* **03** (2014) 028 [1311.1822].

[622] MINERvA collaboration, *Neutrino Flux Predictions for the NuMI Beam*, *Phys. Rev. D* **94** (2016) 092005 [1607.00704].

[623] O.G. Miranda, P. Pasquini, M. Tórtola and J.W.F. Valle, *Exploring the Potential of Short-Baseline Physics at Fermilab*, *Phys. Rev. D* **97** (2018) 095026 [1802.02133].

[624] P. Coloma, J. López-Pavón, S. Rosauro-Alcaraz and S. Urrea, *New physics from oscillations at the DUNE near detector, and the role of systematic uncertainties*, 2105.11466.

[625] J-PARC E61 collaboration, *An intermediate water Cherenkov detector for the Hyper-Kamiokande experiment: overview and status*, *PoS* **ICRC2017** (2018) 1021.

[626] J.R. Wilson, *The Hyper-K Near Detector Programme*, *J. Phys. Conf. Ser.* **1342** (2020) 012053.

[627] P. Ballett, S.F. King, S. Pascoli, N.W. Prouse and T. Wang, *Sensitivities and synergies of DUNE and T2HK*, *Phys. Rev. D* **96** (2017) 033003 [1612.07275].

[628] M. Ghosh and T. Ohlsson, *A comparative study between ESSnuSB and T2HK in determining the leptonic CP phase*, *Mod. Phys. Lett. A* **35** (2020) 2050058 [1906.05779].

[629] S.K. Agarwalla, *Complementarity among next generation long baseline experiments*, .

[630] S. Choubey, D. Dutta and D. Pramanik, *Invisible neutrino decay in the light of NOvA and T2K data*, *JHEP* **08** (2018) 141 [1805.01848].

[631] S. Choubey, S. Goswami and D. Pramanik, *A study of invisible neutrino decay at DUNE and its effects on $\theta_{23}$ measurement*, *JHEP* **02** (2018) 055 [1705.05820].

[632] J. Tang, T.-C. Wang and Y. Zhang, *Invisible neutrino decays at the MOMENT experiment*, *JHEP* **04** (2019) 004 [1811.05623].

[633] P.F. de Salas, S. Pastor, C.A. Ternes, T. Thakore and M. Tórtola, *Constraining the invisible neutrino decay with KM3NeT-ORCA*, *Phys. Lett. B* **789** (2019) 472 [1810.10916].

[634] S. Choubey, S. Goswami, C. Gupta, S.M. Lakshmi and T. Thakore, *Sensitivity to neutrino decay with atmospheric neutrinos at the INO-ICAL detector*, *Phys. Rev. D* **97** (2018) 033005 [1709.10376].

[635] T. Abrahão, H. Minakata, H. Nunokawa and A.A. Quiroga, *Constraint on Neutrino Decay with Medium-Baseline Reactor Neutrino Oscillation Experiments*, *JHEP* **11** (2015) 001 [1506.02314].

[636] J.M. Berryman, A. de Gouvêa, D. Hernández and R.L.N. Oliveira, *Non-Unitary Neutrino Propagation From Neutrino Decay*, *Phys. Lett. B* **742** (2015) 74 [1407.6631].

[637] P. Coloma, D.V. Forero and S.J. Parke, *DUNE Sensitivities to the Mixing between Sterile and Tau Neutrinos*, *JHEP* **07** (2018) 079 [1707.05348].

[638] A. de Gouvêa and K.J. Kelly, *Non-standard Neutrino Interactions at DUNE*, *Nucl. Phys. B* **908** (2016) 318 [1511.05562].

[639] D. Meloni, *On the systematic uncertainties in DUNE and their role in New Physics studies*, *JHEP* **08** (2018) 028 [1805.01747].

[640] M. Masud, S. Roy and P. Mehta, *Correlations and degeneracies among the NSI parameters with tunable beams at DUNE*, *Phys. Rev. D* **99** (2019) 115032 [1812.10290].

[641] P. Bakhti, A.N. Khan and W. Wang, *Sensitivities to charged-current nonstandard neutrino interactions at DUNE*, *J. Phys. G* **44** (2017) 125001 [1607.00065].

[642] M. Blennow, S. Choubey, T. Ohlsson, D. Pramanik and S.K. Raut, *A combined study of source, detector and matter non-standard neutrino interactions at DUNE*, *JHEP* **08** (2016) 090 [1606.08851].

[643] J.M. Berryman, A. de Gouvea, P.J. Fox, B.J. Kayser, K.J. Kelly and J.L. Raaf, *Searches for Decays of New Particles in the DUNE Multi-Purpose Near Detector*, *JHEP* **02** (2020) 174 [1912.07622].

[644] V. De Romeri, K.J. Kelly and P.A.N. Machado, *DUNE-PRISM Sensitivity to Light Dark Matter*, *Phys. Rev. D* **100** (2019) 095010 [1903.10505].

[645] P. Bakhti, Y. Farzan and M. Rajaee, *Secret interactions of neutrinos with light gauge boson at the DUNE near detector*, *Phys. Rev. D* **99** (2019) 055019 [1810.04441].

[646] I. Bischer and W. Rodejohann, *General neutrino interactions from an effective field theory perspective*, *Nucl. Phys. B* **947** (2019) 114746 [1905.08699].

[647] P. Ballett, T. Boschi and S. Pascoli, *Searching for MeV-scale Neutrinos with the DUNE Near Detector*, in *Prospects in Neutrino Physics*, pp. 124–128, 3, 2018 [1803.10824].

[648] S. Choubey and D. Pramanik, *Constraints on Sterile Neutrino Oscillations using DUNE Near Detector*, *Phys. Lett. B* **764** (2017) 135 [1604.04731].

[649] L. Alvarez Ruso et al., *Research and Development for Near Detector Systems Towards Long Term Evolution of Ultra-precise Long-baseline Neutrino Experiments*, 1901.04346.

[650] A. Bashyal, *DUNE and MINERvA Flux Studies and a Measurement of the Charged-Current Quasielastic Antineutrino Scattering Cross Section with $<E_\nu>$ ˜ 6 GeV on a CH Target*, Ph.D. thesis, Oregon State U., 2021. 10.2172/1779472.

[651] DUNE collaboration, *Long-baseline neutrino oscillation physics potential of the DUNE experiment*, *Eur. Phys. J. C* **80** (2020) 978 [2006.16043].

[652] Bishai, ""http://home.fnal.gov/ljf26/DUNEFluxes/"."

[653] A. Donini, M.B. Gavela, P. Hernandez and S. Rigolin, *Neutrino mixing and CP violation*, *Nucl. Phys. B* **574** (2000) 23 [hep-ph/9909254].

[654] *Neutrino Non-Standard Interactions: A Status Report*, vol. 2, 2019. 10.21468/SciPostPhysProc.2.001.

[655] O. Miranda, M. Tortola and J. Valle, *Are solar neutrino oscillations robust?*, *JHEP* **10** (2006) 008 [hep-ph/0406280].

[656] M.D. M. Bishai, "Optimization of the lbnf/dune beamline for tau neutrinos."

[657] P.B. Denton, J. Gehrlein and R. Pestes, *CP -Violating Neutrino Nonstandard Interactions in Long-Baseline-Accelerator Data*, *Phys. Rev. Lett.* **126** (2021) 051801 [2008.01110].

[658] S.S. Chatterjee and A. Palazzo, *Nonstandard Neutrino Interactions as a Solution to the NO$\nu$A and T2K Discrepancy*, *Phys. Rev. Lett.* **126** (2021) 051802 [2008.04161].

[659] S.S. Chatterjee and A. Palazzo, *Interpretation of NO$\nu$A and T2K data in the presence of a light sterile neutrino*, 2005.10338.

[660] L.S. Miranda, P. Pasquini, U. Rahaman and S. Razzaque, *Searching for non-unitary neutrino oscillations in the present T2K and NO$\nu$A data*, *Eur. Phys. J. C* **81** (2021) 444 [1911.09398].

[661] A. de Gouvêa, G. Jusino Sánchez and K.J. Kelly, *Very Light Sterile Neutrinos at NOvA and T2K*, 2204.09130.

[662] R. Majhi, D.K. Singha, K.N. Deepthi and R. Mohanta, *Vector leptoquark $U_3$ and CP violation at T2K, NOvA experiments*, 2205.04269.

[663] Z. Maki, M. Nakagawa and S. Sakata, *Remarks on the unified model of elementary particles*, *Prog. Theor. Phys.* **28** (1962) 870.

[664] P.B. Denton and J. Gehrlein, *A Statistical Analysis of the COHERENT Data and Applications to New Physics*, *JHEP* **04** (2021) 266 [2008.06062].

[665] A.S. Joshipura and S. Mohanty, *Constraints on flavor dependent long range forces from atmospheric neutrino observations at super-Kamiokande*, *Phys. Lett. B* **584** (2004) 103 [hep-ph/0310210].

[666] J.A. Grifols and E. Masso, *Neutrino oscillations in the sun probe long range leptonic forces*, *Phys. Lett. B* **579** (2004) 123 [hep-ph/0311141].

[667] M.C. Gonzalez-Garcia, P.C. de Holanda, E. Masso and R. Zukanovich Funchal, *Probing long-range leptonic forces with solar and reactor neutrinos*, *JCAP* **01** (2007) 005 [hep-ph/0609094].

[668] A. Bandyopadhyay, A. Dighe and A.S. Joshipura, *Constraints on flavor-dependent long range forces from solar neutrinos and KamLAND*, *Phys. Rev. D* **75** (2007) 093005 [hep-ph/0610263].

[669] A. Samanta, *Long-range Forces : Atmospheric Neutrino Oscillation at a magnetized Detector*, *JCAP* **09** (2011) 010 [1001.5344].

[670] A.Y. Smirnov and X.-J. Xu, *Wolfenstein potentials for neutrinos induced by ultra-light mediators*, *JHEP* **12** (2019) 046 [1909.07505].

[671] P. Coloma, M.C. Gonzalez-Garcia and M. Maltoni, *Neutrino oscillation constraints on U(1)' models: from non-standard interactions to long-range forces*, *JHEP* **01** (2021) 114 [2009.14220].

[672] F.J. Escrihuela, O.G. Miranda, M.A. Tortola and J.W.F. Valle, *Constraining nonstandard neutrino-quark interactions with solar, reactor and accelerator data*, *Phys. Rev. D* **80** (2009) 105009 [0907.2630].

[673] M.C. Gonzalez-Garcia and M. Maltoni, *Determination of matter potential from global analysis of neutrino oscillation data*, *JHEP* **09** (2013) 152 [1307.3092].

[674] Y. Farzan and M. Tortola, *Neutrino oscillations and Non-Standard Interactions*, *Front. in Phys.* **6** (2018) 10 [1710.09360].

[675] P.B. Denton and S.J. Parke, *Parameter symmetries of neutrino oscillations in vacuum, matter, and approximation schemes*, *Phys. Rev. D* **105** (2022) 013002 [2106.12436].

[676] P.B. Denton, *A Return To Neutrino Normalcy*, 2003.04319.

[677] K. Babu, G. Chauhan and P. Bhupal Dev, *Neutrino Non-Standard Interactions via Light Scalars in the Earth, Sun, Supernovae and the Early Universe*, *Phys. Rev. D* **101** (2020) 095029 [1912.13488].

[678] J. Venzor, A. Pérez-Lorenzana and J. De-Santiago, *Bounds on neutrino-scalar nonstandard interactions from big bang nucleosynthesis*, *Phys. Rev. D* **103** (2021) 043534 [2009.08104].

[679] A. Medhi, M.M. Devi and D. Dutta, *Imprints of scalar NSI on the CP-violation sensitivity using synergy among DUNE, T2HK and T2HKK*, 2209.05287.

[680] T. Sarkar, *Effect of non-unitary neutrino mixing in Lorentz violation and dark NSI*, 2209.10233.

[681] K.J. Kelly, P.A.N. Machado, S.J. Parke, Y.F. Perez-Gonzalez and R.Z. Funchal, *Neutrino mass ordering in light of recent data*, *Phys. Rev. D* **103** (2021) 013004 [2007.08526].

[682] E. Di Valentino, S. Gariazzo and O. Mena, *Most constraining cosmological neutrino mass bounds*, *Phys. Rev. D* **104** (2021) 083504 [2106.15267].

[683] T2K collaboration, *Search for short baseline $\nu_e$ disappearance with the T2K near detector*, *Phys. Rev. D* **91** (2015) 051102 [1410.8811].

[684] V.V. Barinov et al., *Results from the Baksan Experiment on Sterile Transitions (BEST)*, *Phys. Rev. Lett.* **128** (2022) 232501 [2109.11482].

[685] P.B. Denton, *Sterile Neutrino Search with MicroBooNE's Electron Neutrino Disappearance Data*, *Phys. Rev. Lett.* **129** (2022) 061801 [2111.05793].

[686] S. Hagstotz, P.F. de Salas, S. Gariazzo, M. Gerbino, M. Lattanzi, S. Vagnozzi et al., *Bounds on light sterile neutrino mass and mixing from cosmology and laboratory searches*, *Phys. Rev. D* **104** (2021) 123524 [2003.02289].

[687] A. Dighe and S. Ray, *Signatures of heavy sterile neutrinos at long baseline experiments*, *Phys. Rev. D* **76** (2007) 113001 [0709.0383].

[688] B. Bhattacharya, A.M. Thalapillil and C.E.M. Wagner, *Implications of sterile neutrinos for medium/long-baseline neutrino experiments and the determination of $\theta_{13}$*, *Phys. Rev. D* **85** (2012) 073004 [1111.4225].

[689] D. Hollander and I. Mocioiu, *Minimal 3+2 sterile neutrino model at LBNE*, *Phys. Rev. D* **91** (2015) 013002 [1408.1749].

[690] R. Gandhi, B. Kayser, M. Masud and S. Prakash, *The impact of sterile neutrinos on CP measurements at long baselines*, *JHEP* **11** (2015) 039 [1508.06275].

[691] A. Palazzo, *3-flavor and 4-flavor implications of the latest T2K and NO$\nu$A electron (anti-)neutrino appearance results*, *Phys. Lett. B* **757** (2016) 142 [1509.03148].

[692] J.M. Berryman, A. de Gouvêa, K.J. Kelly and A. Kobach, *Sterile neutrino at the Deep Underground Neutrino Experiment*, *Phys. Rev. D* **92** (2015) 073012 [1507.03986].

[693] D. Dutta, R. Gandhi, B. Kayser, M. Masud and S. Prakash, *Capabilities of long-baseline experiments in the presence of a sterile neutrino*, *JHEP* **11** (2016) 122 [1607.02152].

[694] K.J. Kelly, *Searches for new physics at the Hyper-Kamiokande experiment*, *Phys. Rev. D* **95** (2017) 115009 [1703.00448].

[695] M. Ghosh, S. Gupta, Z.M. Matthews, P. Sharma and A.G. Williams, *Study of parameter degeneracy and hierarchy sensitivity of NO$\nu$A in presence of sterile neutrino*, *Phys. Rev. D* **96** (2017) 075018 [1704.04771].

[696] S. Choubey, D. Dutta and D. Pramanik, *Imprints of a light Sterile Neutrino at DUNE, T2HK and T2HKK*, *Phys. Rev. D* **96** (2017) 056026 [1704.07269].

[697] S.K. Agarwalla, S.S. Chatterjee and A. Palazzo, *Signatures of a Light Sterile Neutrino in T2HK*, *JHEP* **04** (2018) 091 [1801.04855].

[698] S. Gupta, Z.M. Matthews, P. Sharma and A.G. Williams, *The Effect of a Light Sterile Neutrino at NO$\nu$A and DUNE*, *Phys. Rev. D* **98** (2018) 035042 [1804.03361].

[699] S. Kumar Agarwalla, S.S. Chatterjee and A. Palazzo, *Physics potential of ESS$\nu$SB in the presence of a light sterile neutrino*, *JHEP* **12** (2019) 174 [1909.13746].

[700] R. Majhi, C. Soumya and R. Mohanta, *Light sterile neutrinos and their implications on currently running long-baseline and neutrinoless double beta decay experiments*, *J. Phys. G* **47** (2020) 095002 [1911.10952].

[701] Y. Reyimuaji and C. Liu, *Prospects of light sterile neutrino searches in long-baseline neutrino oscillations*, *JHEP* **06** (2020) 094 [1911.12524].

[702] M. Ghosh, T. Ohlsson and S. Rosauro-Alcaraz, *Sensitivity to light sterile neutrinos at ESSnuSB*, *JHEP* **03** (2020) 026 [1912.10010].

[703] J.T. Penedo and J.a. Pulido, *Baseline and other effects for a sterile neutrino at DUNE*, 2207.02331.

[704] K. Goldhagen, M. Maltoni, S.E. Reichard and T. Schwetz, *Testing sterile neutrino mixing with present and future solar neutrino data*, *Eur. Phys. J. C* **82** (2022) 116 [2109.14898].

[705] (IceCube Collaboration)*, IceCube collaboration, *All-flavor constraints on nonstandard neutrino interactions and generalized matter potential with three years of IceCube DeepCore data*, *Phys. Rev. D* **104** (2021) 072006 [2106.07755].

[706] DUNE collaboration, *Prospects for beyond the Standard Model physics searches at the Deep Underground Neutrino Experiment*, *Eur. Phys. J. C* **81** (2021) 322 [2008.12769].